2ND UJNR TSUNAMI WORKSHOP

HONOLULU, HAWAII
5-6 November 1990

PROCEEDINGS

NGDC Key to Geophysical Records Documentation No. 24

2ND UJNR TSUNAMI WORKSHOP

HONOLULU, HAWAII
5-6 November 1990

PROCEEDINGS

Edited by

Ann M. Brennan
and
James F. Lander

CONTENTS

**2ND UJNR Tsunami Workshop
Honolulu, Hawaii, 5-6 November 1990**

INTRODUCTION

This Proceedings contains the formal papers or abstracts presented by the 2nd UJNR Tsunami Workshop held at the East-West Center of the University of Hawaii at Manoa on November 5 and 6, 1990, and an abstraction of the discussions. The UJNR is the commonly use notation for the United States – Japan Natural Resources Development Program, a part of the US – Japan Cooperative Sciences Program. The UJNR organizes its work through some 17 panels, one of which, the Panel on Wind and Seismic Effects created in 1969, is concerned with tsunamis among many other topics. The annual Joint Meeting, essentially by government scientists, is too broad in scope to allow in-depth scientific exchanges on any single topic. This need is met in several ways: exchanging publications and information, scientific visits and topical workshops.

The 1st UJNR Tsunami Workshop was held in Tsukuba, Japan, on May 12-13, 1983, with Drs. Yoshimi Goda of the Japanese Port and Harbor Research Institute and Harold Loomis of the University of Hawaii as co-conveners. It was understood that the U.S. would organize a second workshop after an interval of a few years. However, in the absence of a fixed schedule, the interval between workshops lengthened beyond our intentions. This was added to by delays to find a convenient time and to allow for necessary budgetary lead time.

The workshop/symposium was organized to address three topics:

A: Predictions and Observations of Tsunami Behavior in Coastal Waters and on Land.

B: Applications of Numerical Modeling to Improve Travel Time Predictions, Source Region Definition, Inundations, and Run-Up Prediction.

C: Protective Measures in Japan and the U.S. with regard to the use of Numerical Models and the Design Tsunami Concept.

These topics are similar to those of the 1st UJNR Tsunami Workshop and it was thought to illustrate the progress in these core areas over the intervening years and to emphasize numerical modeling.

The format called for Japanese and U.S. scientists to present their papers with time for individual discussion of each paper. At the end of each topic a longer general discussion was held on the broad area in order to add a workship environment into the symposium setting. The sessions were taped primarily to get the sense of the discussions which are also presented here in brief. Also, much good interaction continued during breaks and out of the reach of our recorders.

Field visits were held both before and after the main work of the workshop including a visit to the Pacific Tsunami Warning Center at Ewa Beach, Oahu, with a detailed briefing by Dr. Gordon Burton, the Director, and to Hilo, Hawaii, where both the tsunami hazard and the on-going destructive volcanic eruption are of geophysical interest. Mr. Harry Kim of the Hawaiian Civil Defense at Hilo discussed both hazards. Visits were made to the Hawaiian Volcano Observatory and the on-going disaster site at Kalapana.

These proceedings were compiled both as a more permanent record for the participants and to provide a copy of the work for others who could not attend.

Co-conveners
James F. Lander
University of Colorado, CIRES
Boulder, CO

Takaaki Uda
Public Works Research Institute
Tsukuba, Japan

February, 1990

ACKNOWLEDGMENTS

2nd UJNR Tsunami Workshop, Honolulu, HI. 5-6 November 1990

Standing - Left to Right: Shigeru Yamaki, Zygmund Kowalik, Eddie Bernard, Sin-Iti Iwasaki, Frank González, Clifford Astill, George Carrier, Gerald Hebenstreit, Kenji Satake, James Lander, Jane Preuss, Costas Synolakis, Patricia Lockridge, Emile Okal, Charles Mader, Gordon Burton, Harry Yeh.

Kneeling - Left to Right: Takaaki Uda, Chiaki Goto, Nobue Shuto, Harold Loomis, Hideo Matsutomi, Fumihiko Imamura, Yoshinobu Tsuji, Masami Okada, Philip Liu.

AGENDA

2ND UJNR TSUNAMI WORKSHOP
EAST-WEST CENTER - UNIVERSITY OF HAWAII, HONOLULU

<u>November 5, 1990</u>

8:30   Opening remarks, **J. Lander and T. Uda**, co-conveners.

   Topic A: Predictions and Observations of Tsunami Behavior in Coastal Waters
              and on Land, **J. Lander**, moderator, 1st session.

8:50   **Tsuji, Y.**, Decay of Initial Crest of the 1960 Chilean Tsunami: Scattering of Tsunami
       Waves Caused by Sea Mounts and the Effects of Dispersion.

9:15   **Gonzalez, F. and Ye.A. Kulikov**, On Frequency Modulation Observed in Two PacTOP
       Deep Ocean Tsunami Records

9:40   **Iwasaki, S.**, On the Generation Mechanism of the Low Frequency T Phase due to
       Tsunamigenic Earthquakes.

10:05   **Hebenstreit, G. and M.S. Moustafa**, Modeling Implications of the 1985 Chilean
       Tsunami.

10:30   Coffee Break

   Topic A (cont.)   **T. Uda**, moderator, 2nd session.

11:00   **Tsuji, Y., and T. Yanuma**, Observation of Standing Edge Waves Trapped on the Shelf
       of Makurazaki Coast.

11:25   **Lockridge, P.**, The Criteria for Identification of Tsunami Events Likely to Produce Far-
       Field Damage, A Data Application.

11:50   **Matsutomi, H.**, Impulsive Force of Timbers Drifted by Tsunamis.

12:15   Lunch

1:05   Group photograph

1:25   **Goto, C.**, Simulation Models of Timber and Oil Spread due to Tsunamis.

1:50   Round table discussion of Topic A led by the presenters with contributions from any
       attendee. **J. Lander and T. Uda**, moderators.

Topic B: Applications of Numerical Modeling to Improved Travel Time Predictions, Source Region Definition, Inundation, and Run-up Prediction, **Z. Kowalik**, moderator, 1st session.

2:30   **Yoon, S.B. and P. Liu**, Stem Waves and Hexagonal Wave Pattern in Shallow Water.

2:55   **Yamaki, S., and T. Uda**, Numerical Simulation and Experimentation on Tsunami Run-Up.

3:20   Coffee Break

3:50   **Carrier, G**, Tsunami Propagation from a Finite Source.

4:15   **Imamura, F. and N. Shuto**, Hydraulic and Numerical Experiments for Non-Linear Dispersive Long Waves in a Two-Dimensional Wave Basin.

4:40   **Yeh, H.**, On Momentum Exchange of a Tsunami Bore at a Shoreline.

5:05   **Loomis, H. G.**, Least Squares Estimations of a Tsunami Source From Wave Records.

5:30   Adjourn

November 6, 1990

Topic B: (cont.) G. Carrier, moderator, 2nd session

8:30   **Shuto, N., C. Goto and F. Imamura**, Numerical Simulation as a Means of Warning for Near-Field Tsunamis.

8:55   **Mader, C.**, Numerical and Hydraulic Modeling of Flooding.

9:20   **Uda, T.**, Experiment on Two Dimensional Transformation of Non-Linear Long Waves Propagating on Slope.

9:45   **Kowalik, Z.**, Numerical Computation of the Tsunami Run-Up.

10:10   **Synolakis, C.**, Impressions from the First International Workshop on Long Wave Runup.

10:35   Coffee Break

11:05   Round table discussion of Topic B led by the presenters with contributions from any attendee. **G. Carrier, and Z. Kowalik**, moderators.

Topic C: Protective Measures in Japan and the U.S. with Regard to the Use of Numerical Models and the Design Tsunami Concept. **C. Mader**, moderator, 1st session.

11:50   **Curtis, G.**, Inundation and Tsunami Waves.

12:15   Lunch

Topic C (cont.): **G. Curtis**, moderator 2nd session

1:10   **Preuss, J.**, Urban Planning For Tsunami Hazards, Grays Harbor, Washington and Lima, Peru.

1:35   **Okada, M.**, Ocean Bottom Pressure Gauge for Tsunami Warning System in Japan.

2:00   **Okal, E., J. Talandier, and D. Reymond**, Automatic Estimations of Tsunami Risk Following a Distant Earthquake Using the Mantle Magnitude M_m.

2:25   **Satake, K.**, Real-Time Determination of Earthquake Source Parameters and Its Application to Tsunami Warnings.

2:50   **Bernard, E.**, Assessment of Project THRUST: Past, Present and Future.

3:15   Coffee Break

3:45   Round table discussion of Topic C led by the presenters with contributions from any attendee. **C. Mader and G. Curtis**, moderators.

4:30   Adjourn

PARTICIPANTS

Dr. Clifford J. Astill
Siting & Geotechnical Systems
Room 1130-B
Earthquake Hazard Mitigation/Engineering
    Directorate
National Science Foundation
1800 "G" Street N.W.
Washington, DC 20550
Tel: 202-357-9500
Fax: 202-357-9803 or 357-7745

Dr. Eddie Bernard
Director, PMEL
NOAA Bin C15700/Bldg. 3
7500 Sand Point way, N. E.
Seattle, Washington 98115-0070
Tel: 206-526-6800
Fax: 206-526-6815

Dr. Gordon Burton, Chief
Pacific Tsunami Warning Center
91-270 Fort Weaver Road
Ewa Beach, HI 96706
Tel: 808-689-8207
Fax: 808-689-4543

Dr. George Carrier
311 Pierce Hall
Harvard University
Cambridge, Ma 02138
Tel: 617-495-3288
Fax: 617-495-9837

Dr. George D. Curtis
Joint Institute for Marine
    and Atmospheric Research
University of Hawaii at Manoa
1000 Pope Road
Honolulu, HI 96822
Tel: 808-956-7895
Fax: 808-942-9714

Dr. Frank Gonzalez
PMEL/NOAA
Bin C15700/Bldg. 3
7600 Sand Point Way, N.E.
Seattle, WA 98115-0070
Tel: 206-526-6803
Fax: 206-526-6815

Dr. C. Goto
Head, Ocean Energy Utilization Lab.
Hydraulic Eng. Div.
Port and Harbor Res. Inst
Min. of Transport
Nagase 3-1-1, Yokosuka Kanagawa 239
JAPAN
Tel: 0468-44-5014
Fax: 0468-42-9265

Mr. R.H. Hagemeyer, Director
National Weather Service, Pacific Region
P.O. Box 50027
Honolulu, HI 96850-4993
Tel: 808-541-1646
Fax: 808-541-1678

Dr. Gerald Hebenstreit
Science Applications Intl. Corp.
1710 Goodridge Drive
P.O. Box 1303
McLean, VA 22102
Tel: 703-448-6562
Fax: 703-821-3576

Res. Asso. Dr. F. Imamura
Dept. of Civil Engineering
Faculty of Engineering
Tohoku University
Aramaki-Aoba, Aoba
Sendai City, Miyagi 980
JAPAN
Tel: 0222-22-1800

Researcher S. Iwasaki
Hiratsuka Exp. Station
National Res. Inst. for Earth
    Science and Disaster Prevention
Nijigahama 9-2, Hiratsuka
Kanagawa 254
JAPAN
Tel: 0463-32-7159
Fax: 0463-33-3635

Dr. Zygmunt Kowalik
Institute of Marine Science
University of Alaska
Fairbanks, AK 99775-1080
Tel: 907-474-7753
Fax: 907-474-7204

*Mr. James F. Lander
Cooperative Institute for Research
    in Environmental Sciences
Campus Box 449
Boulder, CO 80309
Tel: 303-497-6446
Fax: 303-497-6513

Professor Philip Liu
Hollister Hall
Cornell University
Ithaca, NY 14853
Tel: 607-255-5090
Fax: 607-255-9004

Mrs. Patricia Lockridge
NOAA/NESDIS/NGDC/SEGD E/GC1
325 Broadway
Boulder, CO 80303
Tel: 303-497-6337
Fax: 303-497-6513

Professor Harold Loomis
Dept of Ocean Engineering
University of Hawaii at Manoa
Holmes Hall 402
2540 Dole Street
Honolulu, HI 96822
Tel: 808-956-7999
Fax: 808-956-3498

Dr. Charles L. Mader
Joint Institute for Marine and
    Atmospheric Research
University of Hawaii at Manoa
1000 Pope Road
Honolulu, HI 96822
Tel: 808-956-9855
Fax: 808-942-9714

Res. Assoc. Dr. H. Matsutomi
Dept. of Civil Engineering
Mining College
Akita University
Tegata-gakuen-cho 1-1
Akita City, Akita 010
JAPAN
Tel: 0188-33-5261
Fax: 0188-34-9708

Dr. Dennis Moore, Director
Joint Institute for Marine and Atmospheric
    Research
1000 Pope Road
University of Hawaii at Manoa
Honolulu, HI 96822
Tel: 808-956-8083
Tex: 808-956-4104

Mr. M. Okada
Head, First Lab., Seismology
    and Volcanology Div.
Meteorological Res. Inst.
Meteorological Agency
Nagamine 1-1 Tsukuba, Ibaraki 305
JAPAN
Tel: 0298-51-7111
Fax: 0298-51-3730

Professor Emile Okal
Department of Geological Sciences
Northwestern University
Evanston, IL 60201
Tel: 708-491-3194
Fax: 708-491-8060

Dr. George Pararas-Carayannis
Int'l Tsunami Information Center
P.O. Box 50027
Honolulu, HI 96850
Tel: 808-541-1657
Fax: 808-541-1678

Dr. Jane Preuss
Urban Regional Research
Suite 1000, Tower Bldg.
1809 Seventh Avenue
Seattle, WA 98101
Tel: 206-624-1669
Fax: 206-626-5324

Dr. Kenji Satake
Dept. of Geological Sciences
University of Michigan
1006 C.C. Little Bldg.
Ann Arbor, MI 48109-1063
Tel: 313-764-1435
Fax: 313-763-4690

Prof. N. Shuto
Dept. of Civil Engineering
Faculty of Engineering
Tohoku University
Aramaki-Aoba, Aoba
Sendai City, Miyagi 980
JAPAN
Tel: 0222-22-1800

Professor Costas Synolakis
Kaprelian Hall
University of Southern California
Los Angeles, CA 90089-2531
Tel: 213-743-7054
Fax: 213-744-1426

Asso. Prof. Y. Tsuji
Earthquake Res. Inst.
University of Tokyo
Yayoi 1-1-1, Bunkyoku
Tokyo 113, JAPAN
Tel: 03-812-2111 (ex. 5724)
Fax: 03-816-1159

*Dr. T. Uda
Head, Coastal Eng. Div.
Public Works Res. Inst.
Ministry of Construction
Asahi 1, Tsukuba, Ibaraki 305
JAPAN
Tel: 0298-64-2211
Fax: 0298-64-2840

Res. Eng. S. Yamaki
Dept. Coast and Ocean
INA Civil Eng Consultants Co., Ltd
Suidocho 3-1 Shinjuku
Tokyo 163, JAPAN
Tel: 03-268-8236
Fax: 03-268-8256

Professor Harry Yeh
Wilcox FX-10
University of Washington
Seattle, WA 98195
Tel: 206-685-8655
Fax: 206-685-3836

* Co-Conveners

TOPIC A: PREDICTIONS AND OBSERVATIONS OF TSUNAMI BEHAVIOR IN COASTAL WATERS AND ON LAND

J. Lander and T. Uda, moderators

DECAY OF THE INITIAL CREST OF THE 1960 CHILEAN TSUNAMI SCATTERING OF TSUNAMI WAVES CAUSED BY SEA MOUNTS AND THE EFFECTS OF DISPERSION

Yoshinobu Tsuji
Earthquake Research Institute
University of Tokyo
Tokyo, Japan

Introduction

The Chilean tsunami of 24 May 1960 hit the Japanese Islands about 24 hours after the occurrence of the mainshock at the Chilean coast. Nakamura and Watanbe (1961) pointed out that at about 30 tidal stations on the south coasts of the Japanese Islands openly facing to the Pacific Ocean, one or two small crest(s) appeared as the initial motion of the tsunami before the arrival of the big waves and they called it a "forerunner". They suggested that the cause of the generation of the forerunner was a kind of inducted oscillation due to the main wave on the continental shelf. In contrast to that, Imamura et al. (1990) made a numerical simulation of the propagation of the Chilean tsunami by using a mesh scheme covering the whole Pacific Ocean without neglecting the influence of the dispersion and showed that the co-called forerunner is not the induced motion, but the initial crest itself which lost almost all of its energy on the way to the Japanese Islands.

In the present study we consider the reason for the decay of the initial crest of the 1960 Chilean tsunami and discuss the influence of scattering of progressive tsunami waves caused by sea mounts and the influence of the dispersion.

Scattering of Tsunami Wave Caused by Sea Mounts

Form of the scattering wave

On the Pacific Ocean bed many sea mounts and sea rises exist (Figure 1). First, we consider the scattering of a tsunami wave caused by such mounts or rises. We assume the form of the sea mount to be cylindrically symmetric and the section having the form of the normal distribution as

$$\bar{h} = H \exp\left(-\frac{x^2+y^2}{2r_0^2}\right) \tag{1}$$

where H is height of the mount, and $4r_0$ is the effective diameter of the sea mount. The wave profile of the incident tsunami is also assumed in the form of normal distribution as

$$\zeta_0 = A \exp\left\{-\frac{(x-c_0 t)^2}{2\sigma^2}\right\} \tag{2}$$

where c_0 is the velocity of the tsunami and is equal to $sqrt$ $(g\bar{h})$, and the effective length of the

13

tsunami (L) is 4σ. The Fourier transformation of (2) is expressed as

$$\zeta_0 = Re\left\{\sqrt{\frac{2}{\pi}}A\sigma\int_0^\infty \exp\left(-\frac{k^2{}_0\sigma^2}{2}\cdot\right)e^{ik_0(x-c_0t)}dk_0\right\} \qquad (3)$$

If we take one element for wave number k_0, we have

$$\zeta_0 = B(k_0)e^{ik_0(x-c_0t)} = B(k_0)e^{ik_0x}e^{-i\omega t},$$

or we can write it as

$$\zeta_0 = \eta_0(k_0)e^{-i\omega t} \qquad (4)$$

where ω is the angular frequency given as

$$\omega = c_0k_0 = \sqrt{gh_0}k_0 \qquad (5)$$

We can restore the form of the actual waves by integrating on wave number k.

Figure 1. Sea bottom topography of the northwest part of the Pacific Ocean.
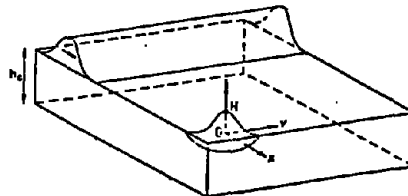
Figure 2. Models of a sea mount/rise and of the incident tsunami.

We assume long wave approximation while neglecting viscosity, bottom friction and the rotation of the earth, then the equation of continuity takes the form

$$-\frac{\partial \zeta}{\partial t} = \frac{\partial}{\partial x}(uh) + \frac{\partial}{\partial y}(vh)$$

(6)

where ζ is sea surface displacement, and u and v are the $x-$ and $y-$ components of the sea water particles. The equations of motion for the x and y directions are expressed simply as

$$\begin{cases} \dfrac{\partial u}{\partial t} = -g\dfrac{\partial \zeta}{\partial x}, \\ \dfrac{\partial v}{\partial t} = -g\dfrac{\partial \zeta}{\partial y}, \end{cases}$$

(7-a, b)

respectively. Eliminating u and v from equations (6) and (7a-b) we have

$$g\frac{\partial^2 \zeta}{\partial x^2} = \frac{\partial}{\partial x}\left(h\frac{\partial \zeta}{\partial x}\right) + \frac{\partial}{\partial y}\left(h\frac{\partial \zeta}{\partial y}\right)$$

(8)

As the component of the incident tsunami waves with wave number k_0 has the angular frequency ω, the induced motion caused by the component also has the same frequency, so we may put it in the form

$$\zeta = \eta(x,y)e^{-i\omega t}$$

(9)

We put

$$\omega^2/gh = k^2$$

(10)

then (8) turns out to be

$$\nabla^2 \eta + k^2 \eta = -(1/h)\nabla h \cdot \nabla \eta$$

(11)

where ∇, ∇^2 are the two dimensional nabla and Laplacian operators for horizontal space.

We assume the surface displacement of original wave (η_0) is a value of one order bigger than that of the induced wave (η_1). Naturally the original incident wave has no component in the y direciton, then we may express the total sea surface displacement as

$$\eta = \eta_0(x) + \eta_1(x,y)$$

(12)

. As the incident tsunami wave runs in the sea with a flat bed, without the effect of the sea mount, the following equation holds

$$\nabla^2 \eta_0 + k_0^2 \eta_0 = 0$$

(13)

15

We also assume the height of the sea mount, H, is one order smaller in comparison to the depth, h_0. Then h $(= H_0 - h)$ also takes one order of value smaller of h_0, so k takes approximately the form

$$k^2 = k_0^2 h_0/h = k_0^2(1 - \bar{h}/h_0)^{-1} \doteqdot k_0^2(1 + \bar{h}/h_0)$$

Substitute this equation and (12) into (11), we obtain

$$\nabla^2\eta_1 + k_0^2\eta_1 = -(\bar{h}_x\eta_{0x} + k_0^2\bar{h}\eta_0)/h_0 \quad . \tag{14}$$

Green's function for the left side of (14) is

$$\nabla^2 G + k_0^2 G = -\delta(X - x, Y - y) \quad . \tag{15}$$

We only select the solution of outgoing wave for (15) as

$$G = i/4 \cdot H_0^{(1)}(k_0|R - r|) \quad , \tag{16}$$

where $H_0^{(1)}$ is the zero-th order Hankel's function of the first kind. We have the solution of (14) in the form

$$\eta_1(X, Y) = \frac{i}{4h_0}\int_{-\infty}^{\infty}\int_{-\infty}^{\infty}(-\bar{h}_x\eta_{0x} + k_0^2\bar{h}\eta_0)\; H_0^{(1)}(k_0|R - r|)dxdy, \tag{17}$$

where $R(X, Y)$ and $r(x, y)$ are the location vectors of the observational point and the integral variables. By using (1) we have

$$\bar{h}_x = (-x/r_0^2)\bar{h}, \quad \eta_{0x} = ik_0\eta_0$$
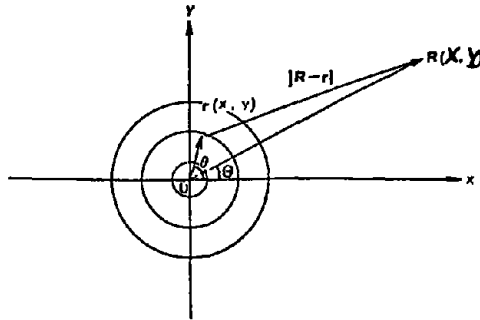
Figure 3. Vectors R and r of the observation and integral points with sea mount.

Then, (17) turns out to be

$$\eta_1(X, Y) = \frac{k_0}{4h_0}\int_{-\infty}^{\infty}\int_{-\infty}^{\infty}\left(-\frac{x^2}{r^2} + ik_0\right)\bar{h}\eta_0\; H_0^{(1)}(k_0|R - r|)dxdy \tag{18}$$

16

After integrating (18) by k_0, we finally obtain the solution for the surface displacement of the scattering wave as

$$\zeta_1(X, Y, t)=\int_0^\infty \eta_1(k)e^{-i\omega t}dk_0 \quad =\sqrt{\frac{2}{\pi}}\frac{A\sigma H}{4h_0}\int_0^\infty k_0 \exp\left(-\frac{k^2\sigma^2}{2}-ic_0k_0t\right)$$

$$\times\int_{-\infty}^\infty\int_{-\infty}^\infty\left(-\frac{x}{r_0^2}+ik_0\right)\exp\left(-\frac{x^2+y^2}{2r_0^2}+ikx\right)H_0^{(1)}(k_0|R-r|)dxdydk_0 \qquad (19)$$

If we consider that the observation point is situated sufficiently apart from the center of the sea mount, then we can use the approximation for Hankel's function as

$$H_0^{(1)}(k_0|R-r|)=\sqrt{\frac{2}{\pi k_0|R-r|}} \exp\, i\left(k_0|R-r|-\frac{\pi}{4}\right) \qquad (20)$$

and moreover we use the relation approximately

$$|R-r|=\sqrt{R^2-2Rr\cos(\Theta-\theta)+r^2}\fallingdotseq R-r\cos(\Theta-\theta) \qquad (21)$$

where Θ and θ are the argument angles of vectors R and r respectively. We apply the approximation (21) in the exponential part of (20), and apply a more coarse approximation $|R-r| = R$ for that in the square root part. Then we obtain

$$\zeta_1=\frac{e^{-i(\pi/4)}A H\sigma}{2\pi h_0\sqrt{R}}\int_0^\infty k_0^{1/2}\exp\left\{-\frac{k_0^2\sigma^2}{2}+ik_0(R-c_0t)\right\}\int_{-\infty}^\infty\int_{-\infty}^\infty\left(-\frac{x}{r_0^2}+ik_0\right)$$

$$\times\exp\left\{-\frac{x^2+y^2}{2r_0^2}+ik_0x-ik_0r\cos(\Theta-\theta)\right\}dxdydk_0 \qquad (22)$$

We notice $r\cos(\Theta-\theta)=x\cos\Theta + y\sin\Theta$, then we have the equation that x and y integrals are separated as follows

$$\zeta_1=\frac{e^{-i(\pi/4)}A H\sigma}{2\pi h_0\sqrt{R}}\int_0^\infty k_0^{1/2}\exp\left\{-\frac{k_0^2\sigma^2}{2}+ik_0(R-c_0t)\right\}I_xI_ydk_0 \qquad (23)$$

where,

$$I_x=\int_{-\infty}^\infty\left(-\frac{x}{r_0^2}+ik_0\right)\exp\left\{-\frac{x^2}{2r_0^2}+ik_0(1-\cos\Theta)x\right\}dx$$

and

$$I_y=\int_{-\infty}^\infty\exp\left(-\frac{y^2}{2r_0^2}-ik_0y\sin\Theta\right)dy$$

Those integrals are analytically calculated as

$$I_x=i\sqrt{2\pi}\,k_0r_0\cos\Theta\exp\left\{-\frac{1}{2}r_0^2k_0^2(1-\cos\Theta)^2\right\}$$

$$I_y=\sqrt{2\pi}\,r_0\exp\left\{-\frac{1}{2}r_0^2k_0^2\sin^2\Theta\right\}$$

17

So we finally have the form of the scattered wave in the form of single integral for k_0 as

$$\zeta_1 = \frac{ie^{-i(\pi/4)}AH\sigma r_0^2}{h_0\sqrt{R}}\cos\Theta\int_0^\infty k_0^{3/2}\exp\left[-k_0^2\left\{r_0^2(1-\cos\Theta)+\frac{\sigma^2}{2}\right\}+ik_0(R-c_0t)\right]dk_0 \quad (24)$$

We can calculate the form of the scattered wave by a numerical calculation of (24), where t is the time measured from the instant that the center of the incident tsunami wave passes the summit of the mount. In (24) time, t, appears only in the form $(R-c_0t)$, which means that the scattered wave is radiated from the summit of the sea mount with the outgoing speed, c. The amplitude is multiplied by $R^{-\frac{1}{2}}$, so the height of the scattered wave decreases inversely proportional to the distance from the summit. As we give $\Theta = \pm \pi/2$, ζ_1 becomes zero, in the direction of the right angle of both sides, no scattered wave propagates.

Energy consideration

We next discuss the energy of the scattering wave. Given the equally partitioned law of energy in the linear theory of wave, it is enough that we consider the potential energy only. The potential energy of the incident wave per unit length is calculated as

$$E_I=\int_{-\infty}^\infty \zeta^2 dx = A^2\int_{-\infty}^\infty \exp\left\{-\frac{(x-c_0t)}{\sigma^2}\right\}dx=\sqrt{\pi}\,A^2\sigma \quad (25)$$

On the other hand the potential energy of the scattering wave is given as

$$E_S=\int_{-\infty}^\infty\int_{-\infty}^\infty\int_0^\infty\int_0^\infty \zeta_1(X,Y,k_0)\zeta_1{}^*(X,Y,k_0')dk_0dk_0'dXdY \quad (26)$$

We put (24) into (26) then we have

$$E_S=\frac{A^2H^2\sigma^2r_0^4}{h_0^2}\int_{-\infty}^\infty\int_{-\infty}^\infty\frac{\cos^2\Theta}{R}\int_0^\infty k_0^{3/2}k_0'^{3/2}\exp\left[-k_0^2\left\{r_0^2(1-\cos\Theta)+\frac{v^2}{2}\right\}-k_0'^2\left\{r_0^2(1-\cos\Theta)+\frac{\sigma^2}{2}\right\}\right]$$

$$\times\cos k_0(R-c_0t)\cos k_0'(R-c_0t)dk_0dk_0'dXdY$$

We re-write the relation in polar coordinates (R,Θ) and notice the relation

$$\int_0^\infty \cos k_0(R-c_0t)\cos k_0'(R-c_0t)dR=\frac{\pi}{2}\delta(k_0-k_0') \quad (27)$$

then we have

$$E_S=\frac{\pi A^2H^2\sigma^2r_0^4}{2h_0^2}\int_{-\pi}^\pi\cos^2\Theta\int_0^\infty k_0^3\exp\left[-2k_0^2\left\{r_0^2(1-\cos\Theta)+\frac{\sigma^2}{2}\right\}\right]dk_0d\Theta$$

$$=\frac{\pi A^2H^2\sigma^2r_0^4}{4h_0^2}\int_{-\pi}^\pi\frac{\cos^2\Theta d\Theta}{[2r_0^2(1-\cos\Theta)+\sigma^2]^2} \quad (28)$$

We write the integral in (28) as I and use transfer as

$$a=2r_0^2+\sigma^2,\quad b=2r_0^2,\quad \alpha=\sqrt{\frac{\sigma^2}{4r_0^2+\sigma^2}},\quad z=\tan\frac{\Theta}{2}$$

18

then we have

$$I=\frac{2}{(a^2+b^2)^2}\int_{-\infty}^{\infty}\frac{(z^2-1)^2}{(z^2+a^2)^2(z^2+1)}dz \qquad (29)$$

The integral can be calculated on the complex plane with the path of the semi-circle as Figure 4. Two poles exist at $Z=i$ and $z=ia$, and the latter is the pole of second order and the residues are given as

$$\text{Res}(i)=\frac{2}{i(\alpha^2-1)^2}, \quad \text{Res}(i\alpha)=\frac{(\alpha^2+1)(\alpha^4-6\alpha^2+1)}{4i\alpha^3(1-\alpha^2)^2}$$

and

$$I=\frac{\pi}{(a+b)^2}\frac{(\alpha^4+2\alpha^3-2\alpha^2+2\alpha+1)}{\alpha^3(\alpha+1)^2}$$
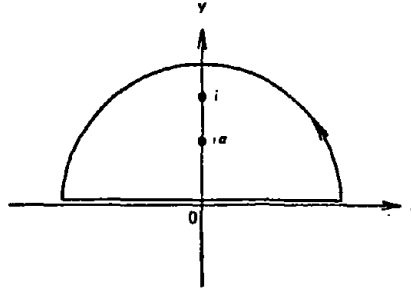
Figure 4. Integral path of (29) and the locations of the poles.

The potential energy of the scattering wave finally takes the form

$$E_S=\frac{\pi^2 A^2 H^2\sigma^2 r_0^4}{4h_0^2(4r_0^2+\sigma^2)^2}\frac{(\alpha^4+2\alpha^3-2\alpha^2+2\alpha+1)}{\alpha^3(\alpha+1)^2} \qquad (30)$$

Here we define "scattering length l by E_s/E_I, which is given by

$$l=E_S/E_I=\frac{\pi^{3/2}H^2\sigma^2 r_0^4}{4h_0^2(4r_0^2+\sigma^2)^2}\frac{(\alpha^4+2\alpha^3-2\alpha^2+2\alpha+1)}{\alpha^3(\alpha+1)^2} \qquad (31)$$

In order to make it convenient for concrete calculations, we deform as

$$l=\frac{\pi^{3/2}}{4}\left(\frac{H}{h_0}\right)^2\left(\frac{r_0}{\sigma}\right)^3 r_0 f\left(\frac{\sigma}{r_0}\right)\doteqdot 1.392\left(\frac{H}{h_0}\right)^2\left(\frac{r_0}{\sigma}\right)^3 r_0 f\left(\frac{\sigma}{r_0}\right) \qquad (32)$$

19

The relationship between σ/r_0 and $f(\sigma/r_0)$ in (32) is shown in Figure 5.
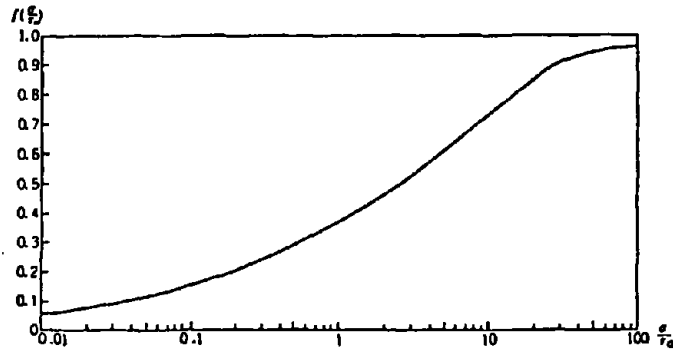
Figure 5. Relationship between σ/r_0 and (σ/r_0) in the equation (32).

As we can see the relationship between σ/r_0 and $f(\sigma/r_0)$, the function f gives a moderate number between zero to unity; we can roughly say that the energy of the scattered wave is proportional to the square of the ratio of the height of the sea mount to the depth of surrounding sea, the fourth power of the diameter of sea mount, and is inversely proportional to the third power of the wave length of the incident tsunami.

Direction of the scattering wave

Equation (28) gives the direction of the scattering wave. The direction is given by

$$E_S(\theta) = \frac{\pi A^2 H^2 \sigma^2}{4 h_0^2} \frac{\cos^2 \theta}{\{2(1-\cos \theta) + \sigma^2/r_0^2\}^2}$$

and is shown in Figure 6. No energy is radiated perpendicular to the direction of the incident wave.
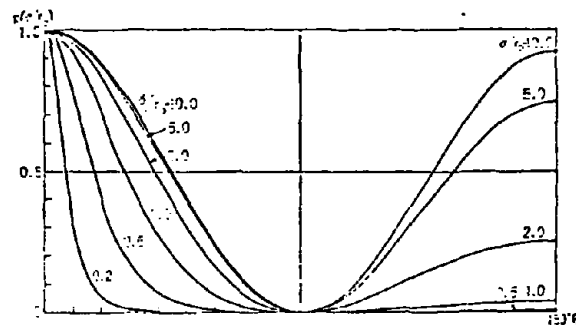
Figure 6. Direction of the radiated scattering wave given in (28).

20

Decay of the initial crest of the 1960 Chilean tsunami caused by the generation of scattering waves

As the scattering length is proportional to the fourth power of the diameter of sea mount, small sized sea mounts can be negligible in quantitative estimations of the decay of the initial crest. We observed forty sea rises between the Chilean coast and the Japanese islands (Figure 7). The result is that, at most, 40% of the initial crest was transferred to the energy of the scattering waves.
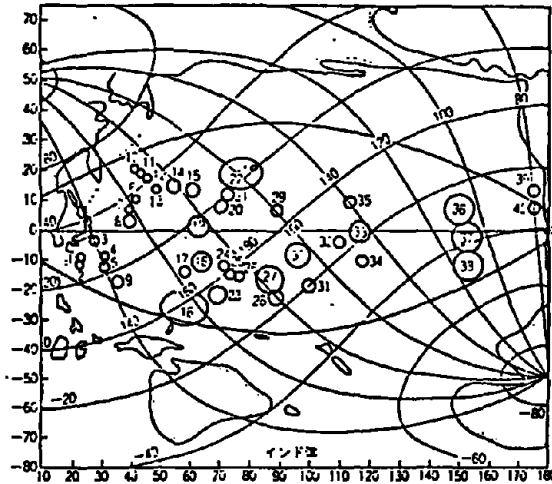
Figure 7. Locations of sea rises/mounts.

Table. 1 List of observed sea rises, name, location, diameter, depth of surrounding sea, height, scattering length (1), and defect ratio to the total energy.

番号 Nc	海山, 海膨名 NAME	位置 LOCATION	d (km)	周辺海域水深 (m)	比高 H (m)	散乱長 l (km)	欠損比率 (%)
1	九州・パラオ海嶺北端	29N 135E	200	5,000	4,500	3.2	0.1
2	大東海台	25N 133E	200	5,000	4,500	3.2	0.1
3	伊豆諸島	32N 140E	320	4,500	4,500	22.5	0.6
4	小笠原諸島	26N 144E	240	5,000	4,000	5.0	0.1
5	火山列島	23N 142E	300	5,000	4,000	11.4	0.3
6	北西太平洋海膨北部	38N 163E	250	5,500	3,000	2.7	0.1
7	〃 中央部	37N 159E	250	5,500	3,000	2.7	0.1
8	〃 南部	33N 158E	400	5,500	3,500	20.6	0.4
9	マリアナ諸島	16N 144E	300	5,000	4,500	14.4	0.3
10	推古海山	44N 170E	150	6,000	5,200	1.0	—
11	仁徳海山群	42N 170E	150	5,500	4,500	0.9	—
12	神功海山群	39N 171E	150	5,500	4,500	0.9	—
13	敏達海山	35N 171E	200	5,500	5,500	4.0	0.1
14	北ハワイ海膨	34N 178E	400	5,500	3,500	20.6	0.4
15	ミッドウェイ島	27N 177W	300	5,000	2,000	2.8	0.0
16	ソロモン海膨 Solomon	2S 160E	1,000	4,500	2,500	443.4	13.7
17	ビキニ環礁	10N 162E	300	5,500	2,500	3.7	0.1
18	マーシャル諸島北部	10N 170E	700	5,500	2,000	52.0	0.8
19	ウェーク・ネッカー海山群	19N 176E	800	5,000	1,000	25.6	0.4
20	ジョンストン環礁	19N 173E	300	5,000	3,000	6.4	0.1
21	同上北方海山群	20N 171E	300	5,000	3,000	6.4	0.1
22	ハワイ諸島 HAWAII	21N 163W	1,000	5,000	2,000	229.9	3.4
23	ナウル南方海膨	3S 170E	600	4,500	1,000	11.1	0.2
24	マキン島	3N 173E	250	4,000	4,000	9.1	0.2
25	ギルバート諸島北端	0N 173E	250	4,000	4,000	9.1	0.2
26	〃 南端	3S 175E	250	4,000	3,500	7.0	0.1
27	サモア諸島 Samoa	12S 170W	700	5,000	4,000	251.7	3.6
28	フィジー・トンガ	10S 180E	500	3,000	3,000	115.2	1.6
29	ベルミラ島	5N 160W	300	5,000	4,000	11.4	0.2
30	ダッグ諸島	9S 163W	900	4,500	1,000	48.4	0.7
31	アンチオープ環礁	20S 169W	300	5,000	1,000	0.7	—
32	タヒチ島	17S 150W	300	4,000	3,000	10.0	0.2
33	ツアモツ諸島	16S 144W	700	4,000	3,000	221.2	3.5
34	ラパ島	27S 145W	250	4,000	2,000	2.3	0.0
35	マルキーズ諸島	9S 140W	400	4,500	4,000	40.2	0.6
36	イースター島	28S 112W	1,000	4,000	1,200	129.3	3.2
37	東太平洋海膨	38S 111W	1,000	4,000	1,000	89.8	2.3
38	同上南部	46S 114W	1,000	4,500	1,000	70.9	1.9
39	サンフェルナンデス島	27S 80W	350	3,500	1,000	2.6	—
40	ファンフェルナンデス島	33S 80W	350	3,500	1,500	5.7	0.4

TOTAL DEFECT 40.1%

Influence of Dispersion

Next we consider the influences of dispersion for a distant tsunami. Pelinovskii (1982) discussed the details of this problem.

We can consider the propagation of a tsunami to the second order approximation of linearity and dispersion as the *KdV* equation as

$$\eta_t + C_0\eta_x + \frac{3}{2}\frac{C_0}{D}\eta\,\eta_x + \frac{1}{6}C_0D^2\eta_{xxx} = 0 \qquad (33)$$

In the present problem linearity can be neglected and so we have

$$\eta_t + C_0\eta_x + C_0D^2/6\ \eta_{xxx} = 0 \qquad (34)$$

If the surface displacement can be expressed in the form

$$\eta = \int u(k)\cdot\sin(kx - \sigma t)\,dk \qquad (35)$$

by using (34) we have the relation between k and σ as

$$\sigma = C_0k - C_0D^2/6\ k^3 \qquad (36)$$

We give the initial tsunami in the rectangular form, taken in the Fourier transferred form as

$$\eta_0 = -2/\pi\int_0^\infty\{\cos(ka) - \cos(kb)\}\sin(kx)\,dk \qquad (37)$$

The exact solution of (34) in the initial form as (37) takes form as

$$\eta = -2/\pi\int_0^\infty\{\cos(ka) - \cos(kb)\}$$

$$\times\sin\{(kx - C_0t) + C_0D^2/6\cdot t\}\,dk \qquad (38)$$

By using the transfer as

$$k(a-b) = m, \qquad (a+b)/(a-b) = 1,$$

$$2C_0t/(a-b) = \tau, \quad 2D^2/\{3(a-b)^2\} = p$$

$$2x/(a-b) = \xi$$

we finally obtain the non-dimensional formula as

$$\eta = 4/\pi\int_0^\infty\sin(1m)\ \sin(m)\ \sin(m\xi + p\,\tau\,m^3)\,dm \qquad (39)$$

which is only a one dimensional integral and can be calculated numerically. Figure 8 is one of the results. With tsunamis, a significant percentage of the initial crests may lose their energy on the way to the Japanese Islands.
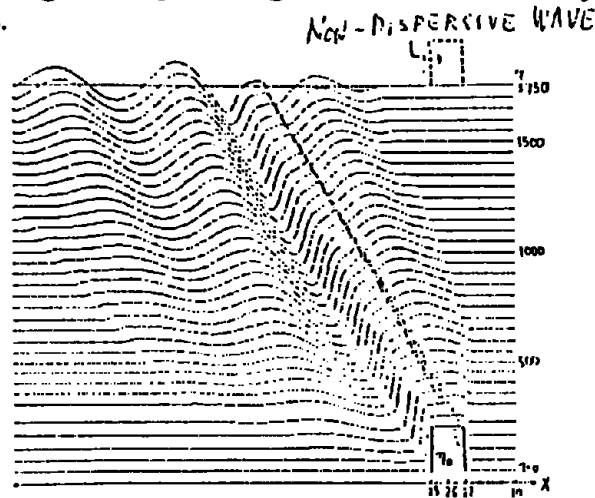
Figure 8. Numerical result of (39) for the case $L/D=0/1$, $l=26.0$.

Discussion

As for the short-distance tsunamis, we can regard the characteristics of the propagating tsunami wave as non-dispersive, simple long waves; but in cases of distant tsunamis traversing across the ocean, we should consider the generation of scattering waves due to sea rises and the influence of dispersion. Roughly speaking, the initial crest of the 1960 Chilean tsunami lost its energy by making scattering waves, about 40 percent, and more energy was lost due to the dispersion. The rotation of the earth makes the influence of the dispersion more effective. If we take the rotation of the earth, the dispersion effect is the most important factor of energy decay of the initial crest of a distant tsunami.

References

Carrier, G.F., 1966. Gravity waves on water of variable depth. *J. Fluid. Mech.*, 24, 4; 641-659.

Cox, C. and H. Sandstrom, 1962. Coupling of internal and surface waves in water of variable depth.

Hagiwara, H. and I. Kayano, 1961. Seismological data of Chilean Earthquakes in 1960, *Report on the Chilean Tsunami of May 24, 1960, as observed along the coast of Japan.* Committee for field investigation of the Chilean tsunami of 1960, Chairman: R. Takahashi. 35-45.

Hatori, T., 1966. Vertical displacement in a tsunami source area and the topography of the bottom. *Bull. Earthq. Res. Inst.*, 44, 1449-1464.

Imamura, F., T. Nagai, H. Takenaka, and N. Shuto 1990. Computer graphics for the study of transoceanic propagation of tsunamis. *Proc. 4th Pacific Congr. Marine Sci. and Tech. (PACON) 90*, 118-123.

Kajiura, K. 1961. On the partial reflection of water waves passing over a bottom of variable depth. *IUGG Monograph*, 24, 206-230.

23

Lautenbacher, C.C., 1970. Gravity wave refraction by islands. *J. Fluid Mech.*, 41(3), 655-672.

Munk, W., 1961. Some comments regarding diffusion and absorption of tsunamis. *IUGG Monograph*, 24, 53-72.

Nakamura, H. and H. Watanbe, 1961. Tsunami forerunner observed in case of the Chile tsunami of 1960. *Report on the Chilean Tsunami of May 24, 1960, as observed along the coast of Japan*. Committee for field investigation of the Chilean tsunami of 1960, Chairman: R. Takahashi, 82-99.

Pelinovskii, E.N., 1982. Non-linear dynamics of tsunami waves. *Inst. Apply. Phys., USSR Academy of Sci.*, p.226. (in Russian)

Takahashi, R. and T. Hatori, 1961. A summary report on the Chilean tsunami. *Report on the Chilean Tsunami of May 24, 1960, as observed along the coast of Japan*. Committee for field investigation of the Chilean tsunami of 1960, Chairman: R. Takahashi, 23-34.

Appendix Figures. Forerunner of the 1960 Chilean tsunami (After Nakamura and Watanbe, 1960)
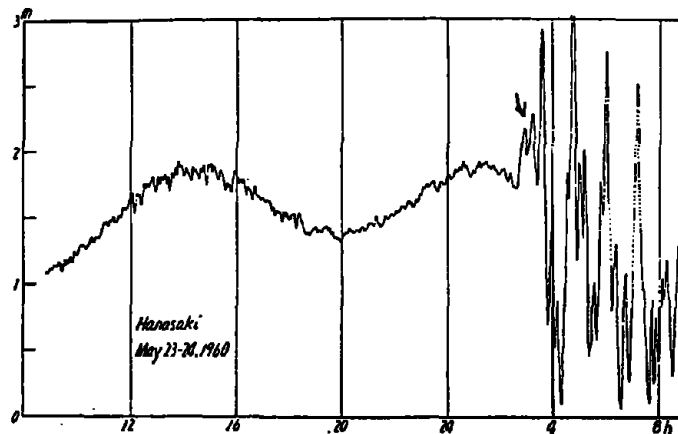
Marigrams for the Chile tsunami of May 24, 1960.
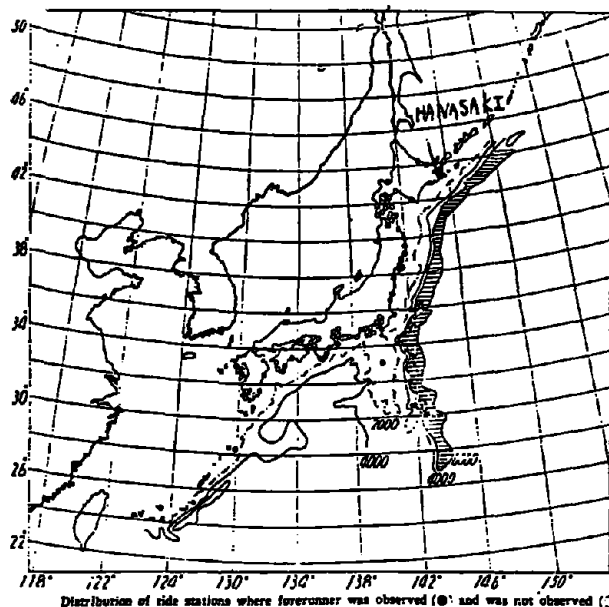
Distribution of tide stations where forerunner was observed (●) and was not observed (○)

Discussion

Comment: In response to a question about the effect of the Coriolis force, it was noted that Dr. Voit, a Russian tsunamist, had written about the effect of the rotation of the earth and pointed out that this increases the dispersion of tsunami waves. Therefore, a higher energy decay needs to be taken into account.

ON FREQUENCY MODULATION OBSERVED IN TWO PACTOP DEEP OCEAN TSUNAMI RECORDS

F.I. González
National Oceanic and Atmospheric Administration
Pacific Marine Environmental Laboratory
Seattle, WA, USA

Ye.A. Kulikov
State Oceanographic Institute
Moscow, USSR

Abstract

Deep ocean tsunami waveforms measured by PacTOP bottom pressure recorders on 30 November 1987 and 6 March 1988 display amplitude and frequency modulation. An analysis of the temporal evolution of spectral energy suggests that frequency dispersion as predicted by classical linear wave theory is an important process governing the evolution of these waveforms.

Introduction

The Pacific Tsunami Observational Program (PacTOP) was initiated in 1986 with the establishment of five deep ocean bottom pressure recorder (BPR) stations in the North Pacific (González, et al., 1987). Since then, a total of four small tsunamis have been successfully measured by the PacTOP network. Two of these tsunamis were generated by magnitude 7.6 M_s earthquakes which occurred in the Alaskan Bight on 30 November 1987 and 6 March 1988. A recent study (González, et al., 1991) compared the observations with numerical simulations using SWAN, a finite difference implementation of the nonlinear shallow water wave equations (Mader, 1988). Fair agreement was found between the data and model for the 6 March 1988 event, but significant differences arose in the case of the 30 November 1987 tsunami. Details of the computed tsunami waveforms were found to be quite sensitive to the specific source assumed, suggesting that an inadequate knowledge of the source geometry and dynamics was the primary cause of the noted discrepancies.

However, the characteristic periods of the observed tsunamis were relatively short, typically 5-10 minutes. For typical ocean depths of 4-5 km, such waves might be expected to be dispersive, and thus the long wave approximation may not be totally appropriate. This work provides a preliminary assessment of whether the modulation of frequency observed in the tsunami BPR records could be ascribed to linear frequency dispersion.

Amplitude / Frequency Modulation and Dispersion

Changes in the amplitude and frequency of modeled or observed sea level oscillations can occur through a number of processes — for example the constructive and destructive interference of ocean waves arising from multiple sources, from different regions of a single finite source, from coastline reflections, and from more subtle bathymetric effects. The term *dispersion* is commonly

reserved for those cases in which the *dispersion relation* $\omega = \omega(\kappa, a)$ linking the wave radian frequency ω, radian wavenumber κ, and wave amplitude a is such that the wave celerity

$c = \omega/\kappa = c(\kappa, a)$ is dependent on the wavenumber and/or the amplitude; wave components of different frequencies and/or amplitudes will therefore *disperse*, hence the terminology (see, e.g. Phillips, 1977; Lighthill, 1978; Whitham, 1974). If linearity can be assumed, i.e. if the amplitude is so small as to have a negligible effect, then $\omega = \omega(\kappa)$ and $c = c(\kappa) = c(\omega)$ and the terms *linear dispersion* or *frequency dispersion* are also frequently used. Similarly, the term *amplitude dispersion* refers to effects induced specifically by dependence of the wave celerity on the amplitude. In this sense, then, dispersion can be viewed as a particular subset of physical processes which can lead to the modulation of amplitude and frequency in a wave record.

Both observations and numerical simulations of the two tsunamis which were examined exhibited modulations in amplitude and frequency (González, et al., 1991). Modulations in the model output could be caused by such things as coastal reflections, the influence of bathymetry, finite source effects, and nonlinear terms in the equations which could give rise to amplitude dispersion; however, since SWAN is based on the long wave approximation, frequency dispersion did not play a role in the evolution of the numerically generated waveforms. A related question regarding the BPR tsunami measurements is of obvious interest. What are the mechanisms responsible for the observed frequency modulation in the records ? More specifically, to what extent can the observed modulations be accounted for by linear frequency dispersion ?

Analysis

For simplicity, consider an ocean of constant depth h, and waves of infinitesimal amplitude a which evolve as a function of time t and the single space dimension x according to

$$\eta(x,t) = a \cos(\kappa x - \omega t) .$$

Such waves are characterized by the dispersion relation

$$\omega^2 = g \kappa \tanh \kappa h ,$$

so that the phase speed or celerity is given by

$$c(\kappa) = \omega/\kappa = [(g/\kappa) \tanh \kappa h]^{1/2} ,$$

and the associated wave energy propagates at the group velocity

$$c_g(\omega) = d\omega/d\kappa = (\omega/2\kappa) [1 + 2\kappa h / \sinh(2\kappa h)] ,$$

where g is the acceleration due to gravity. If a wave is generated at time $t = 0$ and distance D from an observer, then the arrival time of wave energy at the observation point is just

$$t_a(f) = D/c_g(f)$$

where the wave frequency $f = 1/T = \omega/2\pi$ and T is the wave period.

We have subjected tsunami BPR records to an analysis technique developed specifically for the study of nonstationary or transient phenomena, i.e. time series that display temporal changes in amplitude and/or phase (Dziewonski, et al., 1969). This analysis produces estimates of the evolution of energy as a function of frequency and time, i.e. $E(f,t)$, and the results are frequently summarized in the form of a so-called "*f-t diagram* ." Figure 1 presents such a diagram for the BPR record of the 30 November 1987 tsunami obtained at station AK7. The curve which is superimposed on the energy contours corresponds to the expression given above for energy arrival times, $t_a(f)$, with station distance D and ocean depth h set to 1008 km and 4500 m, respectively.
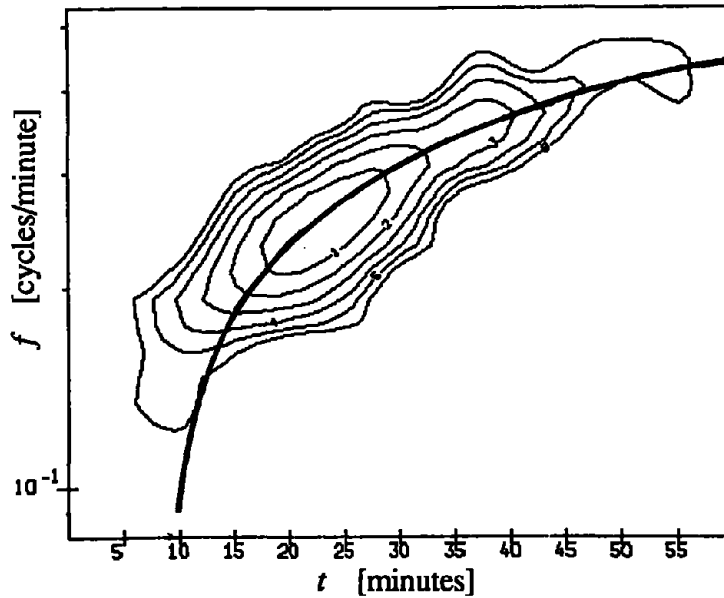
Figure 1. Spectral evolution analysis of the tsunami record obtained at PacTOP station AK7 on 30 November 1987. Contours represent energy decrease from the maximum in dB. Superimposed curve is $t_a(f)$, the expected arrival time function discussed in the text. Time is referred to the start of the analyzed record.

Discussion and Conclusion

The curve of expected arrival time, $t_a(f)$, corresponds very well to the ridge formed by contours of the spectral evolution function $E(f,t)$ presented in the f-t diagram (Figure 1.). Similar correspondence was obtained for a record of the 6 March 1988 tsunami (not shown). Since the ridge defines the time in a tsunami record at which a maximum amount of energy is present at a particular frequency, this strongly suggests that linear dispersion was an important process governing the evolution of both tsunami waveforms.

References

Dziewonski, A., S. Bloch and M. Landisman (1969). A Technique for the Analysis of Transient Seismic Signals. Bulletin of the Seismological Society of America, 59, pp. 427-444.

González, F.I., E.N. Bernard, H.B. Milburn, D. Castel, J. Thomas and J.M. Hemsley (1987). The Pacific Tsunami Observation Program (PacTOP). Proceedings, 1987 International Tsunami Symposium, IUGG, pp. 13-19.

González, F.I., C.L. Mader, M.C. Eble, E.N. Bernard (1991). The 1987-88 Alaskan Bight Tsunamis: Deep Ocean Data and Model Comparisons. Natural Hazards, in press.

Lighthill, J. (1978) Waves in Fluids. Cambridge University Press, Cambridge, 504 pp.

Mader, C.L. (1988) Numerical Modeling of Water Waves. University of California Press, Los Angeles, California, 206 p.

Phillips, O.M. (1977) The Dynamics of the Upper Ocean. Cambridge University Press, Cambridge, 336 pp.

Whitham, G.B. (1974) Linear and Nonlinear Waves. John Wiley and Sons, N.Y., 636 pp.

Discussion

Comment: It was noted that the second group of waves looks like an oscillation which originated not to far from the gage.

Response: That is right. However, the National Earthquake Information Center's listing of earthquakes does not include an earthquake in that region that could have caused this.

Comment: The tsunami itself may have induced some oscillation in a part of the ocean and that's what is being seen.

Response: That is a fairly flat region of the ocean, with a depth of 4500 meters or so. Are there things that can happen in a flat bottom situation which would cause this effect? Presumably the energy would just propagate out of the region.

Comment: The source does not have to be right where the gage is. It could be that something started oscillating, because the second group looks a lot more regular then the rest. It could be originating in the oceanic trench even though it is about 3-400 kilometers to the nearest gage from the trench axis.

Comment: Using records of the same tsunami from Japan, a finite difference computation was made. In this case, the first wave followed along the trench where the ocean is very deep and the velocity is very high. The later phase is sort of an edge wave on the ridge where the velocity is small but the amplitude becomes large; this may apply also to this case.

Response: The travel time computation also allows a plot of the wave fronts. It uses 5 minute bathymetry. The first thing was to see if the wave front curves around and follows through the trench and then leaks into the gage. That did not happen. Looking perpendicular to the wave front, it is clearly traveling over the deep ocean. This gage (No. 20) does not show the coherent feature that shows up in the other three gages. So in terms of some local effect in the vicinity of these three gages, these data are consistent with that hypothesis. However, there is a caveat on this observation. This gage (No. 20) is in a microseismically active region in the volcano caldera and consequently, there is a much louder background noise. Also, since the energy had to travel farther to get to this gage, it could be that this second coherent feature is lost in the noise, or it could be that directivity from the source played a role in recording that second feature of the three gages but not on this gage. The expected travel time is about 10 hours and 20 minutes to Gage No. 20.

ON THE GENERATION MECHANISM OF THE LOW FREQUENCY T PHASE DUE TO TSUNAMIGENIC EARTHQUAKES

Sin-Iti Iwasaki
Hiratsuka Experiment Station
National Research Institute for Earth Science and Disaster Prevention
Kanagawa, Japan

It is widely known that vessels in the ocean felt sea shocks before a tsunami attacked a coast. The cause is thought to be T phase. T phase is the seismic wave generated by its conversion at an ocean bottom. At the 2nd International Tsunami Workshop held in Novosibirsk in 1989, I presented a paper entitled "On the feasibility of a new tsunami warning system by measuring the low frequency T phase". Some of the conclusions were: 1) considering the compressibility of the sea water, another mechanism also can generate a kind of T phase, that is, when a large and shallow earthquake occurs at sea, the sea bottom is displaced and the sea water above the displaced area is compressed and a low frequency wave of condensation and rarefaction is generated; and 2) since this low frequency T phase carries information on the magnitude and the duration of the displacement of the ocean bottom, it is useful for tsunami warnings.

At that time I only showed one record felt by the ship anchored at the harbor. New data are presented in support of the above conclusions. I found 12 examples of earthquakes which accompanied sea chocks and tsunamis. In particular, at the moment of the Sanriku tsunami (3 March 1933), fairly good records of sea shocks were reported by several vessels. The locations of the vessels and tsunami source region are shown in Figure 1. Information about the sea shocks are shown in Table 1. The locations of the vessels were distributed around the tsunami source region except the one which was just above the source region. The duration of sea shocks was 3 minutes or so for the vessels around the source region. However, for the vessel above the source region, it was 2 seconds. Figure 2 shows theoretically calculated wave forms of low frequency T phase. The characteristics of the duration of sea shocks are well explained qualitatively. If we consider only the ordinary T phase, we can not explain these characteristics. It is suggested that the cause of the sea shocks at the moment of tsunamigenic earthquakes is the low frequency T phase.

For tsunami warnings quantitative proofs are needed. To attempt to collect these data, I installed a hydrophone at the Marine Observation Tower and a seismograph at the laboratory of our institute. But no remarkable tsunamis or sea shocks have been experienced so far.

Studies about the use of T phase for tsunami warnings were begun in 1950s. In one of these papers, I found the records of T phase from many circum-Pacific belt shocks detected by the hydrophone at the Kaneohe SOFAR station in Hawaii. Because of its location, Hawaii was attacked by many tsunamis represented by the Chilean Tsunami of May 24, 1960. There is a possibility that the low frequency T phases were recorded by the hydrophone. A precise investigation of the hydrophone records at the Kaneohe station would be helpful for future development.
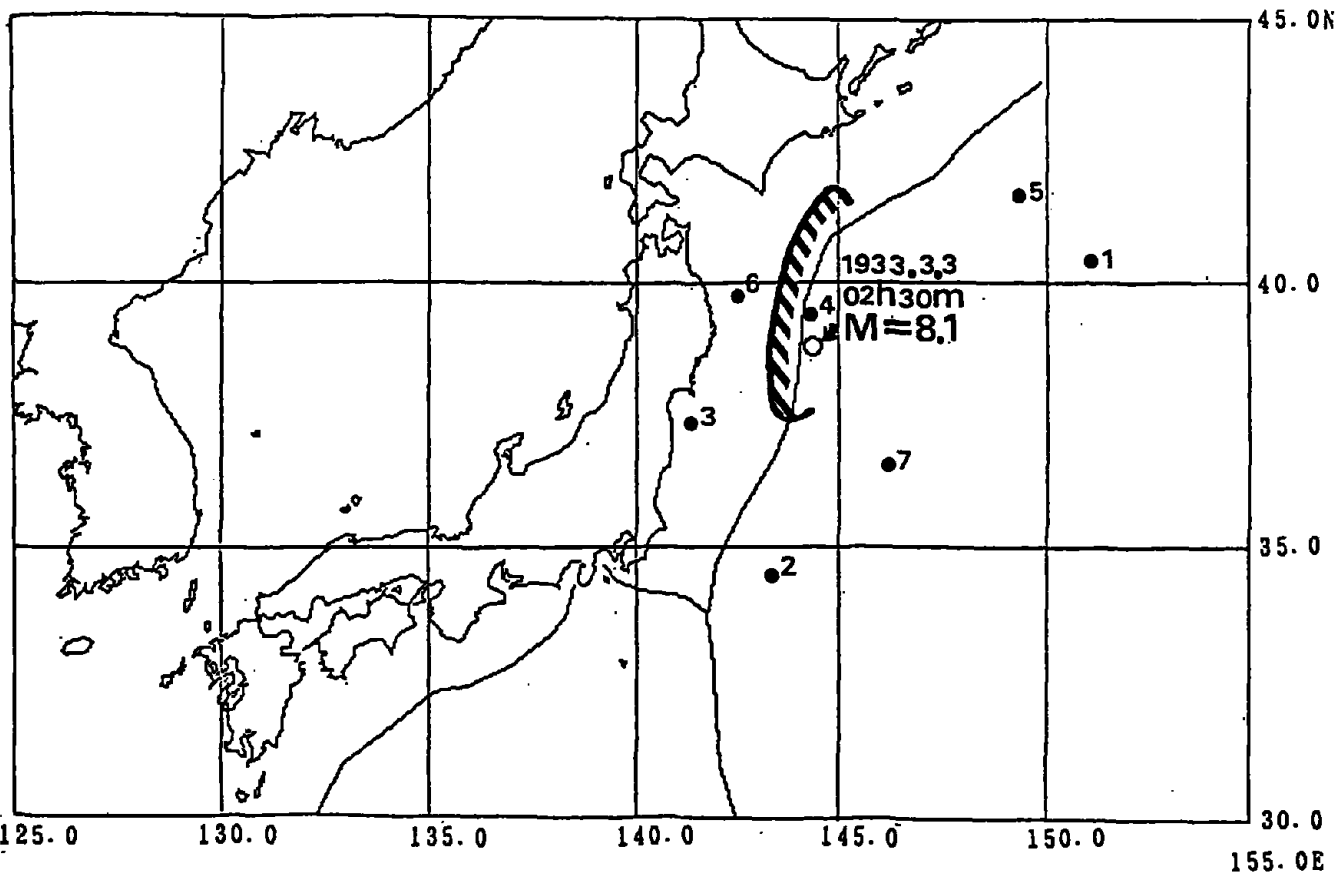
Figure 1.   Source area of 1933 SANRIKU TSUNAMI (HATCHED REGION). Epicenter is denoted by an open circle. Closed circles with numbers denote the locations of vessels which felt sea shocks.

Table 1. Locations of ships, arrival time and duration of sea shocks.

NO.	λ	φ	TIME	DURATION	NOTE
1	E 151.27	N 40.35	h m 03 40	4min.	STRONG VIBRATION LIKE A RACING
2	143.45	34.36	02 33	3min.	VIOLENT VIBRATION
3	141.36	37.38	02 32	3min.	VIOLENT VIBRATION AS IF GOING ASTERN AT FULL SPEED
4	144.13	39.45	04 36	2sec.	VIOLENT SHOCK, AFTERWARD 2 SLIGHT SHOCKS
5	149.30	41.50	02 31	5min.	VIOLENT VERTICAL MOTION AS IF A COMPASS JUMPED
6	142.32	39.57	02. 33	1min.	STRONG VIBRATION
7	146.32	36.37	02 50	3min.	STRONG VERTICAL MOTION

32
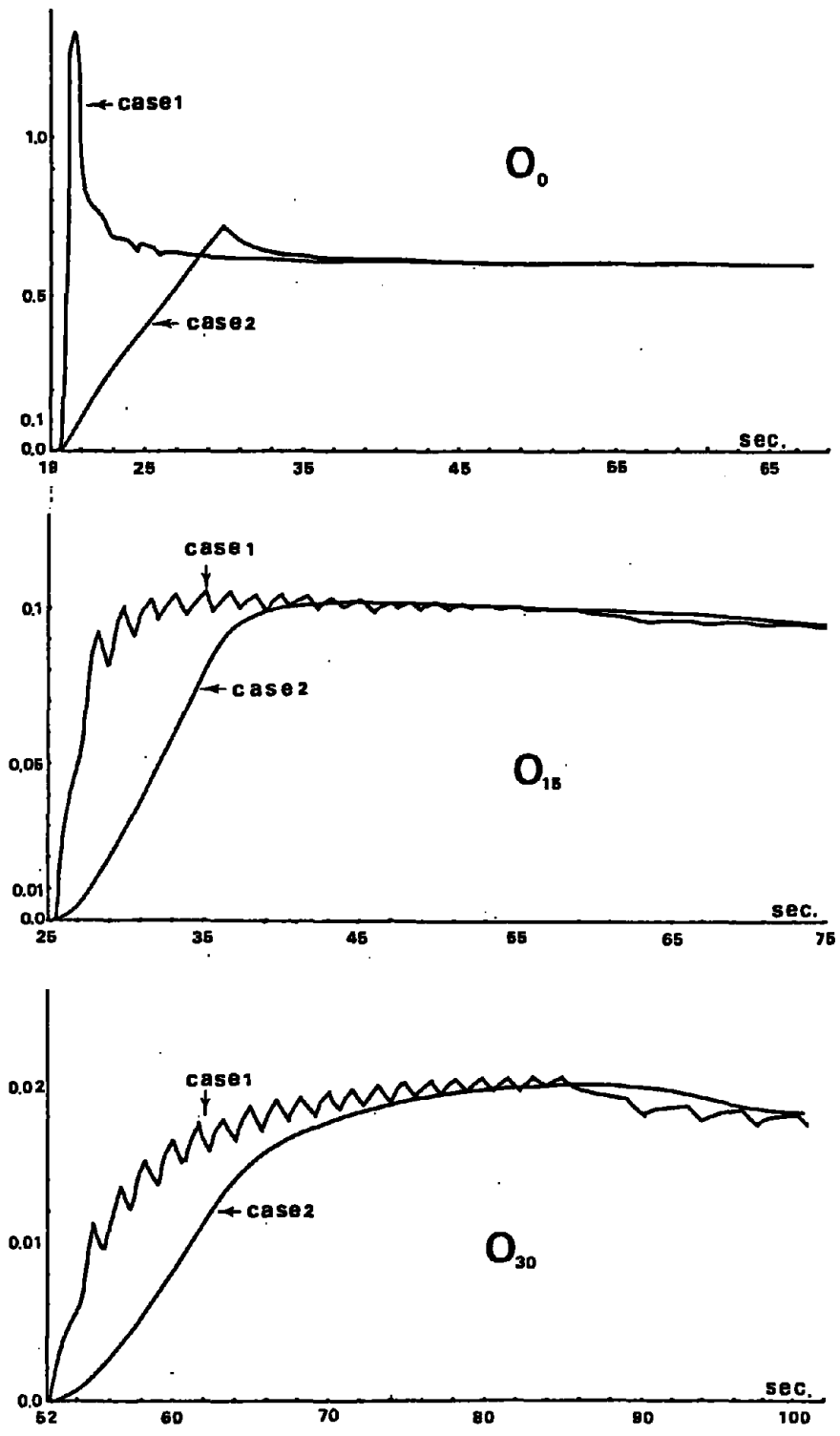
Figure 2.   Calculated wave forms above the tsunami source region (upper), at the distance a tsunami propagates in 15 min. (middle) and in 30 min. (lower).

CASE 1: Abrupt movement of the bottom

CASE 2: Movement of the bottom with a uniform velocity.

The time was measured from the beginning of the displacement.

Discussion:

Comment: In response to a question it was pointed out that although the hydrophones are only 20 meters deep, the seismic acoustic signal or T phase is received directly from the source and not via the SOFAR layer. A small tsunami of April 1990 was not observed due to high noise from wind generated swells.

Comment: The amplitude of the T phase is controlled by the symmetry on a extremely small scale. A big problem with T phases is that they can be generated by deep earthquakes. The Colombia earthquake of 1970 generated notable T phases in the Pacific although its focus was 600 kilometers deep. This may limit this approach.

Response: However, the study uses low frequency T phases of periods of 3 minutes. It seems to be useful in determining the size of earthquake displacements of the sea floor.

Response: The speed of T wave is 1.5 kilometers per second and is affected by the temperature by about one percent or so which means the estimate of the length of the fault is affected by only about one percent.

Comment: The use of signals from under water volcanoes erupting around Japan could be used to calibrate the systems.

MODELING IMPLICATIONS OF THE 1985 CHILEAN TSUNAMI
(Abstract Only)

G.T. Hebenstreit and M.S. Moustafa
Science Applications International Corporation
McLean, Virginia

On March 3, 1985, a great earthquake (M_s=7.8) occurred off the coast of Chile, just southwest of the port of Valparaiso. The earthquake generated a moderate tsunami which did localized damage in the immediate vicinity of the source. No loss of life was reported due to the tsunami.

The tsunami was recorded a seven tide gauge stations along the coast, from Talcahuano (south of Valparaiso) to Arica (at the northern border of the country). Records from six of these gauges (the Talcahuano gauge failed early in the record) have been used by other researchers to estimate the spectral composition of the tsunami and its evolution along the coast. It is clear that the records close to the source contain a mixture of short- and long-period energies, while those farther north are dominated by long-period energies.

This study derives from a series of numerical simulations designed to simulate the tsunami as closely as possible. We used a finite-difference model based on the linearized long wave equations in spherical coordinates, The model grid encompassed the entire Chilean coast from 40°S to 15°S. Sea surface uplift patterns were derived by estimating relevant earthquake parameters (fault length, width, dip, depth, and maximum vertical displacement) and using a point source dislocation model to depict seafloor uplift.

Several simulations were run, each with the source in a different geographical location in the source area. In most aspects the model output agreed well with the character of the observed tsunami, if not with the detailed measurements. Arrival times at the various locations were in general agreement with observations. The trend in observed maximum wave height along the coast also agreed well, with one exception. The structure of the calculated wave time series and the resulting wave spectra also compared favorably in many respects with observations.

The fact that the simulations were reasonably accurate allows us to make some intelligent extrapolations as to the implications of such simulations for detailed tsunami hazard analyses. For example, how well can we rely on these types of coarse simulations to provide input to more detailed studies of specific local areas? Do these types of simulations retain enough of the character of observations to avoid having to perform wide-scale high-resolution model tests over a large area like the Chilean coast? Can these simulations allow us to make intelligent analyses of the behavior of waves on the coastal shelf (as opposed to waves in deeper water)? Can this lead to a deeper understanding of the nature of local tsunami propagation? This study cannot answer these questions, but it can serve to illuminate some of the issues.

Discussion:

Question: In the above model the linear shallow water equations were used. What is the explanation for the disappearance of the high-frequency waves at different locations, since the linear system is without dissipation and especially, why does the numerical model produce that?

Comment: Hal Loomis' comment about the effect of the trench may help to explain the numerical model results. The trench is basically a wave guide and that is frequency dependent in terms of what it trapped and what leaked through. Generally speaking, it may be that the offshore trench in the numerical model is creating these effects.

Response: The wave record at an offshore site beyond the trench still does not show the high frequency energy. That is one of the questions that needs to be assessed.

Question: Does the data up and down the coast show any sign of a leading wave, propagating much faster along the coast, which was first proposed by LeBlond and King in the early 1980's? It would be a type of trapped wave along the deep water region.

Response: No. The tide gages are inside of the harbors, except for Arica, and this phenomenon probably would not be observable.

Question: How long is the coast along which these seven tide gages are located?

Response: It's about 2000 kilometers from Arica to Santigo.

Comment: This is very few gages to verify the computational result with the observed results because a small change in location will have a big change in the result.

OBSERVATION OF STANDING EDGE WAVES TRAPPED
ON THE SHELF OF MAKURAZAKI COAST

Yoshinobu Tsuji and Takashi Yanuma
Earthquake Research Institute
University of Tokyo
Tokyo, Japan

It is well known that at tide gauge stations which are situated on the coast inside a bay, the water level changes due to the normal mode seiche are well recorded. During a tsunami, the normal mode of the bay continues strongly except for the initial few waves. In some cases at a tide gauge which is not located inside a bay, but on the open, linear coastline, the normal mode may also be observed.

Makurazaki harbor is located on the Satsuma Peninsula at the southern part of Kyushu Island. It is known that an extraordinary large oscillation, with a period of ten to twenty minutes, frequently takes place in this port. For example, on the 11th of March 1976, the oscillations began at 9 o'clock and by 10:20, the sea level oscillations with a range of 138cm were recorded. Fishing boats broke loose from their moorings and floated to the mouth of the harbor (Tominaga, 1980).

We considered that the extraordinary oscillations in the harbor were induced by resonance of the fundamental mode of the harbor and a resonant wave mode trapped on the shelf region outside of the harbor.

We made sea level observations at two points about 300 to 500 meters off the linear coast in the vicinity of Makurazaki City by using sea bottom pressure gauges both of which were set on the sea bed about 5 meters deep. We intended to clarify the following:

(1)   whether or not oscillations of a trapped standing edge wave can usually be observed;

(2)   whether or not those trapped wave modes can be identified with theoretically obtained modes;

(3)   whether or not trapped edge waves outside of the bay with a period nearly that of the fundamental mode on the inside of Makurazaki harbor can actually be detected;

(4)   whether or not we can confirm that the resonance of the fundamental mode inside the harbor and some mode outside actually takes place.

The observations were made from the middle of July to September 1989, and three typhoons approached the coast during that period.

We analyzed the data of water level records at the two points and in addition, we digitized the tide gauge record at the Makurazaki tidal station. This gauge belongs to the Makurazaki Meteorological Observatory and is located inside the Makurazaki harbor. We found several peaks in the power spectra of the three points, and all of those are well identified with the theoretically obtained modes of standing edge waves trapped on the shelf region.

We found that the period of the normal mode of Makurazaki harbor is observed as about 16 minutes, which approximately coincides with the theoretically obtained one of 17.5 minutes. On the other hand, we found that a trapped wave mode with a period of 16.6 minutes exists on the shelf region outside the harbor; the mode was detected at the two observational points. We suggest that the extraordinary oscillation in the Makurazaki harbor is induced by the standing edge wave mode with a period of 16.6 minutes trapped on the shelf region.
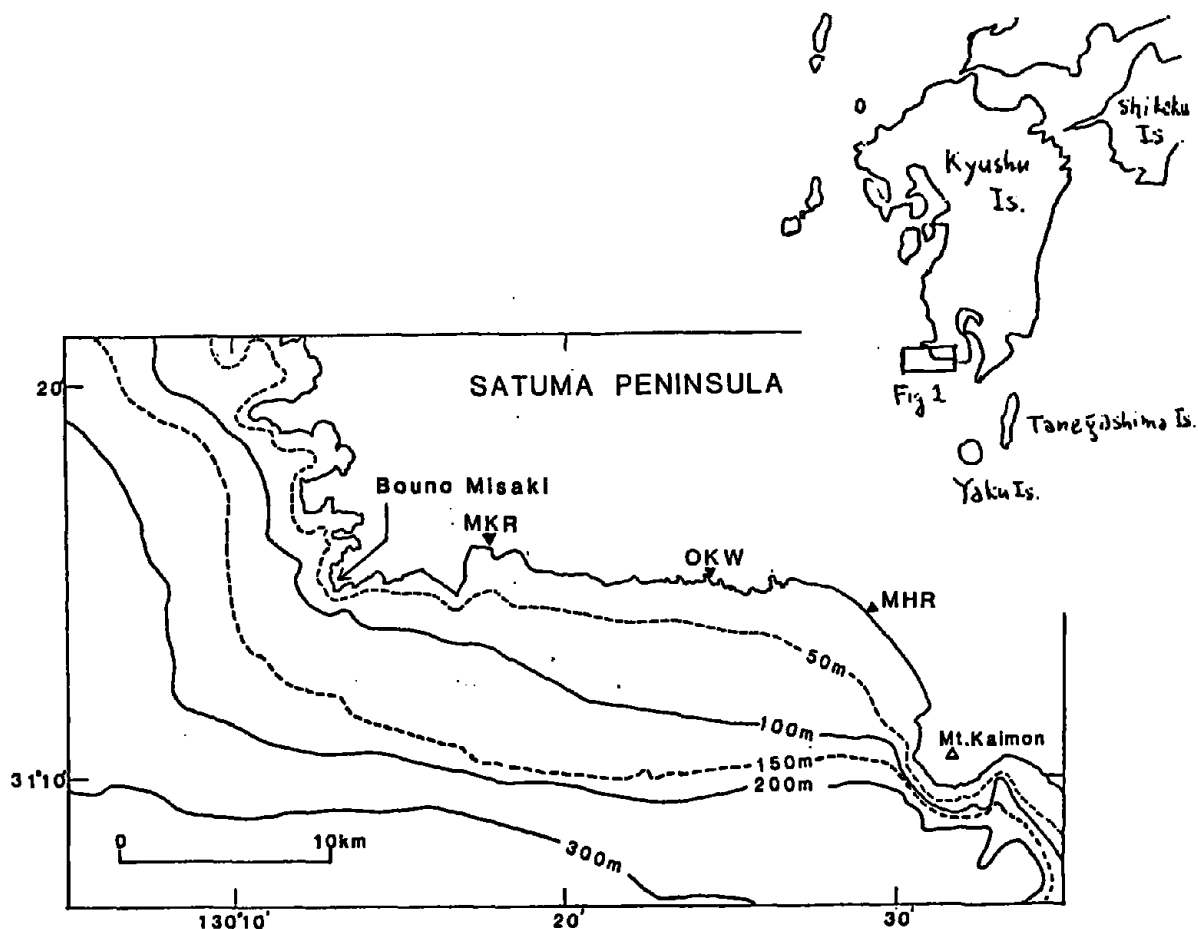
Fig. 1. Location of the sea level observing points. We set pressure sensors on the sea floor at Okawa (OKW) and Maehara (MHR) stations. At both points the depth is about 5 meters. Distance from the shore to the Maehara station is about 500 meters and for Okawa station it is 300 meters. Makurazaki (MKR) tidal station of the Meteorological Observatory is located inside of the harbor.
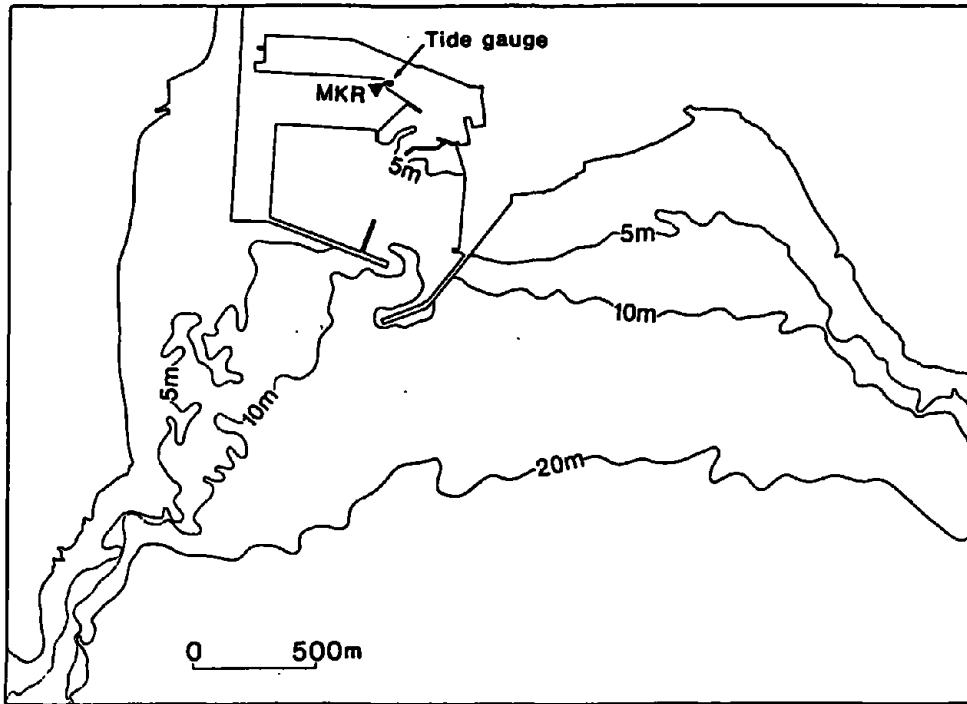
Fig. 2. Detailed map of Makurazaki harbor.

OKW 7/12
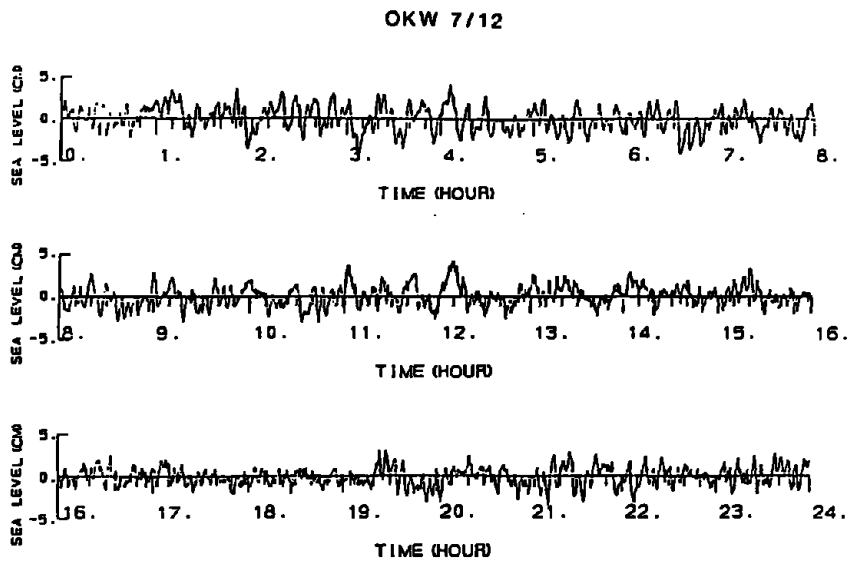
Fig. 3. Example of sea level at Okawa station observed by sea bottom pressure sensor.
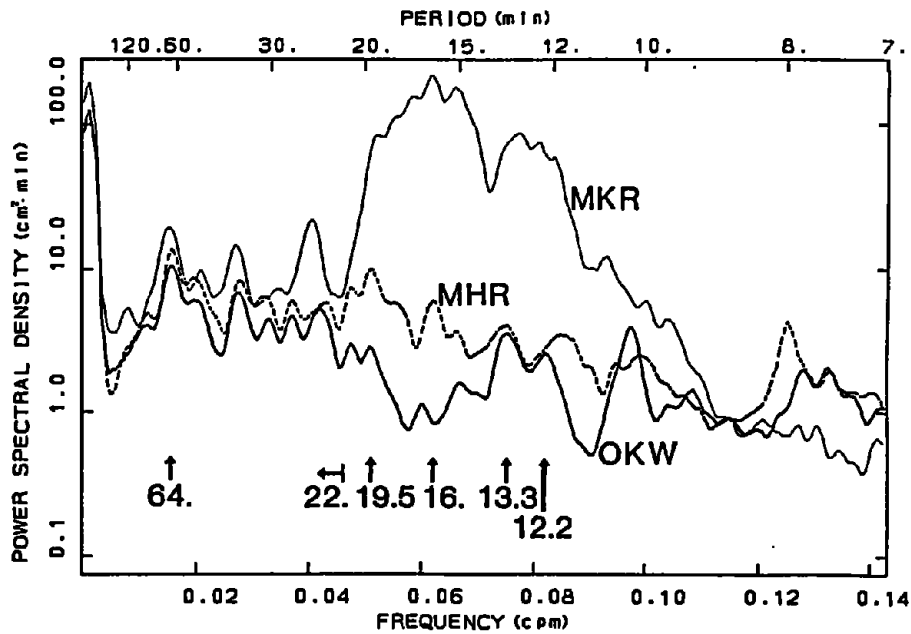
Fig. 4. Power spectra of sea level at Okawa, Maehara, and Makurazaki stations.
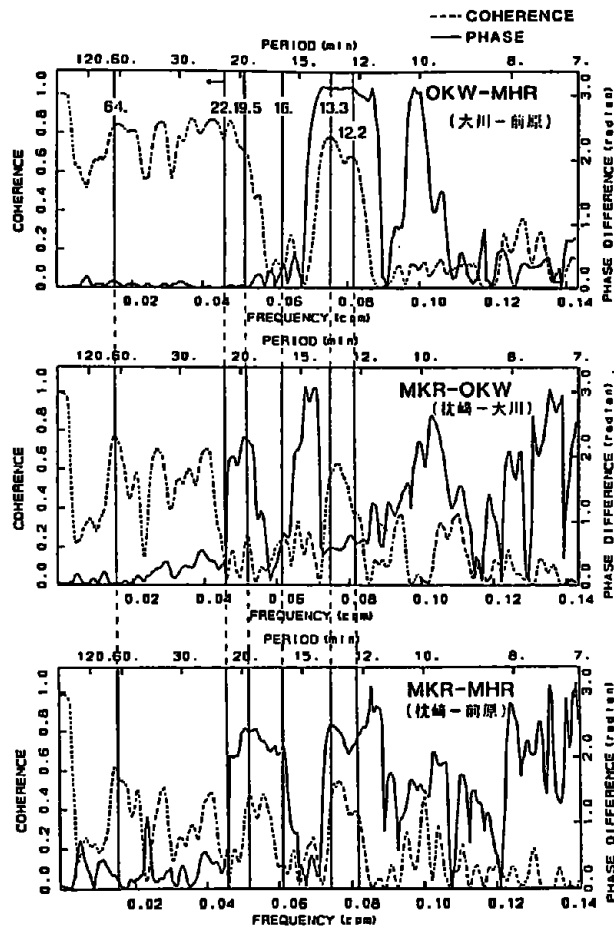
Fig. 5. Coherence and phase difference between OKW-MHR, MKR-OKW, and MKR-MHR. Notice that sea level changes in the outphase (difference of the phase nearly pi radian; 180 degrees) for the peaks of 12.3 and 13.3 minutes, and it changes in the same phase for peaks of 19.5 and 64 minutes. Sea level changes are poorly correlated for the peak around 16 minutes between Maehara and Makurazaki, which implies that the oscillations are due to the difference modes at each location.
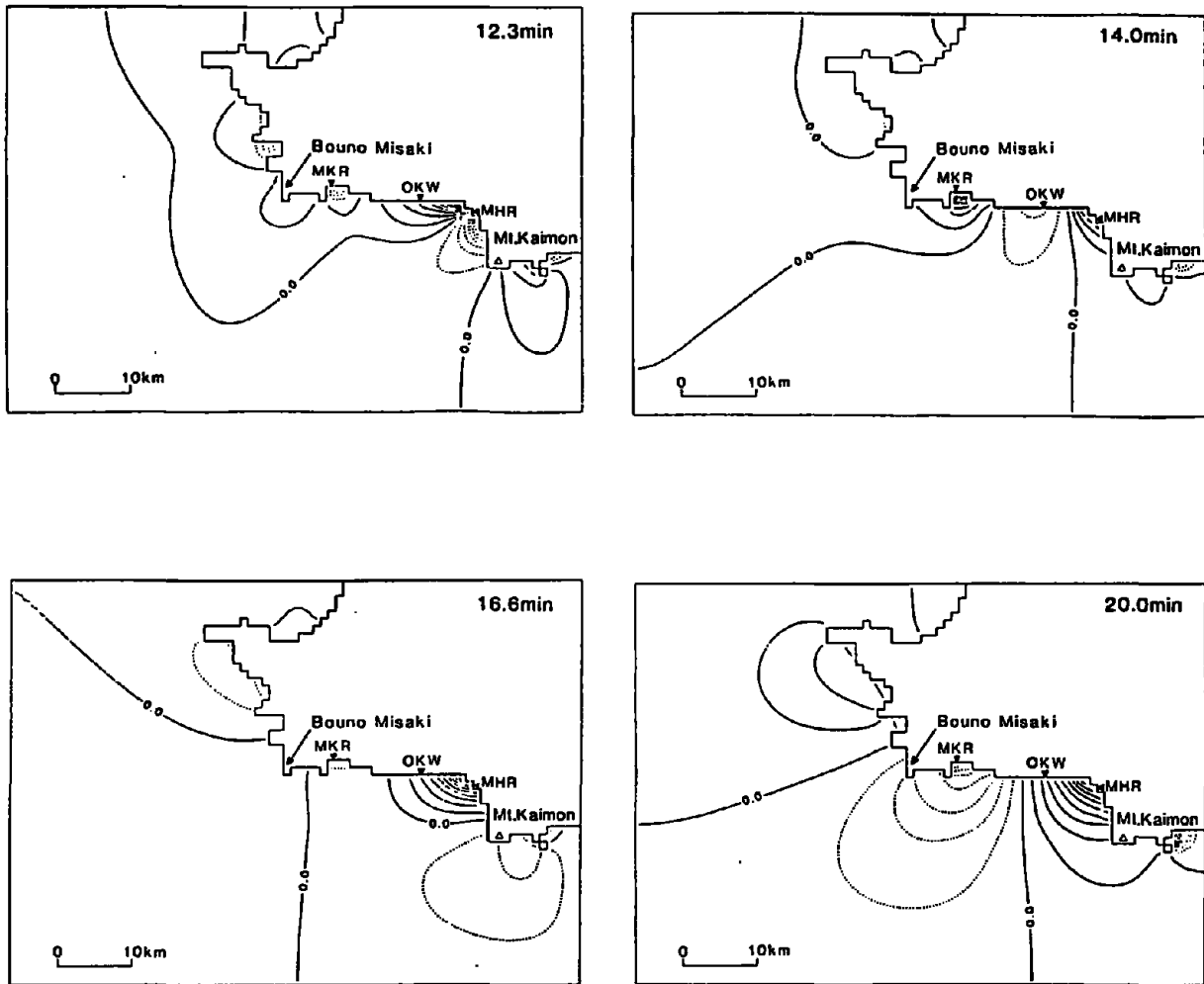
Fig. 6-1-4. Numerically calculated fundamental oscillation of trapped edge waves on the shelf in the vicinity of Makurazaki city. We assumed the sea level on the outside boundaries to be fixed as zero, used three different sizes, and selected such a mode that the eigen value and pattern hardly changes according to the size of frames.

41
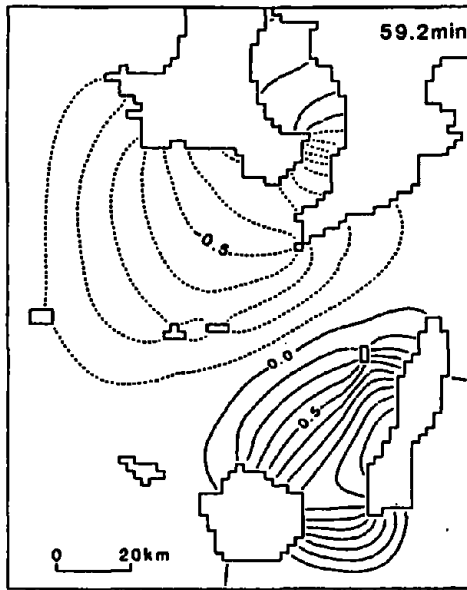
Fig. 7. The pattern of the mode trapped in the Oosumi Straits between Satsuma Peninsula and Tanegasima-Yakushima Islands.
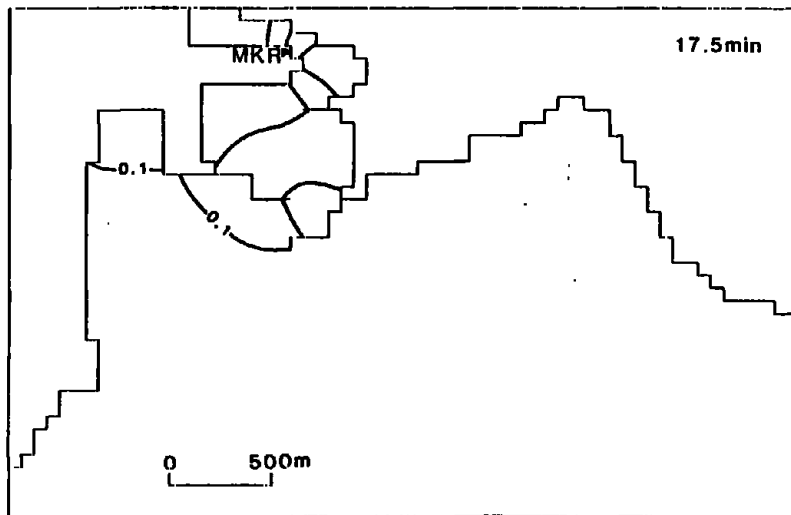
Fig. 8. The pattern of the fundamental mode of the Makurazaki harbor.

THE CRITERIA FOR IDENTIFICATION OF TSUNAMI EVENTS LIKELY TO PRODUCE FAR-FIELD DAMAGE, A DATA APPLICATION

Patricia A. Lockridge
National Oceanic and Atmospheric Administration
National Geophysical Data Center
Boulder, CO, USA

Abstract.

. The National Geophysical Data Center has several unique tsunami data sets each with special limitations. These data and limitations are described. . Some of the data are applied to a practical problem: Can the characteristics of tsunamis that produce Damage At A Distance greater than 1000 km (DAAD tsunamis) be identified for warning purposes.

1.0 Description of Available Data

The world-wide tsunami data are divided into 16 regions: ten in the Pacific Basin (1606 events), four in the Atlantic (124 events), the Mediterranean Sea (199 events), and the Indian Ocean (15 events). The types of data available for each of the sixteen regions vary as does the completeness of the tsunami historical record. The number of known tsunamigenic events in each region since earliest times is dependent not only on the number of actual events in a region, but also on the accuracy of the record keeping for the region. For example, some sparsely settled areas may have recorded an especially devastating event centuries ago, but have experienced only sporadic tsunamis in the intervening years.

The data are of two basic types: origin data containing information about the cause and origin of the tsunami, and tsunami data containing information about the tsunami itself (see fig. 1).

1.1 Origin data

The origin data include:

DATE AND TIME: The date and time are given in Universal Coordinated Time (UTC) if it is known. If no time is given, the date is the local date at the source of the tsunami.

LATITUDE AND LONGITUDE: This is the location of the cause. It may be the earthquake epicenter, or the latitude and longitude of the landslide or volcano.

MAGNITUDE: The earthquake magnitude has an uncertainty of a quarter unit or more. The magnitudes are based on surface waves (Ms) or the equivalent. Epicenters and magnitudes before 1898 are usually based on the maximum intensity of the earthquake.

43

DEPTH: Depth in kilometers of the earthquake hypocenter is given where known.

AREA: Geographical name of the source area.

VALIDITY: The probability of actual tsunami occurrence is indicated by a numerical rating of the validity of the reports of that event: 4 = definite tsunami, 3 = probable tsunami, 2 = questionable tsunami, 1 = very doubtful tsunami, 0 = erroneous entry. By cross-checking data sources, a best estimate of this probability was determined. The validity code is necessary to prevent erroneous entries (i.e. storm surges, erroneous dates) from being reentered in the data base. Not all events have a validity code assigned to them.

CAUSE: The source type codes are E for earthquake, V for volcanic, L for landslide, M for meteorological, X for explosion. Events with an "M" for cause would have a "0" validity since they are not tsunamis as we define them.

REGION NUMBER: Regional boundaries are based on frequency of occurrence of tsunamigenic events, geophysical relations, risk in distant areas, and political justification. In the Pacific basin: P0 = Hawaii; P1 = New Zealand and South Pacific Islands; P2 = New Guinea and Solomon Islands; P3 = Indonesia; P4 = Philippines; P5 = Japan; P6 = Kuril Islands and Kamchatka; P7 = Alaska (including Aleutian Islands); P8 = West Coast of North and Central America; and P9 = West Coast of South America. Non-pacific basin tsunamis include: I0 = Indian Ocean, M0 = Mediterranean Sea, A0 = Southeast Atlantic Ocean, A1 = Southwest Atlantic Ocean, A2 = Northwest Atlantic, and A3 = Northeast Atlantic.

ORIGIN DATA			V A L I D	C A U S E	TSUNAMI DATA							
DATE TIME LAT./LONG. MAGNITUDE DEPTH (KM)	AREA				MAG & INT	LOCATION OF EFFECTS	RUN UP AMP (M)	PER- IOD (MIN)	1ST MOT- ION	ARRIVAL TIME DA-HR:MN	TRAVEL TIME (HRS)	COMMENTS

Fig. 1. Sample Historical Tsunami Data Headings

1.2 Tsunami data

TSUNAMI MAGNITUDE AND INTENSITY: The tsunami magnitude and tsunami intensity are measurements of the size of the tsunami. Tsunami magnitude is defined by Iida and others (1967) as $M = \log_2 h$, where "h" is the maximum runup height of the wave. Tsunami intensity is defined by Soloviev and Go (1974) as $I = \log_2 > 2 h$, where "h" is the average runup height of the wave on the affected coast.

LOCATION OF EFFECTS: Name of geographical area where wave effects were experienced.

RUNUP/AMPLITUDE: The runup is the height in meters that the tsunami reached above a reference level such as mean sea level. However it is not always clear which reference level was used. Two runup values are given in the data base: The maximum runup for each tsunami event

and the runup at the town or area where the tsunami was observed or measured. Often the amplitude in meters is given rather than the runup. When the range rather than the amplitude is given in the tsunami literature, it is divided by two to get a rough approximation of the amplitude. Many events were simply "observed" and no record exists of the actual wave height.

PERIOD: The period is in minutes, and where available is the period of the first cycle.

1ST MOTION: The first motion of the wave, i.e. rise (R) or fall (F).

ARRIVAL TIME: The arrival time is the universal time of the arrival of the tsunami at the location of the effects given in day, hour, and minutes.

TRAVEL TIME: The travel time is the time in hours and minutes that it took the tsunami to travel from the source to the location of effects.

COMMENTS: Comments include damage, deaths, other effects, and comments on the accuracy of the report.

REFERENCES: Bibliography and additional sources of information about each tsunami.

2.0 Limitations of Historical Data

The historical records are perhaps the best sources of information for predicting future behavior of tsunamis. However, if the limitations of the data are not understood, the data may be misleading and may be misinterpreted.

2.1 Confusion with other phenomena, age of the records

The value of historical tsunami catalogs is diminished by errors of several kinds. Tsunamis may be confused with several other phenomena such as unusual astronomic tides and storm surges. This is particularly true of older events in which there was no effort to identify the cause of large waves. Problems also arise in converting dates and times from various calendar and timing systems. Changes in location of reference points for measuring runups can lead to errors. Seismographs for recording earthquakes have been in general existence only since the turn of the century. In addition, early calculations of magnitude were higher by about a factor of 0.5 compared to later calculations. Even in recent literature a number of different values for magnitudes exist for a single event.

2.2 Limited or exaggerated original accounts

Because many reports of tsunamis are based on eyewitness accounts by early settlers, hunters, and others who were not trained observers, the reports may at times be exaggerated or erroneous. Exaggerations can sometimes be identified by familiarity with the location in which the tsunami occurred or by comparing the data with other contemporary accounts.

2.3 Transcription errors

Transcription errors occur as catalogers use earlier compilations. These can be dealt with by referring to the original, and, if possible, the contemporary reference.

2.4 Incorrect interpretation of data

Data may have been recorded accurately in the data base, but users who are unfamiliar with the data may interpret it incorrectly. For example, even though a tsunami is given a validity of "4" and did definitely occur, the tsunami effects may have been "doubtful" at some locations.

2.5 Confusion over measure of wave height

Tsunamis and other waves are recorded instrumentally on tide gages. These instruments routinely record tidal changes. The records produced by these gages are commonly called marigrams. Problems arise from using tide gages designed for recording the twelve hour tide to record tsunamis with periods measured in minutes. The largest waves may be clipped making it difficult to estimate the maximum amplitude, or a very large wave may cause a large gap or destroy the record altogether.

The reported size of the waves given from instrumental measurements is almost always the range, although it may be called wave height, maximum rise or fall, and, incorrectly, amplitude.

Many of the earlier references to wave height use the word "runup," the highest point reached by the wave, in alluding to some reference level such as high water strand, mean sea level, or mean lower low water. Mean lower low water (MLLW) is the baseline for coastal charts in the United States chosen as an aid to navigation. Since it is in wide use for charts, it is referenced in tsunami runup reports. In areas such as Hawaii, where the diurnal tide is about 0.6 m, this uncertainty of the reference level may not be significant, but in Alaska where tides may be more than 5 m, knowing the state of the tide and the reference level are important. Smaller tsunami waves arriving at high tide may be more damaging than larger waves before or after high tide. At some locations in Alaska, for example, the height of the wave for the 1964 tsunami was reported as nearly 6 m. However, this was a 2-m tsunami occurring simultaneously with a 4-m high tide.

2.6 Insufficient data

Because areas affected by early tsunamis were sparsely populated, observers were not present to report the effects. For example, a tsunami recorded in Japan in 1586 was later traced to an earthquake that occurred near Lima, Peru. Historical tsunami data are available for a limited time span. The earliest dated event recorded in Alaska is 1788; in Hawaii and on the west coast of the United States it is 1812. Since many tectonic rupture zones have periodicities in excess of several hundred years, the recorded history of tsunami events is too brief to give a completely accurate risk appraisal for each region.

3.0 Example of a Data Application

Historical tsunami events that caused significant Damage At A Distance greater than 1,000 km (DAAD tsunamis) were examined to determine what characteristics these events had in common. It was hoped that such damaging events could be identified from data available immediately after the event in order to issue an effective warning before deaths occurred. In many areas approximately one hour of warning time is needed to effectively evacuate the citizens. One thousand kilometers was chosen since it is the distance traveled in about one hour by the tsunami in the open sea.

3.1 Method

Nearly two dozen events with far-field damage were identified from the World Wide Tsunami Historical Data Base at the National Geophysical Data Center. Examination of the pre-twentieth century events revealed that the records of both local and far-field wave heights (runups) and local and far-field damage were not complete enough for use in the study. Many areas were still unpopulated even at the turn of the century. A sparse population greatly reduced the chances of observing and/or recording even a large tsunami and largely precluded damage in many areas. For these reasons only twentieth century events were included in the study.

Fourteen DAAD tsunamis occurred in the twentieth century (see Table 1). The locations of the earthquake epicenters of the DAAD tsunamis were noted. The relationship between tsunami wave height at early landfall and several other parameters including earthquake magnitude, tsunami magnitude, tsunami intensity, far-field wave heights, damage, and other effects were examined for these events.

TABLE 1. **TWENTIETH CENTURY DAAD TSUNAMIS**

	Date	Mag	R-Up	Far-Field	R-Up	Damage Location
HAWAII						
1)	Nov. 11, 1975	*7.2	8.0	Catalina I. CA	–	Minor damage
JAPAN						
2)	Aug. 10, 1901	*7.4	*0.6	Kailua, HI	1.2	Several huts lost
3)	Mar. 02, 1933	8.3	29.3	Keauhou, HI	3.3	Considerable damage
KAMCHATKA/KURIL ISLANDS						
4)	Nov. 04, 1952	8.1	18.0	Haena, HI	10.4	$1.0 million damage in HI Ecuador, Peru, and Chile
5)	Feb. 03, 1923	8.3	8.0	Hilo, HI	16.1	$1.5 million damage in HI
6)	Sep. 07, 1918	8.3	12.1	Hilo, HI	1.5	Minor damage Hawaii
ALASKA/ALEUTIAN ISLANDS						
7)	Apr. 01, 1946	*7.3	35.0	Haena, HI	13.7	Severe damage in Hawaii
8)	Feb. 04, 1965	8.2	10.0	Ayukawa, JA	1.0	Minor damage in Japan
9)	Mar. 09, 1957	8.3	15.0	Haena, HI	10.4	Major damage in Hawaii, Japan
10)	Mar. 28, 1964	8.4	70.0	Crescent City	4.3	Severe damage in Canada & West Coast of the United States
WEST COAST SOUTH AMERICA						
11)	Jan. 31, 1906	8.2	5.0	Hilo, HI	1.8	Flooding
12)	Nov. 11, 1922	8.3	9.0	Hilo, HI	2.1	Damage in Hawaii, Taiwan, Philippines, Japan, Samoa
13)	Aug. 17, 1906	8.6	*1.5	Maalaea, HI	3.6	Some damage
14)	May 22, 1960	8.6	25.0	Hilo, HI	10.7	$24 million in Hawaii, severe damage in Japan

*Does not meet the criteria.

3.2 Results

When these 14 DAAD events were plotted on a map, it was obvious that these events were confined to certain areas and did not occur along all coastlines. The twentieth century events all occurred near the coasts of Japan (region P5), the Kuril Islands and Kamchatka (region P6), the Aleutian Islands and Alaska (region P7), and the west coast of South America (region P9). These regions were identified as the source regions of DAAD tsunamis. There was one exception among the 14 DAAD tsunami events. An earthquake off the coast of Hawaii generated a tsunami that caused slight damage on Catalina Island, off California's coast.

Further examination of the 14 DAAD tsunamis revealed that eleven were generated by great (magnitude 8.0 or more) earthquakes. Previous studies had revealed the positive relationship between earthquake magnitude and damaging tsunamis. Examination of the 14 DAAD tsunamis also revealed that twelve had runups greater than 3.9 meters. The two events with runups less than 3.9 m occurred in the first decade of this century, and it is possible that the local runups would have been higher if more complete observations had been made. The following observations were made concerning the three events with magnitudes less than 8.0: The earthquake magnitude of the 1901 event might have been measured differently in later years. The 1946 tsunami is a well known exception to usual tsunami behavior and several theories have been advanced to explain the tsunami-generating mechanism in this case. The 1975 tsunami generated in the Hawaiian Islands caused only minor damage in California.

The three criteria chosen to identify DAAD tsunamis were: location in a DAAD source region, earthquake magnitude greater than 7.9, and local tsunami runup greater than 3.9.

To test the selection criteria, events having each of these criteria were independently selected from all the twentieth century events in the data base. Three hundred fifty events were generated in these DAAD regions in the twentieth century. There were 57 events with earthquake magnitudes greater than 7.9. Twenty-nine of these 57 were from the previously identified DAAD tsunami source regions. Seventy-one twentieth century events had runups greater than 3.9. Of these 71 events, 21 were generated by earthquakes greater than 7.9 magnitude and 43 of the 71 were located in the previously identified DAAD tsunami source regions.

Fifteen events were found to possess all three criteria (see Table 2): they were located in the DAAD source regions; they were generated by magnitude 7.9 or larger earthquakes; and they had maximum runups of greater than 3.9 meters. As had been expected, ten of the fifteen were DAAD tsunamis. These had been previously identified and were the basis for the selection criteria.

However, five events met the three criteria but were not DAAD tsunamis. Four of these events did cause local damage. One event located in the Kuril Islands caused no damage locally, perhaps because of the remoteness of the location. Of the four locally damaging events, three were generated off the coast of Japan and one was generated in the Kuril Islands.

48

TABLE 2.   TSUNAMIS THAT MET THE THREE CRITERIA.

	YEAR	MO	DA	MAG	R-UP	SOURCE REGION	REGION CODE
DL	1906	01	31	8.2	5.0	Colombia-Ecuador	P9
DL	1918	09	07	8.3	12.1	S. Kuril Islands, USSR	P6
DL	1922	11	11	8.3	9.0	N. Chile	P9
DL	1923	02	03	8.3	8.0	Kamchatka Peninsula, USSR	P6
DL	1933	03	02	8.3	29.3	Sanriku, Japan	P5
L	1944	12	07	8.0	20.0	Ryukyu Trench, Japan	P5*
L	1946	12	20	8.1	6.6	Nankaido, Japan	P5*
L	1952	03	04	8.1	6.5	SE. Hokkaido Island, Japan	P5*
DL	1952	11	04	8.3	18.0	Kamchatka Peninsula USSR	P6
DL	1957	03	09	8.3	15.0	C. Aleutian Islands	P7
L	1958	11	06	8.1	4.0	S. Kuril Islands, USSR	P6*
DL	1960	05	22	8.6	25.0	S. Central Chile	P9
	1963	10	13	8.1	4.4	Kuril Islands, USSR	P6*
DL	1964	03	28	8.4	70.0	Gulf of Alaskak-Alaska Pen.	P7
DL	1965	02	04	8.2	10.0	W. Aleutian Islands	P7

D = Destructive at a distance (DAAD), L = Local Destructive
*Met the three criteria but was not a DAAD tsunami

3.3 Conclusions

Tsunamis that caused damage at a distance greater than 1,000 kilometers were found to have region-specific characteristics. Tsunamis generated in Japan and the Kuril Islands appear to be slightly less likely to become DAAD tsunamis than tsunamis generated in Alaska, the Aleutian Islands, and the west coast of South America. It is obviously not advisable to use runup heights and other characteristics of tsunamis with far-field damage generated in Japan to predict the effects of an apparently similar tsunami generated in Alaska or Chile. However, it was possible to use local runup and magnitude of historical tsunamis to predict tsunami behavior within regions. Along the west coast of South America the runup height at the first landfalls gave the clearest indication of the potential for damage at distances greater than 1,000 km. The runup at the first landfalls in Alaska was not as clear an indicator of a DAAD tsunami but surpassed the reliability of the same indicator in Japan, Kamchatka, and the Kuril Islands.

The investigation showed that the three criteria (source region, earthquake magnitude and local runup) did have value in predicting far-field damage from tsunamis. However, in at least two cases a DAAD tsunami would have occurred without warning if the warning had been based solely on the three criteria. This simple investigation illustrates the value of historical tsunami data in predicting behavior of future tsunami events. It also illustrates the limitations of that data and the great importance of acquiring accurate tsunami data from future events. Too few data exist at present. However, as more data from future events become available, more accurate predictions can be made and fewer false alarms will be issued.

References

Iida, K., Cox, D.C. and Pararas-Carayannis, G., 1967. *Preliminary Catalog of Tsunamis Occurring in the Pacific Ocean*. University of Hawaii, Honolulu.

Soloviev, S.L. and Go, Ch.N., 1974. *A Catalogue of Tsunamis on the Western Shore of the Pacific Ocean*. Moscow, Nauka. (Translation by Canada Institute for Scientific and Technical Information, National Research Council, Ottawa, Ontario, Canada.)

Discussion

Comment: The database is of extreme value and a notable effort. Currently, the seismic moment of the earthquake is the parameter of most scientific or quantitative value and needs to be added. It has taken about 15 to 20 years to conclude that the earthquake magnitude is of no value to tsunami studies once we reach the higher levels needed to generate a tsunami.

The magnitude concept should now be replaced with seismic moments. There was a time when moments could only be computed from extensive data sets and they were available for only 2 or 3 earthquakes which had created very large tsunamis. Since the role of the period is now understood and since progress is very good in areas of tsunami seismology, we are now capable of estimating seismic moments for earthquakes in the 1920s and possibly back to 1900. We are capable of finding the differences between an earthquake of magnitude 8 and moments of 10^{28} today which, for all practical purposes, is not going to be very dangerous for tsunamis, and an earthquake with a moment of 10^{30} which can kill 200 people in Japan from a tsunami from Chile. The moment information is a primary parameter and it should be incorporated into your data base. That would explain why when comparing 1933 earthquake in Sanriku and 1960 earthquake in Chile there does not seem to be any reciprocity. There is no reciprocity because we are not talking about the same kind of earthquakes. There is a factor of 15 between their seismic moments. At the least the 1933 Japan earthquake had a seismic moment somewhere in the high 10^{28}, but the Chilean earthquake was 2 or 3 times 10^{30}. So that figure alone explains why we just can not compare the two. There are lists of seismic moments of earthquakes published by Kanamori in 1977. Work on revising the estimates since the early 1900s is on-going.

IMPULSIVE FORCE OF TIMBERS DRIFTED BY TSUNAMIS

Hideo Matsutomi
Department of Civil Engineering
Akita University
Akita, Japan

Abstract

A procedure is developed for predicting the maximum impulsive force F_{dm} on structures with an arbitrary opening ratio due to the collision of timbers drifted by borelike tsunamis. In the course, the apparent inertia coefficient C_{MA} and the impact duration time Δt of timbers are examined, experimentally.

Introduction

Tsunamis often break and form bores over a gently sloping beach or in a river channel. Moreover, such bores sometimes bring with them timbers, ships and other drifting bodies which cause secondary disasters. Nevertheless, few studies have been done on the impact of such drifting bodies. It is very important from the viewpoint of tsunami disaster prevention or mitigation to investigate the various features of the impact.

A few studies have been done on the impulse of timbers brought with waves or bores (Horikawa, 1983; Matsutomi, 1989b, 1990). But, there seem to be no studies on the impulsive force itself. Generally, the impulsive force is related to the safety for sliding of structures, and the impulse is related to the sliding distance of structures. Hence, the impulsive force would be needed in preference to the impulse.

This paper presents a procedure for predicting the maximum impulsive force on structures with an arbitrary opening ratio due to the collision of timbers drifted by borelike tsunamis. For that purpose, variations of the apparent inertia coefficient and the impact duration time of timbers due to the opening ratio and the size of timbers are examined, experimentally. In the experiments, columnar timbers are used, and the generated bore heights are comparable with the diameter of the timbers.

Experiments

A rectangular, glass-walled flume of 0.3m wide, 0.5m high and 11.0m long with a steel horizontal bed was used in the experiments. Bores were generated by the rapid pull-up of a sluice gate installed at a distance of 5.0m from the upstream end of the flume. The impulsive forces were measured at a distance of 5.05m from the gate by means of a strain gauge unit attached to a cantilever with a vertical wall (Matsutomi, 1988). The experimental setup is shown in Figure 1.

The accuracy of the force meter was examined by comparison of the impulsive force measured with the force meter and that measured with the pressure gauges (Matsutomi, 1990). An example of the results which are the cases without timbers is shown in Figure 2. From this figure, it may be concluded that the accuracy of the force meter is satisfactory.

Experimental conditions of the bore generation through all the experiments are summarized in Table 1. In this table, h_1 is the initial water depth in the upstream region, h_0 and U_0 are the initial water depth and the horizontal water particle velocity in the downstream region, respectively. All of the generated bores satisfy the moving hydraulic jump condition (Matsutomi, 1989a).
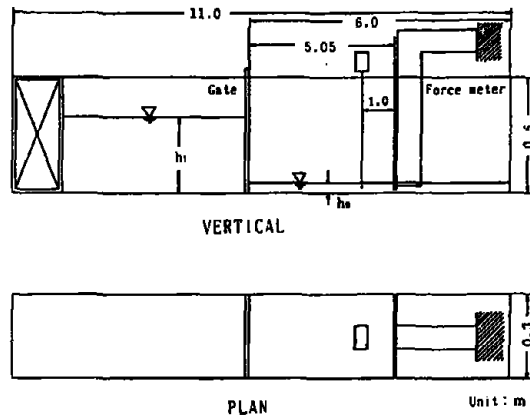
Figure 1. Experimental setup.
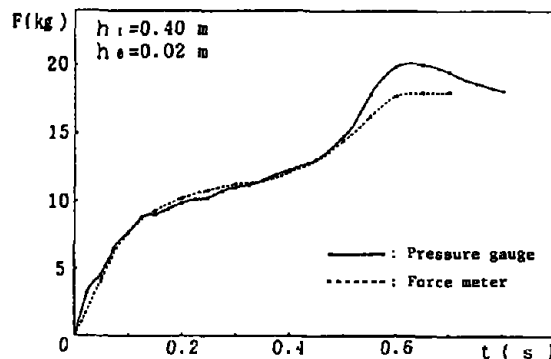
Figure 2. An examination of accuracy.

52

Table 1. Experimental conditions of bore generation

h_1 (m)	h_0 (m)	U_0 (m/s)
0.40, 0.45	0.02	0

In each run, one timber was used, and it was initially placed at a distance of 2.55 m from the gate, directing its longitudinal axis in parallel to the flume (Matsutomi, 1989b). Dimensions of the timbers adopted in the experiments are summarized in Table 2, where D is the diameter, L is the length and W is the weight at the wet state.

Table 2. Dimensions of timbers

D (cm)	L (cm)	(L/D)	W (g)
2.4 ~ 12.0	14.4 ~ 144	6, 8, 12	48 ~ 9060

Slit plastic plates with the opening ratio λ of 2, 20, 33, 50, 70 and 87% were adopted as the wall. Figure 3 shows an example of the wall with λ = 33%. This slit arrangement was maintained for all λ. In the experiments, the behavior of timbers near the wall was also observed with a video system.
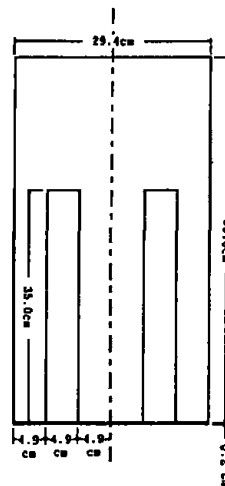
Figure 3. Slit wall with λ = 33%.

Results and Discussions

(1) Impulsive force of timbers

Figure 4 shows examples of the time history of the total impulsive force F for various values of λ. In the figure the peaks around t=0.3 ~ 0.5s are due to the collision of timbers. This figure tells that:

53

1. larger λ yields greater impulsive force of timbers, and it is not ignored compared with the force of bores themselves. This is due to a fender effect of fluid thrown out upwards (Matsutomi, 1990);

2. with a certain value of λ, the magnitude of F at the collision of timbers becomes the same as that at the fall of the fluid thrown out, i.e., t ≈ 0.6s; and

3. the impulsive force of timbers becomes dominant when λ exceeds a certain value.
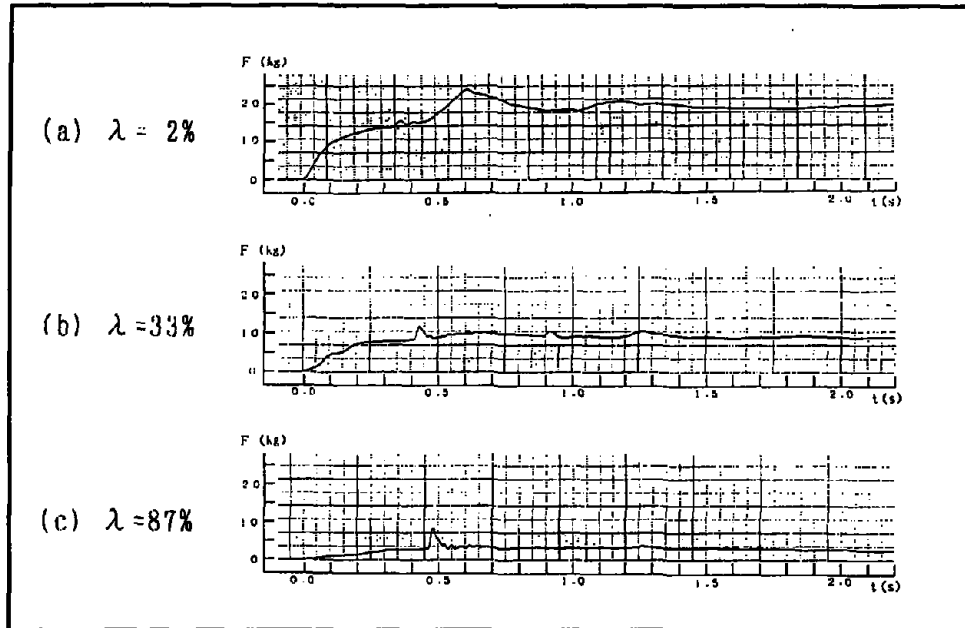
Figure 4. Time histories of the total impulsive force F (h_1 = 0.4m, h_0 = 0.02m, L/D = 8, D = 5.8cm).

(2) Apparent inertia coefficient

Figure 5 shows an example of variations of the apparent inertia coefficient C_{MA} due to λ, where C_{MA} is defined as follows:

$$\int F_d \ dt = C_{MA} \cdot M \cdot U_w \tag{1}$$

In Eq. (1), F_d is the measured impulsive force of timbers, t is the time, M is the mass of timbers at the wet state and U_w is the moving velocity of the rear of timbers immediately before the collision. The reasons why the above U_w is selected as a representative velocity are that:

1) usually, only mean hydraulic quantities in a flow field are given,
2) the moving velocity is not affected by the existence of the wall.

Essentially, the moving velocity in the flow field affected by the wall should be adopted. This is a case for future research. In Figure 5, the circles and triangles are the experimental data averaged for ten runs, I for the data of L/D=8 is the standard deviation and the solid line is the best fit curve for all the data which is expressed as

$$C_{MA} = 0.0123\lambda + 0.34 , \tag{2}$$

54

where the unit of λ is %. Figure 5 tells that the apparent inertia coefficient of timbers defined by Eq. (1) is nearly proportional to λ.

When $\lambda \approx 100\%$, C_{MA} may be interpreted as the original inertia coefficient C_M, and the value becomes about 1.57. This value is almost the same as that (1.5 to 1.6) evaluated by Horikawa (1983). Therefore, Eq. (2) is rewritten as

$$C_{MA} = C_M + 0.0123\lambda - 1.23 \qquad (3)$$

It should be noted that the value of C_M seems to depend on the slenderness ratio (L/D) of timbers (Goto et al., 1982), the ratio of timber length to surface roller length of bores and so on.
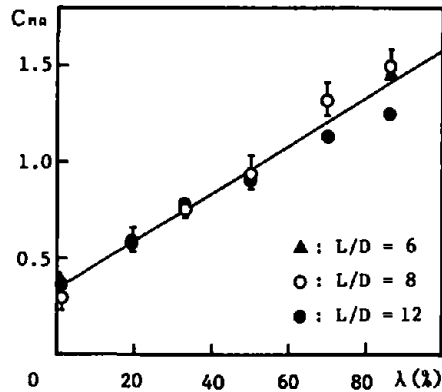
Figure 5. Variations of C_{MA} due to
λ ($h_1 = 0.4m$, $h_0 = 0.02m$,
$D = 5.8cm$).

(3) Impact duration time

Figure 6 shows examples of the time histories of the impulsive force, F_d, of timbers with diameters of various values in $\lambda = 87\%$. Small fluctuations in the records are caused by the natural oscillations of the force meter. Figure 7 shows an example of variations of the impact duration time, Δt, of timbers defined in Figure 8 due to λ. In Figure 7, the opened and closed circles are the experimental data averaged for ten runs. The standard deviations of the data have a tendency to increase as λ becomes smaller. The range was 0.001 ~ 0.008s. These figures tell that:

1. the recorded profile of F_d is approximated by a triangle;
2. the impact duration time is not so fluctuant under the same experimental conditions. This fact is different from that in short waves;
3. greater F_{dm} which is the maximum impulsive force of timbers and is also defined in Figure 8 yields longer impact duration time; and
4. larger λ yields longer impact duration time. However, the impact duration time is almost constant when λ is larger than about 20%.

Because of the strong fluctuations, few studies have been done on the similarity law of Δt is even in short waves. But, in timbers, it is so weak that the discussions seem to be relatively easy. Another reason for the selection of Δt is that higher accuracy is expected in the experiments compared with the forces.

55
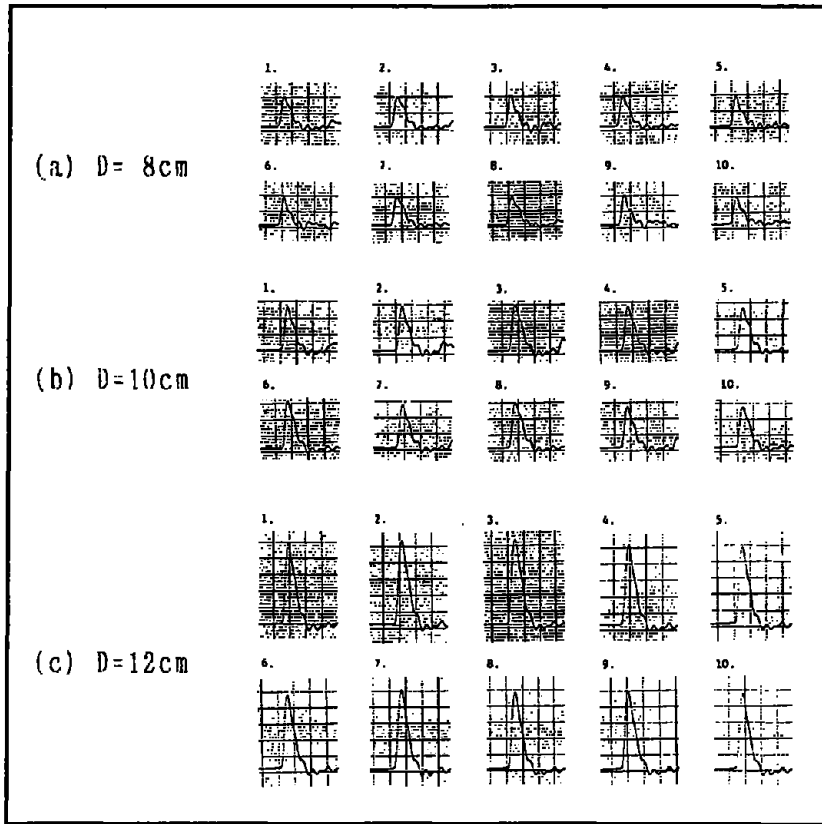
Figure 6. Time histories of the impulsive force, F_d, of timbers
($h_1 = 0.4m$, $h_0 = 0.02m$, $L/D = 8$, $\lambda = 87\%$).
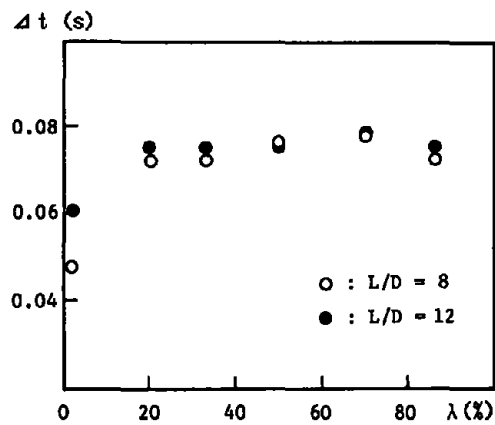
Figure 7. Variations of Δt due to λ ($h_1 = 0.4m$,
$h_0 = 0.02m$, $D = 5.8cm$).
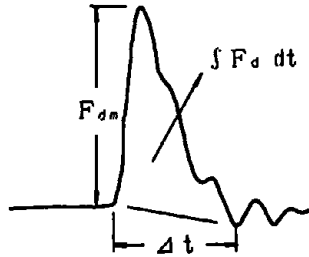
Figure 8. Definition sketch of
Δt and F_{dm}.

Figure 9 shows an example of variations of the impact duration time, Δt, due to D. In the figure, the opened and closed circles are the experimental data averaged for ten runs (the standard deviations except for $D = 2.4cm$ are about 0.001s, which is very small), the line with slope of $1/2$ is the Froude law and the solid line is the best fit curve for the data which is expressed as

$$\Delta t = 0.0563 \cdot D^{0.1666} \tag{4}$$

where the unit of D is cm. This figure tells that:

1. the impact duration time of timbers is not under the rule of Froude law;
2. the impact duration time of timbers does not always depend on the slenderness ration (L/D) if it is within the practical range $(L/D = 8 \sim 20)$.

The first would not change even if the incident bore heights in the experiments are changed with D under the rule of Froude law. The second is readily deduced from the fact that the influence of frictional drag upon the movement of timbers is minor (Goto et al., 1982).
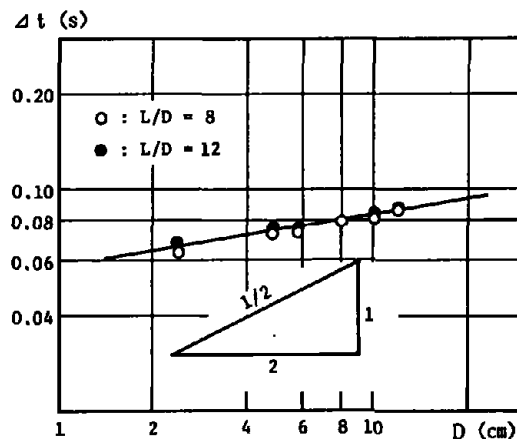
Figure 9. Variations of Δt due to D
$(h_1 = 0.4m, h_0 = 0.02m,$
$\lambda = 87\%)$.

57

Excepting the densities of fluid and timbers, D, L, U_w and the gravitational acceleration g would be considered as the factors which are closely related to Δt. An expression for Δt is obtained from the dimensional analysis as follows:

$$U_w \, \Delta t/D = f \, (L/D, \, gD/U_w^2) \tag{5}$$

Figure 10 shows the relation between $(U_w \, \Delta t/D)$ and $gD/U_w^2)$. In the figure, the opened and closed circles are the experimental data averaged for ten runs, and the solid line is the best fit curve for the data which is expressed as

$$U_w \, \Delta t/D = 0.734 \cdot (gD/U_w^2)^{-0.726} \tag{6}$$

It is also understood that the relation is not always affected by the slenderness ratio of timbers.
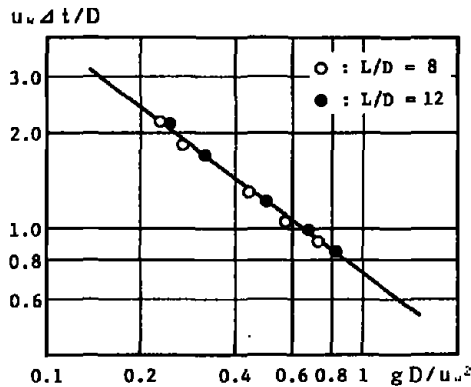
Figure 10. Relation between $(U_w \, \Delta t/D)$ and (gD/U_w^2) $(h_1 = 0.4m,$ $h_0 = 0.02m, \, \lambda = 87\%)$.

From Eqs. (4) and (6), Eq. (7) is estimated as the empirical formula for U_w in the extent of this experiment:

$$U_w = 216 \cdot D^{-0.239} \tag{7}$$

where the unit of U_w is cm/s. For reference, a comparison of the moving velocities of timbers evaluated from Eq. (7) and those measured in the experiments is shown in Figure 11. The experimental data are also averaged for ten runs. From the figure, it is necessary to tell that the effect of (L/D) on U_w is a little large, compared with that on Δt. Essentially, U_w seems to depend on the bore height nondimensionalized by h_0 and so on, as well as the slenderness ratio of timbers. Please, pay attention to the dimensions of Eq. (4) and (7). These are also problems for future research.

58
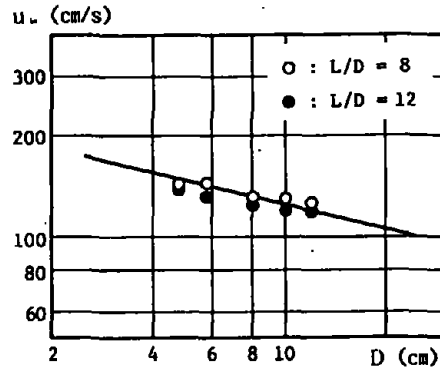
Figure 11. Comparison of empirical and
experimental U_w ($h_1 = 0.4m$,
$h_0 = 0.02m$, $\lambda = 87\%$).

4. Maximum Impulsive force

Based on the considerations in sections (1) and (3), let us assume that F_d has a triangular distribution. From this assumption, we obtain the maximum impulsive force F_{dm} of timbers as

$$F_{dm} = 2.0 \, C_{MA} \cdot U_w / \Delta t \tag{8}$$

According to comparisons, the values calculated by Eq. (8) seem to have a tendency to be much smaller than those derived by the elastic theory (Mizuhara et al., 1980).

Let me show you an example of calculations of Eq. (8) under the conditions of $D = 1m$, $L = 11m$, $\lambda = 87\%$ and the specific gravity $= 0.6$:

$$C_{MA} = 0.0123 \times 87 + 0.34 = 1.41 \tag{9}$$

$$\Delta t = 0.0563 \times 100^{0.1666} = 0.121s \tag{10}$$

$$U_w = 216 \times 100^{-0.239} = 71.9cm/s \tag{11}$$

$$F_{dm} = 2.0 \times 1.41 \times 0.5^2 \times \pi \times 11 \times 0.6 \times 0.719/9.8/0.121 = 8.9 \, ton \tag{12}$$

It is easy to realize that the impulsive force of timbers is fairly large. By the way, 8 ton has been adopted in Japan when the impulsive force of timbers is taken into account in the design of coastal structures.

Conclusions

The variation features of the apparent inertia coefficient and the impact duration time of timbers were examined, experimentally. A procedure was also studied for predicting the maximum impulsive force of timbers. The findings are that:

1. According to circumstances, i.e., the opening ratio λ of structures, the ratio of the bore height to the diameter D of timbers and so on, the impulsive force, F_d, of timbers is not negligible, compared with that of bores themselves;

59

2. The inertia coefficient C_M of timbers is about 1.6 when the bore height and the diameter of timbers are comparable. The value is almost the same as that evaluated by Horikawa (1983);

3. The apparent inertia coefficient C_{MA} of timbers defined by Eq. (1) is nearly proportional to λ;

4. Larger λ yields longer impact duration time, Δt, of timbers defined in Figure 8. However, it is almost constant when λ is larger than about 20%;

5. The impact duration time of timbers is not likely to be under the rule of Froude law;

6. The impact duration time of timbers does not always depend on the slenderness ratio (L/D) if it is within the practical range $(L/D = 8 - 20)$;

7. A procedure for predicting the maximum impulsive force, F_{dm}, of timbers drifted by bores is presented.

Acknowledgements

References

Goto, C., Z. Sasaki and N. Shuto, 1982. Timbers spread due to tsunamis. *Proc. 29th Japanese Conference on Coastal Engineering*, p.491-495. (in Japanese)

Horikawa, K., 1983. Destructive force due to the collision of drifting bodies. *Rep. of Study supported by the Grant from the Ministry of Education*, no.A-58-2, p.858-92. (in Japanese)

Matsutomi, H., 1988. Impulsive force on walls due to the collision of a bore. *Proc. JSCE*, no.399, p.147-155. (in Japanese)

Matsutomi, H., 1989a. An examination of moving hydraulic jump condition. *Proc. 33rd Japanese Conf. on Hydraulics*, p.271-276. (in Japanese)

Matsutomi, H., 1989b. Impulsive force due to the collision of a bore with drifting timbers (1). *Proc. Coastal Eng.*, JSCE, vol.37, p.574-578. (in Japanese)

Matsutomi, H., 1990. Impulsive force due to the collision of a bore with drifting timbers (2). *Proc. Coastal Eng.*, JSCE, vol.37, p.654-658. (in Japanese)

Mizuhara, K., A. Takei and N. Minami, 1980. Fundamental study on the check of drifting woods (2). *New Sabo*, no.114, p.9-16. (in Japanese)

Discussion

Comment: In response to questions it was noted that in the experiment the timbers were 2.5 meters from the wall, but that the distance was not a factor in the analysis. The deformation of the steel walls under the timbers impact was also neglected as the relative elasticity of the steel to wood was 1 to 23. Although some timbers might impact the steel wall broadside, only the more dangerous end-on impact were studied.

Comment: In response to the question of replicability by varying the strength of the bore and perhaps, the ratio of the length to the diameter of the timbers, it was noted that this pattern was chosen based on experience with earlier experiments on how the timbers would react.

Comment: In the case of the 1960 Chilean tsunami, there was a very bitter experience with this kind of phenomenon. Once a timber with a diameter of 60cm hits a Japanese wooden house it would be completely destroyed. But the Chilean tsunami which struck a Japan city was not a bore, but a flow. It may be necessary to extend the experiment to longer tsunami periods or in terms of velocities which would be expected from tsunamis.

SIMULATION MODELS OF TIMBER AND OIL SPREAD DUE TO TSUNAMIS

C. Goto
Hydraulic Engineering Division
Port and Harbour Research Institute,
Ministry of Transport,
Yokosuka, Japan 239

Abstract

Numerical models of timber and oil spread due to tsunamis are developed. The models are applied to Miyako Bay, on the North Sanriku Coast of Japan. It is assumed that 6,000 timbers are being stored on both the ground and in a lumber harbor and that 2,000 m^3 of oil spill from tanks due to an earthquake. The input tsunami is the same magnitude as the Tokachi-oki tsunami which hit in 1968.

Introduction

Once floated and washed away by tsunamis, timbers stored in port areas often become destructive forces to houses and other port facilities. Inflammable materials, such as oil stored in large quantities, also may be potentially devastating if discharged because of earthquakes and tsunamis.

Hydraulic experiments were carried out in order to determine the drag coefficient and virtual mass coefficient of a timber as well as the diffusion coefficient of timbers (Goto, 1982). These coefficients are important to describe the behavior of timbers in water flow. A model was built to estimate the motion of timbers in a tsunami flow. The motion consists of two parts, a mean motion and a diffusion. The mean motion is governed and determined by the mean current induced by tsunamis, combining the drag and added-mass effects of timbers. The diffusion is determined by a consideration that the spread of timbers around their center of gravity follows a random process, the variance of the probability density of which is equivalent to the magnitude of diffusion obtained by experiments.

A simulation model of oil drift has also developed by the author (Goto, 1985). The method used is for transport during a short time period only, since no effects of surface tension are included. The model equations are derived from the Navier-Stokes equations and the continuity equation and are solved by FDM scheme.

In the paper, these methods are applied to Miyako Bay, on the North Sanriku Coast of Japan. It is assumed that 6,000 timbers are being stored on both the ground and in a lumber harbor and that 2,000 m^3 of oil spill from tanks due to an earthquake. The input tsunami is the same magnitude as the Tokachi-oki tsunami which hit in 1968.

Numerical Method of Timber Spread

We assume that the motion of timber consists of two parts, a mean motion and a diffusion. The mean motion is governed and determined by the mean current induced by tsunamis, on combining the drag and virtual mass effects of timbers. The mean motion of timbers is governed in following equations,

$$\rho_t V \frac{dU_t}{dt} = \rho V \frac{dU}{dt} + \rho(C_M - 1) V (\frac{dU}{dt} - \frac{dU_t}{dt}) - \frac{1}{2} \rho C_D A (U_t - U) |U_t - U| \qquad (1)$$

where U_t and U are speed vectors of timbers and water particles, respectively. And ρ_t and ρ express the density of timbers and water. In this equation, C_M denotes the virtual mass coefficient and C_D, the drag coefficient. These coefficients are determined by hydraulic experiments as follows:

$$C_M = 1.78 \qquad (2)$$

$$C_D = (0.91 + 32.5\ R_e^{-1/2})^2 + 0.1\ F_r^{1/4} \qquad (3)$$

where R_e and F_r indicate the Reynolds and Froude numbers of the timbers spread.

The diffusion is determined by a consideration that the spread of timbers around their center of gravity follows a random process, the variance of the probability density of which is equivalent to the magnitude of diffusion obtained by experiments. The position of timber X after an infinitesimal time, Δt, is expressed in following equation,

$$X = X_0 = \int_0^t U_t dt + \sum_{k=0}^{n\Delta t} \sqrt{24 k \Delta t}\ (\xi^k - 0.5) \qquad (4)$$

where ξ^k is given as a random function uniformly distributed in the interval -1 and 1. k denotes the diffusion coefficient determined by the hydraulic experiment as the following equation,

$$k = 0.032\ U * h \qquad (5)$$

In Eq. (5), U^* is the friction velocity of water flow and h is the water depth.

Numerical Method of Oil Spread

As preliminary studies dealing with forces in action permit simplification of the problem, the spread of oil is divided into three regimes: gravity-inertia, gravity-viscous and surface tension-viscous. From the Navier-Stokes equations and the equation of continuity, we assume that the vertical acceleration of oil particles is negligible compared with the gravity acceleration, then we have the governing equations of the spread of oil as follows:

$$\frac{\partial D}{\partial t} + \frac{\partial M}{\partial x} + \frac{\partial N}{\partial y} = 0 \qquad (6)$$

$$\frac{\partial M}{\partial t} + \frac{\partial}{\partial x}(uM) + \frac{\partial}{\partial y}(vM) + gD\frac{\partial \eta}{\partial x} + \frac{\tau_x}{\rho_0} = 0 \qquad (7)$$

$$\frac{\partial N}{\partial t} + \frac{\partial}{\partial x}(uN) + \frac{\partial}{\partial y}(vN) + gD\frac{\partial \eta}{\partial y} + \frac{\tau_y}{\rho_0} = 0 \qquad (8)$$

where (u, v) denotes spread speed of oil; ρ_0, the oil density; D, the oil thickness; η, the height of oil surface from original plane; (M, N) the discharge flux of oil spread; and τ_x and τ_y indicate the interaction forces between the oil and the tsunami current.

Application to Miyako Bay

Numerical simulation models of timber and oil spread are applied to Miyako Bay on the North Sanriku Coast of Japan. It is assumed that 6,000 timbers are being stored on ground and in a lumber harbor and that 2,000 m^3 of oil spill from tanks due to an earthquake. The input tsunami has the same magnitude as the Tokachi-oki tsunami of 1968.

The work is divided into three parts: computation of the tsunami current, spread of the timbers and the oil. The motion of the tsunami current is computed by the finite difference scheme, TOHOKU MODEL, using the shallow water theory and a grid size of 50 m. The motion of timbers and oil is also computed by the finite difference scheme governed by Eqs. (1)-(8).

Figure 1 shows the numerical results of timber spread at 40, 60, 80 and 100 minutes after the tsunami occurred. The black circles indicate the grid size of 50 m where timbers are found. Numerical results of the oil spread at 10 minute intervals after the tsunami occurred are shown in Fig. 2. The shaded area indicates the region of drifting oil.

As the results indicate, it is concluded that the present method can be applied, without difficulty, to actual topography of a complicated geometry.

References

Goto, C. et al. (1982) Timbers spread due to tsunamis. *Proc. 29th Japanese Conf. on Coastal Eng.*, p.491-495. (in Japanese)

Goto, C. (1985) A simulation model of oil spread due to tsunamis. *Proc. JSCE*, no.357, p.217-223. (in Japanese)

Discussion

Comment: In tracing the timbers there is one parameter, kappa, related to diffusion or dispersion, which must be determined by experiment.

t=40min.   t=60min.   t=80min.   t=100min.
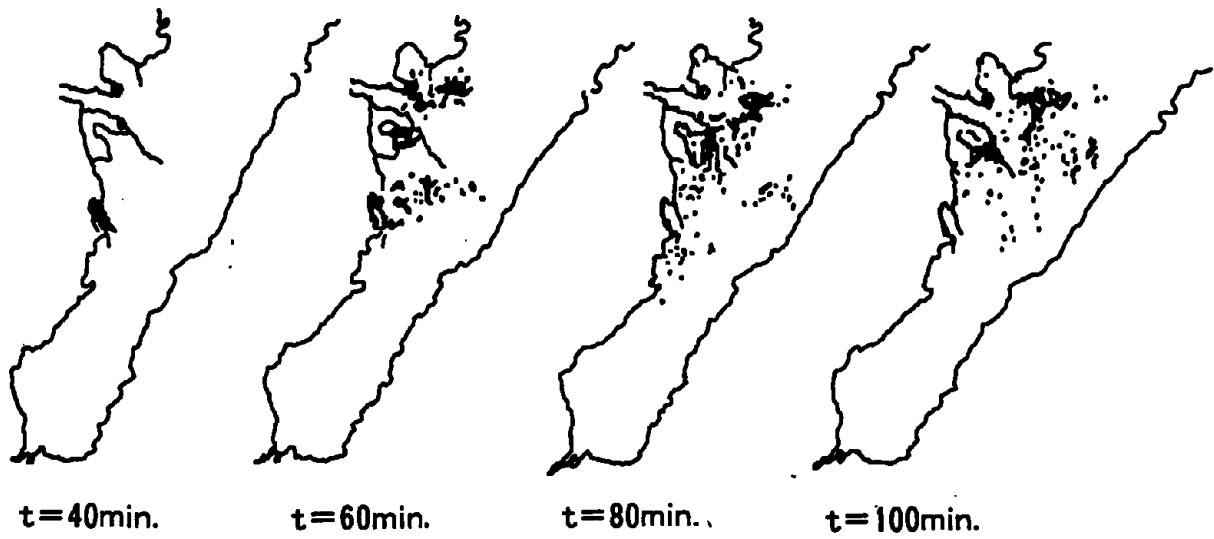
Figure 1. Numerical results of timber spread.

t=40min.   t=50min.   t=60min.   t=70min.   t=80min.

t=90min.   t=100min.   t=110min.   t=120min.
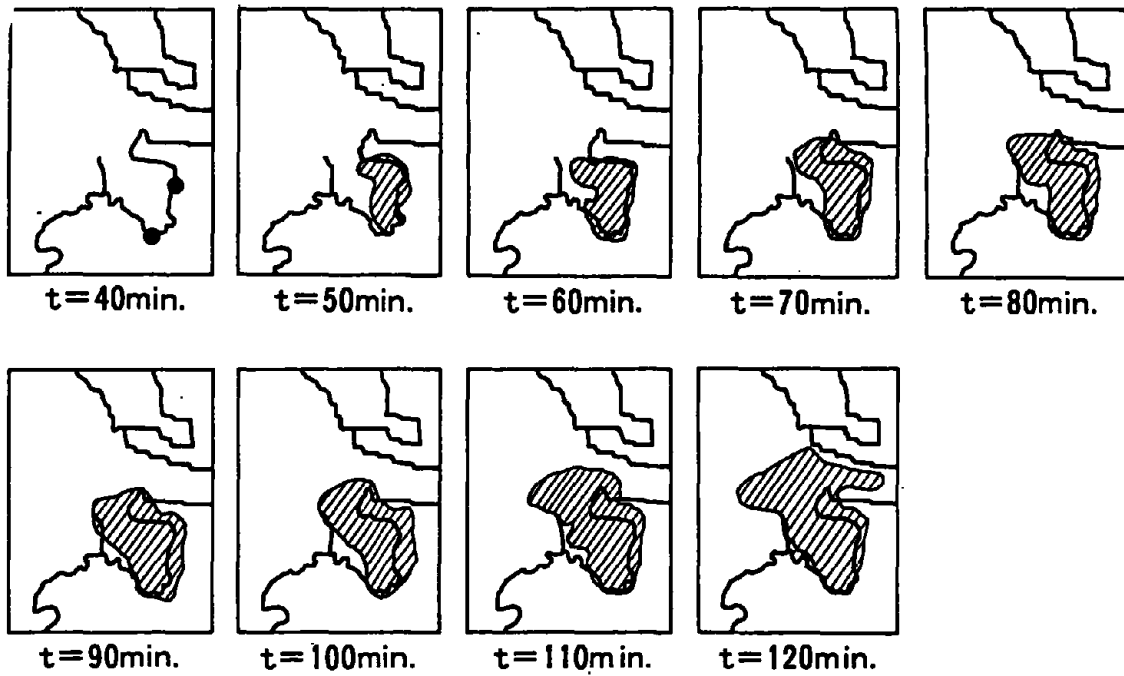
Figure 2. Numerical results of oil spread.

ROUND TABLE DISCUSSION OF TOPIC A

The workshop is divided into three broad areas. In this period following the first group of papers, larger issues can be addressed and a workshop experience can be introduced to the predominantly symposium environment. Some questions which should be addressed include what progress has been made since the first UJNR Tsunami Workshop, what areas look promising, and how frequently should these topics be discussed.

Comment: Seven years ago during the first workshop there were many theoretical talks and very few talks with actual data which contrasts significantly with this morning's talks. Probably 2 weeks after that first workshop in Japan, the 1983 Sea of Japan tsunami took place and there were several subsequent tsunamis. It is clear there are capabilities in place that were not available before 1983. That is a great step forward and certainly the advances made in the last seven years, while not totally as a result of new observations but certainly to a large measure, let us know what defines the modeling directions to be taken. The next big challenge is to understand the forces in the very near shore and over-land. No one has talked about what needs to be measured in this environment. Wave heights are to be the principal measured quantity but in the inshore inundation zone, we need new measurements to support the modeling activity. What new observational tools should be developed for future tsunamis? There has been great progress in the last seven years because there has been a balance between observation and modeling. The models are in place but where are the observations for the near-shore effects?

Comment: The capability to make good accurate deep ocean measurements of tsunamis' bottom pressure records is available and now the emphasis should be on developing near-shore inundation measurements. It is going to be harder than the deep ocean measurements. In the deep ocean measurements, a big ship is needed to do the work, but once the instrument is in the water and on the bottom, in the case of a bottom pressure recorder, the environment is rather benign. Problems found near-shore, particularly with biological fouling, can be very serious both for pressure gages and current meters. Now measurement of currents is needed. Also there are very serious problems, which Dr. Tsuji addressed earlier, with the temperature sensitivity of many transducers of both diaphragm type and the pressure gage instruments. With both diaphragm and quartz crystals there is inevitably a temperature sensitivity but in the deep ocean, that's not a serious problem. In the near-shore region there are large swings of temperature and it can really make it difficult to interpret the records. In summary it is going to be even more difficult perhaps than the deep ocean problem.

Question: There are only a few deep ocean gages out now. Will there be a need in the near future, five years or so, for some use of the abandoned or underused telephone cables for deep ocean gages or the need for putting some more of the bounce-up type gages? Or once a couple of these events have been recorded, will there still be a need for deep-ocean type monitoring?

Response: Recently the telephone cable from Japan to Guam was retired and replaced by an optical fiber cable. The Japanese Earthquake Research Institute accept the retired cable from the telephone company. They are planning to attach tsunami and seismic sensors with electro-magnetic sensors near Saipan Island and expect to record tsunamis in deep water in real time. It would take about three hundred million dollars to lay the sea bottom cable, in this case, the cable was obtained for about three million dollars (U.S.), including the cost to attach the sea bottom sensors.

67

There are problems in using the sea bottom sensors at of about 50 meters depth. One problem in Japan comes from the oysters around the Tokyo region. After about two months in summer, the sensors are covered with oysters, and so quit working. If the sensors are deeper, up to 200 meters, the biological interference is not bad. Another problem is scraping due to the fish trolling; up to half of the current meters may be lost due to scraping. A deeper placement of the instruments would be necessary for continuous measurements. It is estimated that to measure tsunamis with battery operated instruments and to send the information by radio to a satellite would cost about 0.6 million U.S. dollars. This experiment may be useful for the safety of coastal towns and would be useful for the inversion to get the seismic source. On one small tide gage station near Sendai, one record was obtained for 2 November 1989 for one of the small tsunamis which happened off the coast of Sanriku. Professor Abe pointed out that a tidal gage record from inside the bay is very difficult to use to make inversions to the original source, but for the sea bottom sensors from isolated islands, good information can be obtained. These data are useful for inversion studies and for warning the nearby coastal communities. The pop-up sensor can be cheaper, but for warning purposes the cable-connected type is needed to get operational data.

Comment: The flooding problem has so many variables associated with it that any one solution is not useful for any other situation. An idea that would be useful would be take a quality, such as momentum flux across the boundary the shore line. All this momentum flux gets turned around and becomes a wave going the other direction because of the impact of the water on the ground. So the momentum flux itself ought to be a fair measure of what the tsunami is going to do on land without looking in detail at the hydrodynamic water motions.

In the past theoreticians and modelers have focused on such things as tsunami run-up as opposed to energy and momentum considerations which are the really significant causes of death and destruction near-shore. One thing to think about is a better way of characterizing the damage potential of a tsunami in terms of energy and momentum flux. Engineers have thought about this and there ought to be a better parameter for the tsunami scientist to use than just wave height.

The momentum can be calculated if the wave height and particle velocities are known so if the current is measured, momentum can be calculated. This needs not be measured directly because of the hydrodynamic equations are known for a wave in one place, it can be interpolated for some other place. In an average way the momentum can be calculated but not in detail at points along the shore line. Even a blurred picture of whole coast maybe a quality that is useful.

The actual current measurement of momentum flux and the actual conditions may be difficult to get due to the long interval between tsunamis as well as the continuing maintenance problems. If this measurement is replaced with the results of the computation, and then compared with large scale hydraulic experiments for verification, then in this way the order of the magnitude of the computation can be verified with the models. A major concern is how to reduce the tsunami disaster.

Comment: There are two important things which should be solved in the near future: 1) force or current velocity and 2) a wave profile in order to determine the magnitude of the expected flooded area. Japan has sea walls 5 or 6 meters high. However in a major tsunami, the wave is much higher, up to 30 meters, and will overflow and inundate the shelter area. In order to determine the quantity of water brought in by this tsunami, an accurate wave profile is needed to determine the exact initial profile. Without this, an accurate estimate of the disaster potential of the tsunami can not be made. One urgent need is a method to determine the accurate initial profile, perhaps by

using the inversion method. Without this, progress in reducing the tsunami disaster can not be made.

Comment: It is quite clear that now very good numerical methods, very good analytical techniques exist. Once the initial conditions are known, runup can be calculated. What is needed is 1) very good initial data and 2) very good inundation data. Maybe Frank Gonzales can explain his ideas for pressure. One part of the problem that is missing is that once a tsunami has occurred with some inundation, what was the time history at some point along the coastline.

Response: The idea would address the problem of infrequency of tsunamis. It would begin perhaps to address the idea of the maintenance problem, but that is still a very serious problem. Basically, the idea is to develop a cheap pressure gage with at least 50% to 75% reliability which would be able to lie dormant for a period of about 10 years and deploy these gages at a number of selected sites on the shore, around the Pacific rim. They need to be capable of acquiring pressure data at about 15-second intervals for a period of a couple of days triggered by some kind of a pressure head device. Now the technology to put that type of package together exists today. If the costs could be kept low enough it would make such a scheme practical. They could be implanted and left. There would need to be a testing program, of course. They would be left there for as long as it took for a tsunami to occur and, after a tsunami occurred, they would be recovered with the expectation that at least 50% to 75% of them had gathered reliable data. The problem is not a technology problem, but it a human problem—vandalism. Where can they be put, and can this be coordinated with local civil authorities? The concept is worth considering. Another idea by Dick Seymor at Scripps Institute of Oceanography was to use downward-looking acoustic or laser sensors attached to buildings; this would minimize the vandal problem. Again they could be triggered by a pressure head of water, by a little sensor at the bottom of building or something like that. The problems are hard in terms of making inundation zone measurements but with some original thinking there could be some progress on this problem. The water currents will be difficult to measure but the pressure measurements would be very important in providing a time series of inundation height on land.

Comment: Once while working in an electronics laboratory measuring the stability of oscillators, it was observed that if someone walked around in the laboratory, the capacitance between the person and the elements of the oscillators would cause the frequency to change. If in various places along the coast, oscillators which were internally coupled to the environment was placed, then the rise and fall of the water would change the frequency of the oscillator and could be a measurement of the rise and fall of the water itself.

Comment: There are two distinct aspects to the seismic source and tsunami generation. The first one is that in order to make a quick warning, one needs to make a quick decision as to what has happened immediately after the earthquake. That is becoming easier and there will probably be some talks tomorrow about the quick estimation of the source process. But to make an assessment of what may happen in a future tsunami, a totally different approach is needed. For this we need more study of historical tsunamis and historical seismic earthquakes because, like tsunamis, huge earthquakes are an infrequent phenomenon and the typical recurrence time of large earthquake or tsunami would be a hundred years or so. Therefore, the history is needed to estimate what is going to happen in the future. That is the second important orientation.

We have the seismic gaps information pretty well in hand. It tells us where we might expect some future large earthquakes and tsunamis and gives us the location of areas where monitoring instruments might be concentrated.

Comment: Regarding the historical earthquakes, it is very difficult to assess the question of recurrence of earthquakes because all that is available to work with, in many cases, are dates. There is a very interesting paper by Kanamori et al. regarding the mechanism of rupture in the Nankai trough of Japan, where he shows that occasionally the whole trough ruptures over a large distance and in some instances, only half of it ruptures and the rest is left to a later time. Fortunately, in Japan, these things have been pretty well documented. In the case of Ecuador, there was a major earthquake with a tsunami in 1906 and another one in 1979. It is still an open question at this point whether these are exact replicas of each other or whether the 1979 earthquake might have been somewhat smaller than the one in 1906. So when using seismic gaps, we have to be very careful that a sample recurrence in time does not necessarily mean a quantitative periodicity of the earthquake itself. There would be even further complications if the earthquake did repeat itself, the tsunami may not.

Comment: Recently, tsunami data from San Diego for two Japanese earthquakes in Sanriku were obtained from the National Geophysical Data Center in Boulder, Colorado, one from 1944-46 and the other from 1854. The two tide gage records are surprisingly very different. So that means, from historical and seismic catalogs, the rough recurrence time is known to about one-hundred years, but that does not necessarily mean the same thing will happen. Probably future tsunamis will be different again.

Both the two 1854 and the two 1944-1966 earthquakes ruptured only half of the maximum zone for each earthquake.

Possibly changes in the harbor at San Diego could account for this. The whole question of tide gages in harbors is a very difficult one. The notorious stilling well tide gages that have such poor, non-linear response functions have been almost completely replaced by bubbler gages. The theoretical response function of the bubbler gage, is quite good, even in the tsunami periods.

Comment: There should be very little distortion. However, the problem is that the bubbler gage response can be adjusted, at each station. There are little valves that control the amount of gas going out of the pressure and the appearance of the bubbler gage records from a particular harbor taken a year apart are quite different in terms of their response. It is the unknown human factor that makes it very difficult to judge the response of those gages. But, the seismic gaps are a very good guide to us as a community as to where we should be putting our resources in terms of limited instrumentation, limited ship time, etc. Gonzáles reported on a 3 or 4 mm tsunami that had traveled over 6,000 miles, and was registered on the gage from that 7.5 earthquake on 5th April. If there were more of these kinds of gages around the Pacific, especially sited to take advantage of the probabilities of earthquakes from the seismic gaps, we would probably get good records at a large percentage of them because these gages are quite sensitive.

Comment: The gage is now deployed near the Shumagin gap and it recorded the far-field tsunami from Japan. It would be important to have had near-field data from the seismic source. It would be desirable to have one or two gages off the coast at every seismic gap around the Pacific. That would be the way to distribute them. Unfortunately, the seismic gap (Parkfield, California) which is most certain to be filled is on a continental stretch and I don't expect that it will create a tsunami.

Comment: The Parkfield earthquakes did cause small tsunamis in 1857 and 1901 from landslides in Monterey Bay as did the recent Loma Prieta earthquake. These are strike slip faults and would not be expected to generate tsunamis of tectonic displacement.

Comment: In terms of the interest of seismologists in bottom pressure recorders, there are potential connections in that they also will register seismic surface waves. However, there is a lot of difficulty in interpreting them. It is not very well understood, although the fundamental physics is. It would yield some offshore seismic data - and there is not much data from OBSs.

One major problem with OBSs is that their lifespan is on the order of a month, and most of them are recording short-period data.

Comment: The Alaskan gages were designed for long duration deployments just because they can not be serviced in the Gulf of Alaska during the winter. A gage that will stay out there 15 months is needed. To get good surface wave data, however, you need one- or two- or three-second data, and a gage is being developed which can do this. It will be deployed this summer (1991) and will take 15-second data. Charles Cox at Scripps Institute of Oceanography uses a different pressure gage and has developed the storage and power packages to keep an instrument down for up to 10 months. The technology is there to store very high rate data and to develop a gage that would also contribute to seismological concerns in terms of surface wave measurements and would be very long duration, ocean seismometer for surface waves.

TOPIC B: APPLICATIONS OF NUMERICAL MODELING TO IMPROVED TRAVEL TIME PREDICTIONS, SOURCE REGION DEFINITION, INUNDATION, AND RUN-UP PREDICTION

Z. Kowalik, and G. Carrier, moderators

STEM WAVES AND HEXAGONAL WAVE PATTERN IN SHALLOW WATER

Sung B. Yoon and Philip L.-F. Liu
School of Civil and Environmental Engineering
Cornell University
Ithaca, NY, USA

Abstract

Forward diffraction of cnoidal waves by a straight breakwater in shallow water is studied based on the parabolic approximation of Boussinesq equations. The relative importance between nonlinearity and angle of incidence is discussed in relation to the development of stem waves and hexagonal waves.

Introduction

Since Perroud (1957) experimentally discovered the existence of stem waves due to the oblique incidence of solitary waves, many researchers have investigated the stem waves experimentally and theoretically. For instance, Nielsen (1962) and Berger & Kohlhase (1976) experimentally showed that stem waves also exist for a periodic wave train obliquely incident on a straight breakwater. Yue & Mei (1980) and Liu & Yoon (1986) numerically demonstrated that stem waves can also be generated by the obliquely incident stokes waves along a breakwater or a depth discontinuity. Based on the parabolic approximation of Boussinesq equations, Yoon & Liu (1989) illustrated the development of stem waves along a breakwater due to a cnoidal wave train with a small angle of incidence.

Hammack, Scheffner & Segur (1990) performed a series of laboratory experiments for cnoidal waves and supported Yoon & Liu's prediction of the development of stem waves qualitatively. They also showed that, when the angle of incidence becomes large, the stem waves do not grow and the hexagonal pattern of short crested waves similar to Genus-2 waves are formed near the breakwater. The Genus-2 waves are the exact solution to KP equations for biperiodic-permanent waves first given by Segur & Finkel (1985). The existence of Genus-2 waves is fully supported by the laboratory experiments of Scheffner (1988) and is also reported in Hammack, Scheffner & Segur (1989). These biperiodic permanent waves were studied numerically by Bryant (1982) for shallow water waves and by Roberts (1983) and Roberts & Peregrine (1983) for Stokes waves. Kirby (1990) presented also the biperiodic waves using his discrete angular spectrum model for a cnoidal wave train.

In this paper, we present some applications of Yoon & Liu's (1989) parabolic approximation model for the case of large angles of incidence to demonstrate the generation of the hexagonal pattern of short crested waves. Some differences between stem waves and hexagonal waves are discussed.

Governing equations

The dimensionless form of Boussinesq equations can be written as (e.g., Peregrine, 1972):

$$\frac{\partial \zeta}{\partial t} + \nabla \cdot [(h + \epsilon\zeta)\vec{u}] = 0 \tag{1}$$

$$\frac{\partial \vec{u}}{\partial t} + \epsilon\vec{u}\cdot\nabla\vec{u} + \nabla\zeta = \mu^2 \{\frac{1}{2} h \frac{\partial}{\partial t} \nabla[\nabla\cdot(h\vec{u})] - \frac{1}{6} h^2 \frac{\partial}{\partial t} \nabla(\nabla\cdot\vec{u})\}$$
$$+ O(\epsilon^2, \epsilon\mu^2, \mu^2) \tag{2}$$

where

$$\epsilon = \frac{a_o'}{h_o'} \ll 1 \ , \quad \mu^2 = \frac{\omega'^2 h_o'}{g} \ll 1 \ , \tag{3}$$

ζ denotes the free surface displacement and $\vec{u}$ represents the depth-averaged horizontal velocity vector. The quantities with a prime in Eq. 3 denote dimensional parameters; a_o' is the wave amplitude, h_o' the water depth, ω' the frequency and g the gravitational acceleration, respectively. The small parameters, ϵ and μ^2, are assumed to be in the same order of magnitude.

The free surface displacement and the velocity vector can be expressed in Fourier series forms (Liu et al.,1985):

$$\zeta(x, y, t) = \frac{1}{2} \sum_n \zeta_n(x, y) e^{-int}, \quad n = \pm 1, \pm 2, \ldots \tag{4.a}$$

$$\vec{u}(x, y, t) = \frac{1}{2} \sum_n \vec{u}_n(x, y) e^{-int}, \quad n = \pm 1, \pm 2, \ldots \tag{4.b}$$

in which $(\zeta_{-n}, \vec{u}_{-n})$ are the complex conjugates of $(\zeta_n, \vec{u}_n)$. Substituting Eq. 4 into the Boussinesq equations and eliminating the velocity vector from the resulting equations, a set of nonlinear mild-slope equation for ζ_n can be obtained. In the present study, the water depth is assumed to be slowly varying only in x-direction, i.e., $h = h(x)$ for convenience. When the angle of incidence is small, we assume:

$$\frac{\partial \zeta_n}{\partial y} \sim O(\mu) \ , \quad \frac{\partial^2 \zeta_n}{\partial y^2} \sim O(\mu^2) \tag{5}$$

The nonlinear mild-slope equations can be simplified to be:

$$\frac{\partial^2 \zeta_n}{\partial x^2} + \frac{\partial^2 \zeta_n}{\partial y^2} + \frac{n^2}{h} (1 + \frac{\mu^2 n^2 h}{3})\zeta_n + \frac{1}{h} \frac{\partial h}{\partial x} \frac{\partial \zeta_n}{\partial x} - \frac{\epsilon}{2h^2} \sum_{s \neq n}$$
$$n(n + s)\zeta_n \zeta_{n-s} = 0 \tag{6}$$

It is convenient to introduce the amplitude function Ψ_n such that

$$\varsigma_n - \Psi(x, y)e^{in\int \frac{1}{\sqrt{h(x)}}dx} \tag{7}$$

Substituting Eq. 6 into the mild-slope equation and adopting the usual parabolic approximation

$$\frac{\partial \Psi_n}{\partial x} \sim O(\mu^2) \quad , \quad \frac{\partial^2 \Psi_n}{\partial x^2} \sim O(\mu^4) \tag{8}$$

we simplify Eq. 6 to be

$$2in\sqrt{h}\frac{\partial \Psi_n}{\partial x} + h\frac{\partial^2 \Psi_n}{\partial y^2} + (in\frac{\partial \sqrt{h}}{\partial x} + \frac{\mu^2 n^4 h}{3})\Psi_n = \frac{\epsilon}{2h}\sum_{s\neq n}n(n+s)\Psi_s\Psi_{n-s} \tag{9}$$

which is a parabolic partial differential equation for Ψ_n and can be solved by an efficient finite-difference scheme, e.g., Crank-Nicolson method.

Stem waves

As shown in Fig. 1, a straight breakwater is located along the x-axis ($x>0$) and the infinitely long directional wave maker along the y-axis ($y<0$) generates a uniform cnoidal wave train. The angle between the direction of propagation of waves and the breakwater is θ, which is assumed to be small. Along the breakwater, no-flux boundary condition is required.

$$\frac{\partial \Psi_n}{\partial y} = 0 \quad , \quad \text{on } y=0. \tag{10}$$

Along the open boundary, $y = L$, which is far from the breakwater, the scattered waves are assumed to be negligible and the incoming uniform cnoidal waves are allowed with the following boundary condition:

$$\frac{\partial \Psi_n}{\partial y} = im_n\Psi_n \quad , \quad \text{on } y=-L. \tag{11}$$

where m_n is the wave number component of each harmonic in the y direction obtained numerically through an iterative scheme. Along x=0, where computations start, obliquely incident cnoidal waves are specified as:

$$\Psi_n - a_n e^{i\alpha_n y\sin\theta} \tag{12}$$

where α_n is the wave number of each harmonic given by

$$\alpha_n - n + \frac{\mu^2 n^3}{6} - \frac{\epsilon}{4a_n}\sum_{s\neq n}(n+s)a_s a_{n-s} \tag{13}$$

The amplitudes a_n can be found for incident cnoidal waves by imposing the uniformity condition (Yoon & Liu, 1989):

$$\alpha_n - n\alpha_1 = 0 \tag{14}$$

Eq. 14 provides N-1 nonlinear algebraic equations for N+1 unknowns, i.e., a_0', a_1, a_2, ... a_N where N is the total number of harmonics included in the computation. The additional equation can be obtained from the energy conservation law. Thus
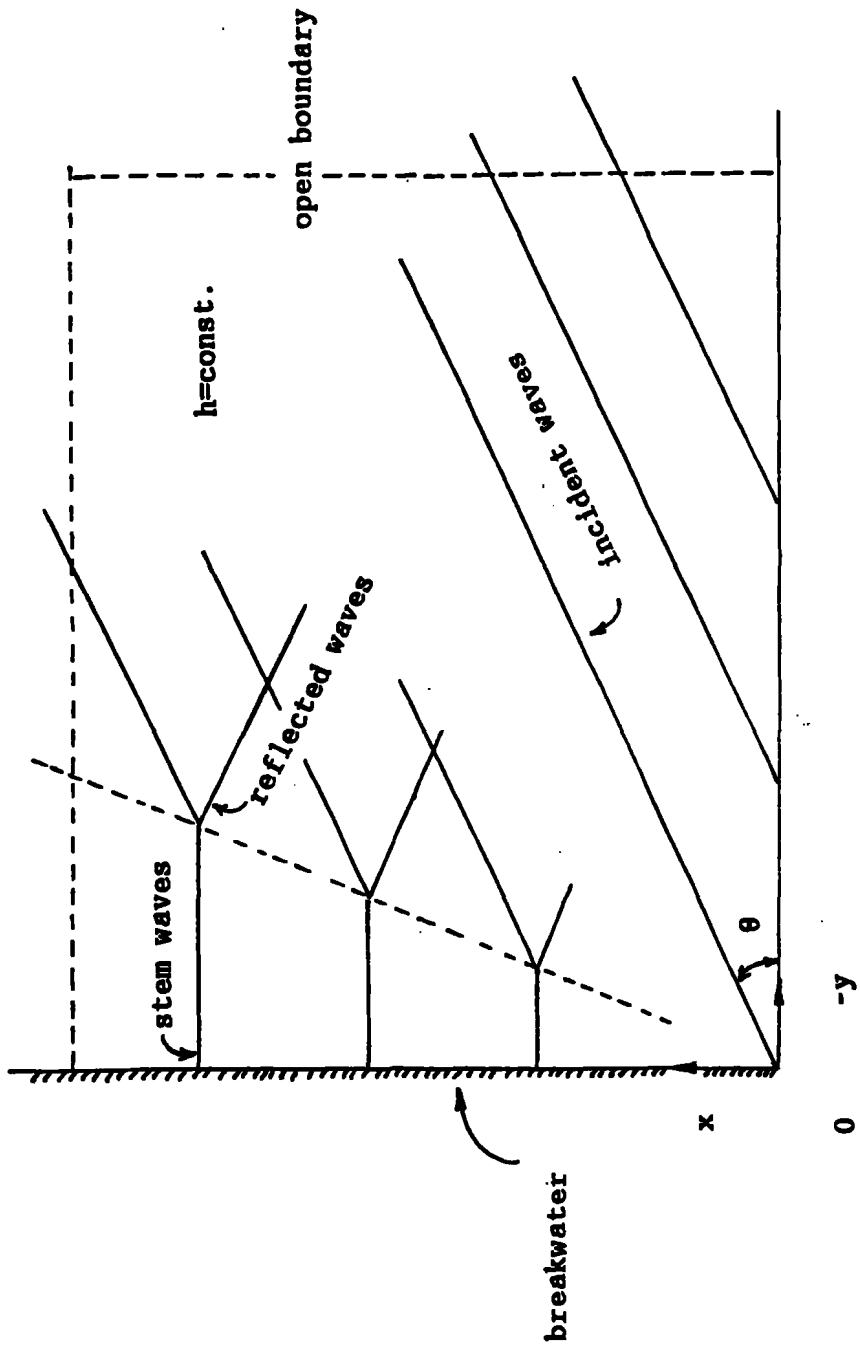
Figure 1 Definition sketch of computational domain for stem wave test

$$\sum_{n=1}^{N} a_n^2 = 1 \tag{15}$$

The relationship between the wave height H_o' and wave amplitudes of each harmonic a_n can be expressed as:

$$H_o' = 2a_o' (a_1 + a_3 + a_5 + \ldots) \tag{16.a}$$

When the crest wave height H_c', measured from mean sea level to crest of waves, is given, the following alternative equation can be used

$$H_c' = a_o' \sum_{n=1}^{N} a_n \tag{16.b}$$

In some cases, the wave length λ_o' instead of wave period T_o' is provided, then the additional equation is required,

$$\alpha_1 \frac{\lambda_o'}{\sqrt{gh_o'}} = T_o' \tag{17}$$

The resulting N+1 (or N+2) nonlinear algebraic equations are solved by the Newton-Raphson method.

Using the wave parameters given in the first column of Table 1, the development of stem waves along the straight breakwater is simulated for small ($\theta=20^o$) and large ($\theta=45^o$) angles of incidence. The water depth is constant ($h_o = 10m$). In the numerical computations, the grid size $\Delta x = \Delta y = \pi/15$ is used. The open boundary is placed at $y = -L = -20\pi$. To show the differences between linear and nonlinear theories, the linear results without nonlinear terms are also calculated.

For the case of small angle incidence, ($\theta=20^o$), the contour plots and the three dimensional picture of the instantaneous free surface elevation are shown in Fig. 2. The generation and evolution of stem waves along the breakwater are clearly visible. The crests of stem waves are normal to the breakwater and the width of stem waves is growing with distance from the tip of breakwater. These nonlinear features has also been observed through the experiments of Nielsen (1962) for a cnoidal wave train. More details on the effects of nonlinearity and the angle of incidence can be found in Yoon & Liu (1989). On the other hand, the linear results shown in Fig. 3 indicate partial standing waves in the y direction instead of stem waves. The width of first standing waves, measured parallel to y-axis from the breakwater to the first node, becomes more or less constant after some distance along the breakwater. Since the reflected waves are strong, the second and third standing waves are developed next to the first one.

When the angle of incidence is large ($\theta=45^o$), the parabolic approximation is not valid, since the assumption Eq. 5 is violated. In this case, we assume:

$$\frac{\partial \Psi_n}{\partial y} - \frac{\partial^2 \Psi_n}{\partial y^2} \sim 0(1) \tag{18}$$

and the nonlinear terms in Eq. 6 and Eq. 9 will contain the lateral derivative terms (see Liu, Yoon & Kirby, 1985). In the present study, however, we employ Eq. 6 and 9 to show the general feature of large angle of incidence. Using the same wave parameters as in the case of small angle of incidence, the

79

Table 1: Wave parameters

	Stem Wave Test	HSS Experiment
given data	$H_o' = 4m$ $T_o' = 19.43sec$ $h_o' = 10m$	$H_c' = 3.3cm$ $\lambda_o' = 2m$ $h_o' = 20cm$
	$\epsilon = 0.1703$ $\mu^2 = 0.1067$ $U_r = 1.5961$ $a_o' = 1.70331m$	$\epsilon = 0.1303$ $\mu^2 = 0.3675$ $U_r = 0.3546$ $a_o' = 2.6061cm$
	$a_1 = 0.77390$ $a_2 = 0.52596$ $a_3 = 0.30308$ $a_4 = 0.15793$ $a_5 = 0.07734$ $a_6 = 0.03637$ $a_7 = 0.01661$ $a_8 = 0.00742$ $a_9 = 0.00325$ $a_{10} = 0.00139$	$a_1 = 0.96918$ $a_2 = 0.24188$ $a_3 = 0.04599$ $a_4 = 0.00778$ $a_5 = 0.00123$ $a_6 = 0.00019$ $a_7 = 0.00003$ $a_8 = 0.0$ $a_9 = 0.0$ $a_{10} = 0.0$
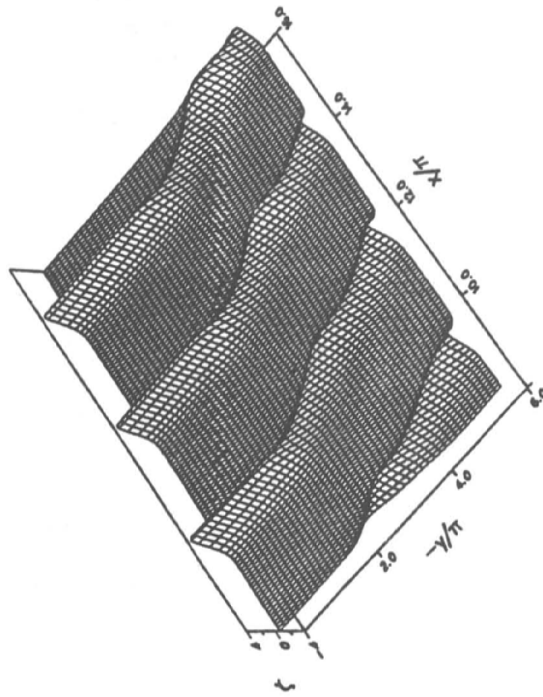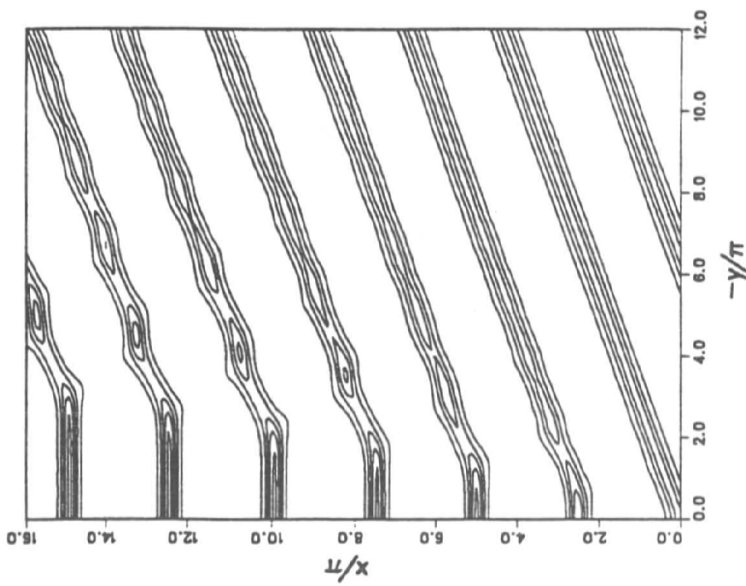
Figure 2 Instantaneous free surface elevation ($\theta=20°$, nonlinear)
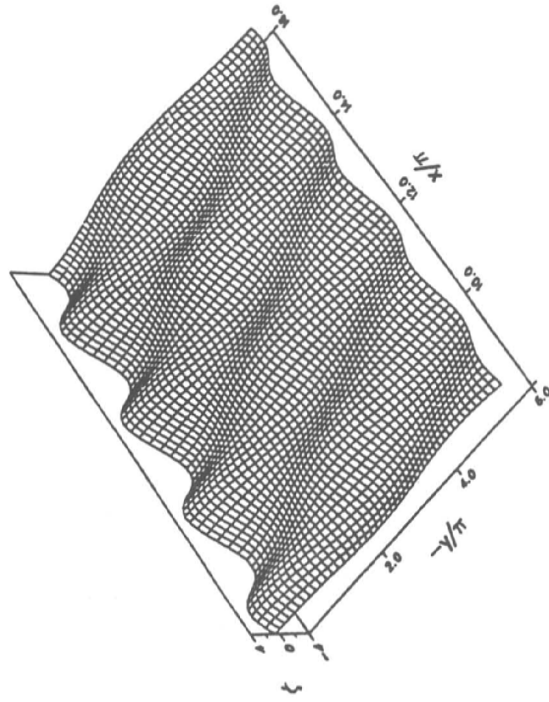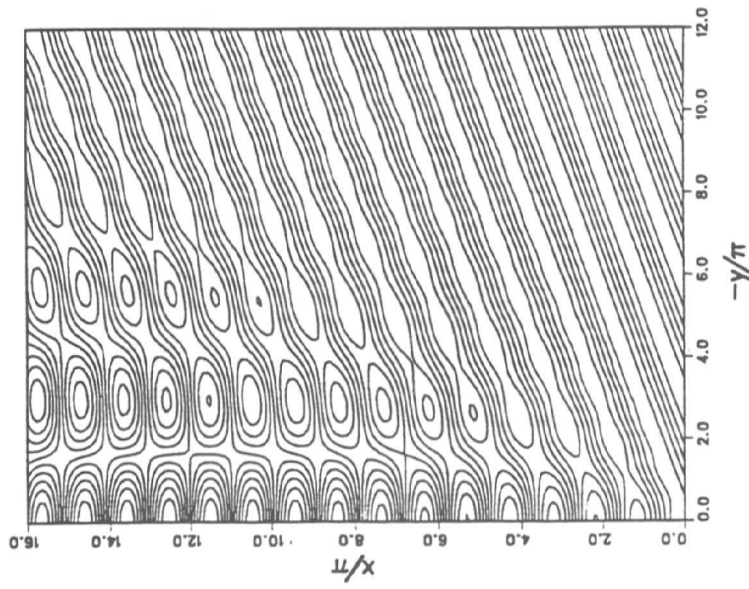
Figure 3   Instantaneous free surface elevation ($\theta=20°$, linear)

82

instantaneous surface profiles are presented for the nonlinear and the linear cases in Fig. 4 and Fig. 5, respectively. The nonlinear interactions between incident and reflected waves are relatively weak. Thus the stem waves grow slowly and the reflected waves are somewhat strong outside the stem region. The wave pattern near the breakwater exhibits a hexagonal shape of short crested waves. Nielsen (1962) also observed this hexagonal pattern of waves in his experiments when the nonlinearity of incident waves is weak and the angle of incidence is large. On the other hand, the wave field from the linear theory shows well-developed standing waves in the y direction resulting from the linear superposition of incident and reflected waves.

Hexagonal waves

Nielsen's (1962) experiment, also cited in Wiegel (1964), shows hexagonal waves near the breakwater when the angle of incidence is large and the nonlinearity of incident waves is small. Through the oblique interactions of two equal uniform wave trains generated by directional wave maker, Hammack, Scheffner & Segur (1989) presented the permanent shape of hexagonal waves which are periodic in x and y directions.

The hexagonal waves were studied numerically by Bryant (1982) using double Fourier harmonics for cnoidal waves. Segur & Finkel (1985) obtained the exact solutions to KP equations. They coined Genus-2 waves for the permanent biperiodic wave with the shape of hexagonal waves. Kirby (1990) also demonstrated the existence of hexagonal waves using a discrete angular spectrum model. In the Stokes wave regime, Roberts (1983) and Roberts & Peregrine (1983) among others showed the biperiodic hexagonal waves numerically using perturbation analysis.

Hammack, Scheffner & Segur (1990) performed laboratory experiments for the reflection of uniform cnoidal waves from a vertical wall in the wave basin shown in Fig. 6. The width and length of wave basin are 13.26 m and 18.55 m, respectively. The water depth is kept constant (h_o=20 cm) up to 12.55 m from the directional wave maker and then a slope of 1/30 is installed to provide an energy absorber through wave breaking. A cnoidal wave train with a wavelength of 2 m and a crest wave height of 3.3 cm is generated with the angle of incidence 27.9^o. The Ursell number ($U_r = \epsilon/\mu^2$) of incident waves is 0.3546 which is much smaller than that used in stem wave test ($U_r = 1.5961$). Thus the nonlinear effect is expected to be weak. The crest lines obtained from the video image (see Fig. 7b) show the hexagonal wave pattern near the wave gauge array along x = 11 m (0>y>-5 m).

In the numerical computations the wave parameters given in the second column of Table 1 are used to prescribe the incident waves along the wave maker. The equal step size of 0.05 m is employed in both directions. Ten harmonics (N=10) are included in the computation. The contour plot of instantaneous surface profile (Fig. 7) shows that the stem waves do not grow and the reflected waves are somewhat strong. As a result, the reflected waves interact with incident waves to form a hexagonal wave pattern near the wave gauge array. Fig. 7a is the three dimensional picture of hexagonal wave pattern simulated using the present numerical model. A qualitative agreement between experimental and numerical wave patterns can be clearly observed in this figure. A quantitative comparison can be made if the experimental data are provided. The accuracy of present model can be improved if the wave breaking and large angle approximation satisfying Eq. 18 are included.
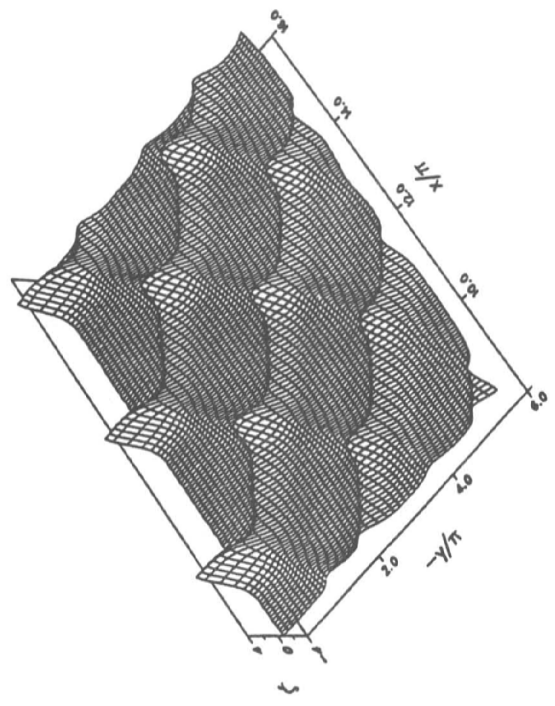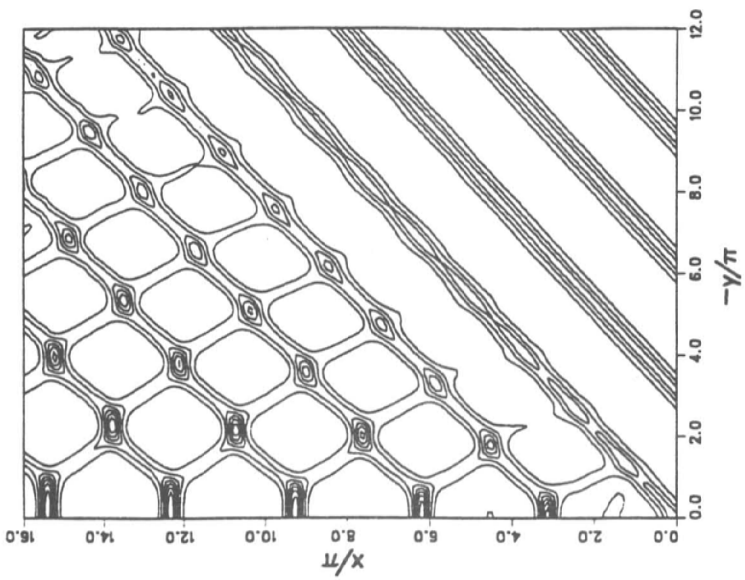
Figure 4   Instantaneous free surface elevation (θ=45°, nonlinear)
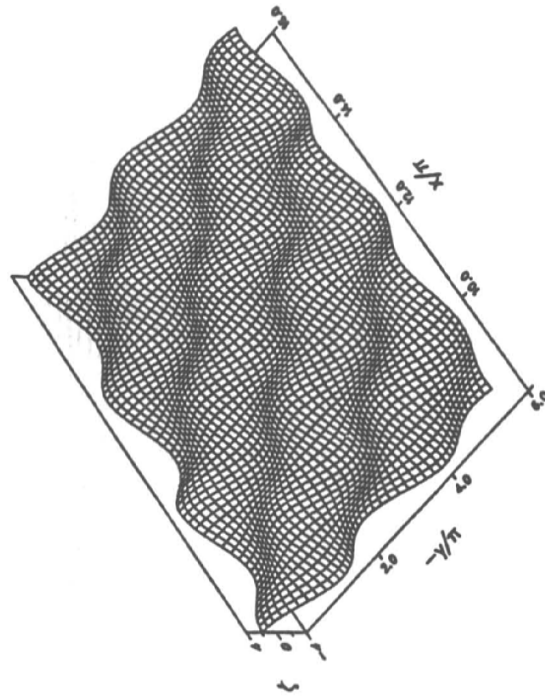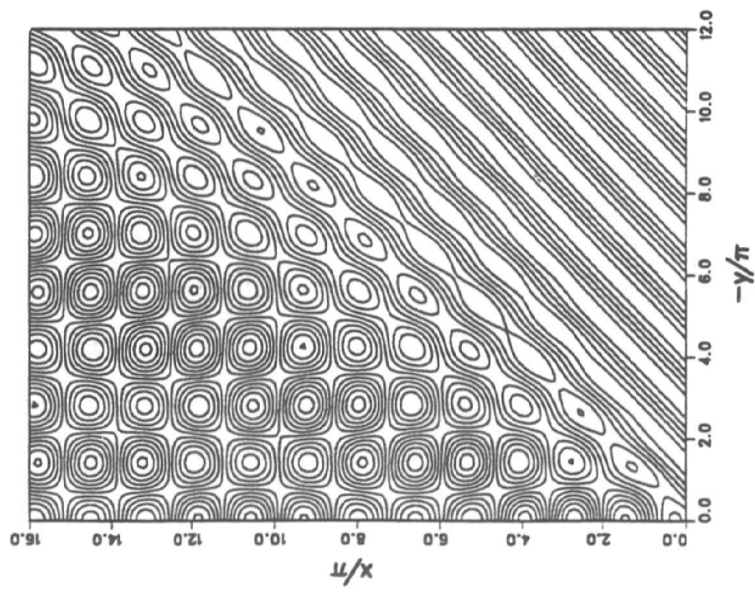
Figure 5 Instantaneous free surface elevation (θ=45° , linear)
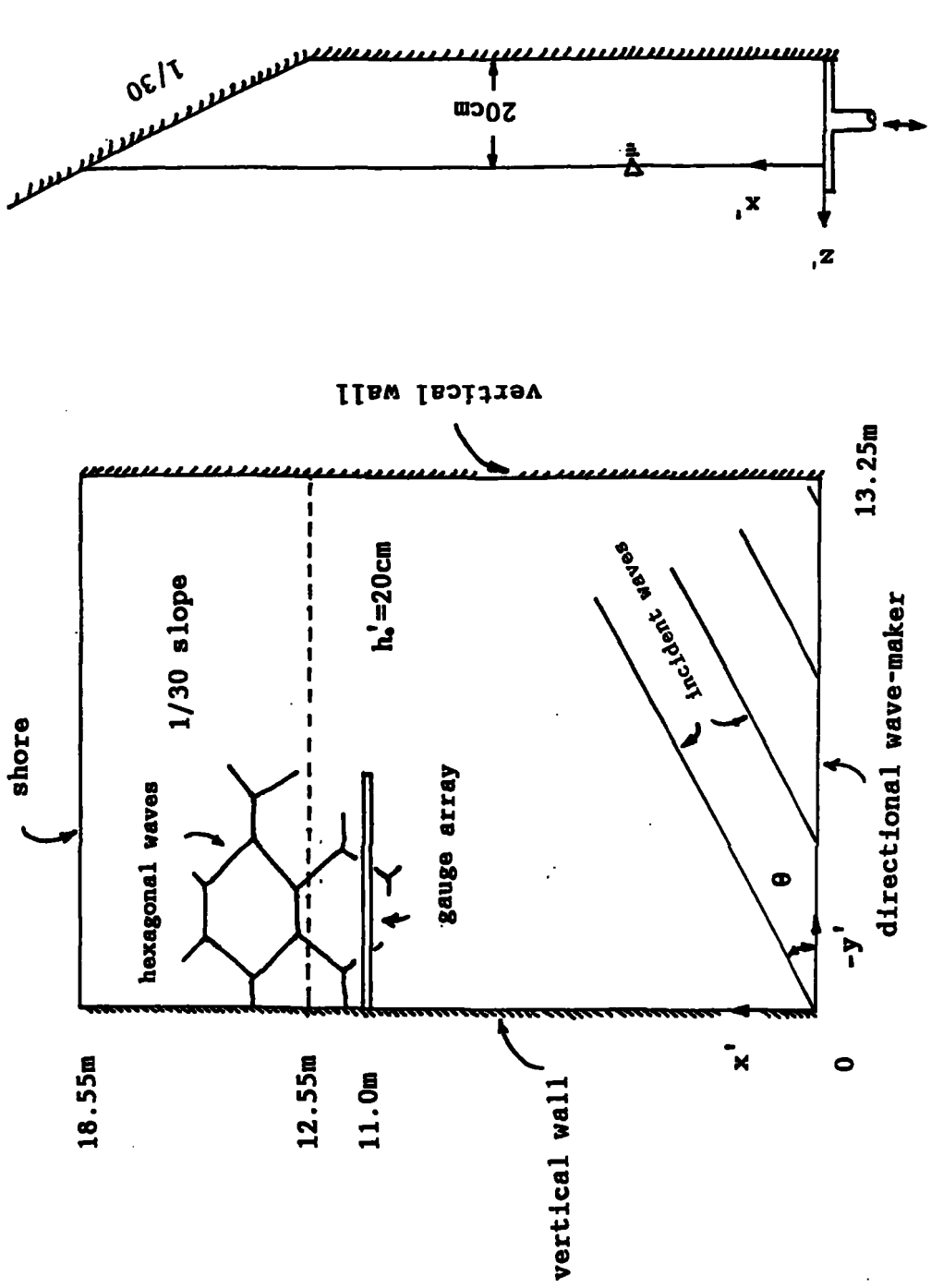
Figure 6   Experimental set-up of Hammack, Scheffner & Segur (1990)
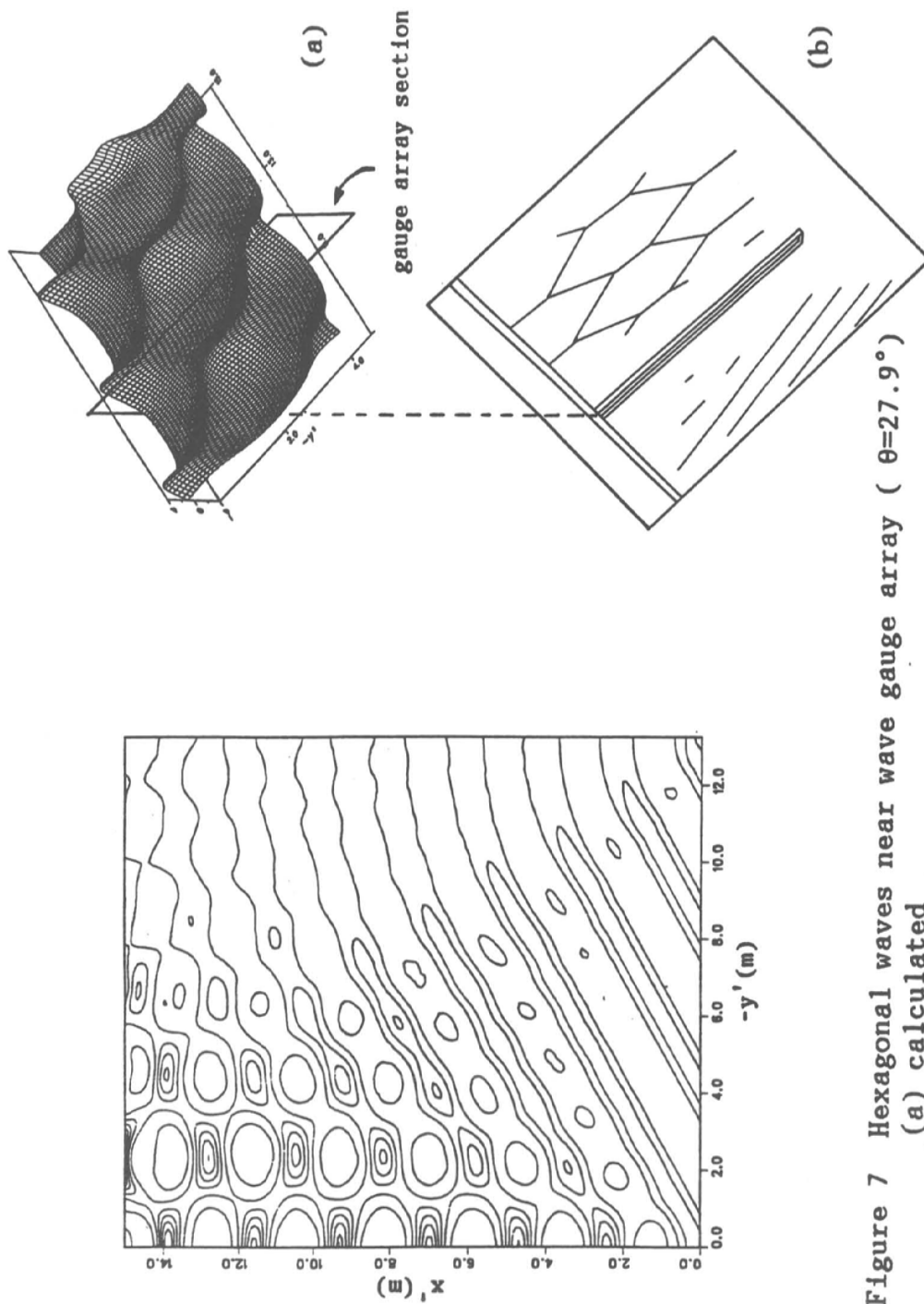
Figure 7 Hexagonal waves near wave gauge array (θ=27.9°)
(a) calculated
(b) experiment (Hammack, Scheffner & Segur 1990)

87

Conclusion

Using the parabolic approximation of Boussinesq equations, we demonstrate numerically that stem waves and hexagonal waves can be generated along a straight breakwater by an incident cnoidal wave train. The development of stem waves and hexagonal waves depends on the relative importance between nonlinearity and angle of incidence of the incident wave train. When the nonlinearity represented by Ursell number is large and the angle of incidence is small, most of the energy provided by incident waves feeds the stem waves due to nonlinear effects and only the small portion of energy is reflected. As a result, the stem waves develop along the breakwater and the width of stem waves increases. With little reflection, it is hard to create a hexagonal wave pattern next to the stem region. When the angle of incident is increased, the nonlinear effect becomes weak. The energy feeding from incident waves to stem waves is accordingly reduced and large portion of energy is reflected. The stem waves glow slowly and the hexagonal wave pattern outside the stem region becomes evident. For the case of small Ursell number and large angle of incidence, a regular reflection similar to linear waves occurs. The stem waves disappear and the hexagonal waves dominate.

Acknowledgment

References

Berger, V. & Kohlhase, S. (1976), Mach-reflection as a diffraction problem. Proc. 25th Conf. Coastal Engrg., ASCE, 1, 796-814.

Bryant, P.J. (1982), Two-dimensional periodic permanent waves in shallow water. J. Fluid Mech., 115, 525-532.

Hammack, J., Scheffner, N. & Segur, H. (1989), Two-dimensional periodic waves in shallow water. J. Fluid Mech., 209, 567-589.

Hammack, J., Scheffner, N. & Segur, H. (1990), Discussion on stem waves along breakwater. J. Waterway, Port, Coastal and Ocean Engrg., ASCE, (in press).

Kirby, J.T. (1990), A discrete angular spectrum model for nonlinear shallow water waves. Part 1. Waves in laterally uniform domains. (private communication).

Liu, P.L.-F. & Yoon, S.B. (1986), Stem waves along a depth discontinuity. J. Geophys. Res., 91(C3), 3979-3982.

Liu, P.L.-F., Yoon, S.B. & Kirby, J.T. (1985), Nonlinear refraction-diffraction of waves in shallow water. J. Fluid Mech., 153, 184-201.

Nielsen, A.H. (1962), Diffraction of periodic waves along a vertical breakwater for small angles of incidence. IER Tech. Report HEL-1-2, Univ. of California at Berkeley.

Peregrine, D.H. (1972), Equations for water waves and the approximation behind them. Waves on Beaches, R.E. Meyer, ed. Academic Press, Inc., 95-121.

Perroud, P.H. (1957), The solitary wave reflection along a straight vertical wall at oblique incidence. Ph.D. Thesis, Univ. of California at Berkeley.

Roberts, A.J. (1983), Highly nonlinear short-crested water waves. J. Fluid Mech., 135, 301-321.

Roberts, A.J. & Peregrine, D.H. (1983), Notes on long-crested water waves. J. Fluid Mech., 135, 323-335.

Scheffner, N. (1988), Stable three-dimensional biperiodic waves in shallow water. Miscellaneous Paper CERC-88-4, Coastal Engineering Research Center, Vicksburg, Mississippi.

Segur, H. & Finkel, A. (1985), An analytical model of periodic waves in shallow water. Stud. Appl. Math., 73, 183-220.

Wiegel, R.L. (1964), Water wave equivalent of Mach-reflection. Proc. 9th Conf. Coastal Engrg., ASCE, Lisbon, Portugal, 82-102.

Yoon, S.B. & Liu, P.L.-F., (1989), Stem waves along breakwater. J. Waterway, Port, Coastal and Ocean Engrg., ASCE, 115(5), 635-648.

Yue, D.K.P. & Mei, C.C. (1980), Forward diffraction of Stokes waves by a thin wedge. J. Fluid Mech., 99, 33-52.

Discussion

Comment: A two-dimensional numerical simulation for this problem was made by Russian scientists. One result is that the angle of incident and the reflectance angle are not the same. And moreover, if the angle to the walls is more than 50° even if the non-linearity is taken into account, it appears to be perfect reflection.

Response: It has been documented that for solitary waves if the angle of incidence is greater that probably 45°, then the stem wave is not involved and it would be a more or less reflective wave and if it is less than 20° then the reflective wave is almost zero. In between there is a partial reflection plus the stem wave - and not a basic three wave system. With a cnoidal wave situation, it is a little difficult to find that particular angle. In trying to do some of these things, there are different factors which come into play. It is not obvious that it is a solitary wave.

NUMERICAL SIMULATION AND EXPERIMENT ON TSUNAMI RUN-UP

Shigeru Yamaki
I.N.A. Civil Engineering Consultants Co., Ltd.
Tokyo, Japan

Takaaki Uda
Public Works Research Institute
Ministry of Construction
Ibaraki, Japan

1. Introduction

In May, 1983, the coasts along the Sea of Japan were severely damaged by a large tsunami caused by the Nihonkai-Chubu earthquake. After the incident, various preventive works against future tsunami hazards were proposed. In the planning of these works numerical simulations were carried out for predicting the areas of inundation or the critical height of coastal dikes. There often exist sand dunes or shore protection facilities such as coastal dikes or detached breakwaters along the coast of Japan. The complicated fluid motion around these structures calls for a sophisticated simulation model for predicting tsunami run-up. However a rather simple model is desirable for practical use, since numerical simulation of a tsunami must normally cover an extensive region to take into account the three-dimensional topography.

The numerical model used here is based on the shallow-water equations which are solved by a finite difference method with simple boundary conditions. The validity of the numerical model should be examined on the basis of field data on run-up height. In fact, detailed data on the water level or current velocity around a structure are necessary in the investigation of its effect but difficult to obtain. In this study, hydraulic experiments were conducted as well as numerical simulations on tsunami run-up on a coast with a sand dune or a structure, and the obtained temporal and spatial distributions of water level and velocity were compared.

2. Method of Hydraulic Experiments

The hydraulic experiments were carried out in a wave basin as shown as Figure 1. The basin was equipped with a pneumatic-type tide generator at its offshore end and narrowed with two parallel side walls in order to obtain a solitary wave of large height.

A sandy beach with a uniform slope, a coastal dune, a coastal revetment and a detached breakwater were modeled, where the model scale of 1/100 is assumed. The shape of the topographic models and the conditions of incident wave are summarized in Table 1.

The distributions of water level and current velocity were measured with capacitance-type wave gauges and propeller-type current meters set at 5mm above the bottom. The run-up height was also measured.
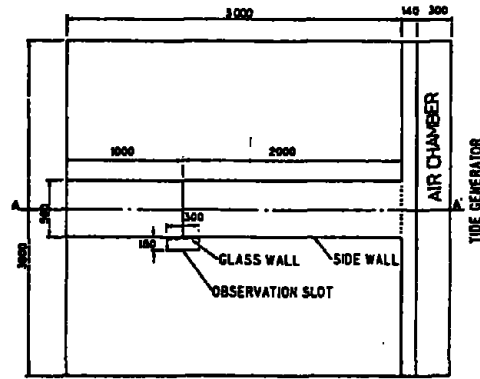
a) Plane view.
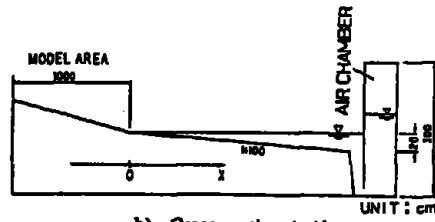
b) Cross section A-A'.

Figure 1. Experimental setup

Table 1   Dimensions of models, wave conditions and run-up heights.

Model type	Conditions (height)	Tp (sec)	Ho (cm)	Rm (cm)	Rc (cm)
Uniform slope beach	1/20	12	6.5	17.0	16.7
		15	7.7	19.8	19.9
		18	8.4	21.3	21.9
	1/30	12	6.0	15.7	15.1
		18	8.6	20.7	21.6
Coastal dune	(6cm)	18	8.6	20.4	19.9
	(12cm)	18	9.0	16.5	16.2
Coastal revetment	Vertical wall (4cm)	18	8.7	22.0	21.9
Detached breakwater	Impermeable (5cm)	12	6.1	14.5	14.2
		18	8.8	20.0	21.4
	Impermeable (6cm)	12	6.8	15.4	15.2
	Permeable (6cm)	12	6.7	16.4	15.6

Tp : duration of the pulse wave used to control the wave generator.
Ho : wave height in front of the generator.
Rm : measured run-up height.
Rc : calculated run-up height.

A solitary wave was generated at the end of the basin propagated over the bottom slope, changing its profile. At the distance of 15 m from the wave generator, the wave front dispersed to form two or three short-period waves and then they broke (Figure 2). Finally, the breaking bore was incident to the coastal models.
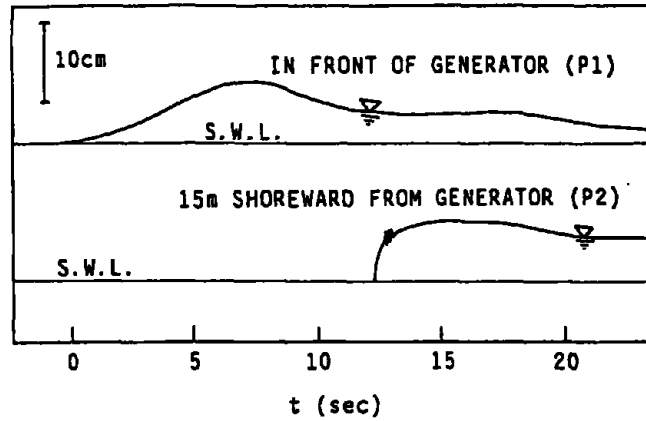
Figure 2. An example of a wave profile.

3. Numerical Method

In the numerical model used in this study, shallow-water equations were solved by a leap-frog finite difference method with a 5 cm grid and 0.02s time interval. The wave profile measured in front of the generator in each case of experiment was used as a boundary condition. The fundamental equations are written as follows:

$$\frac{\partial \eta}{\partial t} + \frac{\partial Q}{\partial x} = 0 \tag{1}$$

$$\frac{\partial Q}{\partial t} + \frac{\partial}{\partial x}\left[\frac{Q^2}{D}\right] + g\,D\frac{\partial \eta}{\partial x} + \frac{g\,n}{D^{7/3}}\,Q^2 = 0 \tag{2}$$

where
η : water elevation
D : total water depth
n : Manning's roughness coefficient
Q : flow flux

The method by Iwasaki and Mano (1979) was employed in determining the moving boundary condition at the wave front.

The value of n was changed from 0.010 to 0.015 and was adjusted to minimize the difference between the measured and the calculated run-up heights in the case of uniform 1/20 slope. As a result, n was determined at 0.012 to obtain the best fit.

93

The flow flux through the permeable detached breakwater is calculated using following equation:

$$\frac{1}{\lambda}\frac{\partial Q}{\partial t} + g\,D\frac{\partial \eta}{\partial x} + \frac{f}{2\,l}\frac{Q2}{D} = 0 \tag{3}$$

where λ : porosity (concrete blocks = 0.5)
l : width of detached breakwater
f : drag coefficient (=8.6, assumed)

4. Comparison between Experimental and Numerical Results

The measured run-up heights are compared with simulated heights in Figure 3. The differences between the experimental and the simulated run-up heights were less than 10%; they agreed very well.
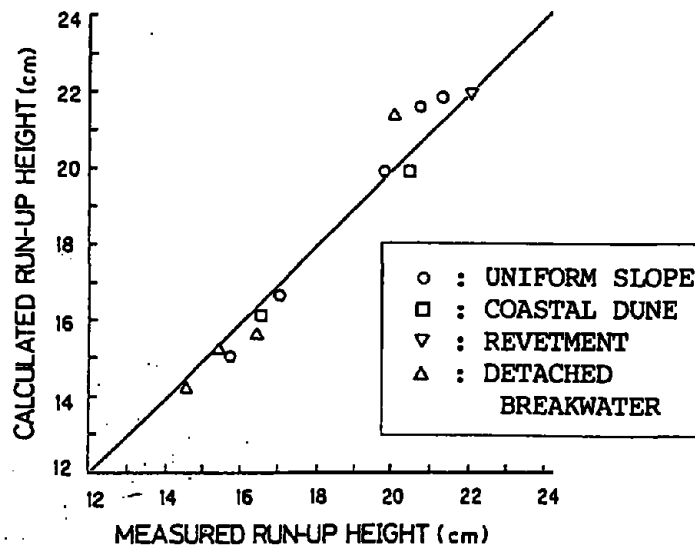
Figure 3. Comparison of measured and calculated run-up heights.

The results of experiment and simulation on the water level and velocity are compared in Figures 4 through 6 for the cases of Tp=18s with a uniform 1/20 slope, a coastal dune and impermeable detached breakwaters. In these figures, a) and b) show time series of water level and velocity at several points, and c) shows the spatial profile of the water level. The reference level of the water surface is selected at the still water level in the offshore region and at the dry bed height on the beach, respectively. Since uni-directional current meters were used, the absolute values of velocity are shown in the figures describing its variations. The current normally changes direction as the velocity crosses zero level.
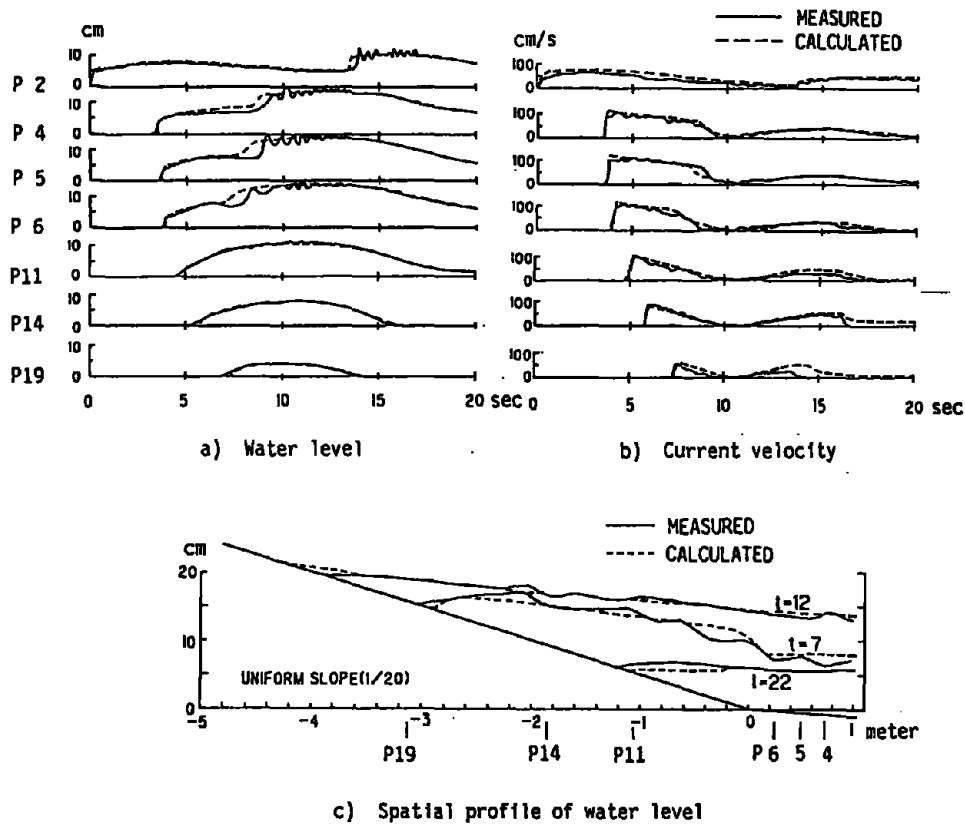
Figure 4. Measured and calculated profiles of water level and velocity (with a uniform 1/20 slope).
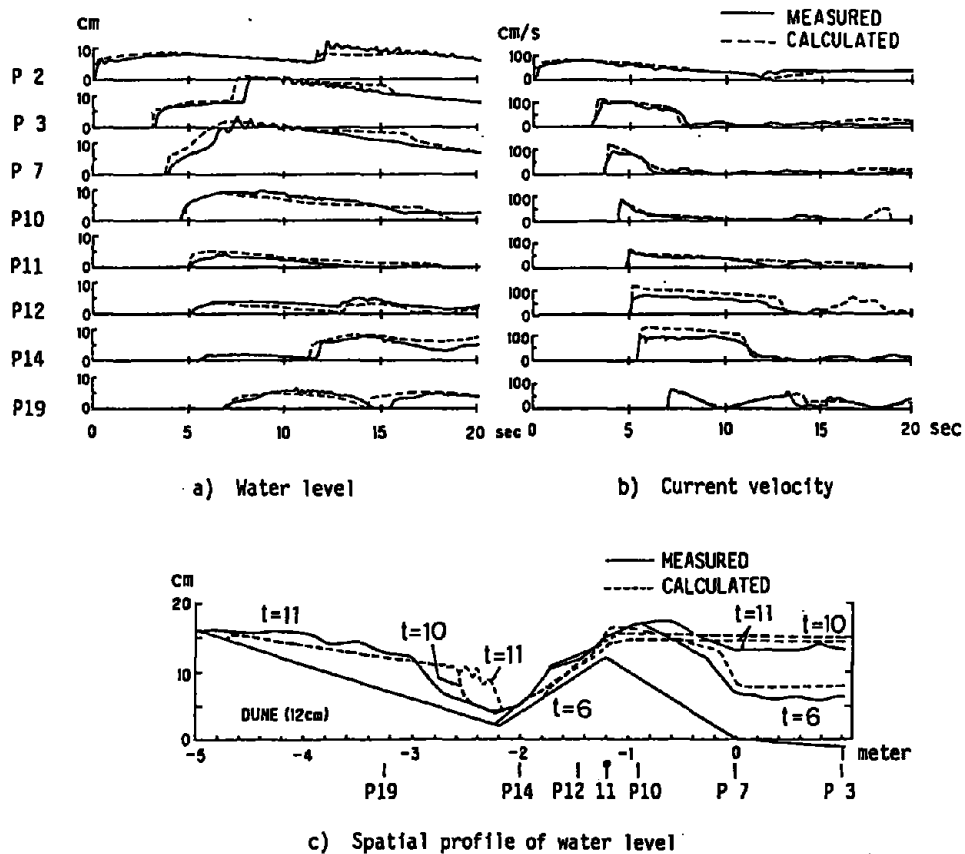
Figure 5. Measured and calculated profiles of water level and velocity (with a coastal dune).

4.1 Uniform 1/20 slope

In Figure 4 it is clearly seen that the tsunami changed its profile as it propagated toward the shore with the breaking bore running up on the slope. Short-period waves reflected on the slope are observed between P2 and P6. These short-period waves cannot be predicted in principle through the simulation since the fundamental equations used include no frequency dispersion term. In general, however, the measured and the simulated water level variations as well as velocity variations are in good agreement, although breaking and mixing at the wave front are not considered in the simulation model.

4.2 Coastal dune

It appears in Figure 5a that the simulated water level is higher than that measured on the dune crest (P11), while in Figure 5b the simulated and measured velocities are approximately equivalent. Furthermore, the water levels agree well during the initial stage of run-up at P12 and P14 on the landward slope of the dune, where the calculated velocities are considerably larger compared with the measured. These facts imply that the mass flux is overestimated in the simulation on and around the dune crest. Consequently, the reflected wave at P16 in the simulation is considered to be generated earlier than in the experiment. This also causes the phase difference observed in Figure 5c, that is, the spatial profile at t=10s in the simulation agrees rather with that at t=11s in the experiment. The reason for the above-mentioned overestimation of mass flux may possibly be the drag due to the separation of current at the dune crest. In fact, the velocities at points located offshore from P11 are in good agreement during the run-up period as shown in Figure 5b.

In spite of all this disagreement in details, it is concluded that the overall picture of run-up motion around a coastal dune can be well simulated by applying this simple model.

4.3 Detached breakwaters

The breakwater was expressed in term of the bed level change at one grid point. The simulation was done by using solely the fundamental equations in the case with the impermeable breakwater and using the fundamental equations and Eq. (3) in the case with a permeable breakwater.

The results of the case with an impermeable detached breakwater are shown in Figure 6. The incident wave was partially reflected at P5 as shown in Figure 6a and the rest overflowed the breakwater. The water level at the top of the breakwater was higher in the experiment than in the simulation during the run-up period, while the measured and the calculated velocities are almost the same at P5 (Fig. 6b). A rapid current, keeping shallow depth, was observed at P7 in the experiment, whereas the water level rose at the early stage in the simulation. As can be seen from Figure 6c, the difference in the water level is large in the range between the crown and the immediate shoreward point of the breakwater, and a current with shallow depth develops on the slope at the initial stage of wave run-up.

The video tape records show that the overflow reached 10 cm onshore from the breakwater in the experiment. This phenomenon cannot be reproduced in the present calculation, because the overflow condition is simply given at a grid point only. In order to precisely predict the water motion, it is necessary to take into account the water surface slope and the drag around the breakwater as in the study of Goto and Shuto (1983).

a) Water level   b) Current velocity

c) Spatial profile of water level
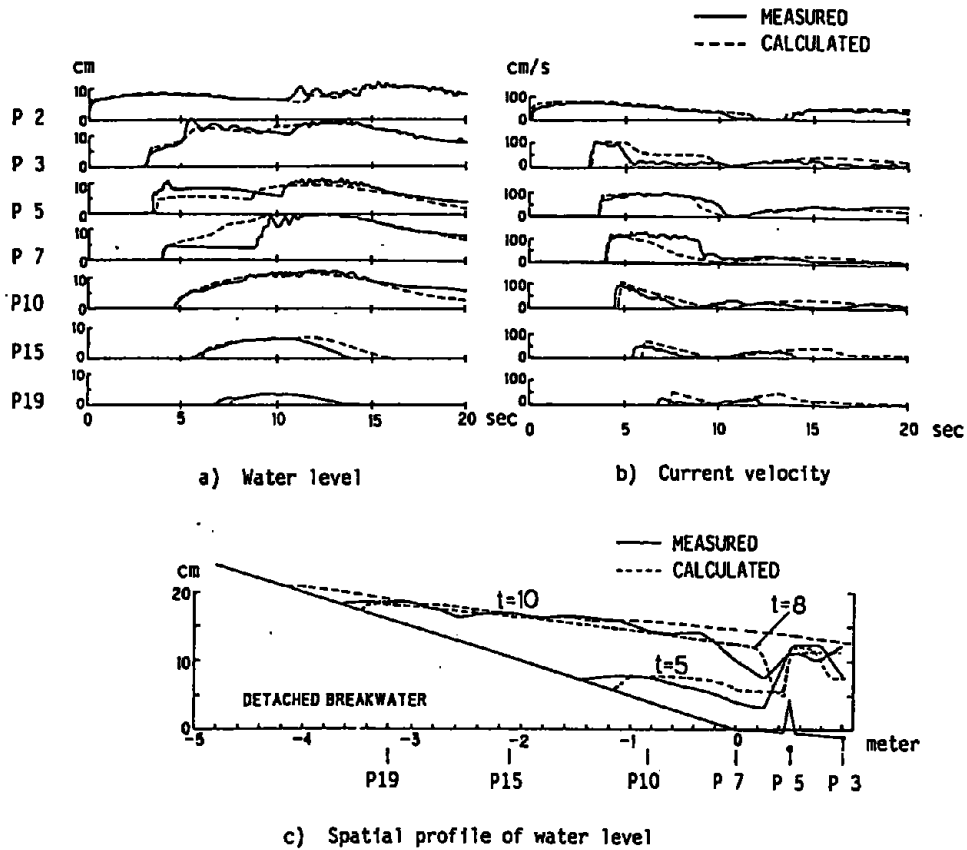
Figure 6. Measured and calculated profiles of water level and velocity
(with an impermeable detached breakwater).

In the case with a permeable breakwater, the separation of current is less predominant at the top of the breakwater. As a consequence, the experiment and the simulation shows a better agreement than in the preceding case as shown in Figure 7.

a) Water level   b) Current velocity
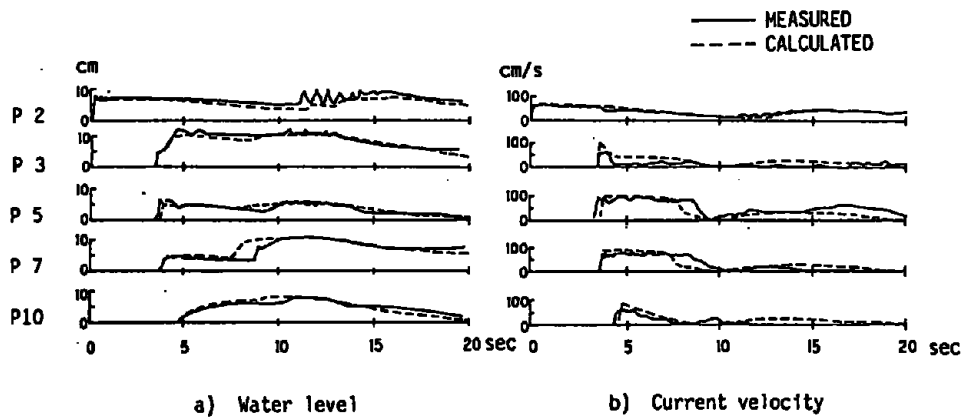
Figure 7. Measured and calculated profiles of water level and velocity
(with a permeable detached breakwater).

5. Conclusions

The main conclusions of this study are summarized as follows:

(1) The results of numerical simulation were compared with those obtained through physical experiments on tsunami run-up on a coast with a sand dune or a structure. It was found that the simple model presented here can simulate the tsunami behavior with sufficient accuracy for practical use except in the close vicinity of the structure.

(2) A permeable detached breakwater often constructed in Japan can be well modeled by a bed level change in one grid, if the drag coefficient is properly given.

Acknowledgements

References

Homma, H., 1940. Discharge coefficient of low dams. *Proc. JSCE*, 26(9), p.849-862. (In Japanese)

Iwasaki, T. and A. Mano, 1979. Numerical simulation of two-dimensional tsunami run-up using Eulerian coordinates. *Proc. 26th Japanese Conf. on Coastal Eng.*, pp.70-73. (In Japanese)

Goto, C. and N. Shuto, 1983. Effects of large obstacles on tsunami inundations. In: *Tsunamis - Their Science and Engineering*, K. Iida and T. Iwasaki, eds. Terra Pub., Tokyo, p.511-525.

Discussion

Response: In response to a question it was mentioned that very smooth concrete was used for these simple experiments without any dunes or breakwaters.

Comment: From figure 4, it can be concluded that for the variation of the measured runup height with the calculated runup height there is no difference among the different types of coastal structures. The agreement is the same for all types of coasts including the uniform slope, the coastal dune and the vetments? This implies that the model is equally good in all situations.

Comment: There is an entire literature, at least in the U.S., on solitary wave runup, and usually one of the ways of looking at the results is dimensionless terms, in terms of the normalized maximum runup. It would be very useful to add in the data column a column that has the depth as some sort of reference, so that people can look at the results in some dimensionaless manner. Since this is one particular case, one cannot easily generalize it for other cases. Otherwise it is difficult to determine the undisturbed depth. That is very important in terms of trying to interpret these results. For example, these are non-breaking waves. If the depth is taken to be 20 cm, this means that the waves are of the order of about 8 cm divided by 20, or a 0.4 solitary wave on a 1 to 20 beach slope. That has to break. Maybe it is not breaking because of the bottom friction. That is another very interesting effect. But it is important to actually have the depth there so that it can be

determined whether it is a breaking or non-breaking wave, and what is the undisturbed depth.

Response: The described approach is good for practical use for coasts where tsunami attacks may occur. Where the runup height of the model is used to simulate the runup height on the coast and it does quite well.

Comment: The model is ingenious. It is frequently used in special cases and it is convenient to use a dimensionless model as an indicator. In the future the more general case may be developed.

Comment: In Table 1, the ratio of the runup heights to the waves in front of the generator, R_m to H_o, it is approximately the same ratio whether there is a uniform slope or a coastal dune and whether there is breakwater which is permeable or impermeable. Furthermore, the ratio of these numbers is just about the same number in the paper by Carrier and Greenspan for the runup on a sloping beach. The ratio of R_m to H_o is approximately the same for all configurations.

Response: The incident tsunami height is too large in comparison with the topographic height which is probably the reason the ratio is uniform.

Comment: The effects of calculations on shallow water over barriers has been examined before and is in agreement with this paper. It is not within the region of the barriers, and the shallow water theory can not be used. However, the Navier-Stokes models can be used. That has been compared with experimental data and calculations like those in books on the numerical modeling of detonations. In the region of the barriers, it is possible to calculate by leaving the shallow water theory and using the full Navier-Stokes models; that has been demonstrated.

TSUNAMI PROPAGATION FROM A FINITE SOURCE

George F. Carrier
Harvard University
Division of Applied Sciences
Cambridge, MA, USA

Abstract

Much of the analysis of Tsunami propagation has dealt with waves that are initiated by a sea-bottom displacement that extends over an indefinitely long strip of that sea-bottom. The displacements associated with real seismic events are confined largely to irregular strips of large but finite aspect ratio [1]. We analyze here waves that are initiated on such a strip and that propagate across a region of finite depth. We invoke the classical shallow water gravity wave theory to obtain rather comprehensive descriptions of the non-dispersive aspects of the waves and we use the Boussinesque form of shallow water theory to extract a characterization of the dispersive effects.

1. Introduction

A schematic diagram of the configuration to be treated here is given in Fig. 1. The occurrence of a sudden, short-lived, non-uniform, seismically generated, vertical excursion of a segment $(x_1, x_1 + \ell)$ in Fig. 1) of the sea floor implies an almost simultaneous vertical displacement of the sea surface and the gravity wave so initiated radiates outward from that source. When the displaced segment of the sea-floor lies in deep water (e.g.5 km) but has lateral dimensions that are large compared to that depth the initial surface displacement has a shape that is a smoothed replica of the sea-floor displacement. More precisely, the ratio of the magnitude of the spectral intensity of the surface displacement to that of the sea-floor displacement is of order $[\cosh(|K|d)]^{-1}$ where K is vector wavenumber and d is the depth of the water. Furthermore, the propagating wave undergoes a dispersion in which, when the wave has travelled a distance q from its source, the spectral contributions whose wavelengths are small compared to $(q/d)^{1/3}d$ have travelled so slowly that they no longer contribute to the shape or intensity of the energetic leading wave system.* Accordingly, nothing of importance is lost when we postulate for our analysis a family of sea-bed displacements whose spectra are already devoid of short wavelength contributions.

---

* This is all quantified in [2] and [3].
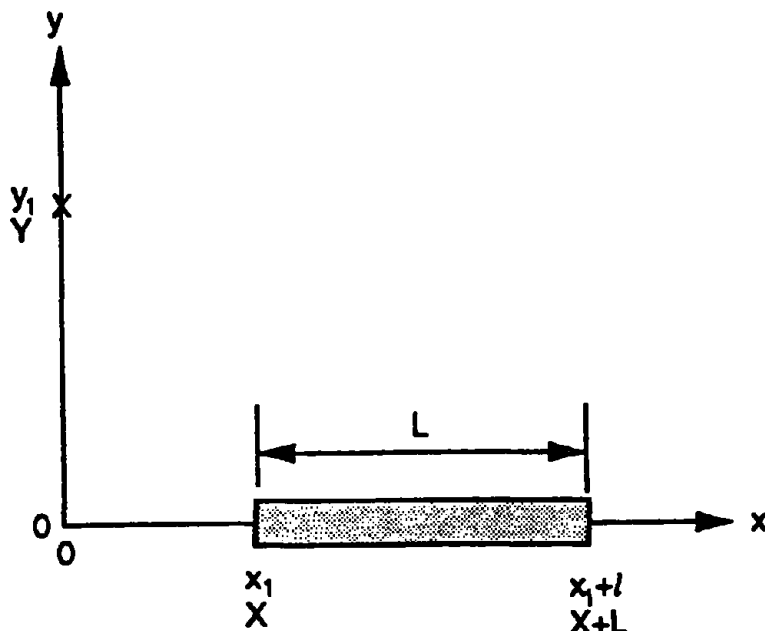
FIGURE 1

Wave field configuration indicating coordinate variables (x,y), Dimensional coordinates $(x_1, x_1+\ell)$ of source domain, dimensionless strip location $(X, X+L)$ and wave arrival locale of interest $(y,$ or $Y)$.

In fact, our primary interest is focused on ground displacements that are confined to a strip of length, ℓ, are nearly uniform in x (see Fig. 1 and Eq. (3.1)) and could be constructed as a superposition of individual displacements each of whose y dependence is $e^{-\alpha_i(y-\beta_i)^2}$. Actually, each wave field whose analysis we carry to completion is one that is generated by a ground displacement that is approximately given by (again see Eq. (3.1))

$$\eta(x,y,0) \begin{cases} \cong 2e^{-y^2/a^2} & \text{in } x_1 < x < x_1 + \ell \\ \\ \cong 0 & \text{elsewhere} \end{cases}$$

Whatever the initiating motion may be (we never know until long after the event what that motion has been) our interest here lies in the wave height $\eta(t)$ [more properly $\eta(x, \ell, y, t)$] that arrives at position (o, Y) (see Fig. 1) from the source region as a function of time. η also depends on the source width k and other parameters but these are submerged in the non-dimensionalization of the problem until the "user" chooses numerical values that define the configuration of interest to him and "backs out" from the results the dimensional wave height as a function of position and time. Before proceeding to the analysis we should note that dispersion can play a significant role when the Gaussian source has a half-width that is less than $(q/d)^{1/3}$ d. The infinite aspect ratio theory in [2] gives a useful quantification of this effect and is extended to cylindrically symmetric waves in this paper. A direct quantification of the dispersive effects for the strip geometry of this paper will be a goal of an ongoing study.

102

2. Analysis

Classical shallow water (or long wave) theory suggests that the wave height $\eta(x,y,t)$ of waves whose lateral characterizing dimensions are large compared to the depth can be suitably approximated by solutions of

$$gd\,\Delta\eta - \eta_{t^*t^*} = 0 \qquad (2.1)$$

where Δ is the Laplace operator in dimensional coordinates, d is the depth, and t^* is the time.

For this investigation it is very advantageous to introduce one particular "fundamental solution" of this equation[#] -- that for which

$$\eta(x^*,y^*,0) = 2\,e^{-(x^{*2}+y^{*2})/a^2} \quad \text{and} \quad \eta_t(x^*,y^*,0) = 0 \ ;$$

it is then very advantageous to choose

$$x = x^*/a, \quad y = y^*/a, \quad r^2 = x^2 + y^2, \quad t = \sqrt{gd}\; t^*/a$$

The asterisks denote dimensional quantities and will not appear again in this paper. The fundamental solution $\eta(r,t)$ is now defined by

$$r^{-1}(r\eta_r)_r - \eta_{tt} = 0 \qquad \text{in } t > 0, \ 0 \le r < \infty \qquad (2.2)$$

with

$$\eta(r,0) = 2e^{-r^2} \qquad \eta_t(r,0) = 0. \qquad (2.2a)$$

An exact integral representation of the solution is:

$$f(r,t) = \int_0^\infty \rho J_0(\rho r)\cos(\rho t)\, e^{-\rho^2/4}\, d\rho \qquad (2.3)$$

This integral has been evaluated numerically as a function of r for each of t = 5,10,15...50. Its values for t=50 are listed in table (2.1) and they are depicted for several values of t in Fig. (2a). In that Figure, the ordinate is

$$F([r^2-t^2]/2t,t) = (t/50)^{1/2}\; f(r,t) \ ;$$

the reader will see readily that

$$F([r^2-t^2]/2t,t) \cong (t/50)^{1/2}\, f(r,t) \quad \text{when } t \ge 15 \qquad (2.4)$$

is a very accurate approximation.

Henceforth we use

$$G([r^2-t^2]/2t) = F([r^2-t^2]/2t,50) \qquad (2.5)$$

and we will use $\sqrt{50/t}\; G([r^2-t^2]/2t)$ as though it were the exact description of the fundamental solution, f.

The appendix contains a very abbreviated account of an analytic approximation procedure followed by a guessing game that provides an analytic recipe (curve fit) to $\sqrt{50/t}\; G([r^2-t^2]/2t)$. It is

$$G(s) \cong M(s) = -.066\frac{d}{ds}\left\{ \begin{array}{ll} [(s^2/2)^{1/4}K_{1/4}(s^2/2)\,e^{-s^2/2}] & \text{when } s > 0 \\[2mm] [(|s^2/2|)^{1/4}\{K_{1/4}(|s^2/2|)+\pi\sqrt{2}\,I_{1/4}(|s^2/2|)\}\,e^{-s^2/2}] & \text{when } s < 0 \end{array} \right\}$$

$$(2.6)$$

[#] The wave generation for the strip source region will be constructed in section 3 using this fundamental solution as a Green's function.

TABLE 2.1

s	G(s)	s	G(s)	s	G(s)	s	G(s)
-15.0	-0.0009	-10.4	-0.0015	-5.8	-0.0037	-1.2	-0.0420
-14.9	-0.0009	-10.3	-0.0015	-5.7	-0.0038	-1.1	-0.0410
-14.8	-0.0009	-10.2	-0.0015	-5.6	-0.0039	-1.0	-0.0383
-14.7	-0.0009	-10.1	-0.0016	-5.5	-0.0040	-0.9	-0.0337
-14.6	-0.0009	-10.0	-0.0016	-5.4	-0.0041	-0.8	-0.0268
-14.5	-0.0009	-9.9	-0.0016	-5.3	-0.0042	-0.7	-0.0178
-14.4	-0.0009	-9.8	-0.0016	-5.2	-0.0044	-0.6	-0.0070
-14.3	-0.0009	-9.7	-0.0017	-5.1	-0.0045	-0.5	0.0051
-14.2	-0.0009	-9.6	-0.0017	-5.0	-0.0046	-0.4	0.0181
-14.1	-0.0009	-9.5	-0.0017	-4.9	-0.0048	-0.3	0.0314
-14.0	-0.0010	-9.4	-0.0017	-4.8	-0.0049	-0.2	0.0446
-13.9	-0.0010	-9.3	-0.0018	-4.7	-0.0051	-0.1	0.0572
-13.8	-0.0010	-9.2	-0.0018	-4.6	-0.0053	0.0	0.0684
-13.7	-0.0010	-9.1	-0.0018	-4.5	-0.0055	0.1	0.0777
-13.6	-0.0010	-9.0	-0.0019	-4.4	-0.0057	0.2	0.0845
-13.5	-0.0010	-8.9	-0.0019	-4.3	-0.0059	0.3	0.0882
-13.4	-0.0010	-8.8	-0.0019	-4.2	-0.0061	0.4	0.0890
-13.3	-0.0010	-8.7	-0.0020	-4.1	-0.0064	0.5	0.0873
-13.2	-0.0010	-8.6	-0.0020	-4.0	-0.0066	0.6	0.0834
-13.1	-0.0011	-8.5	-0.0020	-3.9	-0.0069	0.7	0.0779
-13.0	-0.0011	-8.4	-0.0021	-3.8	-0.0072	0.8	0.0711
-12.9	-0.0011	-8.3	-0.0021	-3.7	-0.0075	0.9	0.0634
-12.8	-0.0011	-8.2	-0.0022	-3.6	-0.0079	1.0	0.0552
-12.7	-0.0011	-8.1	-0.0022	-3.5	-0.0083	1.1	0.0469
-12.6	-0.0011	-8.0	-0.0022	-3.4	-0.0087	1.2	0.0388
-12.5	-0.0012	-7.9	-0.0023	-3.3	-0.0092	1.3	0.0314
-12.4	-0.0012	-7.8	-0.0023	-3.2	-0.0097	1.4	0.0250
-12.3	-0.0012	-7.7	-0.0024	-3.1	-0.0102	1.5	0.0195
-12.2	-0.0013	-7.6	-0.0024	-3.0	-0.0109	1.6	0.0150
-12.1	-0.0012	-7.5	-0.0025	-2.9	-0.0116	1.7	0.0112
-12.0	-0.0012	-7.4	-0.0025	-2.8	-0.0124	1.8	0.0083
-11.9	-0.0012	-7.3	-0.0026	-2.7	-0.0133	1.9	0.0059
-11.8	-0.0012	-7.2	-0.0026	-2.6	-0.0143	2.0	0.0041
-11.7	-0.0012	-7.1	-0.0027	-2.5	-0.0155	2.1	0.0028
-11.6	-0.0013	-7.0	-0.0027	-2.4	-0.0169	2.2	0.0019
-11.5	-0.0013	-6.9	-0.0028	-2.3	-0.0184	2.3	0.0013
-11.4	-0.0013	-6.8	-0.0029	-2.2	-0.0202	2.4	0.0009
-11.3	-0.0013	-6.7	-0.0029	-2.1	-0.0223	2.5	0.0006
-11.2	-0.0013	-6.6	-0.0030	-2.0	-0.0246	2.6	0.0004
-11.1	-0.0014	-6.5	-0.0031	-1.9	-0.0272	2.7	0.0002
-11.0	-0.0014	-6.4	-0.0032	-1.8	-0.0300	2.8	0.0001
-10.9	-0.0014	-6.3	-0.0032	-1.7	-0.0329	2.9	0.0001
-10.8	-0.0014	-6.2	-0.0033	-1.6	-0.0358	3.0	0.0000
-10.7	-0.0014	-6.1	-0.0034	-1.5	-0.0383		
-10.6	-0.0015	-6.0	-0.0035	-1.4	-0.0403		
-10.5	-0.0015	-5.9	-0.0036	-1.3	-0.0416		
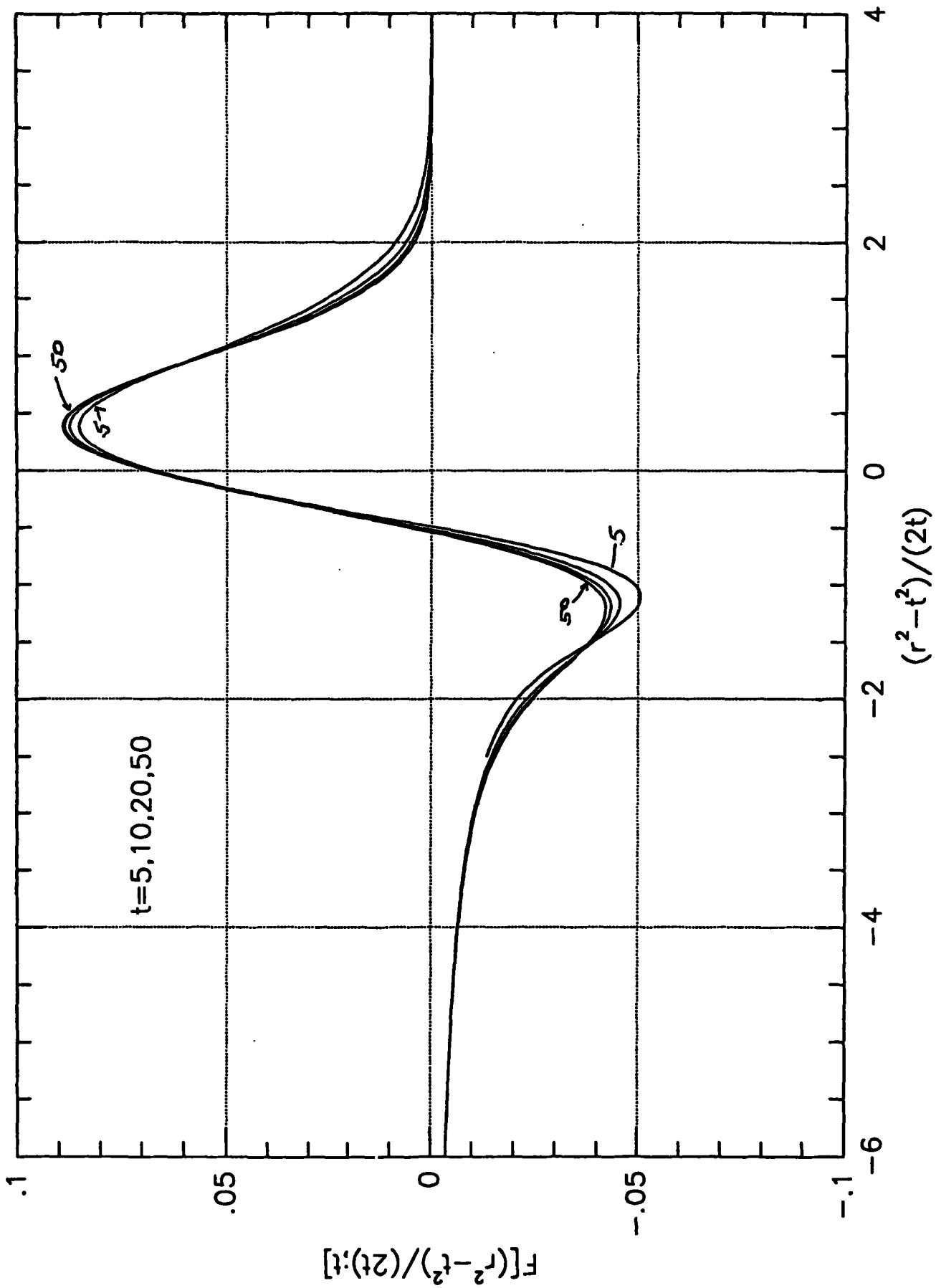
Figure 2a

$F(r^2 - t^2/2t, \ t)$ vs. $r^2 - t^2/2t$ for several values of t. Note that
$F(\alpha, t) - F(\alpha, 50)$ is very small for $t \geq 20$. For $t \geq 20$, $F(\alpha, t) \sim .05 (-\alpha)^{-\xi/2}$.
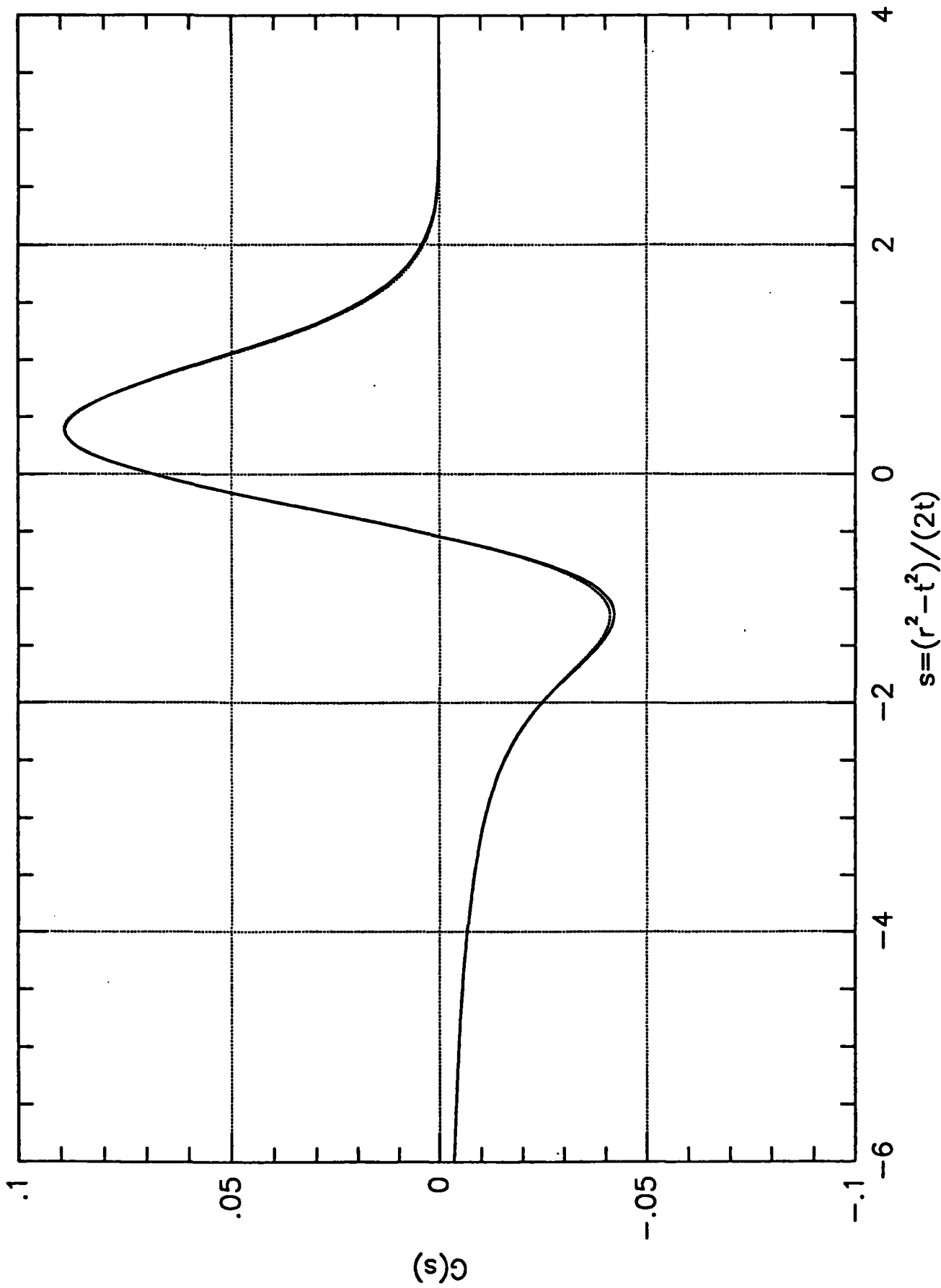
Figure 2b

G(s) (solid curve) and M(s) (dotted) vs s.

where
$$s = [r^2 - t^2]/2t \quad \cdot$$
Fig. (2b) provides a comparison of G(s) with M(s).

He who wishes to use this approximation should note that, for $s \geq 0$, the function $K_{1/4}$ is available (or can be called) from the IMSL Math Library.

3.   Radiation from a strip

We now explore the wave field that is initiated by the initial sea-bed displacement that produces

$$\eta_{strip}(x,y,0) = \frac{1}{\sqrt{\pi}} \int_X^{X+L} 2 \, e^{-[(x-x')^2 + y^2]} \, dx'$$

$$= [erf(X+L-x) - erf(X-x)] \, e^{-y^2} \tag{3.1}$$

and $\eta_t(x,y,o) = 0$.

For the special case in which $X+L \to \infty$ and $X \to -\infty$, $\eta_{special}(x,y,o) = 2e^{-y^2}$ and is the initial condition for the infinite aspect ratio (one-dimensional) initiation against which we would like to compare the finite aspect ratio results. With finite X and L, $\eta_{strip}(x,y,o)$ is an initial displacement that is very nearly uniform in x on the strip except in a small ($\delta x = O(1)$) neighborhood of its ends.

The solution of Eq. (2.2) with these initial conditions is:

$$\eta_{strip}(x,y,t) = \pi^{-1/2} \int_X^{X+L} (50/t)^{1/2} \, F\{([y^2-t^2]/2t) + ([x^2-x'^2]/2t), t\} \, dx' \tag{3.2}$$

and will be approximated, when $t \geq 15$, by

$$\eta_{strip}(x,y,t) \cong \pi^{-1/2} \int_X^{X+L} (50/t)^{1/2} \, G\{[(y^2-t^2)/2t] + ([x^2-x'^2]/2t)\} \, dx' \tag{3.3}$$

In particular

$$\eta_{strip}(o,Y,t) = \pi^{-1/2} \int_X^{X+L} (50/t)^{1/2} \, G\{([Y^2-t^2]/2t) + (x'^2/2t)\} \, dx' \tag{3.4}$$

and, with $x'^2/2t = s$

$$\eta_{strip}(o,Y,t) = \frac{5}{\sqrt{\pi}} \int_{X^2/2t}^{(X+L)^2/2t} G\left(\frac{Y^2-t^2}{2t} + s\right) \frac{ds}{\sqrt{s}} \tag{3.5}$$

Again, it is an elementary numerical task to carry out this integration for any given combination of X, L, and Y and each of those t for which $\eta_{strip}(o,Y,t)$ is large enough to be interesting. A more appropriate notation for $\eta_{strip}(o,Y,t)$ is

$$\eta_{strip}(0,Y,t) = H(X,L,Y;t) \, . \tag{3.6}$$

107

Details of the phenomenology will differ among the many possible configurations but it is informative to study in Figs (3a,b,c) the plots of $H(X,L,Y;t)$ vs. t for several configurations. In particular, as one would expect and as earlier investigators have suggested, the degradation of the

wave height with distance becomes $O\left(\frac{1}{\sqrt{r}}\right)$ as r^2 becomes large enough. More

dramatic, however, is the degradation of the wave height with increasing offset (i.e. X). Also interesting, but not surprising in view of the structure of G, is the development of a two-signed wave form.

4. Pulse Persistence

An interesting question that can be approached in an elementary way asks: For a given L and with X=0, what is the largest distance Y at which the strength of the arriving pulse from the finite source differs very little from 1/2 the strength of the pulse emanating from the source line extending from $-\infty$ to ∞. In the schematic diagram in Fig. 4, the outer annulus depicts at t=Y the region to which the positive values of G are confined and the adjacent annulus depicts the region in which, at the same time, G could be well approximated by a negative valued Gaussian. Equation (3.4) states that the integral that gives the value of η_{strip} at any y (see Fig. 4) and at time t=Y

is the integral of $\sqrt{50/t}$ $G([y^2+x^2-t^2]/2t)$ from 0 to L. We also know that the same integrand, when integrated over $0 < x < \infty$ gives $\eta = (1/2)\eta_{1-D}$. However, for $y > y_1$, there is in, $x > L$, no significant contribution of that integrand to the latter integral and therefore one can be certain that the leading part of the wave from the source of length L differs negligibly from the wave produced by the source lying in $(0,\infty)$.

In particular, let Y_1 be that y above which, at time t, the 1-D Gaussian from the ∞ source would be confined. Then, it follows from the foregoing that

the full 1-D Gaussian distribution of η arrives at Y if $Y_1^2+L_1^2 \geq (Y_1+Q)^2$, i.e.

since $Q \cong 3$, $Y_1 \leq L_1^2/6$.

One can repeat this argument when the question concerns the arrival of the full 1-d η_{max} rather than the full (two-sided) Gaussian. In that case a smaller value of Q is pertinent. Since the question of interest has many variants, the most useful "fact" to quote may be: The distance along the perpendicular bisector to the source strip of length 2L to which the pulse persists without significant diminution from the infinite strip intensity is of order $L^2/6$. In dimensional terms that distance is $\ell^2/6a$.

5. Dispersion

When the distance traveled in water of constant depth by a gravity wave is large enough the differences in phase velocity among its Fourier components imply a waveform that differs markedly from that found using the non-dispersive theory. A variant of the classical shallow water theory represented by Eq. (2.2) that captures the effects of that dispersion to lowest order is that of Boussinesque [4]. The differential equation that replaces (2.2) is, when h = d/a.

$$(1-h^2/3 \, \Delta)\eta_{tt} - \Delta\eta = 0 \tag{5.1}$$
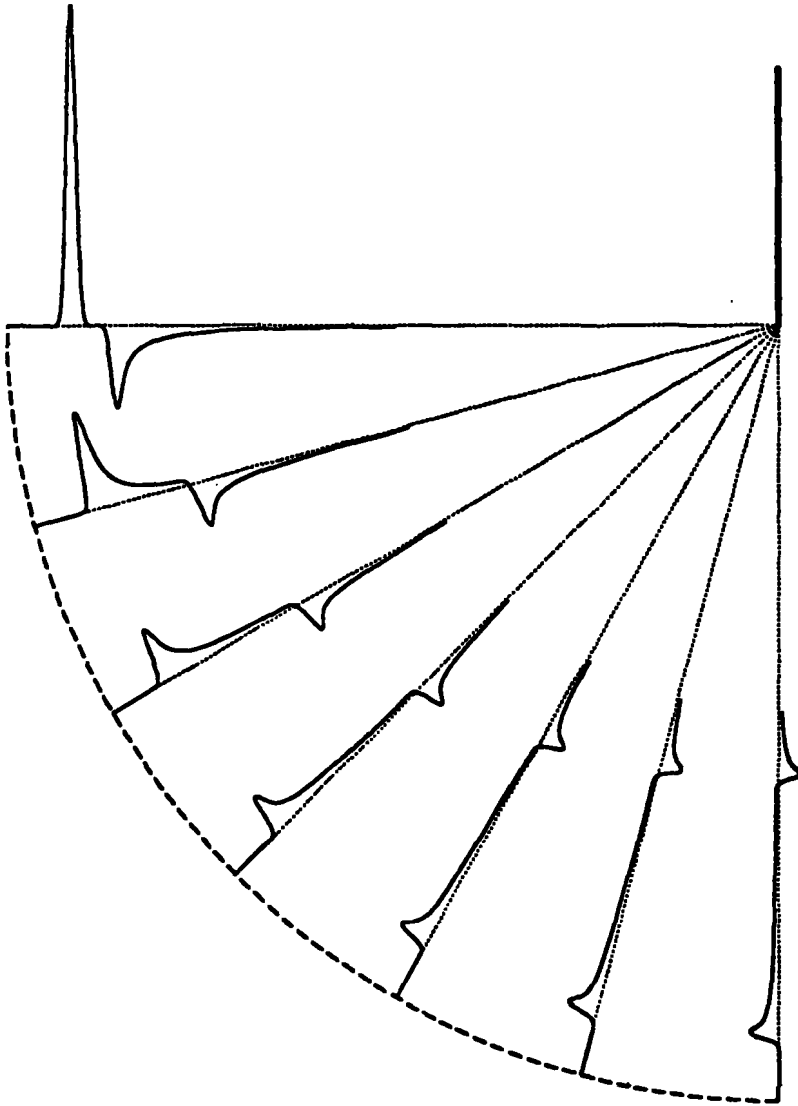
r=120   L=40

Figure 3a

$\eta_{strip}(o,Y,t)$ vs t for various (X,Y) for which $X^2 + Y^2 = (120)^2$. These are <u>not</u> plots of η vs position for fixed t but one can make useful inferences related to wave shape from these graphs. t is measured radially inward and all curves are plotted to the same scale but Fig. 3b should be used to pick off numerical values. The peak displacement for the $\theta=0$ curve is one-half of that that would obtain for a source lying in $-40 < x < 40$ and one lying in $-\infty < x < \infty$.
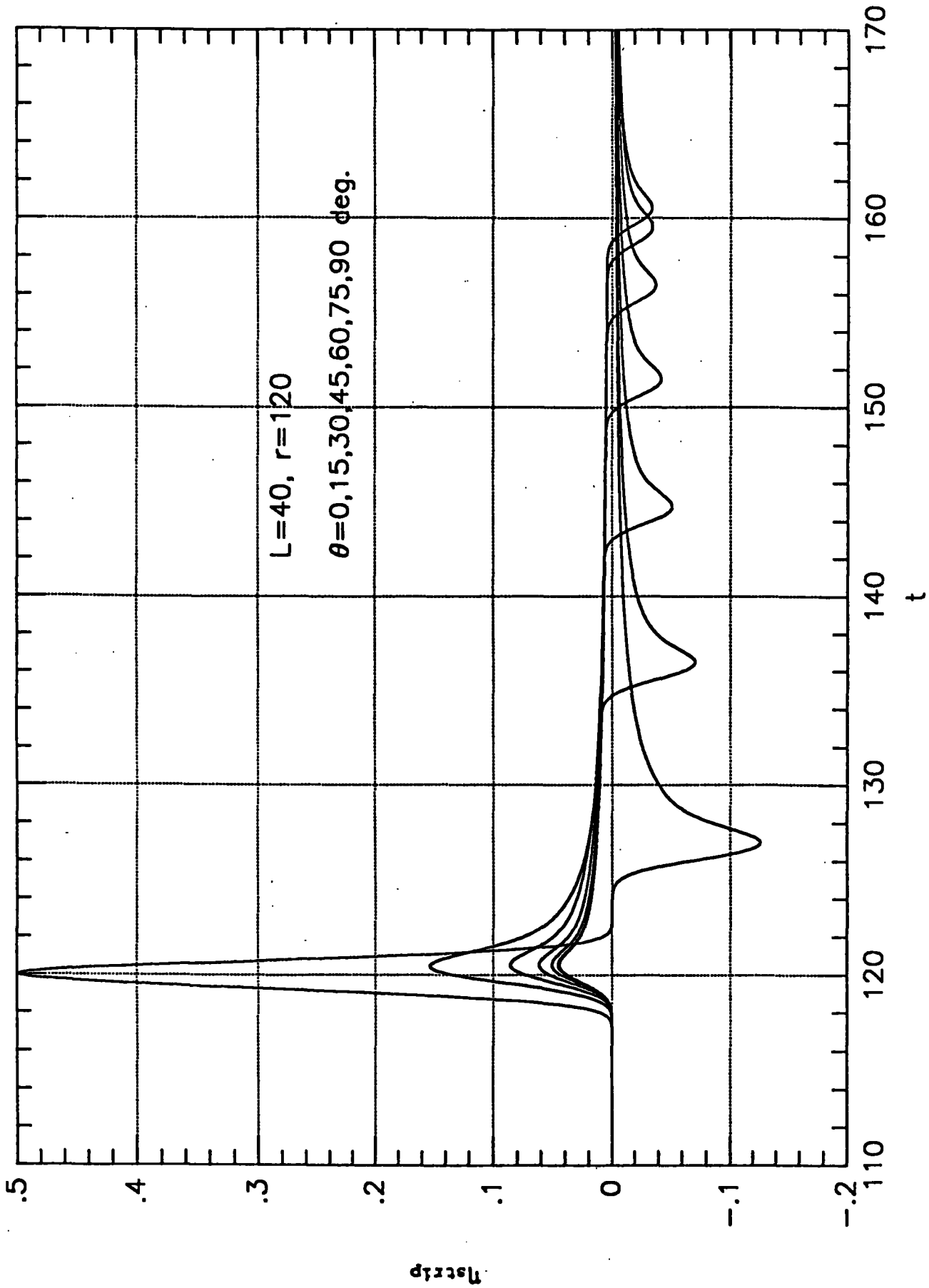
Figure 3b

$\eta_{strip}(0,Y,t)$ as a function of t for the same X, Y combinations of Fig. 3a.

110
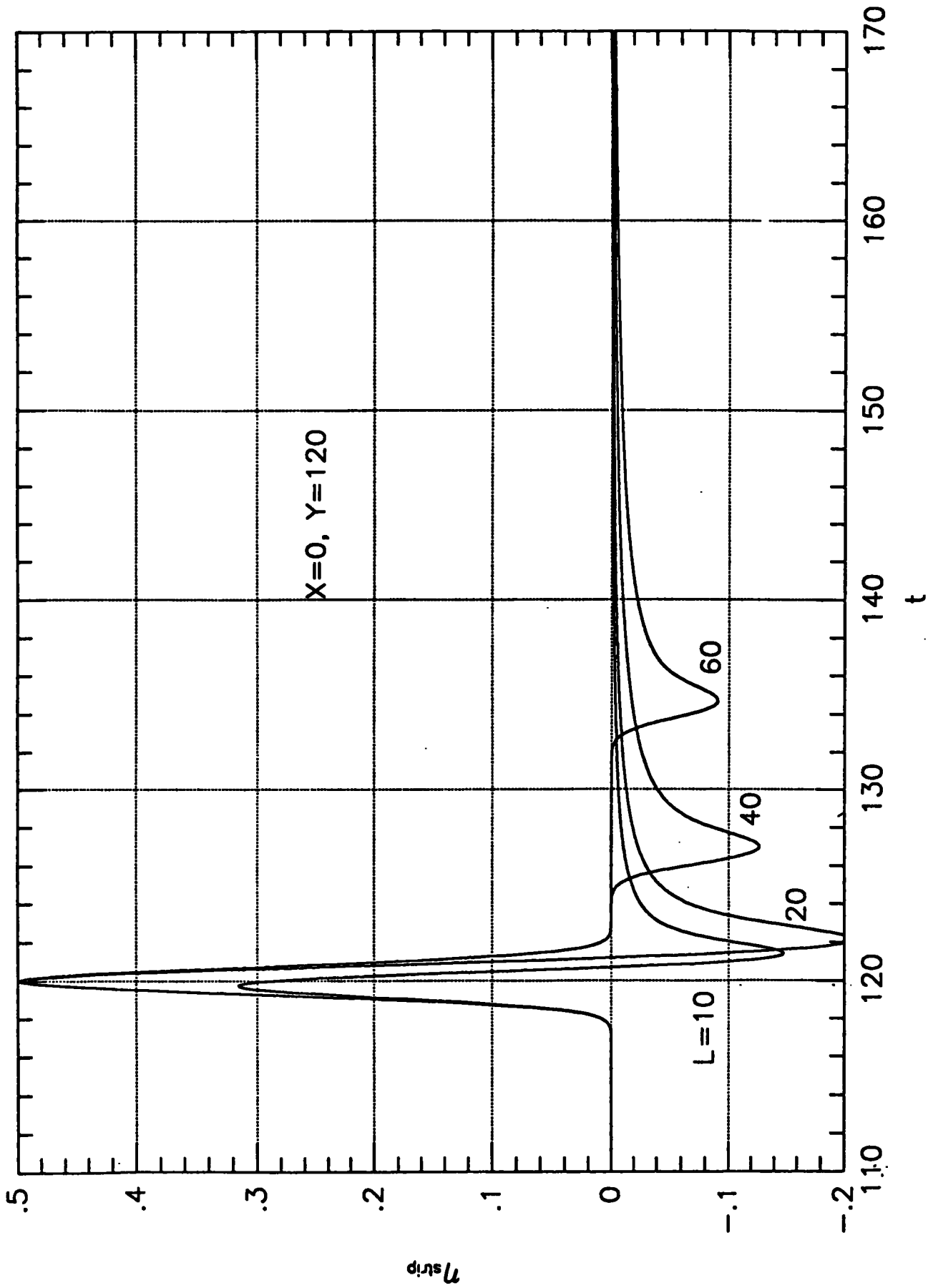
Figure 3c

$\eta_{strip}(0,Y,t)$ for X = 0, Y = 120 and various L.

111

and its solution on $x^2+y^2 < 0$ with initial conditions (2.2a) is

$$\phi(h, r, t) = \int_0^\infty \rho\, J_o(\rho r)\cos\left(\rho t / \sqrt{1+h^2\rho^2/3}\,\right) e^{-\rho^2/4}\, d\rho \qquad (5.2)$$

Once again, the integral (5.2) can be evaluated with all necessary accuracy by machine computation. The results are depicted in Fig. 5a and b for t=50 and several values of h.

One can infer from these graphs, a clear qualitative picture of the degradation of the leading wave from the finite source that would be implied by dispersion. Further discussion of the effects of dispersion on the structure of the leading wave can be found in Kajiura [5]. In a continuation of this work, we plan to evaluate more accurately the run-up of waves generated on strips of finite aspect ratio and we intend to include explicit
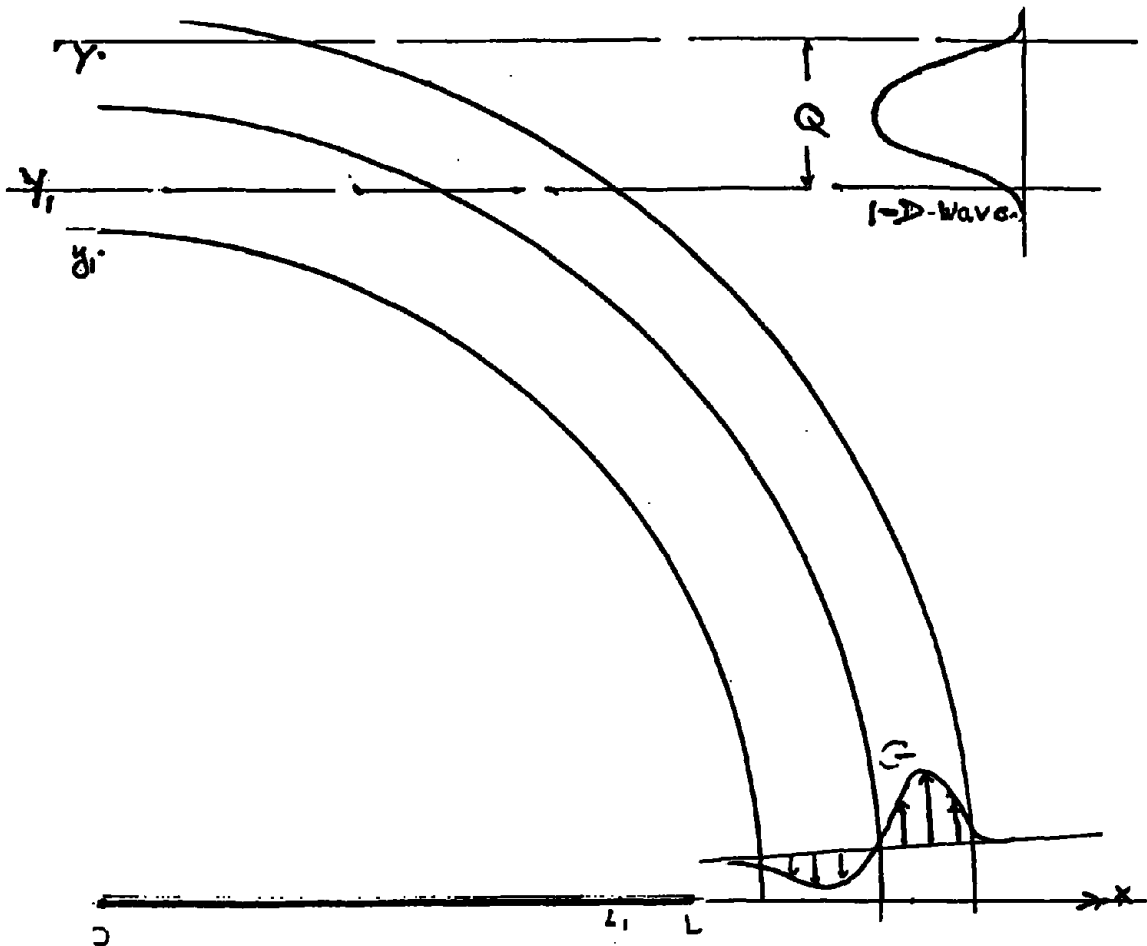
Figure 4

Schematic of behavior of G and of 1-D wave at time t. For source of length L, the waveheight at any $y > y_1$ is $\int_0^L G\,dx \equiv \int_0^\infty G\,dx.$

112
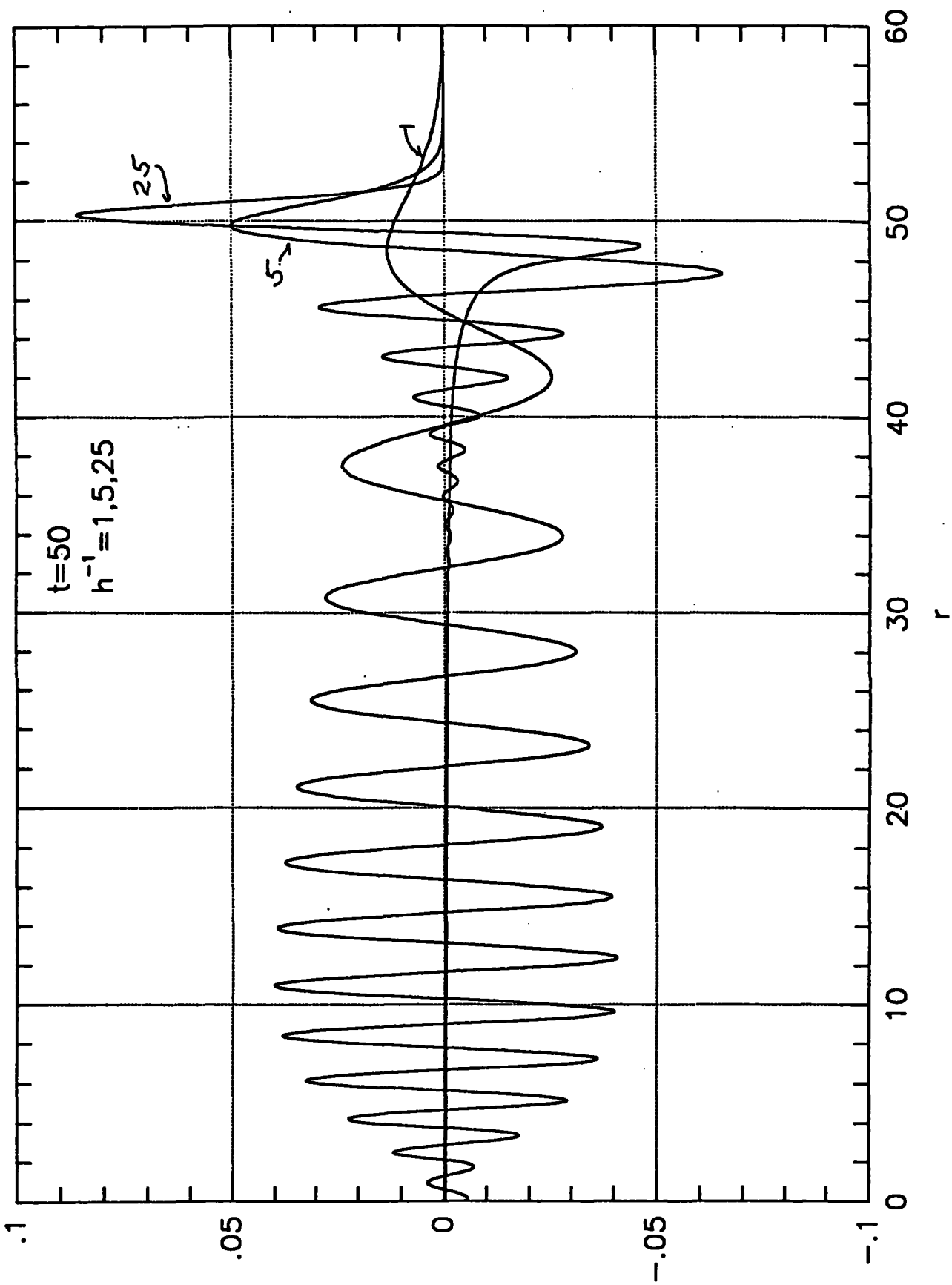
Figure 5a

Curve depicting the effects of dispersion on what would be f in the absence of dispersion.

113
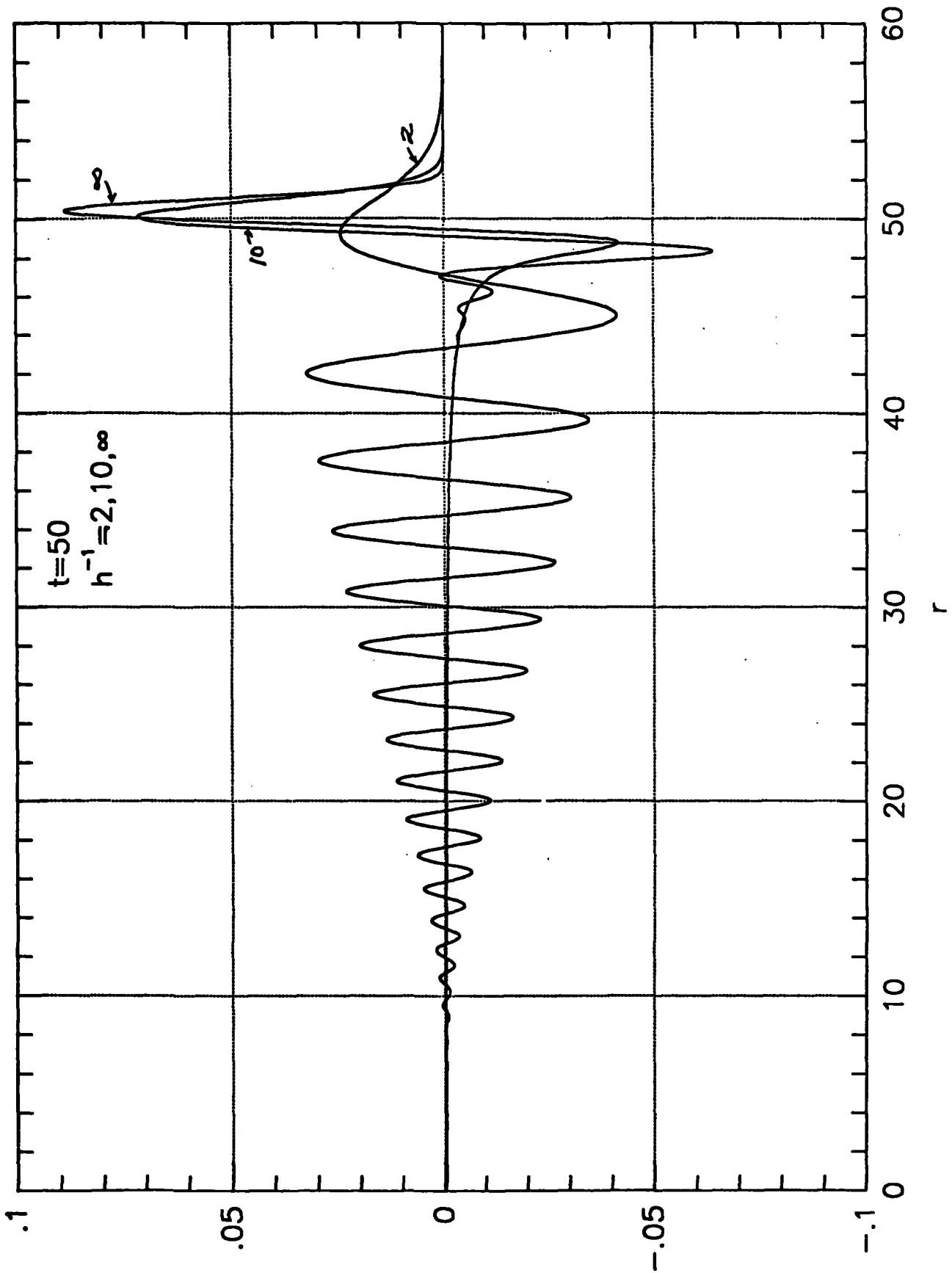
Figure 5b

Curve depicting the effects of dispersion on what would be f in the absence of dispersion.

114

illustrations of the effects of dispersive propagation on those run-up phenomena.

References

1. Van Dorn, W. G. (1965) Tsunamis. Advances in Hydroscience, Vol. 2, Academic Press, New York.

2. Carrier, G.F. (1966) Gravity waves on water of variable depth. Journal of Fluid Mechanics 24, p. 641-659.

3. Carrier, G.F. (1971) Dynamics of tsunamis. (In: Mathematical Problems in the Geophysical Sciences, - Vol. 1 - Geophysical Fluid Dynamics, Reid, W.H., ed. American Mathematical Society.)

4. Stoker, J.J. (1957) Water waves: The mathematical theory with applications. Pure and Applied Mathematics, Vol. 4, Interscience, New York.

5. Kajiura, K. (1963) The leading wave of a tsunami. Bulletin, Earthquake Research Institute, Toyko University 41, p. 535-571.

6. Foster R.M.; Campbell, G.A. (1948) Fourier Integrals. D. Van Nostrand Co., New York.

HYDRAULIC AND NUMERICAL EXPERIMENTS OF NON-LINEAR DISPERSIVE LONG WAVES IN A TWO-DIMENSIONAL WAVE BASIN

Fumihiko Imamura
Department of Civil Engineering
Tohoku University
Sendai, Japan

Nobuo Shuto
Disaster Control Research Center
Tohoku University
Sendai, Japan

Abstract

Hydraulic experiments are carried out in a wave basin, the two horizontal portions of which are connected by a slope of 1/10. A sine wave of 10 seconds is repeatedly generated. It gives soliton fissions in front of and behind the slope. Results of hydraulic experiments in a wave basin are compared with the computed results of the shallow-water theory and the Boussinesq equation. The shallow-water theory is solved by the leap-frog scheme, while the momentum equation of the Boussinesq equation is solved by S.O.R. method. Wave heights and wave profiles are compared in detail. The shallow-water theory gives good agreements until the frontal wave steepness exceeds 0.02. Although the Boussinesq equation gives better agreements, the computed wave crest height is sometimes higher than that measured on the intermediate slope.

1. Introduction

When the 1983 Nihonkai-Chubu earthquake tsunami hit the north Akita coast, evaluation of soliton fission was observed and recorded. Solitons at the tsunami front had wave periods of about 10 seconds. The dispersion effect which is usually neglected in numerical simulations should be included two-dimensionally. In section 2, hydraulic experimental setups and procedures are described. A sine wave which began from a fall was generated. In section 3, experimental results are shown on two parallel lines along the side walls of the wave basin. Three characteristics are given: wave-height-to-water-depth ratio (η/H), frontal wave steepness, and water-depth-to-wave-length ratio (H/L). In section 4, numerical simulations are briefly described. The shallow-water theory and the Boussinesq equation are used. In Section 5, hydraulic and numerical results are compared. In order to analyze the wave profile in detail, a relative error is defined, and the major wave is divided into three parts: the first fall, the succeeding rise and the second fall.

2. Set-up and Procedure of the Hydraulic Experiment

A wave basin, 55 m long and 14.75 m wide, was used in the experiments. The water depth was 50 cm near the wave generator, and was 30 cm at the other end. The two portions were connected with a slope of 1/10 at x = 23.5 m from the generator. Long waves were generated by a hydraulic wave generator. Inflow from and outflow to the reservoir tank through pipes were

electronically controlled by changing the opening angle of a butterfly valve. This system ensured generation of the same waves repeatedly. One cycle of sine wave, one trough and a succeeding crest, was generated, with the propagation angle of 20° included toward the left side wall. This angle was set to make the two-dimensional dispersive effect.

3. Results of the Hydraulic Experiment

Two lines were selected parallel to the side walls to show the transformation of waves. The line A was along the left wall and the line B along the right side wall. Along the line A, the generated first crest kept its superiority. At 17.5 m from the generator, the first fission was recorded. The second fission was recorded after the waves passed the intermediate 1/10 slope. Along the line B, in contrast, fission behind the first crest began earlier, just after the beginning of the propagation, and the first wave became lower than the second wave.

Figure 1 (a), (b) and (c) show the change of wave characteristics along lines A and B. The frontal wave steepness is defined as the ratio of the vertical to horizontal distance between the first trough and the succeeding crest. Along the line A, η/H and the frontal wave steepness only gradually increased in water of 50 cm depth, and increased rapidly after the wave passed the intermediate slope with an exception at x = 35 m where the second fission appears. H/L in the water of 50 cm depth was nearly constantly equal to 0.02. H/L along the line B in the water of 50 cm depth was also nearly equal to 0.03, suggesting that the wave length was shorter than along the line A, or that the dispersion effect was stronger. In further discussion, the generation of a Mach stem at the left wall may not be ignored.
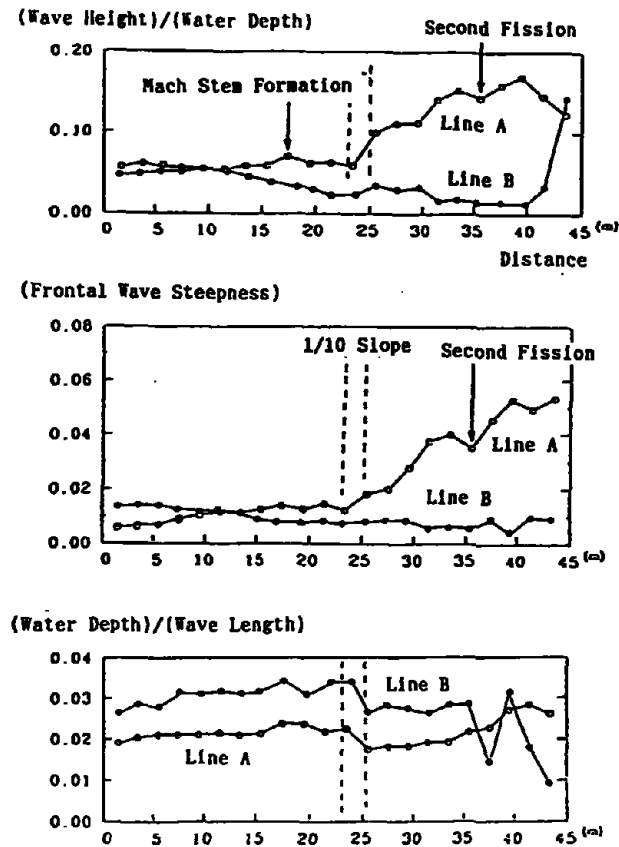
Figure 1 First wave characteristics.

4.   Numerical Experiment

Two different sets of equations were used: the Boussinesq equation and the shallow-water theory. In the Boussinesq equation, the effect of the slope in the dispersion term was neglected, because its magnitude is less than 1/100 that of the other effects according to Nagao *et al.* (1985). These equations were discretized with the space-staggered scheme in which velocity, water surface elevation, and water depth were given at different grid points. The momentum equations of the Boussinesq equation were implicitly solved by the S.O.R. method, while the rest of the equations were solved by the leap-frog method.

5.   Comparison Between the Hydraulic and Numerical Experiments

(1)   Time history

Time histories at x = 11.5, 23.5, 29.5 and 35.5 m along the line A are compared in Figure 2. The results by the Boussinesq equation (solid lines) well simulate the measured (dotted line) results; i.e., the first fission which begins at x = 11.5 m, its growth after waves pass the intermediate 1/10 slope, and the second fission at x = 35.5 m.

(2)   Wave height

The relative error of wave height, defined as

$$\{ \text{[measured]} - \text{[computed]} \}/\text{[computed]} \times 100\%$$

is discussed. Near the intermediate 1/10 slope, the Boussinesq equation gave a larger error than the shallow-water theory. The computed wave by the Boussinesq equation showed a higher crest than the measured, although the overall shape was similar to the measured.

(3)   Frontal wave steepness

Up to the toe of the intermediate 1/10 slope, the shallow-water theory, the Boussinesq equation and the measured data agreed with each other. When the wave passed over the intermediate 1/10 slope, the shallow-water theory gave a bigger frontal wave steepness than the measured data, whereas the Boussinesq equation agreed very well with the measured data. The dispersion effect acted to reduce the frontal wave slope. The upper boundary of the region where the shallow-water theory gave good results may be 0.02 in terms of the frontal wave steepness.

119
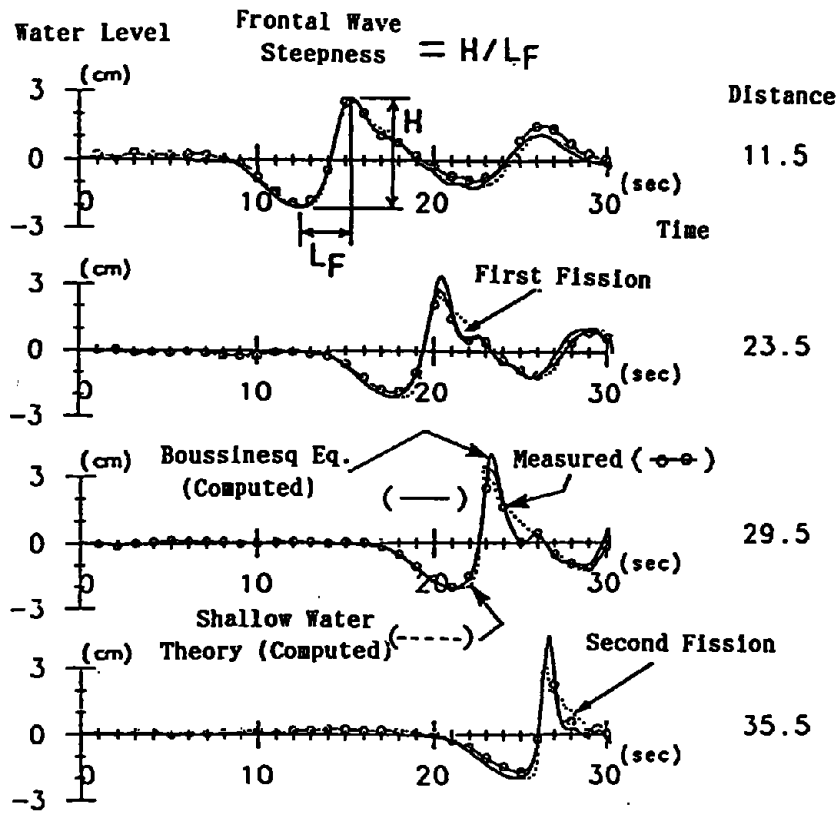
Figure 2   Comparison of time histories between the numerical and hydraulic experiments.

(4)   Detailed comparison for the first wave

The first wave was divided into three parts: the first fall from the still-water level to the trough, the succeeding rise to the crest, and the second fall from the crest to the still-water level. This second part corresponds to the frontal wave steepness, and the third part to the appearance of the fission. The relative error is defined as follows:

$$\frac{\Sigma\,|measured - computed|}{\Sigma\,|measured|} \times 100\%$$

In the first part, the two equations yielded the same relative error. The major cause of this discrepancy was not the equation but the accuracy of measurement, or say, the difficulty in determining the precise position of the still-water level. An error of the magnitude 3 - 5%, therefore, can be overlooked as an error of measurement, not computation, in the following comparison.

In the second part, the rise from the trough to the crest, the error of the shallow-water theory gave a larger difference than the error of the Boussinesq equation. The major cause of the difference was the convective term which acted to steepen the frontal slope. In the Boussinesq equation, the dispersion term moderates this tendency. However, the Boussinesq equation gave unsatisfactory results on the intermediate 1/10 slope and in the later stage beyond $x = 35$ m. This was caused by the overgrowth of the crest on this 1/10 slope. The exclusion of the effect of bottom slope in the dispersion term may be one of the causes of this discrepancy or a higher approximation may be necessary.

In the third part, the shallow-water theory did not give the sharp fall. Due to the same reason as above, the Boussinesq equation yielded a relatively large error in this part, because the computed crest came later than the measured crest. Although the Boussinesq equation generally gave satisfactory results, it gave a higher crest which appeared slightly later than the measured crest.

6. Conclusion

The shallow-water theory is applicable if the local steepness at the wave front is less than 0.02. Up to this value, the theory gave good wave profiles. Even after the beginning of the soliton fission, it gave better estimates than Boussinesq equation as far as the wave crest height was concerned. As the soliton developed, the Boussinesq equation became better, although this equation sometimes gave higher crests than the measured. The Boussinesq equation used in the present paper lacked the contribution of the bottom slope in the dispersion term. It was not determined whether this lack was the main cause of the discrepancy in evaluating the crest height or if a higher approximation was necessary to simulate the hydraulic experiment.

Reference

Nagao, M., C. Goto and N. Shuto, 1985. Numerical simulations of nonlinear dispersive long waves. *Proceedings of 32nd Japanese Conference on Coastal Engineering*, p.114-118.

ON MOMENTUM EXCHANGE OF A TSUNAMI BORE AT A SHORELINE

Harry Yeh
Department of Civil Engineering
University of Washington
Seattle, WA, USA

A gradual increase in water-surface elevation is usually present just in front of a tsunami formed as a turbulent bore. The analysis of this leading tsunami shows that the local leading wave has characteristics that the horizontal component of fluid velocity is maximum near the bed and minimum at the surface. Base on this characteristic, it is suggested that this leading wave is the one which causes the "momentum exchange" process occurred during the transition of a tsunami bore to runup at the shoreline.

INTRODUCTION

Based on their analyses (Whitham, 1958; Keller et al., 1960; Ho and Meyer, 1962), the shallow-water wave theory predicts that the height of a bore and its propagation velocity decrease gradually as it approaches the shoreline. Then, the height tends to vanish at the shoreline; the fluid velocity u and bore front velocity U increases rapidly to approach their common finite value, whereas their accelerations become infinity at the shoreline. This behavior at a shoreline involving the rapid and complete conversion of potential to kinetic energy is often called "bore collapse".

The genuine bore-collapse phenomenon, however, never occurs in a real fluid environment because the prediction of rapid vanishment of the bore height by itself contradicts the shallow-water wave approximation, i.e. the pressure field becomes no longer hydrostatic. Furthermore, the height of a bore must be finite at the shoreline -- no matter how small it is the height cannot vanish. The experimental results (Yeh and Ghazali, 1988; Yeh et al., 1989; Yeh 1990) demonstrated the detailed bore process at the shoreline. Based on their results, the transition process at the shoreline was found to involve the "momentum exchange" between the bore and the small wedge-shaped water body along the shore; the bore front itself does not reach the shoreline directly, but the large bore mass pushes the small, initially quiescent water in front of it. The term "momentum exchange" is used here to describe this transition since the process is analogous to the collision of two bodies; a fast-moving large mass (i.e. bore) collides with a small stationary mass (the wedge-shaped water mass along the shoreline). Yeh (1990) pointed out that this momentum exchange process might be a key for the explanation of destructive tsunami effects along the shoreline. However, neither Yeh and Ghazali (1988), Yeh et al. (1989), nor Yeh (1990) provided a plausible physical explanation for this process. The purpose of this paper is to clarify the mechanism of the momentum exchange process.

ANALYSIS

If the bore front were considered to be a discontinuity of flow as modelled in the shallow-water wave theory, conservation of momentum predicts that a sudden acceleration of propagation must occur near the shoreline since a mass of water diminishes in front of the bore as it approaches the shore. However, a real bore front has a finite length (not a discontinuity) and the local flow at the front cannot be described by the shallow-water wave theory (not a hydrostatic pressure field). Suppose that there is a smooth precursor of a bore moving with the same speed as the bore

propagation, U, and it is small enough to be considered to be a linear wave. Such a precursor can be found as a gradual increase in water-surface elevation just ahead of the turbulent bore front. In water of uniform depth, such a leading wave has the velocity potential, ϕ, of the form,

$$\phi_n = - A_n\, e^{-k_n(x - ct)}\cos k_n (y + h),\qquad\qquad (1)$$

with the dispersion relation

$$\omega_n^2 = gk_n \tan k_n h,\qquad\qquad (2)$$

where the x-coordinate points in the inshore direction from the shoreline, the y-coordinate points vertically upward from the bed of quiescent water depth h, c is the propagation speed $c = \omega_n/k_n$, g is the acceleration of gravity, A_n is a constant, and the subscript n denotes the mode number. The velocity potential ϕ together with the dispersion relation (2) satisfies with the Laplace equation in the fluid domain, the linearized free-surface boundary condition, and the no-flux boundary condition along the horizontal bottom. Equation (1) is just like the representation of the outskirts of a solitary wave as pointed out by Lamb (Art. 252, 1932). Also this type of the solution is often termed as the evanescent modes. The evanescent modes are often considered to be unimportant away from a physical boundary because the magnitudes of the modes decay exponentially.

Equation (1) shows that the horizontal velocity component $u = \partial\phi/\partial x$ increases with depth, i.e. the velocity is the maximum at the bottom boundary, which is opposite to an oscillatory wave solution. The greater horizontal velocity near the bottom evidently creates the "shoving" action near the shore which is consistent to the momentum exchange process.

Similar waves (the evanescent modes) on a uniformly sloping beach with $\beta = \pi/4m$, where β is the beach slope from the horizontal and m is a positive integer, is inferred from the oscillatory wave solution provided by Hanson (1926) and can be found to be

$$\phi = \mathcal{R}e\,[\, e^{\omega t}\,[\, C_{0,2}\exp(- ikx - ky)$$

$$+ \sum_{j=1}^{m-1}\sum_{p=1}^{2} C_{j,p}\exp\{(-1)^{p+1}\,ky\cos 2j\beta - kx\sin 2j\beta + i(- kx\cos 2j\beta + (-1)^p\,ky\sin 2j\beta)\}$$

$$+ C_{m,1}\exp(- kx - iky)]],\qquad\qquad (3)$$

where $\mathcal{R}e$ is the real part of the function, and

$$\omega^2 = gk,$$
$$C_{m,1} = (i - 1)\,A = C_{m-1,2},$$
$$C_{j,1} = - i\, C_{j,2}\tan j\beta,$$
$$C_{j-1,2} = C_{j,1},$$

and $i^2 = -1$, A is a constant, and the y-coordinate points vertically upward from the equilibrium water elevation. Again, (3) satisfies with the Laplace equation in the fluid domain, the linearized

free-surface boundary condition and the boundary condition along the uniformly sloping bottom, i.e. $\sin\beta \ \partial_x\phi = \cos\beta \ \partial_y\phi$ on $x\sin\beta = y\cos\beta$. It can be shown from (3) that that the water surface η monotonically increases in the offshore direction, hence the solution (3) is physically viable only if it describes a local flow near the shoreline and the offshore boundary condition is provided, such as a bore advancing toward the shore. The horizontal components of fluid particle velocity, u, is also found from (3) that instead of a uniform velocity profile over the depth, fluid particles at the leading bore front can have increasing velocities with depth. Near the shoreline, this nonuniform velocity effect manifests itself as "pushing" the wedge of water along the shore.

CONCLUSIONS

Based on the linearized potential water-wave theory, the leading wave in front of a bore was considered to be the evanescent modes of the solutions, which are locally present and controlled by the flow in the bore. A greater velocity with depth, associated with the leading wave, might be the one which is responsible to cause the momentum exchange process at the shoreline when a advancing bore collapses into a runup motion.

REFERENCE

Hanson, E.T., 1926. The theory of ship waves. Proc. R. Soc. London Ser. A. 111, 491-529.

Ho, D.V. & Meyer, R.E., 1962. Climb of a bore on a beach. 1: Uniform beach slope. J. Fluid Mech. 14, 305-318.

Keller, H.B., Levine, D.A. & Whitham, G.B., 1960. Motion of a bore over a sloping beach. J. Fluid Mech. 7, 302-316.

Lamb, H., 1932. Hydrodynamics, 6th ed. Cambridge University Press.

Whitham, G.B., 1958. On the propagation of shock waves through regions of non-uniform area of flow. J. Fluid Mech. 4, 337-360.

Yeh, H., 1990. Tsunami Bore Run-Up. Natural Hazards. (in press).

Yeh, H.H. & Ghazali, A., 1988. On bore collapse. J. Geophys. Res. 93, 6930-6936.

Yeh, H., Ghazali, A., and Marton, I., 1989. Experimental Study of Bore Runup. Journal of Fluid Mechanics, 206, 563-578.

Discussion

Comment: The situation is not only that you have a very light velocity along the bottom relative to the rest of the water column but also that the vertical velocity is larger than that. So it is not only a pushing motion but a lifting motion as well on some object. This would be a mechanism having bearing on the lifting of the large concrete structures off the beach by the 1983 Sea of Japan tsunami.

LEAST SQUARES ESTIMATIONS OF A TSUNAMI SOURCE FROM WAVE RECORDS

Harold G. Loomis
Department of Ocean Engineering
University of Hawaii
Honolulu, HI, USA

Abstract

A method is proposed for finding the amplitude distribution in space of an instantaneous ocean bottom displacement that produced wave records at a number of wave gauges. A weighted least squares fitting of the observed wave records to synthetic waves calculated by Green's functions from the assumed source produces a set of initial source displacements that best fit the measured waves. A second method finds a correction to an assumed set of source displacements to best fit observed wave records. Weighting constants are used to adjust scales and to weight the confidence in the assumed source values and the accuracies of the measured wave records.

1. Reciprocity of Unit Response Functions.

Suppose that a linear numerical hydrodynamic model of the ocean exists that encompasses possible tsunami source regions and also points where time observations can be made. Charles Mader of JTRE has such a model on a $1/3^\circ$ grid that could be linearized. Using that model we calculate response functions

$K_{ij}(t)$ = Response at P_j due to unit impulse at time t=0 at source point Q_i.

Figure 1 shows the situation that is contemplated. Response functions are calculated numerically between each mesh point in a

possible source region and each mesh point corresponding to a wave gauge.
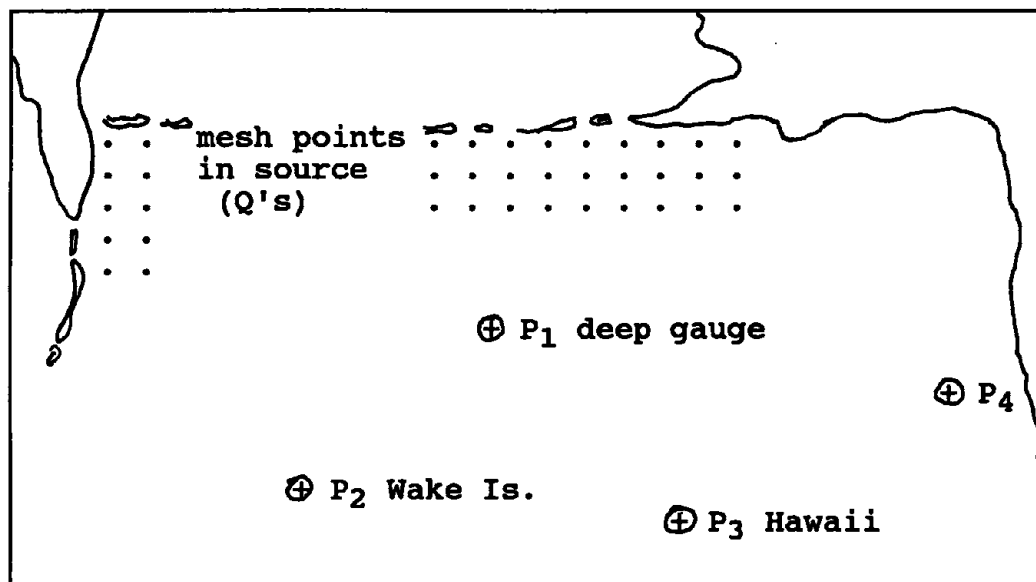
Figure 1.   Sketch of tsunami source regions and wave gauges.

There are only a few observation points at tide gauges and deep sea gauges.   There will be many possible points of the mesh which could lie in a tsunami source region.   This suggests using the reciprocity property of the response function (Loomis, 1979). Surprisingly, it is true in theory (Morse and Feshbach, 1953) and in numerical schemes which I have tested, that the response at P due to a unit impulse at Q is exactly equal to the response at Q due to a unit impulse at P.   That is

$$K_{QP}(t) = K_{PQ}(t).$$

This means that one can put a unit impulse at a point in the mesh corresponding to a recording gauge and record the time histories at those points in the mesh which could possibly be at a tsunami source.   These then are the response functions which will be used in the estimation of the deformation at the tsunami source.

Incidentally, there is another useful product at this point. Because of the reciprocity of the response functions one can examine the size of the response functions at tsunamigenic regions and decide which regions are liable to produce large tsunamis at the observation locations.

128

A typical response function will look something like that shown in figure 2.
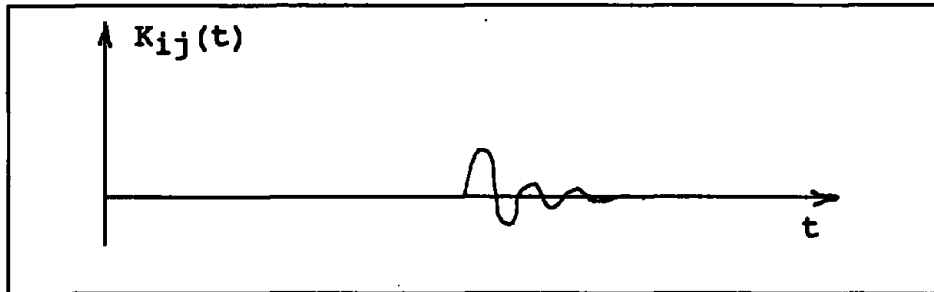
Figure 2. Wave at P_j due to unit impulse at Q_i.

At this point note that there is only a portion of the response function that would correspond to a direct wave from the source region. We could artificially set the response function equal to zero outside of this time slot. Instead we simply consider at the observation point P_j an interval of time T starting at time t_j as being significant for us.

The response functions calculated above are used in the two methods of estimating the source deformation which are described below.

2.   Simple Least Squares Estimation of Source Deformation.

We are going to calculate a set of source displacement constants c_i , i=1, ...,n to minimize the square of the weighted difference between an observed tsunami $n_j^o(t)$ and a calculated tsunami given by

$$n^c_j(t) = \sum_{i=1}^{n} c_i K_{ij}(t)$$

The expression to be minimized is given by

$$s^2 = \sum_{j=1}^{m} W_j \cdot [\int_{t_j}^{t_j + T} (n_j^o(t) - \sum_{i=1}^{n} c_i K_{ij}(t))^2 dt.$$

The set of weighting factors, W_j, is chosen according to how much confidence you have in the observed and in the calculated record at observation point P_j. Adjustments of relative size can also be included in the weighting factors. One might assign

129

larger weights to deep gauges nearer the source and lower weights to tide gauge records that are more distant and/or are more affected by local conditions.

The expression above is minimized by solving the normal equations found by

$$\partial s^2/\partial c_i = 0, \text{ for } i = 1,2, \quad ,n.$$

This is a standard problem in least squares fitting and is easily solved.

In what follows we define an inner product as the integral of the two functions over that part of time corresponding to the arrival of the main part of the tsunami directly from the source. That is

$$(n^e_j, K_{ij}) = \int_{t_j}^{t_j+T} n^e_j(t) \cdot K_{ij}(t) \, dt$$

$$(K_{kj}, K_{ij}) = \int_{t_j}^{t_j+T} K_{kj}(t) \cdot K_{ij}(t) \, dt.$$

With these definitions, the c_i's are solutions of the equations

$$\sum_{j=1}^{m}(n^e_j, K_{ij}) = \sum_{k=1}^{n} c_k \sum_{j=1}^{m} (K_{kj}, K_{ij}), \quad i=1,2,\ldots,n.$$

Note that the seismological description of the earthquake would dictate which points are candidates for inclusion in the source region. Including points not actually in the source region could only improve the fit of the calculated wave to the observed wave at the expense of true source points.

The more a priori information that is used the better the solution. Along this line, there is an alteration of this method which works as follows.

3. Using Wave Observations to Improve an A Priori Estimate of a Tsunami Source.

It is assumed that a given source deformation can be reasoned from seismological considerations. The response functions are calculated between the given source points and the observa-

tion points as mentioned above. Weights, W^s_i, are assigned according to your confidence in the assumed source motion. Another set of weights, W^o_j, are assigned to observed wave data according to your confidence in the records and to adjust the scale of different records.

The expression to be minimized is the weighted sum of the squared error in the assumed source motion and the squared error in the wave observations. This is

$$s^2 = \sum_{i=1}^{n} W^s_i \ (\Delta s_i)^2 + \sum_{j=1}^{m} W^o_j \int_{t_j}^{t_j+T} (n^o_j(t) - n^c_j(t))^2 \ dt$$

where $n^o_j(t)$ is the observed wave and $n^c_j(t)$ is the calculated wave from the displacements $s_i + \Delta s_i$, $i=1, \dots, n$, where s_i is the assumed source displacement and Δs_i is the correction to be calculated. These calculations amount to matrix multiplications of inner products of response functions $K_{ij}(t)$ with each other and with the wave records as described above. This is an essential step in being able to solve the problem. Note that the Δs_i appear in both of the sums above. Minimizing the above expression leads to a set of n linear equations in the source corrections Δs_i. The equations to be solved are

$$\sum_{i=1}^{n} \Delta s_i \cdot [\delta_{ik} \cdot w^s_k + \sum_{j=1}^{m} w^o_j \cdot (K_{ij}, K_{kj})] = \sum_{j=1}^{m} w^o_j \cdot [(n^o_j, K_{kj}) -$$

$$\sum_{i=1}^{n} s_i \cdot (K_{ij}, K_{kj})], \quad k=1,2, \dots, n$$

where δ_{ik} is the Kronecker delta, m is the number of observation points and n is the number of source points.

Since this method uses more a priori information than the previous one, the result is more likely to be reasonable. One can also allow for uncertainties in the numerical model by assigning a weight function to the numerical calculations too. These ideas come from work done by Bennett and McIntosh (1982) on tides and inverse modeling in general.

References.

Bennett, A.F. and P.C. McIntosh (1982) Open ocean modeling as an inverse problem: tidal theory. J. Phys. Oceanography, 12(10), pp. 1004-1018.

Loomis, H.G. (1974) Solution of the linear, long-wave hydrodynamic equations by using unit impulse functions. In: Heath, R.A. and M.M. Cresswell, eds. <u>Tsunami Research Symposium, 1974.</u> Royal Society of New Zealand and Unesco, Paris, pp. 155-158.

Loomis, H.G. (1979) Tsunami predictions using the reciprocal property of Green's functions. J. Marine Geodesy, vol. 2, no. 1, pp. 27-29.

Morse, P.M. and H. Feshbach (1953) <u>Methods of Theoretical Physics.</u> McGraw-Hill, New York, pp. 834-849.

Discussion

Comment: In response to a question it was pointed out that the construction of the functions at the point of observation requires a linear superposition of the response functions which requires a linear model. A model such as SWAN would have to be made linear.

NUMERICAL SIMULATION AS A MEANS OF WARNING FOR NEAR-FIELD TSUNAMIS

N. Shuto
Department of Civil Engineering
Tohoku Univeristy
Sendai, Japan

C. Goto
Ocean Energy Utilization Laboratory
Port and Harbor Research Institute
Ministry of Transport
Yokosuka, Japan

F. Imamura
Department of Civil Engineering
Tohoku Univeristy
Sendai, Japan

Abstract

The feasibility of quantitatively forecasting a near-field tsunami prior to its arrival is examined, provided that the initial tsunami profile can be determined from fault parameters calculated using a method similar to that of Izutani and Hirasawa. Examination of basic equations, boundary conditions and grid lengths has led to the conclusion that the following combination is the best to perform rapid, accurate, and detailed numerical forecasting: the linear long wave theory discretized with the staggered leap-frog scheme, perfect reflection at the land boundary, and a grid length varying from 5.4 km out at deep sea to 0.2 km at the shoreline. With the aid of a super computer, tsunami heights along every 200 m of Japan's Sanriku coast, 250 km long, can be obtained within 7 minutes after the occurrence of an earthquake. This method gives enough time for warning transmission and for evacuation of residents because the standard arrival time of tsunamis in this district is 25 to 30 minutes.

Introduction

Modern tsunami prevention works in Japan started just after the Chilean tsunami of 1960, which had a maximum run-up height of the order of 5 m. In the following five years, sea walls 5-6 m high were built along coasts of the Sanriku district and others severely damaged by the tsunami. Additionally, along other coasts, structures of a similar height were constructed to prevent storm surge inundation and beach erosion. As a result, most of Japan's coastline is now protected against medium magnitude tsunamis by coastal structures. However, in order to deal with huge tsunamis, other methods, which include early warning methods and moving buildings to higher elevations, must be taken into consideration.

Since 1952 the Japan Meteorological Agency (JMA) has been responsible for tsunami forecasting. This agency utilizes a diagrammatic forecasting model which is based on an empirical relationship among the magnitude of the tsunami, the distance to the epicenter (or equivalently, the time difference in arrivals of P- and S-waves), and the amplitude of seismic waves recorded at a given distance from the epicenter. The magnitude of tsunami is divided into four classes: major tsunami, tsunami, tsunami alert, and no tsunami. The sentences of alert messages are officially prefixed. When a major tsunami is expected, its corresponding alert message indicates only that a tsunami higher than 3 m will strike.

In 1968 when the Tokachi-oki earthquake tsunami hit, the tsunami defense structures which had been designed using the 1960 Chilean tsunami as a basis for crown height had already been built. This tsunami was of medium magnitude and was almost completely stopped by the coastal structures. As a consequence of this event, younger coastal residents who have never experienced any huge tsunamis have come to fully rely upon the tsunami defense structures. Although older residents are sure that a huge tsunami can easily exceed the height of existing structures, it is now very difficult to decide for local residents in general whether or not these 6 m high sea walls can stop a major tsunami forecasted by the JMA. Either from the reliance on the existing coastal structures or the difficulty in decision making, coastal residents are becoming indifferent to taking immediate action to evacuate when a tsunami is forecasted. It is believed that if this trend is continued, many lives will be lost when the next huge tsunami hits the Sanriku coast.

One method that can be used to improve the present situation is to make accurate numerical forecasting, and to warn the population with detailed information. This method, however, may not be rapid enough to provide an advance warning, which is a necessary factor in tsunami forecasting. For the case of a near-field tsunami in the Sanriku coast, only 25 to 30 minutes will be available between an earthquake generation and the tsunami attack. If it is assumed that at least 15 minutes are required to transmit the information and evacuate the residents, then the computer numerical simulation and the human decisions must be completed in less than 10 minutes.

During this limited time two major steps must be carried out, i.e., a rapid estimation of fault parameters of the earthquake, and the quick completion of the tsunami numerical simulation. Information concerning earthquake fault parameters can be found in Kanamori and Given (1983), Okal and Talandier (1986), and Izutani and Hirasawa (1987a,b). The present paper is concerned only with the problem of making computer numerical simulations that satisfy optimum conditions of rapidity, accuracy, and detail. This problem is called the "RAD optimum problem" in the present paper.

In section 2 discussions are given for the forecasting method with a flow chart and the area where the forecasting is conducted. The Izutani-Hirasawa method is employed to rapidly estimate fault parameters.

In section 3 the "RAD optimum problem" is solved by a super computer using several equations, boundary conditions and grid lengths. The Meiji Great Sanriku tsunami of 1896 is used as an example. The time duration of the numerical forecasting is measured from the generation of an earthquake to the completion of the numerical simulation.

In section 4 the solution (an optimum set of equations, boundary conditions, and grid lengths) is applied to the 1968 Tokachi-oki earthquake tsunami as a performance test.

In section 5 the required time to forecast tsunami heights is summarized.

Numerical tsunami forecasting methods and application area

Figure 1 shows the major steps in the forecasting procedure, beginning with the generation of an earthquake and ending at the issue of a warning.

```
┌──────────────┐
│  Earthquake  │
└──────────────┘
       │
┌──────────────────────────────┐
│ Determination of Hypocenter   │
└──────────────────────────────┘
       │
┌──────────────────────────────┐
│ Estimation of Fault Parameters │
└──────────────────────────────┘
       │
┌──────────────────────────────┐
│ Tsunami Numerical Simulation   │
└──────────────────────────────┘
       │
┌──────────────────────────────┐
│ Prediction of Tsunami Height   │
└──────────────────────────────┘
       │
┌──────────────┐
│ Warning Issue │
└──────────────┘
```
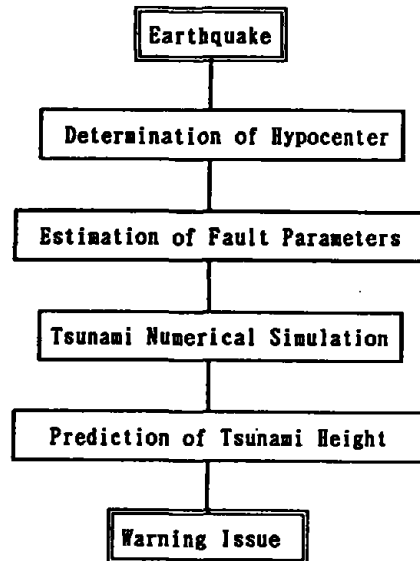
Figure 1.   Flow chart of the proposed
tsunami warning system.

Figure 2 shows the determination process of fault parameters necessary to estimate the initial tsunami profile. The angle of inclination and slip of the fault are determined from the initial P-wave using the conventional method. The most difficult parameters to estimate are the length and width of the fault plane, which are usually determined from the extension of the aftershock area. If the conventional method is used, the dimensions of the fault plane can not be estimated before the arrival of the tsunami. Izutani and Hirasawa (1987a) proposed a new method to rapidly estimate these parameters, where the fault length and the direction of rupture propagation are determined using the observed duration of strong motion. The width and dip slip of the fault can be estimated with empirical relationships (e.g., Abe, 1975). The earthquake magnitude is then determined from the arrival time and maximum amplitudes of the P- and S-waves. If the travel time of seismic waves and the duration of strong motion are included, the parameters can be determined within 5 minutes after the generation of an earthquake.

With the parameters thus determined, the Mansinha-Smylie method (1971) can be used to calculate the vertical displacement of the sea bottom, which is considered equal to the initial tsunami profile. Following this step the tsunami numerical simulation is conducted.

In the present study the forecasting area is Japan's Sanriku coast, 250 km long, shown by the hatched area in Figure 3. The simulation is made in the area from 36° 20'N to 43° 00'N and from 139° 40'E to 145° 20'E.
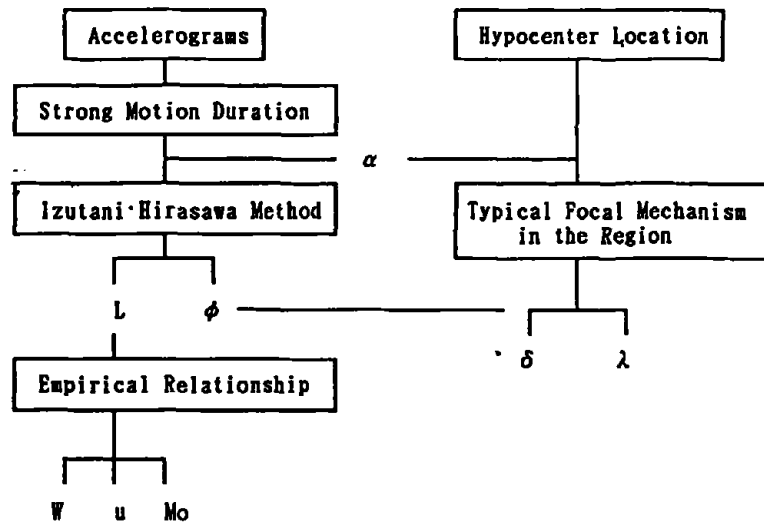
Figure 2.   Process to determine fault parameters L:fault length,
W: fault width, u:amount of slip α:station azimuth at the
epicenter, δ:dip angle, λ: slip angle, MO:seismic moment,
φ:direction of rupture propagation.
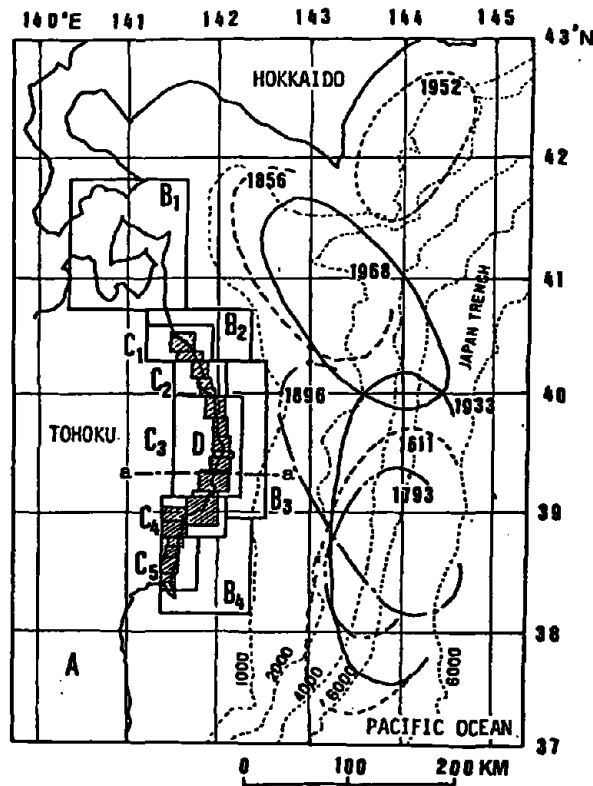
Figure 3.   Computation regions, and estimated
source areas of past tsunamis with
attached numerals giving year of occurrence.

136

A solution of the RAD optimum problem

(1) Selected tsunami

Japan's Sanriku coast (the Pacific Ocean side of the Tohoku district) has historically suffered from relatively frequent tsunami attacks. The ellipses in Figure 3 show estimated source areas of past major tsunamis, with the attached numerals indicating their years of generation. Many tsunamis of were generated along the Japan Trench, with the largest being the tsunami of 1611, although only a few accurate historical records of this tsunami exist. The second largest was the Meiji Great Sanriku tsunami of 1896, which claimed more than 21,000 lives and had a maximum run-up height of more than 30 m above the mean sea water level. Using this tsunami, the Imamura-Iida scale of the tsunami magnitude, m=4, was established. The third largest was the Showa Great Sanriku tsunami of 1933, which had a maximum run-up height of more than 25 m and claimed over 3,000 lives. The tsunami magnitude, m=3, in the Imamura-Iida scale was determined as corresponding to this tsunami.

The Meiji Great Sanriku tsunami was selected to solve the "RAD optimum problem" for the Sanriku district. The fact that this tsunami with its large run-up height would surely overtop the existing sea walls made it an adequate tsunami to examine the assumption on land boundary conditions. An additional advantage of using this tsunami is that a sufficient number of tsunami traces had been recorded and their elevations had been measured. The initial profile of this tsunami can not be determined using the Izutani-Hirasawa method, because no seismic wave data were available. Instead the initial profile determined by Aida (1977) was employed. He carried out tsunami numerical simulations for four assumed initial profiles, assuming that the earthquake mechanism was similar to the 1968 Tokachi-oki earthquake tsunami. He determined the best initial profile by comparing the computed inundation heights with the measured tsunami trace heights and the computed arrival time with two tide records available.

(2) Governing equations

In numerical simulations of hindcasting the run-up heights of near-field tsunamis, two types of governing equations are generally used. In a sea deeper than 50 m, the linear long wave theory is generally said to be accurate enough for practical purposes. In a sea shallower than to be 50 m, the shallow-water theory which includes the bottom friction is usually used. However, when the 1983 Nihonkai-Chubu earthquake tsunami hit the Japan Sea coast, the development of a train of short waves emanating at the tsunami front was observed, thus suggesting that dispersion effects are also important.

Taking the above mentioned facts into consideration, three types of equations are compared with each other in the present paper: the linear long wave theory, the shallow-water theory with bottom friction, and the Peregrine equation. For the sake of simplicity, one-dimensional computations were carried out along the line a-a' in Figure 3, drawn through the neighborhood of the center of the source area of the Meiji Great Sanriku tsunami.

Figure 4 compares the tsunami profiles computed with the three methods in the sea deeper than 500 m at time intervals of 100 seconds. The linear and shallow-water equations were computed using an explicit scheme, the staggered leap-frog scheme, while the Peregrine equation was computed using an implicit scheme. In order to suppress numerical errors a spatial grid 1.35

km wide was used, which was smaller than the usual size for 3 km to 5 km. The selection of this small grid size was made so that more than 20 grid points in one wave length would be secured throughout the computation area, so that no numerical decay of the major wave component of the tsunami would take place before its arrival at the coast (Shuto et al., 1986). Figure 4 shows no differences between the tsunami profiles by the linear theory (dashed line) and those by the shallow-water theory (dotted line). The Peregrine equation gives only slightly different results (solid line) owing to the dispersion effect which reduces the major wave crest and generates a wave train behind it. However, the difference in height of the major crest is negligibly small from the practical point of view for tsunami forecasting. Therefore it is concluded that the linear theory gives satisfactory tsunami prediction results in a sea deeper than 500 m.
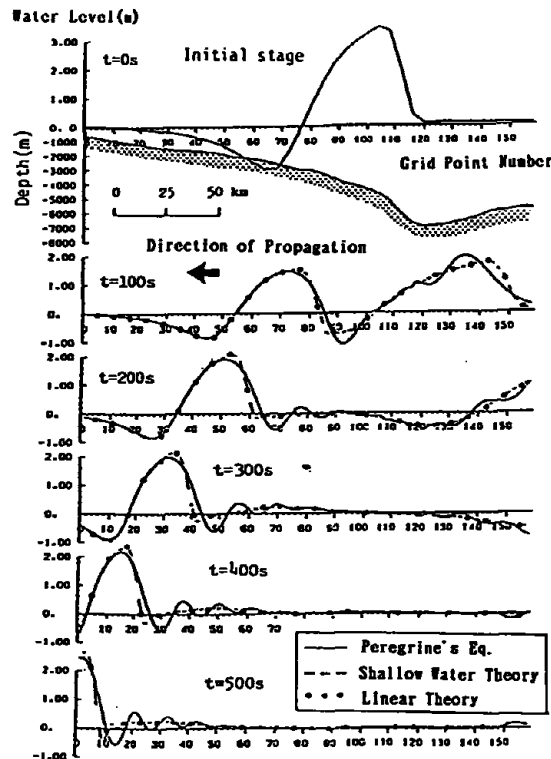
Figure 4.   Comparison of calculated wave profiles
in seas deeper than 500 m.

In a sea shallower than 500 m, the grid length should be made finer since the wave length becomes shorter. Results computed using a grid length of 0.2 km are shown in Figure 5. The linear theory (dashed line) gives the same result as the shallow-water theory (dotted line). The Peregrine equation shows a similar tendency to the results determined in a sea deeper than 500 m.

138
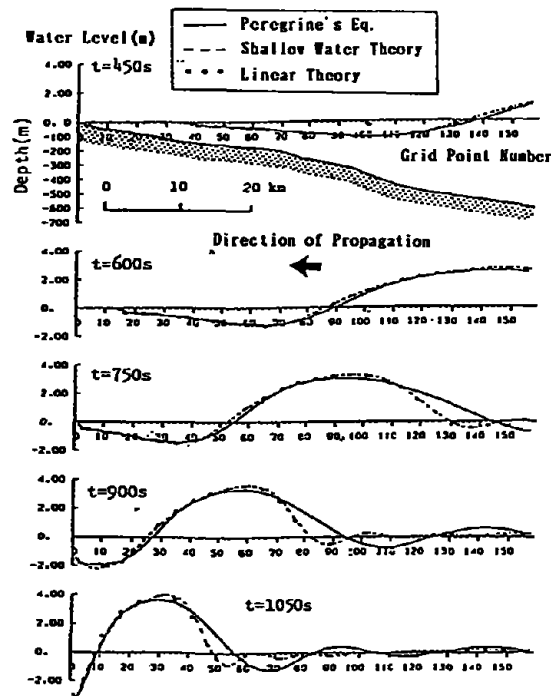
Figure 5. Comparison of calculated wave profiles in seas shallower than 500 m.

Figure 6 shows spatial distributions of the highest water levels. The x-coordinate is the travel distance from the generating area: the point 0 km is the initial position of the major wave crest, the point 100 km corresponds to the boundary between the deep and shallow regions, and 150 km is located at the shoreline. A sudden drop of the maximum water level from 3.5 m to 1.2 m around the 30 km point is caused by the splitting of the major crest into two waves, one propagating shoreward and the other seaward. Beyond the 30 km point, the tsunami height increases owing to shoaling. There are no significant differences between the linear and shallow-water theories, except in the very shallow regions where the truncation error, caused by the convection term, introduces numerical dissipation in to the shallow-water theory. The Peregrine equation gives a slightly lower tsunami height, because the dissipation effect acts to split the major wave of the initial profile, but does not yet increase the height by the effect of water surface curvature which is dominant in the very shallow region.

Table 1 gives the resulting CPU time for the three methods. The shallow-water and Peregrine equations require 1.6 and 17 times longer time respectively than the linear theory.

The above results showing little difference among tsunami heights in spite of large differences in the CPU time indicate that the linear long wave theory is best for tsunami numerical forecasting from the point of view of accuracy and computation speed, not only in a deep sea but also in a shallow sea.

139
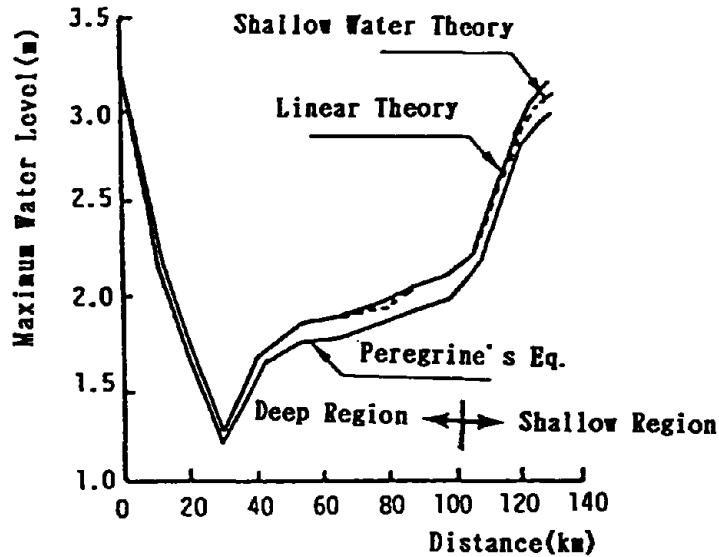
Figure 6. Comparison of calculated wave heights.

Table 1. Required CPU time for the one-dimensional problem.

Governing Equation	Grid Size	Time Interval	CPU Ratio
Linear Theory	1.35km	2.5s	1.0
Shallow Water Theory			1.6
Peregrine's Equation			17.1

(3) Spatial grid lengths

(i) Deep region

Supported by the results in the preceding section, the linear long wave theory was used to examine the effects of the grid length on accuracy and rapidity for the case of a two-dimensional problem. Three grid lengths of 2.7, 5.4 and 10.8 km were selected, by taking into consideration that grid lengths on the order of 5 km have often been used in tsunami simulations.

Figure 7 is a three dimensional example of the results using a grid of 2.7 km at 6-minute intervals. The left figure is the initial profile of the Meiji Great Sanriku tsunami, having a maximum water surface elevation of 4.0 m. The major and minor axes of the tsunami source are approximately 200 km and 50 km long.

140
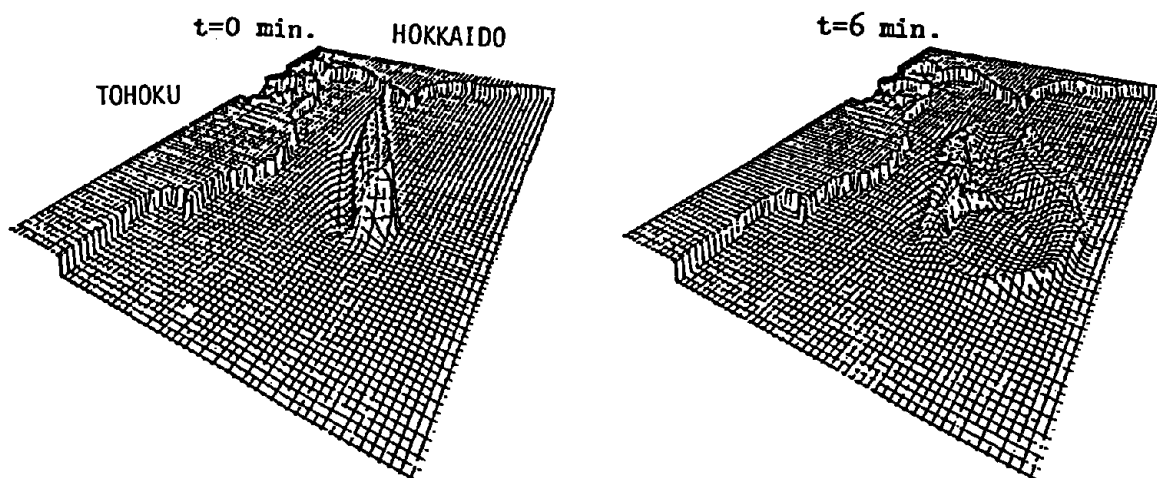
Figure 7. Three dimensional expressions of the 1896 Meiji Great Sanriku tsunami computed using a 2.7 km grid.

Figure 8 compares the time histories of water surface elevations for the three grid lengths at 6 points along the 100 m water depth contour. The numerals indicate the maximum water surface elevations obtained using the 2.7 km grid. Among three grid lengths, the shorter grid lengths yield the higher maximum water surface elevations and the shorter wave period behind the major wave crest. This is an expected result of numerical dispersion which is inherent in the leap-frog scheme of the present simulation. The reason why a water depth of 1,000 m was selected for comparison is as follows. When the computer capacity is not large enough compared to the number of grid points and the time required for a full computation, it is the normal technique to divide the computation into an offshore and an inshore computation. In the offshore computation the entire region is covered with a net of coarse grids, whereas in the inshore computation a net of fine grids was used to allow observation of more limited areas, including areas of special concern. At the inshore computation's open boundary which is usually set in the neighborhood of the 1,000 m contour, the outputs of the offshore computation are used as the boundary condition.

Table 2 summarizes the resulting CPU times and the maximum water surface elevations when a grid length of 5.4 km was used as the standard. The CPU times for the 2.7, 5.4, and 10.8 km grids are in the ratio of 7 : 1 : 1/7, while the maximum water surface elevations form the ratio of 1.06 : 1 : 0.82. If the grid length is reduced from 5.4 km to 2.7 km, the accuracy is improved by 6% at a cost of increasing the CPU time by a factor of seven. If the CPU time is reduced by seven times using a grid length of 10.4 km, the largest error becomes 18%. This error is not considered acceptable, both from the standpoint of numerical forecasting, and also from the present practice of tsunami hindcasting.

141
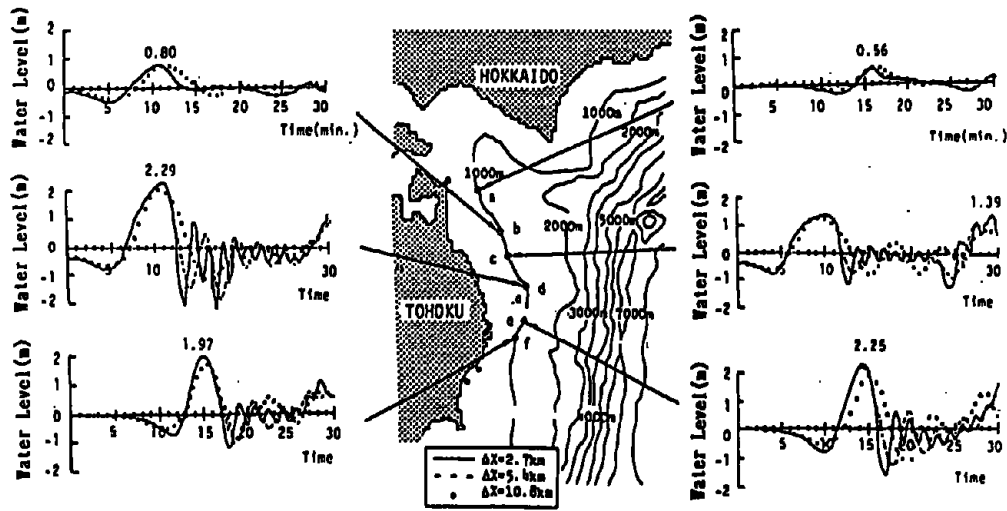
Figure 8.   Comparison of time histories of water surface elevations for three different grid lengths in a water depth of 1,000 m.

Table 2.   Comparison of the CPU time and the maximum water surface elevation in deep seas, using a 5.4 km grid as a standard.

Grid Size		2. 7km	5. 4km	10. 8km
Time Interval		10s		20s
Number of Grids		46. 800	11. 700	2. 925
Reproduction Time		30 min.		
CPU Ratio		7. 39	1. 0	0. 14
Ratio of the Maximum Water Level	a	1. 06	1. 00	1. 04
	b	1. 01	1. 00	0. 96
	c	1. 06	1. 00	0. 99
	d	1. 06	1. 00	0. 93
	e	1. 06	1. 00	0. 84
	f	0. 98	1. 00	0. 82

Therefore the largest grid length was set equal to 5.4 km in the region A of Figure 3. Closer to the shore, the grid length was further reduced to 1.8 km for the regions B1 - B4, and to 0.6 km for the regions C1 - C5, to prevent a deterioration in final results.

142

(ii) <u>Shallow Region</u>

The present tsunami simulation proceeded continuously from the deep region to the shallow region and then to land, i.e., from coarser grids in the regions A, B and C to even finer grids in the region D. Three grid lengths of 0.2, 0.3 and 0.6 km were selected in the region D for comparison.

The three figures in Figure 9(a) show the coastline expressed with the three different grid lengths. For the 0.2 km grid, contours of the sea bottom and the sub-regions D_1 to D_{22} are also shown.

Figure 9(b) compares the computed maximum water surface elevations in the case of 0.2 km grid lengths with the observed records. At a location where only one recorded data point was available, the data are shown with a circle. At a location where several different values were obtained, a bar connecting the upper and lower values is drawn. In the area north of Miyako, located near the center of the considered coastline, the computed results are smaller than the observed data, whereas the computation yields larger heights than the observation south of Miyako. On the average, however, the computed results agree fairly well with the observed data.

Figure 9(c) shows relative percentage differences of the results for $\Delta X = 0.3$ km and $\Delta X = 0.6$ km, when compared with the results for $\Delta X = 0.2$ km. At places where the computed tsunami height was large, the results for the 0.3 km and 0.6 km grids were often lower than the results for the 0.2 km grid. This is partly due to the deterioration caused by expressing the topography using coarse grids, and partly due to the spatial grid averaging effects for the tsunami wave characteristics. A computed water surface elevation at a grid point means that the value is spatially averaged in the mesh represented by this grid point. When a coarse grid length is used, the detailed distribution of water surface elevation disappears owing to the averaging effect. Therefore, in order to predict the detailed local behavior of the tsunami, a fine grid length is preferable.

Table 3 shows the grid length, the time interval, the total number of grid points, and the ratio of the CPU time required to reproduce the 90-minute time history of the Meiji Great Sanriku tsunami. If the grid length is reduced by half, the CPU time increases by a factor of two.

(4) <u>Shoreline boundary conditions</u>

Throughout the preceding discussions, the actual situations along the shoreline were neglected under the assumption of perfect reflection at the land boundary, i.e., no overtopping of breakwaters and sea walls, and no run-up or inundation on land. If a sea wall is overtopped by a tsunami, the perfect reflection assumption no longer holds true and only partial reflection occurs. If the inundation on land is considered, the water surface elevation may become lower than that obtained using the assumption that vertical, infinitely high sea walls completely prevent inundation, because water can then spread over a wider area. In addition, the volume of inundating water depends upon the predicted wave profiles and current velocities which are different for different theories. The method considered best in Section 3.3 may yield inaccurate results near the shoreline and on land because it uses the linear theory with a 0.2 km grid.

143
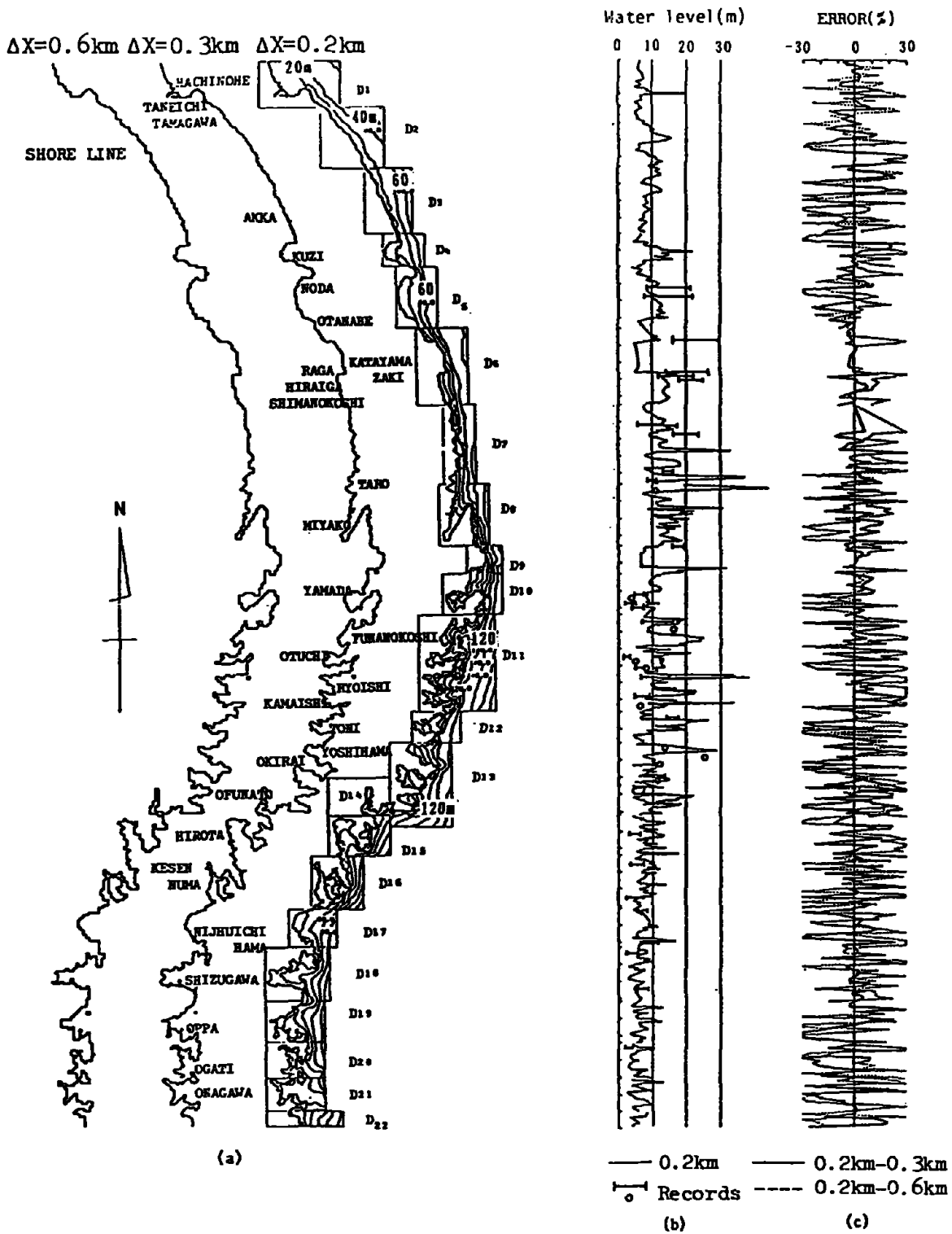
Figure 9(a) Coastal line digitized with different grids. (b) Comparison of the measured
data with the computed results using a 0.2 km grid. (c) Comparison of the computed
results using the 0.2 km grid as a standard.

Table 3.   Comparison of the CPU time in shallow seas, using a
                0.2 km grid as a standard.

Grid Size	0.2km	0.3km	0.6km
Time Interval	3.0 s		
Number of Girds in Region D	91.120	40.496	10.124
Reproduction Time	90 min.		
CPU Ratio	1.0	0.65	0.38

Effects of the land boundary conditions, as well as the selection of equations, must be examined in detail. The area to be examined is Miyako Bay which is near the center of the Sanriku coast. This bay is typical of the bays located on the Ria-type coast. At the middle of its northern shore there is a long breakwater extending almost to the line of the central axis of the bay. Additionally, sea walls with crest heights of 5 to 6 m were built along the entire bay shoreline.

In order to examine the accuracy of the linear theory using a 0.2 km grid, true values are needed for comparison. Recorded data are not satisfactory for this purpose, because they are neither sufficient in number, nor do they reflect the effects of coastal structures recently built. Two numerical simulations were therefore carried out, using the shallow-water theory with a fine 0.05 km grid, to provide the "true values". One simulation considered the case with no structures, i.e., similar to the bay and coast when the Meiji Great Sanriku tsunami hit in 1986. The computed results were compared with the recorded data and the simulation method was confirmed to be reliable. The second simulation was carried out for the case with the existing 1980 sea walls and breakwaters. Because many grid points were included in the two computations, each computation was divided into an offshore and an inshore computation. The offshore computations were done as discussed in Section 3.3, and the inshore computations were made in the areas shallower than 100 m. The tidal level was set equal to Tokyo Post (T.P.) 0 m, being nearly equal to the mean sea water level.

Figure 10 compares time histories of water surface elevations obtained with three methods at six points in Miyako Bay. Solid lines are the shallow-water theory with the existing sea walls and breakwater (1980), dashed lines are the shallow-water theory without any structures (1896), and dotted lines are the linear theory with perfect reflection. The attached numerals are the maximum water surface elevations obtained by the shallow-water theory. As far as the maximum water surface elevation is concerned, there are only slight differences in the three methods, although the wave profiles do show some differences. Thus the linear theory, using perfect reflection and 0.2 km grid, gives satisfactory forecasting estimates.

145
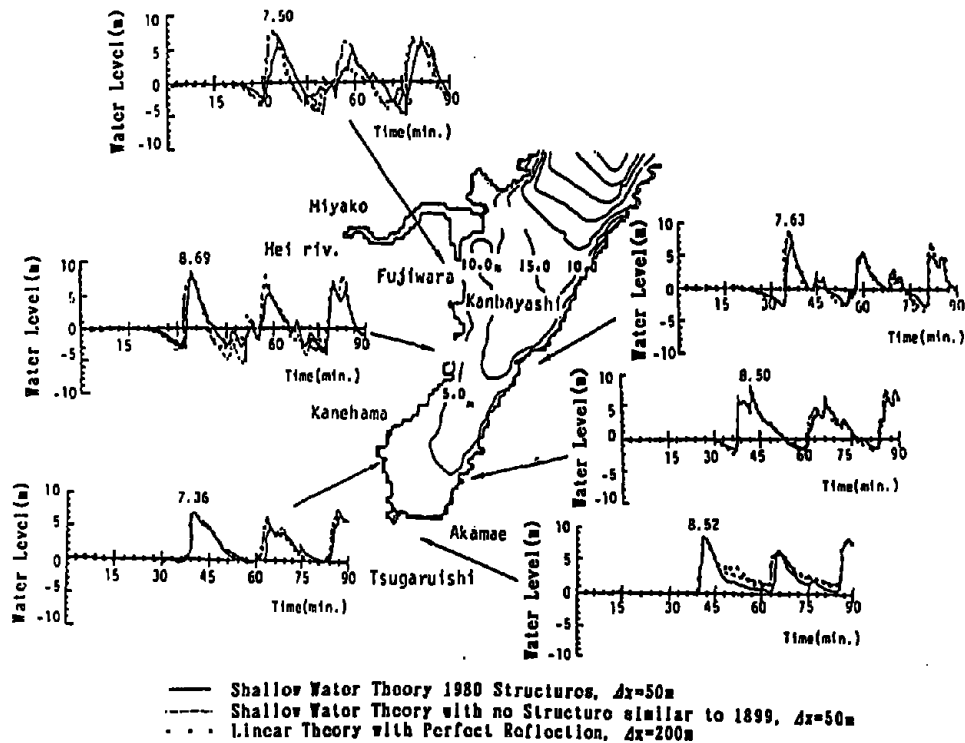
Figure 10. Comparison of water surface elevations in Miyako Bay.

Figure 11 shows more clearly the resulting differences in the three methods. The contours of water surface elevation are shown by solid lines (the attached numerals show values in m), and also shown are the water current velocity vectors at the time 40 minutes after the earthquake. Notice in Figure 11(a) that a large swirling motion is formed around the breakwater. Even though the tsunami height exceeds the existing sea walls, the inundated area is narrower than that in Figure 11(b). The inundated area of Figure 11(b) is the largest among the three methods, and velocity patterns and strengths seems to be different from Figure 11(a), especially in the inundated area and around the structures. This difference, however, occurs only locally, and it does not affect other parts of the bay, whereas the water surface elevations do not show any difference. Velocity patterns and strengths in Figure 11(c) are noticeably different from Figure 11(a) which is considered to be "true value" results, whereas the water surface elevationa show negligible differences.

It is concluded that the linear long wave theory, using perfect reflection and a 0.2 km grid, can predict with negligible errors the most important property of the tsunami forecasting, ie., the maximum water surface elevation.

(5) The solution of the "RAD optimum problem"

The best combination of equations, boundary conditions, and grid lengths are summarized as follows.

146
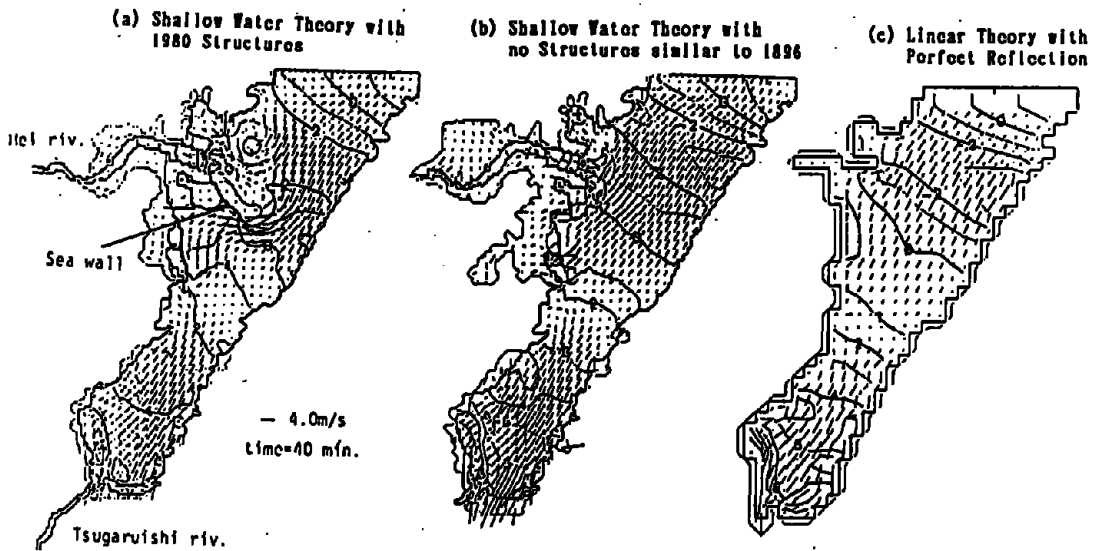
Figure 11. Differences due to boundary conditions and grid lengths.

The following linear long wave equations are used.

$$\frac{\partial \eta}{\partial t} + \frac{\partial M}{\partial x} + \frac{\partial N}{\partial y} = 0$$

$$\frac{\partial M}{\partial t} + gh\, \frac{\partial \eta}{\partial x} = 0 \tag{1}$$

$$\frac{\partial N}{\partial t} + gh\, \frac{\partial \eta}{\partial y} = 0$$

where η is the water surface elevation, h is the still water depth, M and N are discharges per unit width in the x- and y-directions, t is time, and g is the gravitational acceleration.

The equations are discretized using the staggered leap-frog scheme. The area in the present study is divided into regions of four classes as shown in Figure 3. The region A is the deep sea where 5.4 km grids are used. In the shallow sea a finer grid is used, i.e., 1.8 km grids in the region B (4 sub-regions), 0.6 km grids in the region C (5 sub-regions), and 0.2 km grids in the region D (22 sub-regions).

The shoreline boundary condition assumes perfect reflection: that is, vertical sea walls are assumed to completely stop inundation. No structures such as breakwaters are taken into the simulation.

147

Application example

(1) Test tsunami case

The 1968 Tokachi-oki earthquake tsunami was selected as a test case. This tsunami was nearly completely stopped by sea walls, and records concerning data about this tsunami are abundant and accurate enough to be used for comparison.

Fault parameters of the earthquake were given by Kanamori (1971) and by Izutani and Hirasawa (1987), and are summarized in Table 4. The former used more accurate information such as the aftershock area, while the latter used their own method which was utilized in the present study.

Table 4. Fault parameters for the 1968 Tokachi-oki earthquake.

	Length	Width	Dip Direction	Dip Angle	Slip Angle	Amount of Slip
Izutani&Hirasawa	190km	95km	-35°	20°	148°	3.3m
Kanamori	150km	100km	-24°	20°	142°	4.1m

(2) Prediction accuracy

The Izutani-Hirasawa method determines fault parameters immediately after strong seismic motion is recorded, but some estimation errors do occur. These errors affect the initial profile of a tsunami and their effects propagate with the computed tsunami. Thus they may deteriorate the accuracy of the final results.

By using the Izutani-Hirasawa method to determine fault parameters, and by computing the initial profile with the Mansinha-Smylie method, the present method is applied to evaluate whether it can produce reliable information used to forecast tsunamis. Figure 12 shows the computed result of tsunami height along the central part of the Sanriku coast. Figure 12(a) shows the computation sub-regions and the maximum water surface elevation contours. Figure 12(b) shows the maximum water surface elevations along the shoreline. The bars indicate measured tsunami trace heights and show maximum and minimum values.

If the accuracy is measured in terms of Aida's K (geometric mean of the ratio of the measured to computed height) and κ (geometric variance) values, then in this case K = 1.37 and κ =1.67. These values are not as good as those of K = 1.31 and κ = 1.37 obtained by Aida (1978), who made computations using the fault parameters of Kanamori (1971). However, because Aida used measured data at only six points, as compared with the present study's 84 points, the present results are considered acceptable. Additionally because the K value ranges form 0.8 to 1.2 in a usual tsunami hindcasting in which the initial tsunami profile is adjusted by a trial-and-error method to yield the best fit, the value K = 1.37 is practically acceptable.

WATER LEVEL (m)

0 2 4 6 8 10

Taro

Miyako

Ishihama

Yamada

Funakoshi

Murohama

Kamaishi

Hongo

Sanriku

⊢⟶⊣ : Records
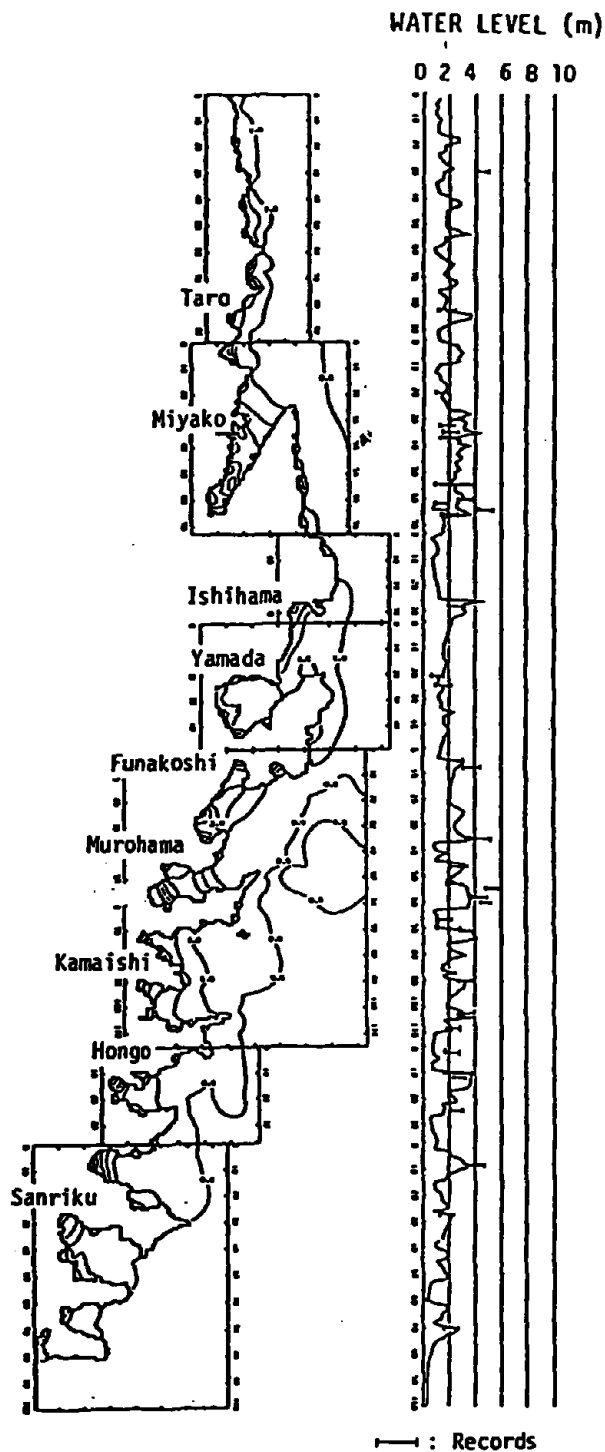
Figure 12. Comparison between the measured data
and the predicted results for the case of the 1968
Tokachi-oki earthquake tsunami.

149

The times required to determine fault parameters are shown in Table 5, obtained in the Observation Center for Earthquake Prediction, Faculty of Science, Tohoku University. A total of 754 seconds are required. However, if a super computer is used, this time can be shortened to less than one tenth this value.

Table 5. CPU item required for the determination of fault parameters.

	Required CPU	Computer Type
Epicenter, Magnitude	720s	OKI 50/60 (0.4MIPS)
Strong Motion Duration	30s	HITAC M240H (3.3MIPS)
Fault Parameters	4s	HITAC M280H (15MIPS)

The CPU time necessary for the present simulation is given in Table 6. Using a general purpose computer, e.g., NEC ACOS 1000 (9.2 MFLOPS), the computation is performed with a virtual memory system that requires input output operations in and from external memories. If a super computer is used, e.g., NEC SX-1 (750 MFLOPS) that has excellent vector operation functions, no time is lost when performing input-output operations, and only 1 minute is required to reproduce 90 minutes of real time tsunami.

Table 6. Comparison of the CPU time of the tsunami simulation.

Computer Type	ACOS1000	SX-1	CPU Ratio
Data Input and Initialization	9.3 s	0.36 s	25.83
Sea Bottom Deformation	32.4 s	7.25 s	4.47
Tsunami Simulation	1559.0s	57.22 s	27.24

Evaluation of future tsunami warning scheme

Figure 13 shows the required item to issue a tsunami warning, using a super computer to estimate fault parameters and to simulate the tsunami.

It is assumed that a network of seismographs to gather the data is well distributed with the distance from an epicenter to the seismic station in the range of about 200 km at the nearest to about 400 km at the farthest.
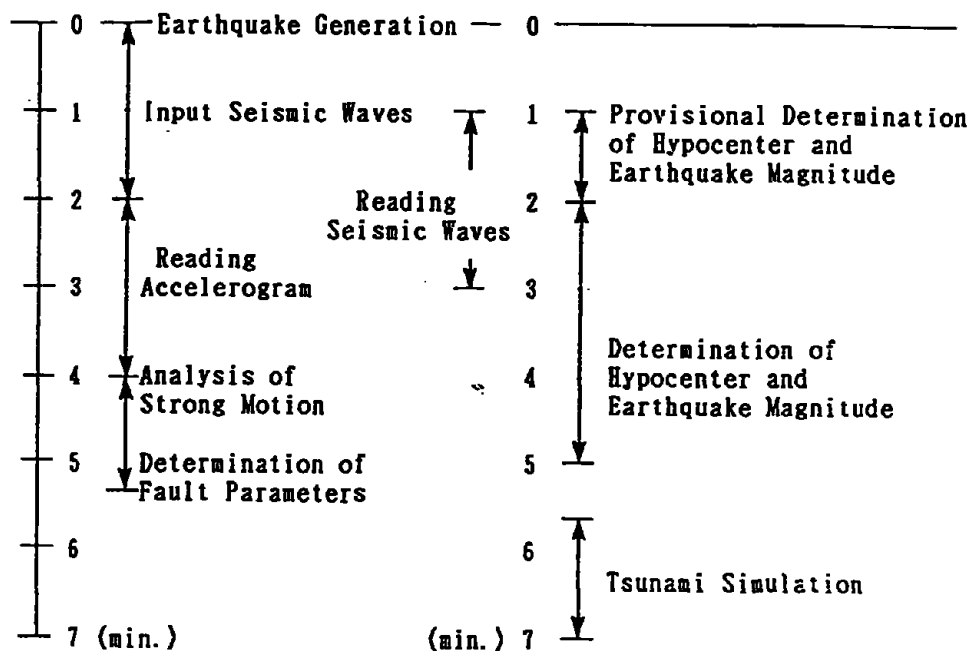
Figure 13. Event, procedure, and required time to perform tsunami forecasting
and warning using the present method.

The travel times of P- and S-waves to the nearest station are 33 sec and 55 sec, respectively, and to the farthest, 60 sec and 100 sec. If the fault length is 200 km, then the corresponding rupture time is about 100 sec, and therefore 3 to 4 minutes are required for data acquisition. Fault parameters are then calculated within 1.5 min., with the tsunami simulation being finished in another 1.5 min. Thus ideally, accurate and detailed results can be completed in just 7 minutes.

Now assuming that 10 minutes are needed for information transmission, 8 to 13 minutes are still available for coastal residents to evacuate. The above estimates use a 25 to 30 minute standard arrival time for tsunamis hitting the Sanriku coast, based on the fact that the source area for a major tsunami is located along the Japan Trench.

Concluding remarks

Accuracy and speed of the tsunami numerical forecasting are examined for tsunamis in the Sanriku coast. The present method is a feasible means of quantitive tsunami forecasting if the maximum tsunami heights are the required information. In order to use this method in practical forecasting, however, there are several problems to be examined and solved. For example, the present observation network of seismographs should be improved to be suitable for the determination of tsunami sources.

151

References

Abe, K., 1975. Reliable estimation of the seismic moment of large earthquakes. *J. Phys. Earth*, 23, pp.381-390.

Aida, I., 1977. Simulations of large tsunamis occurring in the past off the coast of the Sanriku district. *Bull. Earthq. Res. Inst.*, 52, pp.72-101 (in Japanese).

Aida, I., 1978. Reliability of a tsunami source model derived from fault parameters. *J. Phys. Earth*, 26, pp.57-73.

Aida, I., 1984. A source model of the tsunami accompanying the 1983 Nihonkai-Chubu earthquake. *Bull. Earthq. Res. Inst.*, 59, pp.93-104 (in Japanese).

Goto, C. and Shuto, N., 1983. Numerical simulation of tsunami propagations and run-up. *Tsunamis, Their Science and Engineering*, edited by K. Iida and T. Iwasaki, Terrapub/Reidel, pp.439-451.

Ismamura, F. and Goto, C., 1988. Truncation error in numerical tsunami simulation by the finite difference method. *Coastal Engineering in Japan*, 31, No.2, pp.245-263.

Izutani, Y. and Hirasawa, T., 1987a. Rapid estimation of fault parameters for near-field tsunami warning. *Natural Disaster Science*, 9, No.1, pp.99-113.

Izutani, Y. and Hirasawa, T., 1987b. Use of strong motion duration for rapid evaluation of fault parameters. *J. Phys. Earth*, 35, pp.171-190.

Kanamori, H., 1971. Focal mechanism of the Tokachi-oki earthquake of May 16. *Tectonophysics*, 122, pp.1-13.

Kanamori, H. and Given, J.W., 1983. Use of long-period seismic waves for rapid evaluation of tsunami potential of large earthquakes. *Tsunamis, Their Science and Engineering*, edited by K. Iida and T. Iwasake, Terrapub/reidel, pp.37-49.

Mansinha, L. and Smylie, D.E., 1971. The displacement fields of inclined faults. *Bull. Seism. Soc. Amer.*, 61, No.5, pp.1433-1440.

Okal, E.A. and Talandier, J., 1986. T-wave duration, magnitudes and seismic moment of an earthquake - Application to tsunami warning. *J. Phys. Earth*, 34, pp.19-42.

Shuto, N. *et al.*, 1986. A study of numerical techniques on the tsunami propagation and run up. *Science of Tsunami Hazards*, 4, No.2, pp.111-124.

Discussion

Question: Basically a comparison has been made of the effects on the calculation of grid length and other things. What is the sensitivity of the results to the estimate of the source function? How important is that? Also if that turns out to be a major source of error with the existing seismological techniques, since linear theory is used, is it possible to incorporate tide gage data or pressure measurements to modify the linear theory results by several multiples?

Response: In reply to the second question that is a very good idea because there are several different kinds of mechanisms of tsunami generation. As an example, in the May 1983 Sea of Japan tsunami case, the half-state was very weak, but the tsunami was very high. In order to make corrections to the computed results rapid information on the in situ measured data is needed. The reply to the first question is that the error in the estimation of the source mechanism is the most crucial error, which very greatly affects the final results. Most important is the relation of the orientation of a fault with the major contour line of the topography. It determines the duration of the major energy transmission. The tide does not have such a large effect.

NUMERICAL AND HYDRAULIC MODELING OF FLOODING

Charles L. Mader
Joint Institute for Marine and Atmospheric Research
University of Hawaii
Honolulu, HI, USA

Abstract

Tsunami waves and their interaction with a marina were numerically modeled using the SWAN code which solves the shallow water long wave equations. The calculated results agree with hydraulic model observations. The calculated degree of inundation in the marina depends upon the tsunami period with greater flooding occurring for longer wave length tsunamis.

Tsunami Hazard Evaluation

The magnitude of the tsunami hazard at any land site depends on the extent of inundation of the land by tsunamis at the site, expected water depths and velocities within the inundation zone, and the exposure of persons and property within the potential inundation zone. There is no definite upper limit to the power of tsunamis approaching a coastal site. Tsunami hazard must be expressed in terms of expected average recurrence intervals or frequencies. What is expected in the future can be judged only on the basis of what has occurred in the past. The power of tsunamis that have approached the coast can be estimated from the extent of inundation and the runup heights on land. All estimates of tsunami hazard are site-specific and based on runup heights of historic tsunamis.

In the last decade procedures have been developed and applied for flood insurance purposes by the U. S. Army Corps of Engineers[1,2]. These procedures built upon historical wave height data compiled at the University of Hawaii and utilized a numerical model to synthesize the maximum tsunami wave crest as a function of frequency of occurence. This information was used to develop the inundation maps as part of a National flood insurance program.

The resulting highly synthesized wave heights from the flood insurance program with additional historical inputs provide reasonably authentic worst-case tsunami wave

155

heights as a function of frequency of occurence. Usually the wave heights fall within the envelope of the 1946, 1957 and 1960 tsunami events. To determine the tsunami evacuation zones the wave is then "runup" on the shore at selected points using a one-dimensional model described by Bretschneider and Wybro in reference 3 and Cox in reference 4. Critical factors in the inundation calculation include accurate topographic information and surface roughness. A contour line is drawn between points thus generated, representing the maximum probable inundation. Where possible it is compared with historical inundation information, flood insurance map lines and adjusted if warranted.

The modeled marina was to have been in a region with well documented topography on the South Kohala Coast on the Island of Hawaii. For the marina site, the 200-year tsunami wave height 61 meters inland was estimated by Curtis and Smaalders[1] to be 3 meters using the techniques described. This corresponds to a wave height of about 2.6 meters above mean sea level at the shoreline and a wave height of 2.47 meters in 9 meters of water. This results in a wave amplitude (peak to trough) of 4.9 meters which is expected to occur once in every 200 years or has a 0.5 percent chance of being equalled or exceeded this year or any other year. Such a wave will result in 3 meter runup at the site using the standard one-dimensional runup model for a surface roughness Manning "n" of 0.0325.

The surface roughness for typical Hawaiian terrain is described in reference 3 and 5. A Manning "n" of 0.0325 corresponds to a roughness characteristic of lava and grass with isolated trees. An "n" of 0.04 corresponds to many trees, boulders and high grass. The maximum inundation changes by only 9 meters out of 120 over this range of the roughness parameter in the site region.

Roughness in the numerical model in the SWAN code is described using the De Chezy friction model. The De Chezy coefficient depends not only on the bed roughness but also on the depth. The De Chezy coefficient is related to the Manning "n" by the depth to the 1/6 power. While not directly comparable, for the depths in the site region a De Chezy friction constant of 50 results in about the same friction effect as a Manning "n" in the 0.03-0.04 range.

The Numerical Model

The tsunami waves and their interaction with the marina topography were numerically modeled using the SWAN code which solves the shallow water long wave equations. It is described in detail in the monograph *Numerical Modeling of Water Waves* [6].

The long wave equations solved by the *SWAN* code are

$$\frac{\partial U_x}{\partial t} + U_x \frac{\partial U_x}{\partial x} + U_y \frac{\partial U_x}{\partial y} + g \frac{\partial H}{\partial x}$$

$$= FU_y + F^{(x)} - g \frac{U_x (U_x^2 + U_y^2)^{1/2}}{C^2 (D + H - R)} \, ,$$

$$\frac{\partial U_y}{\partial t} + U_x \frac{\partial U_y}{\partial x} + U_y \frac{\partial U_y}{\partial y} + g \frac{\partial H}{\partial y}$$

$$= -FU_x + F^{(y)} - g \frac{U_y (U_x^2 + U_y^2)^{1/2}}{C^2 (D + H - R)} \, ,$$

and

$$\frac{\partial H}{\partial t} + \frac{\partial (D + H - R)U_x}{\partial x} + \frac{\partial (D + H - R)U_y}{\partial y} - \frac{\partial R}{\partial t} = 0 \, ,$$

where

U_x	= velocity in x direction (i index)
U_y	= velocity in y direction (j index)
g	= gravitational acceleration
t	= time
H	= wave height above mean water level
R	= bottom motion
F	= Coriolis parameter
C	= coefficient of DeChezy for bottom stress
$F^{(x)}, F^{(y)}$	= forcing functions of wind stress and barometric pressure in x and y direction
D	= depth.

Flooding was described using positive values for depths below normal water level and negative values for elevations above normal water level. Only positive values of the $(D + H)$ terms in the above equations were permitted. This method results in both flooding and receding surfaces being described by the *SWAN* code.

As described in the monograph, the *SWAN* code has been used to study the interaction of tsunami waves with continental slopes, shelves, bays and harbors.

The *SWAN* code has been used to study the interaction of tsunami waves with continental slopes and shelves, as described in reference 7. Comparison with two-dimensional Navier-Stokes calculations of the same problems showed similar results, except for short wavelength tsunamis.

The *SWAN* code was used to model the effects of tides on the Musi-Upang estuaries, South Sumatra, Indonesia, by Safwan Hadi.[8] The computed tide and water discharge were in good agreement with experimental data.

The *SWAN* code was used to model the large waves that were observed to occur inside Waianae harbor under high surf conditions in reference 9. These waves have broken moorings of boats and sent waves up the boat-loading ramps into the parking lot. The numerical model was able to reproduce actual wave measurements. The *SWAN* code was used to evaluate various proposals for decreasing the amplitude of the waves inside the harbor. From the calculated results, it was determined that a significant decrease of the waves inside the harbor could be achieved by decreasing the harbor entrance depth. Engineering companies used these results to support their recommendations for improving the design of the harbor.

The effect of the shape of a harbor cut through a reef on mitigating waves from the deep ocean was studied using the *SWAN* code in reference 10. It was concluded that a significant amount of the wave energy is dissipated over the reef regardless of the design of the harbor. The reef decreased the wave height by a factor of 3. The wave height at the shore can be further decreased by another factor of 2 by a "V"-shaped or parabolic bottom design.

Other examples of applications of the *SWAN* code are presented in reference 11. They include the wave motion resulting from tsunami waves interacting with a circular and triangular island surrounded by a 1/15 continental slope and from surface deformations in the ocean surface near the island. The effects of a surface deformation in the Sea of Japan similar to that of the May 1983 tsunami was modeled. The interaction of a tsunami wave with Hilo Bay was described.

The *SWAN* code was used to model the effect of wind and tsunami waves on

Maunalua Bay, Oahu as described in reference 12. The model reproduced the observed wave behavior at various locations in the bay for a 1.2 meter south swell with a 15 second period. A study was performed of the effect of an enlarged and deeper channel. The code was used to model the interaction with Maunalua Bay of waves outside the bay having periods of 15, 30, 60 seconds and a tsunami wave with a 15 minute period. Wave amplitudes of 0.3 to 1.8 meters were considered with tides from mean lower low water to high tide (a 0.55 meter range). The same wave profiles within 10% were calculated at various locations studied throughout the bay for the current and the proposed bay with a larger and deeper entrance channel. The small difference between the current and the proposed bay varied with the wave period. The largest difference was found for the 30 second wave. The 15 minute period tsunami wave doubled in amplitude as it passed over the bay and was highest at high tide. Severe flooding in the regions near the shore line was predicted. The tsunami effects were unrelated to channel configuration. The calculated wave behavior at any location in the bay was a strong function of the entire bay with a complicated and time varying pattern of wave reflections and interactions.

The interaction of a 200 year tsunami wave with a site of well documented topography on the South Kohala Coast of the Island of Hawaii was described in reference 13. The tsunami wave was calculated to flood the land to the 3 meter level and inundate the land between 90 and 120 meters from the shoreline. These results agree with the results obtained using the procedures developed and applied for flood insurance purposes by the U. S. Army Corps of Engineers and the recent JIMAR study at the University of Hawaii of tsunami evacuation zones for the region [1].

Application of the Numerical Model

The *SWAN* code was used to model the interaction with the marina topography shown in Figure 1 of waves having 30 second, 15 minute and 30 minute periods. The waves were directed parallel to the shoreline and to the marina entrance for maximum effect. The tsunami wave amplitude (peak to trough) in 9 meters of water was 4.9 meters which is expected to occur once in every 200 years or has a 0.5 percent chance of being equalled or exceeded this year or any other year. Such a wave will result in 2.4 to 3 meter inundation at shore near the marina. The effect of roughness of the terrain on the flooding was described using a De Chezy coefficient of 50 which is equivalent to the Manning "n" of 0.0325 to 0.04 used in the JIMAR and flood insurance programs. The effect of roughness is small.

The space resolution in the numerical model grid was 15.24 meters. The numerical calculations were performed at 0.5 second intervals. The calculations were performed on an IBM PS/2 Model 80 computer using a special version of the *SWAN* code that

includes flooding and MCC developed graphics. A calculation required 1 to 6 hours of computer time.

A physical scale model of the marina and foreshore area was built at the Hydro Research Science testing facility in Santa Clara, California and used to study the effect of 0.6 meter and 1.3 meter high, 12 hour period tide or storm surge waves and the effect of 1.3 meter high, 15 second period waves.[14] A comparision of the scale model and numerical results may be made using the following table. The station locations are shown in Figure 2.

Location	Physical Model	*SWAN* Calculation
No 2	0.82	0.79
No 3	0.30	0.33
No 4	0.06	0.09
No 7	0.09	0.09

The hydraulic and numerical models are in good agreement for the short period wind waves. The hydraulic model was also used to study the effect of tides and surges. The water level in the marina was almost equal to the imposed offshore height of the tide or surge. A tsunami wave may have a period between 10 and 30 minutes so the flooding resulting from a tsunami wave is expected to be between the small amount of flooding associated with short period wind waves and the maximum flooding associated with long period surges and tides.

The interaction of a 2.5 meter high (above MLLW at 9 meter depth) 15 and 30 minute period tsunami wave with the marina was numerically modeled. The picture contour plots of the topography used to describe marina are shown in Figure 1 and the line contour plots are shown in Figure 2. Figure 2 also shows the location of the marina stations used for the wave histories shown in Figure 5. The interaction of the 15 minute period tsunami with the marina topography is shown in Figures 3 and 4. The picture and line contour plots show the ocean flooding the land outside the marina to about 2.75 meters above MLLW and inundating the land some 90 meters from the shoreline. The presence of the marina does not significantly change the flooding along the coast. The wave histories at the various locations in the marina are shown in Figure 5 for the tsunami with a period of 15 minutes. Calculations were also performed for a 30 minute tsunami wave. A comparision of the maximum inundation at the various stations in the marina for a 15 and 30 minute tsunami may be made using the following table.

Location	15 min. Period	30 min. Period
No 1	3.0	3.3
No 2	3.0	3.0
No 3	1.8	2.3
No 4	1.6	2.0
No 5	1.7	2.1
No 6	1.6	2.0
No 7	1.6	1.9

The degree of inundation in the marina depends upon the period of the tsunami with greater inundation in the marina occurring for longer period tsunamis. A 15 minute tsunami results in marina inundations of 65 to 75% of the initial tsunami height and a 30 minute tsunami results in inundations of 75 to 95% of the initial tsunami height. Since the travel time from the entrance to the back of the marina is 2 to 3 minutes and a 15 minute period tsunami reaches its first maximum in 3.75 minutes and then starts to decay, the wave energy inside the marina is less for short period waves and increases as the wave period increases.

If the tsunami arrives at the same time as high tide, the maximum inundations would be 0.6 meter higher. A 200-year, 15 minute tsunami would result in a 2.75 meter level of inundation in the marina and a 30 minute tsunami would result in a 2.9 meter level of inundation.

The flooding and interaction with complicated geometries such as marinas by waves with periods from wind to tsunami waves can be numerically modeled.

REFERENCES

1. George D. Curtis and Mark Smaalders, "A Methodology for Developing Tsunami Evacuation Zones," Proceedings of International Tsunami Symposium 89 (1989).

2. James R. Houston, Robert D. Carver, Dennis G. Markle, "Tsunami Elevation Elevation Frequency of Occurrence for the Hawaiian Islands," Technical Report H-77-16, U. S. Army Engineer Waterways Experiment Station, Vicksburg, Miss. (1977).

3. C. L. Bretschneider and P. G. Wybro, "Tsunami Inundation Prediction," Proceedings of 15th Coastal Engineering Conference (1976).

4. Doak Cox, "Potential Tsunami Inundation Areas in Hawaii," Hawaii Institute of Geophysics Report No. 14 (1961).

5. C. L. Bretschneider, H. J. Krock, E. Nakazaki and F. M. Casciano, "Roughness of Typical Hawaiian Terrain for Tsunami Run Up Calculation," University of Hawaii Department of Ocean Engineering report (1988).

6. Charles L. Mader *Numerical Modeling of Water Waves,* University of California Press, Berkeley, California (1988).

7. Charles L. Mader, "Numerical Simulation of Tsunamis," Journal of Physical Oceanography, Vol. 4, pp. 74–82 (1974).

8. Safwan Hadi, "A Numerical Tidal Model of Musi-Upang Estuaries." A dissertation submitted to Oceanography Department of University of Hawaii (1985).

9. Charles L. Mader and Sharon Lukas, "Numerical Modeling of Waianae Harbor," Aha Hulikoa Hawaiian Winter Workshop Proceedings (January 1985).

10. Charles L. Mader, Martin Vitousek, and Sharon Lukas, "Numerical Modeling of Atoll Reef Harbors," Proceedings of the International Symposium on Natural and Man-Made Hazards, Rimouski (1986).

11. Charles L. Mader and Sharon Lukas, *"SWAN* – A Shallow Water, Long Wave Code: Applications to Tsunami Models," Joint Institute for Marine and Atmospheric Research report JIMAR 84-077 (1984).

12. "Oahu Intraisland Ferry System - Draft Environmental Impact Statement," State Department of Transportation, Harbors Division (1988).

13. Charles L. Mader "Modeling Tsunami Flooding," Proceedings of the Pacific Congress on Marine Science and Technology - PACON 90 (1990).

14. "Hydraulic Model Study of the Mauna Lani Marina" Hydro Research Science Inc., Santa Clara, CA. report 192-89 (1989).

Discussion

Comment: The model takes about four hours to run on a PC or a couple of minutes on a CRAY Computer.

Shoreline

Ocean

0

Shore

Bottom Topography

Shoreline

Shoreline
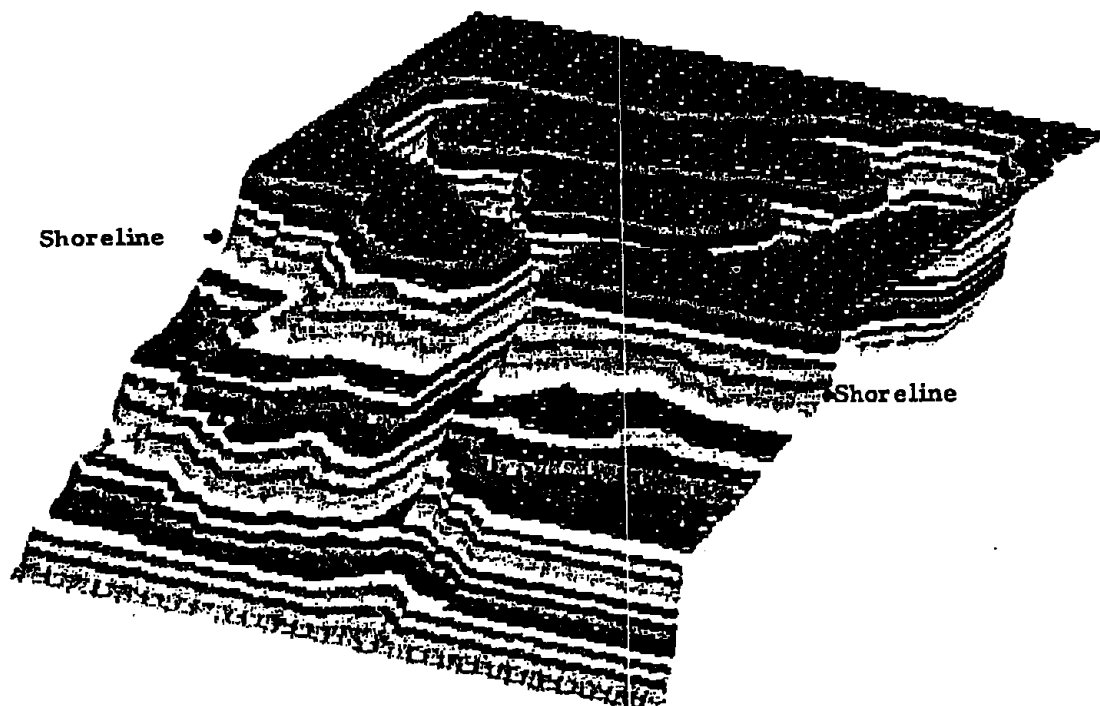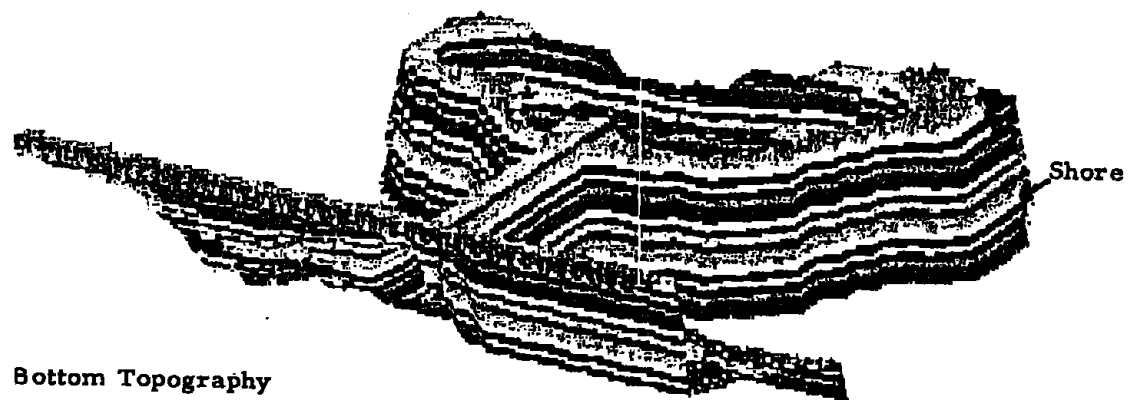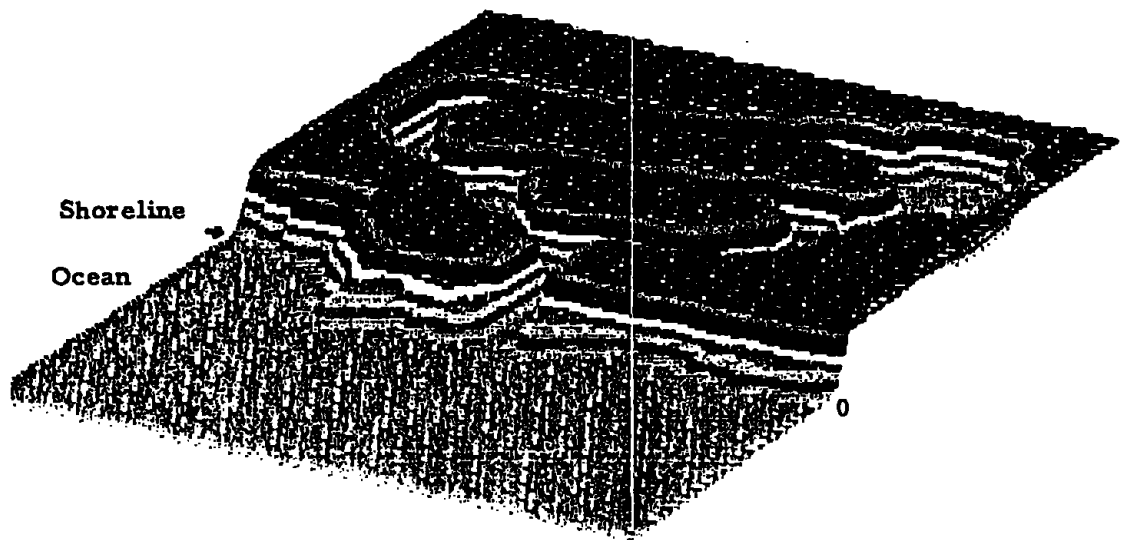
Fig. 1 The marina topography used in the numerical modeling. The contour interval is
0.36 meter.
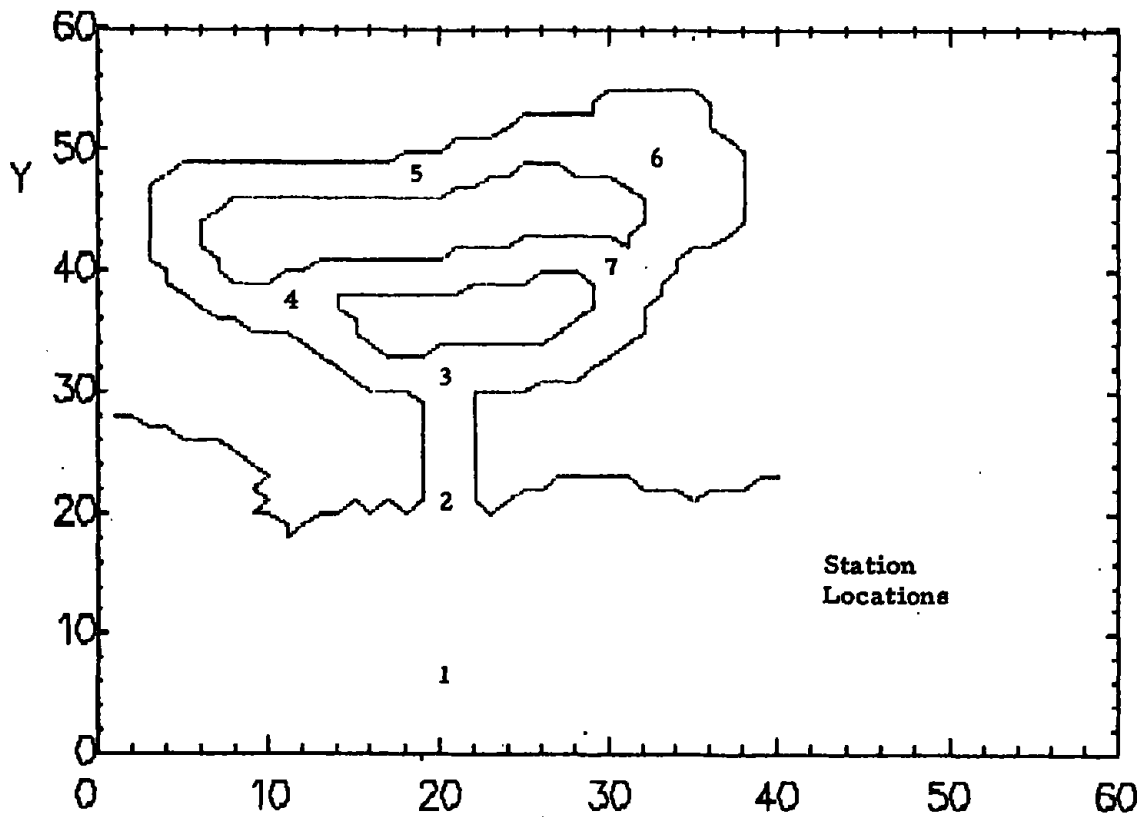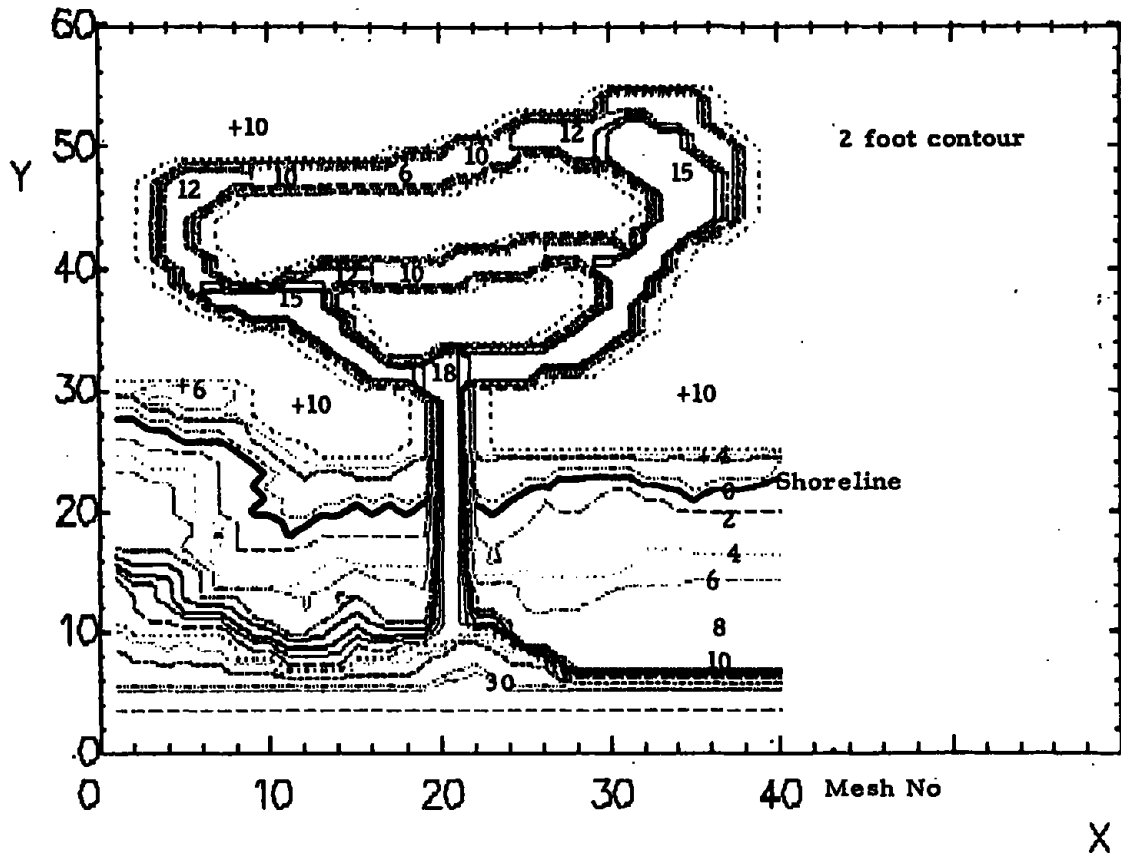
Fig. 2 The marina topography used in the numerical modeling and the location of the stations for reporting detailed wave histories. The contour interval is 0.61 meter.
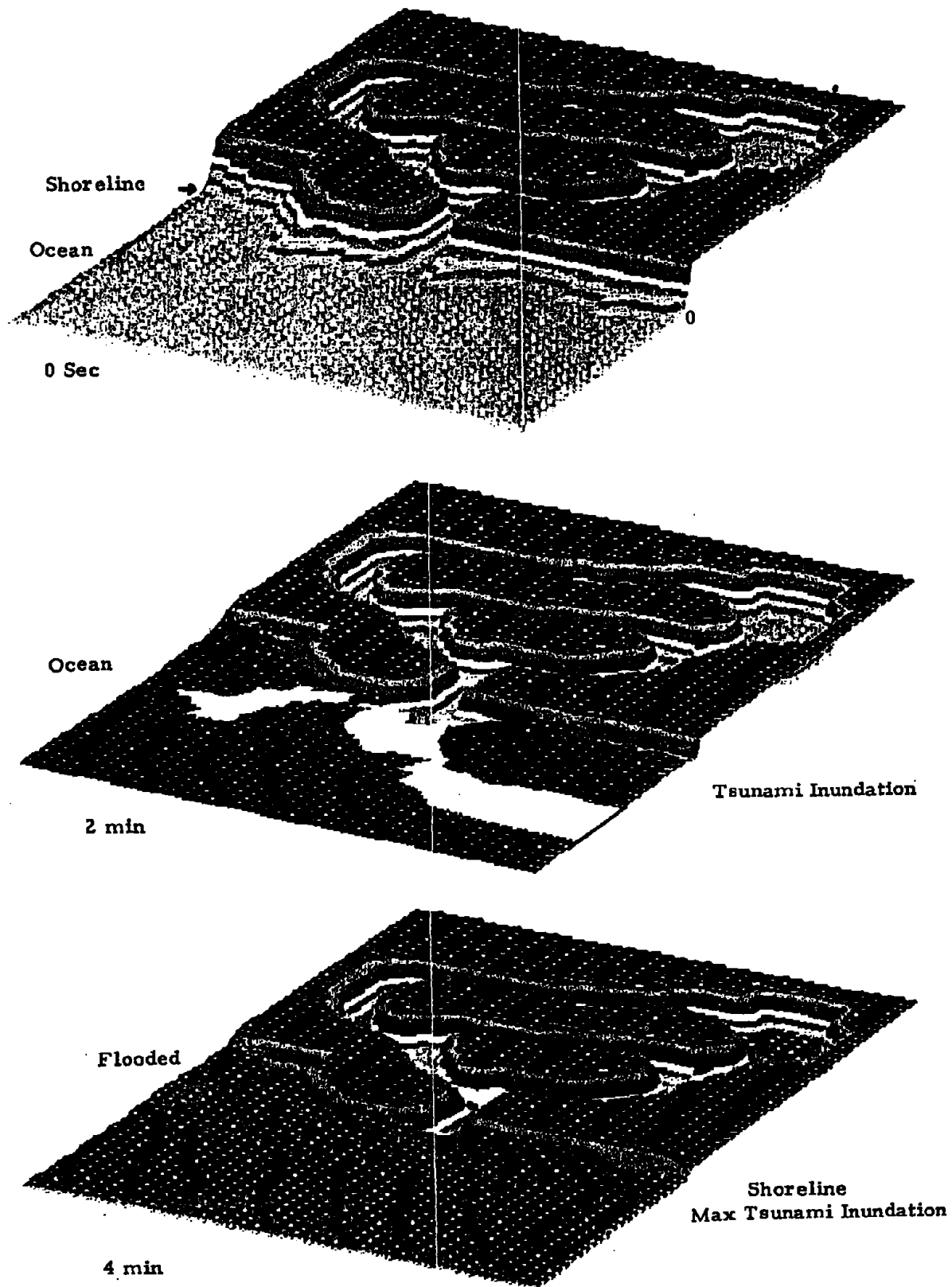
Fig. 3 The ocean surface and land above water level topography at 0, 2, 4 minutes (time of maximum tsunami shoreline flooding). Flooding to the 2.75-meter level is shown. The contour interval is 0.36 meter.

165

Ocean

Marina
Max Tsunami Inundation

6 min

Ocean

Tsunami
Withdrawal
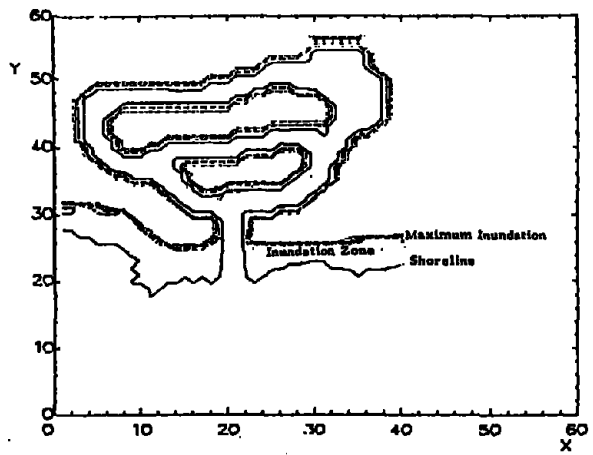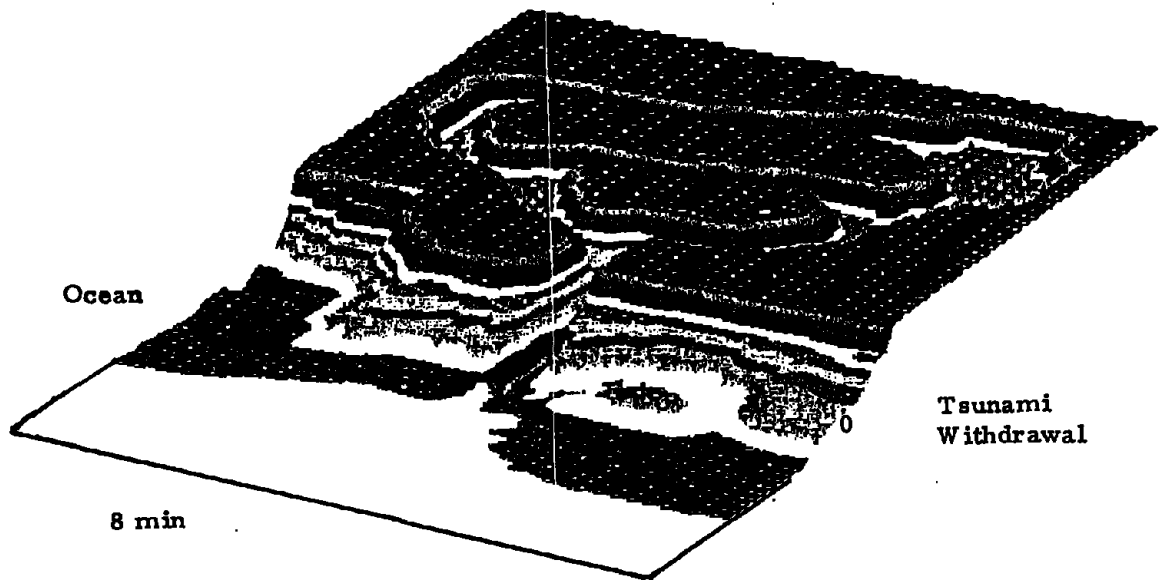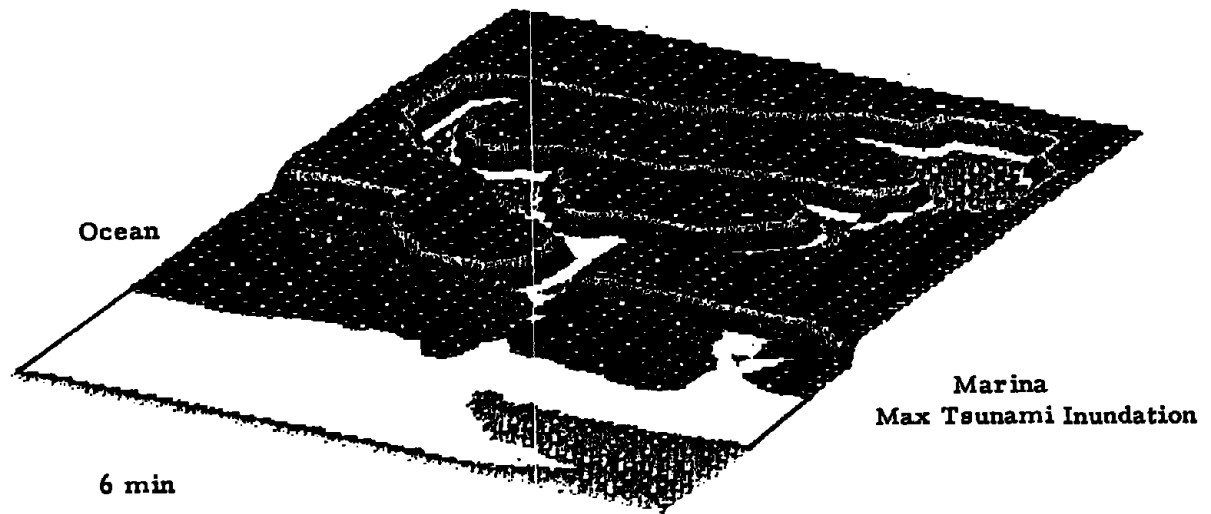
8 min

Fig. 4 Continuation of Figure 3 showing the topography at 6 and 8 minutes. At 6 minutes the maximum marina inundation has occurred and by 8 minutes the tsunami withdrawal has exposed some of the ocean bottom surface. The inundation zone and maximum inundation are shown.

166
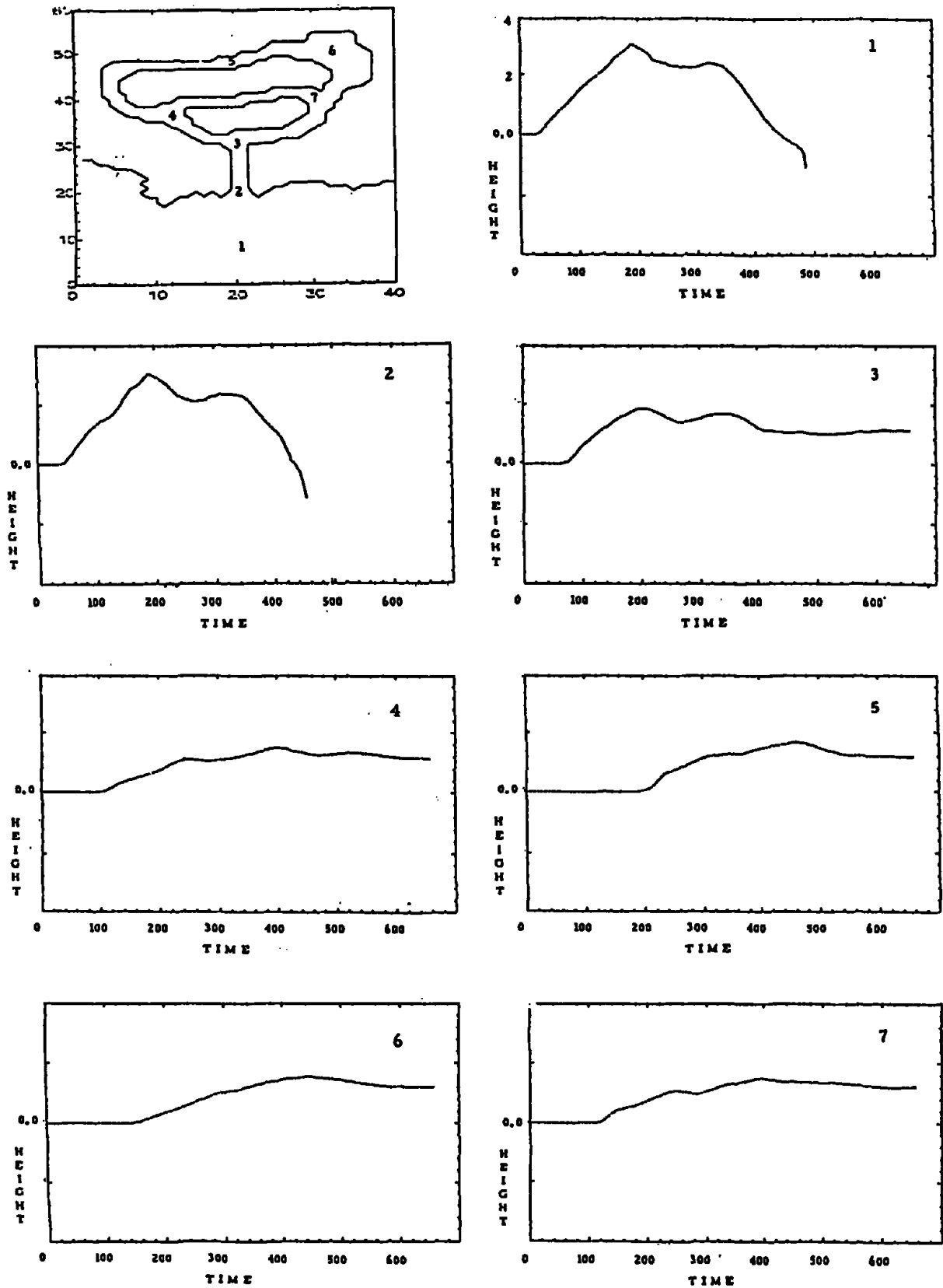
Fig. 5 The wave histories at various locations in the marina for a 15 minute period tsunami.

EXPERIMENT ON TWO DIMENSIONAL TRANSFORMATION OF NON-LINEAR LONG WAVES PROPAGATING ON SLOPE

Takaaki Uda
Public Works Research Institute
Ministry of Construction
Ibaraki, Japan

Abstract

The formation process of the edge bore is experimentally investigated under the condition that the undular bore propagates over a slope. Temporal and spatial changes in water level are extensively measured in a wave basin of obliquely sloping walls. It is found that an edge bore with eddies is formed over the bottom slopes of $\tan\beta=1/5$ and $1/10$, whereas in the case of the slope $1/20$ and $1/30$, an edge bore is not formed. The generation of an edge bore is classified by using the parameters of the slope $\tan\beta$ and angle θ between the directions of the incident solitary wave and the sloping wall.

Introduction

The Nihonki-Chubu Earthquake Tsunami occurred on May 26, 1983 causing large amounts of damage to the north Akita Coast facing the Sea of Japan. In this tsunami some specific wave forms were observed. Tsunami waves, which propagated over the mildly sloping continental shelf, formed the undular bore with short period cnoidal waves in front of them (Shuto, 1985). Furthermore, at some locations along the long stretch of the Akita Coast, edge waves were confirmed (Shuto, 1985). Photos 1-3 in which tsunami waves propagating northward along coastline were recorded at a short time interval clearly show the formation of the bores. This bore corresponds to the edge bore, since the wave height near the shoreline seems to be higher than that at offshore locations and the wave orthogonal is approximately parallel to the shoreline. Chen (1961) investigated the wave propagation over a sloping wall making a small angle (θ) to the direction of incident waves with changing θ and the slope inclination (tanβ) (Fig. 1). By this experiment edge bore was classified into three categories depending on the values of θ and tanβ: (1) the pattern propagating with the formation of the eddy in front of the wave, (2) the pattern propagating with irregularity in front of the wave although no eddy is formed, and (3) the one propagating without the formation of the eddy or mixing (Fig. 2). In addition, Chen (1961) classified the breaking and non-breaking waves on a sloping wall by using the values of θ and tanβ for the parameter, and pointed out that many ripples were formed behind the edge bore.

This study aims to investigate the formative process of the edge bore under the condition that the undular bore propagates over a uniform mild slope. Chen (1961) carried out his experiment to study the formative process of the edge bore over a comparatively steep slope such as $1/3 < \tan\beta$

Photo. 1   Tsunami propagation at
           North Akita Coast(1).

Photo. 2   Tsunami propagation at
           North Akita Coast(2).
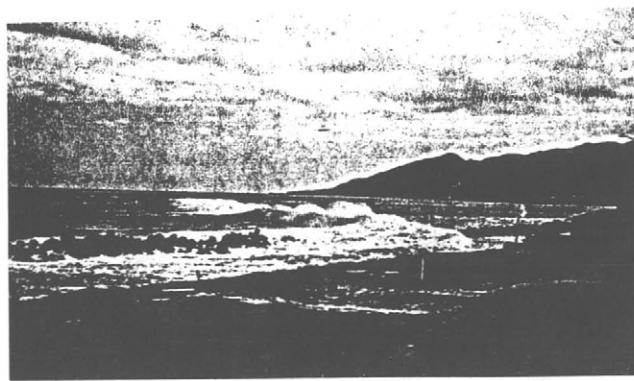
Photo. 3   Tsunami propagation at North Akita Coast(3).
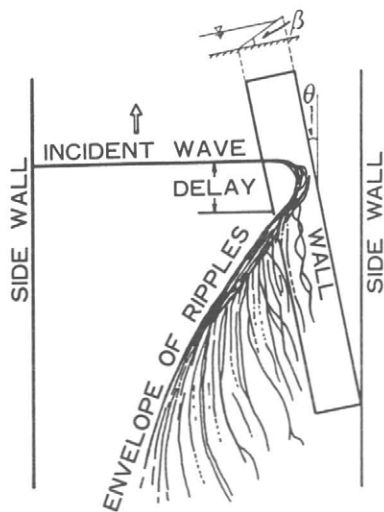
Fig. 1   Experiment of
           edge bore (Chen, 1961).
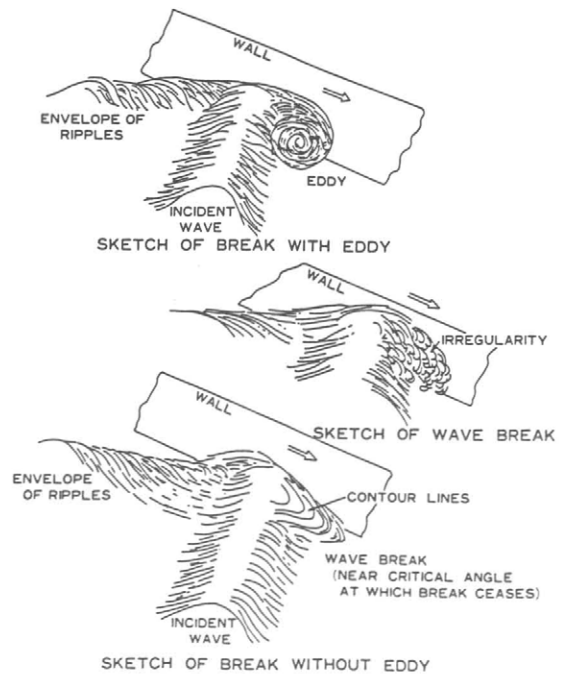
Fig. 2   Classification of edge bore
           (Chen, 1961).

170

$(20° < \theta)$. In the present study a range of the slope inclination $1/30 < \tan\beta < 1/5$ is selected, taking into account that the slope of a natural sandy beach is milder than the case above mentioned. In addition, the critical value of $\tan\beta$, at which waves reflect without the formation of the edge bore, is examined.

Method of Experiment

Experimental facilities include the wave basin made of concrete (about 30 m in length and width, and a bottom slope $1/100$) and the tide generator with an air chamber of $3*3*30$ m (Fig.3). In the experiment, the wave basin was divided into three parts and the central part, of 15 m wide, was used to generate the incident wave of about 5 cm high. The horizontal coordinate system (x, y) is fixed at a point 0 in the corner of the wave basin, and the x axis is taken seaward, and the y axis is perpendicular to the x axis. The still-water level is determined in such a way that the water depth in front of the tide generator becomes 29.85 cm with the fixed shoreline position at x=0 m (landward limit of the wave basin). The tide generator is a pneumatic type, and a solitary wave can be generated through a change in air pressure inside the air chamber, which in turn is controlled by a function generator. In the experiment, temporal changes of water level and wave crest distribution are obtained through measurements at about 100 points. A video recorder is also used for observing the edge bore.

Characteristics of Non-Linear Long Wave

Figure 4 shows the incident wave profiles measured in front of the tide generator. The wave height of waves A and B are about 3 and 4 cm, respectively. An example of shoaling of the generated wave (wave B) is shown in Fig. 5. Time (t) is measured with reference to the time when the water level at P_0 in front of the tide generator begins to rise, and the reference of the water level is taken to the still-water level. The incident waves propagated as bore over the mild bottom slope showed soliton fission at x=7.3 m. Between x=7.3 m and 5.8 m the wave height of the cnoidal waves in front of the bore increases. On the other hand the wave height of the first wave decreases at x=5.55 m because of wave breaking. In spite of the energy loss by wave breaking, the wave height (5 cm) of the bore observed after the cnoidal waves in the wave profile at x=5.3 m is the same as the one at x=10.3 m far from the shoreline.

Experimental Result of Edge Bore

In the experiment on the edge bore, a wooden wall of the slope $\tan\theta$, which also makes an angle θ to the direction of the incident waves, was placed in the wave basin. The value of θ changes in two cases ($\theta=20°$ and $30°$), and that of $\tan\beta$ changes in four cases ($\tan\beta = 1/5$, $1/10$, $1/20$ and $1/30$). In total, seven cases are selected by the combination of these variables. Figure 6 shows the experimental setup of the sloping wall. Since the bed slope is $1/100$, the shoreline, as shown by a broken line, is not parallel to the edge line of the wooden slope. The still-water depth is always kept $h_s=0$ at x=0 m. And the y' axis normal to the shoreline is fixed on the shoreline for the auxiliary coordinate system.
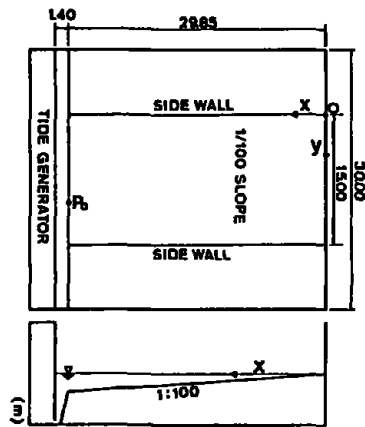
Fig. 3   Experimental setup of tsunami wave basin.
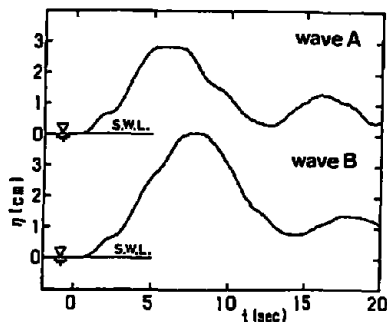
Fig. 4   Wave profiles at a position P_0 in front of tide generator.
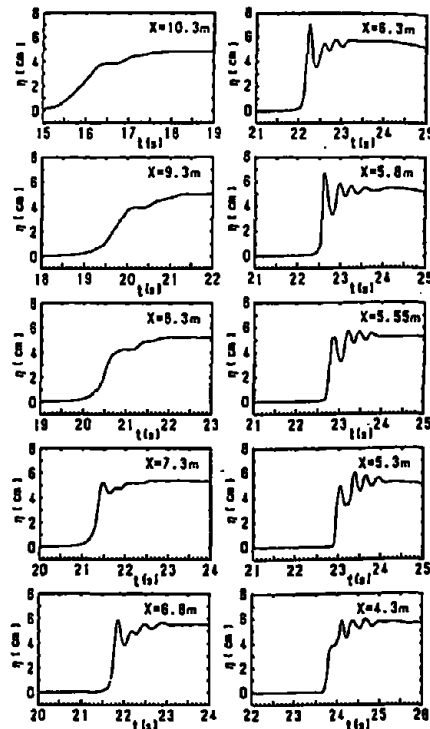
Fig. 5   Shoaling of incident wave (wave condition B).

Figure 7 shows the wave profile changes in the case of wave condition B, θ =30° and tanβ = 1/10. The wave height of bores along y=14.0 m is about 4 cm, and soliton fission is observed in front with the propagation of waves. On the other hand, along y'=0 m, some wave profiles show water level rise of about 8-9 cm after a time. Since the wave height of the incident bores along y=14.0 m is about 4 cm and the wave height near the shoreline is twice as high, this water level rise is considered to be attributable to the wave reflection from the bottom wall of the slope tanβ=1/10. The wave profiles between the measuring points having the same x coordinate can be compared in order to investigate the formation of the edge bore. The front part of wave profiles along y'=1.4 m and y'=14.0 m is approximately the same, although the front part of wave profiles along y'=0 m at shoreline is considerably different from those along y'=1.4 m. In addison along y'=1.4 m, the water level rises with a time lag from the arrival of the wave front, which means that the wave is reflected from the sloping wall. All these facts show that the two-dimensional transformation of waves accompanied by the formation of the edge bore takes place landward of the shoreline, and the incident and reflected waves separately propagate seaward of the shoreline. Along y'=0 m there exist many steps at the front part of the bore in the region of x<7.0 m. The phase difference between the front part of the bore of which wave height is about 3 cm and the reflected bore of which wave height is 8.2 cm is approximately 1.3 sec at a point of x=7.0 m and y'=0 m, whereas the time lag of those bores along x=4 m becomes shorter to about 0.9 sec. Along y'=-0.6 m located on land, there exist stepwise wave profiles between x=5.0 m and x=7.8 m, and they interact

172
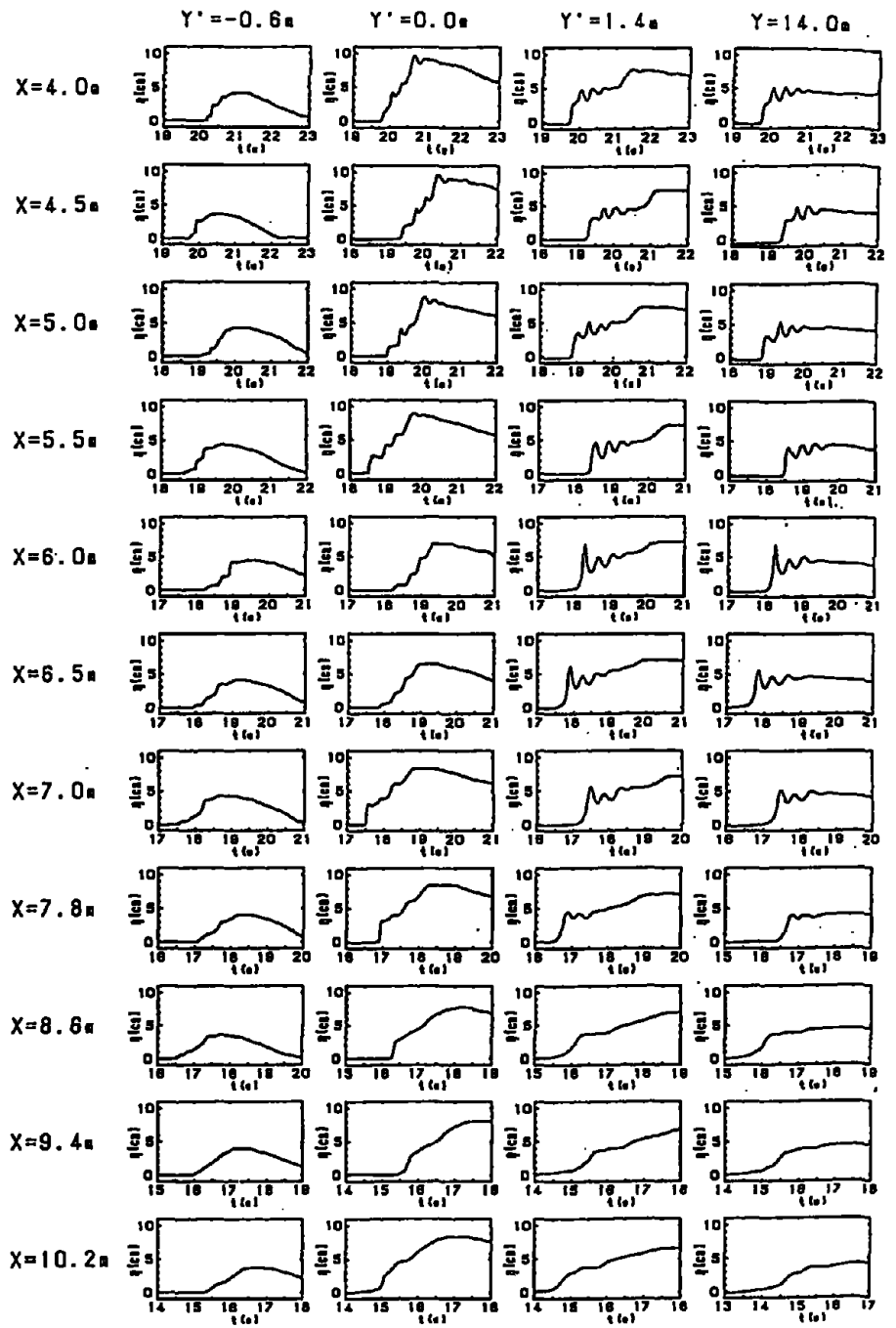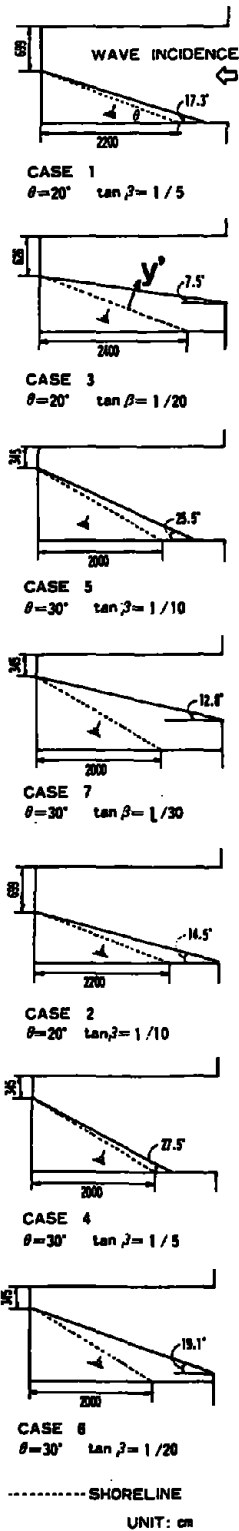
Fig. 7 Wave profiles (wave condition B, θ = 30 , tanβ =1/10).

Fig. 6 Setup of wooden slope
of various inclinations.

with the propagation of wave. Finally it is concluded that reflected waves catch up with the incident waves landward of the shoreline and cause the water level rise of the wave front. Photos 4-6 show the continuous change of the propagating bore. In Photo 4 there exist three steps landward of the shoreline. In Photo 5 these steps are combined to form the edge bore. In addition, a large scale circulating current develops in Photo 6. The edge bore is generated in the vicinity of the shoreline by the wave transformation mentioned above.
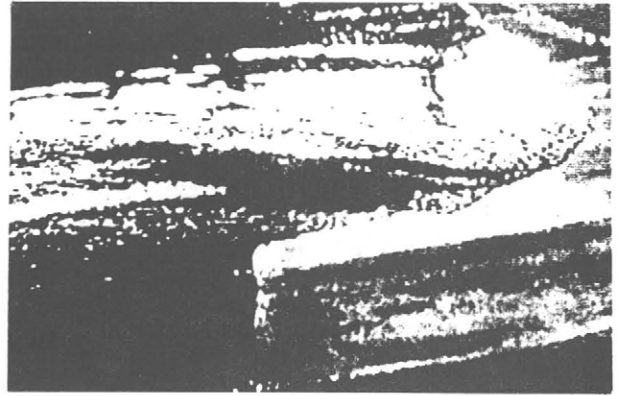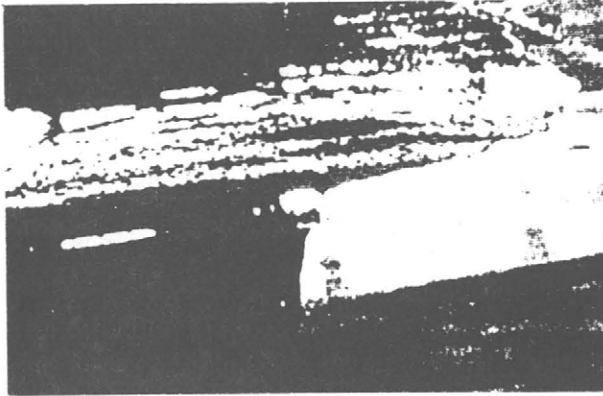
Photo. 4 Generation of the edge bore near the shoreline (1) (wave condition B, $\theta = 30°$, $\tan\beta = 1/10$).

Photo. 5 Generation of the edge bore near the shoreline (2) (wave condition B, $\theta = 30°$, $\tan\beta = 1/10$).
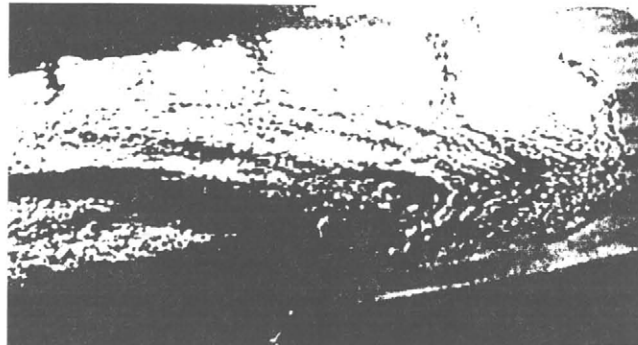
Photo. 6 Generation of the edge bore near the shoreline (3) (wave condition B, $\theta = 30°$, $\tan\beta = 1/10$).

In the cases of $\tan\beta = 1/20$ and $1/30$ the water level rise due to wave reflection from the sloping wall was not observed at measuring points located on and off the shoreline. Photo 7 shows the wave propagation over the slope of $1/30$. On this bottom slope the edge bore is not generated and incident waves only run up the sloping wall. In this case wave energy is dissipated by wave breaking and bottom friction, and hence, wave reflection from the sloping wall is weak. Thus the occurrence of the non-linear wave interaction is rather rare. Although in the case of $\tan\beta = 1/20$ gradual rise of water level due to the wave reflection was observed at measuring points on the shoreline after a certain time elapse from the arrival of the front wave; such water level rise was not observed in the case of $\tan\beta = 1/30$.

Wave crest distribution can be drawn if the arrival time of the wave crest is measured at every measuring point and the reference time is defined as the time when the wave front reaches the most shoreward measuring point. Figure 8 shows the wave crest distribution in the case of $\theta = 30°$, wave B and $\tan\beta = 1/30$. On the mild slope, a usual wave reflection pattern is seen and the edge bore is not formed.

174

Finally the occurrence of various type of edge bore is classified as shown in Table 1. In the case of θ = 20° and 30°, the edge bore is not observed on a bottom slope milder than 1/20. The formation of eddies is dominant at θ = 30° rather than at θ = 20°, whereas ripples are more frequently observed at θ = 20°.
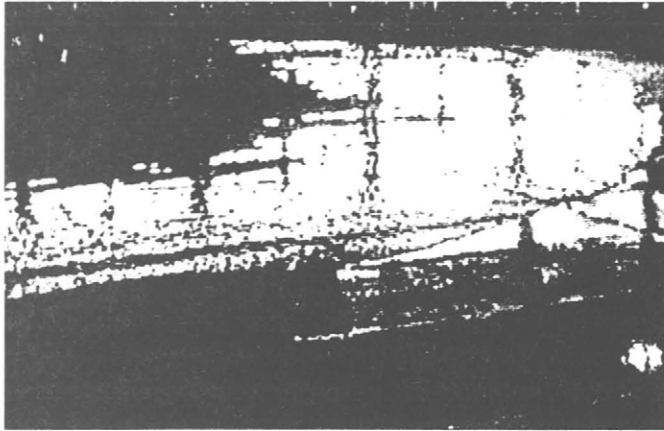
Photo. 7   Wave propagation over a slope of 1/30 (wave condition B, θ = 30°).
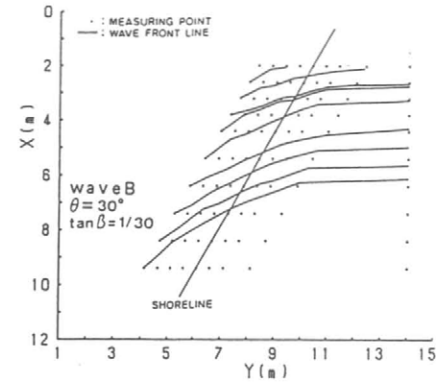
Fig. 8 Wave crest distribution (wave condition B, θ = 30°, tanβ =1/30).

Table 1   Classification of occurrence of various type of edge bore.

θ	tan β	WAVE	EDGE BORE	EDDY	RIPPLE
20°	1/5	A	○	△	○
		B	○	○	○
	1/10	A	○	×	×
		B	○	△	×
	1/20	A	×		
		B	×		
30°	1/5	A	○	○	△
		B	○	○	△
	1/10	A	○	△	×
		B	○	○	×
	1/20	A	×		
		B	×		
	1/30	A	×		
		B	×		

○:remarkable
△:obscure
×:nil

Conclusions

Edge bore with eddies was formed over the bottom slopes of tanβ = 1/5 and 1/10, whereas it was not formed in the case of the slope 1/20 and 1/30. Although the formation of eddies is dominant in the case of θ = 30° compared with θ = 20°, the wave transformation over the slope of θ = 20° is similar to the one over the slope of θ = 30°. The generation of edge bore was classified by using the parameters of the slope tanβ and the angle θ between the directions of incident solitary wave and the sloping wall.

175

References

Chen, T.C. (1961) Experimental study on the solitary wave reflection along a straight sloped wall at oblique angle of incidence. *B.E.B. Tech. Memo.*, no.124.

Shuto, N. (1985) Nihonkai-Chubu Earthquake Tsunami on the North Akita Coast. *Coastal Eng. in Japan*, vol.28, p.255-264.

NUMERICAL COMPUTATION OF THE TSUNAMI RUN-UP

Zygmunt Kowalik
Institute of Marine Science
University of Alaska
Fairbanks, AK, USA

Introduction

To study tsunami run-up the vertically integrated set of equations of motion and continuity is usually used:

$$\frac{\partial u}{\partial t} + u\frac{\partial u}{\partial x} + v\frac{\partial u}{\partial y} = -g\frac{\partial \zeta}{\partial x} - \frac{ru\sqrt{u^2 + v^2}}{D} \tag{1}$$

$$\frac{\partial v}{\partial t} + v\frac{\partial v}{\partial y} + u\frac{\partial v}{\partial x} = -g\frac{\partial \zeta}{\partial y} - \frac{rv\sqrt{u^2 + v^2}}{D} \tag{2}$$

$$\frac{\partial \zeta}{\partial t} = -\frac{\partial(Du)}{\partial x} - \frac{\partial(Dv)}{\partial y} \tag{3}$$

All notations are standard with u directed along the x direction, and v along the y direction, ζ is the sea level variation and D is the total water depth, $D = H + \zeta$.

Numerical models, constructed by Reid and Bodine (1968), Sielecki and Wurtele (1970) and Flather and Heaps (1975), were able to simulate the extent of inundation, but not the actual processes of wave propagation, breaking, and interaction with the coastal structures. This approach was quite successful in predicting flooding due to a major tsunami in Chile (Hebenstreit et al., 1985). A very extensive and thorough study by Lewis and Adams (1983) resulted in a complicated numerical solution for the one-dimensional problem only. Kowalik and Bang (1987) derived a solution using a different numerical algorithm, but again, only to the one-dimensional case. The boundary point between dry and wet domains is a singular point. Its position can be calculated from the equation of motion and continuity by directional derivatives only. One has to suggest a tsunami "predictor" which will move the boundary between dry and wet grid points. The best known approach was proposed by Sielecki and Wurtele (1970). They applied an extrapolation of the sea level to the first dry point based on the continuity equation (3). Denoting m as an index of time integration and j as an index of space integration along the x direction, the extrapolated level can be found as:

$$\zeta_j^{m+1} = (\zeta_j^m)_{ext} - \frac{T}{h}\{[(uD)_{j+1}^m]_{ext} - (uD)_j^m\} \tag{4}$$

Here:

$$(\zeta_j^m)_{ext} = 2\zeta_j^m - \zeta_{j-1}^m \tag{4a}$$

$$[(uD)_{j+1}^m]_{ext} = 2(uD)_j^m - (uD)_{j-1}^m, \tag{4b}$$

T is time step and h is space step of numerical integration. Kim and Shimazu (1982), on other hand, applied an equation of transport neglecting friction and inertia. Observations of the tsunami in shallow water suggest that it behaves like a bore and not like the long waves on the gently sloping beaches. Hibberd and Peregrine (1979) studied the run-up and back-wash by considering the long wave equations together with the wave front condition represented by a bore. Their condition is based on the fact that total depth equals zero at the boundary and $\zeta = -H$. To find velocity at the shoreline this condition can be incorporated into an equation of motion. Considering frictionless motion along the x direction one can write from (1)

$$\frac{\partial u_s}{\partial t} + u_s \frac{\partial u_s}{\partial x} = g \frac{\partial H}{\partial x} \tag{5}$$

The next step, which made wave front prediction more realistic, was an inclusion of the dissipative effects. Matsutomi (1983) proposed a new wave-front condition which depends on the time-varying friction parameter. Mader (1988) suggested a somewhat different and very simple approach to the proposed moving boundary. The movement of the boundary follows from the equation of continuity written for the upwind-downwind form. Thus, if velocity is positive in point j the depth differences are considered between points $j+1$ and j; for the negative velocity the differences are taken between points $j-1$. Because the whole process involves only the equation of continuity, the volume is always conserved, which may be not the case for the various extrapolation procedures.

The final choice of the boundary condition will depend on the comparison of analytical or numerical computations and observations. The experiments carried out in a wave tank by Yeh (1987) did show discrepancies between the observed bore front and the proposed analytical or numerical solution. Such experiments are very helpful in searching for realistic wave-front conditions.

Along with the hydrodynamical problems, the mathematical problems connected with discontinuity and nonlinearity make the runup problem very difficult. Strong nonlinearity and discontinuity are often sources of the computational instability which requires sophisticated filtering techniques (Lewis and Adams, 1983). A small error near the boundary, due to the approximation of a different order from the general set of equations, will generate the short wave oscillations which rapidly propagate into the whole computational domain (Marchuk et al., 1983). To delete the shore period oscillations three approaches are feasible:

1. Shapiro's space filter constructed on nine grid points (Shapiro, 1970;Lewis and Adams, 1983). The filtered value is calculated as

$$\overline{F_j} = \frac{1}{256}[186F_j + 56(F_{j-1} + F_{j+1}) - 28(F_{j-2} + F_{j+2}) + 8(F_{j-3} + F_{j+3}) - (F_{j-4} + F_{j+4})] \quad (6)$$

2. High order upstream derivative method. The high order finite difference formulas constructed on the seven point stencil (Kowalik and Bang, 1987) and applied to the advective term also generate stable solution.

3. Filtering by the additional horizontal friction term. By proper tuning this term can be used as a short wave filter without distorting the long period harmonics.

Along with the above described line of research, a second approach has been evolving. In this approach, a transformation of variables is applied and the independent variables x, t are transformed as

$$X = \frac{x}{l(t)} \quad \text{and} \quad T = t \quad (7)$$

where $l(t)$ is the distance from the origin of coordinate to a shore line. Through this transformation the variable region $0 \le x \le l(t)$ is transformed into a fixed region $0 \le X \le 1$, and no special boundary condition is required. The method has been extensively applied in USSR by L'atkher et al. (1978), in England by Johns (1982) and in Japan by Takeda (1984).

To check numerical results, comparisons against the exact solutions can be performed. Here an analytical solution for the wave running up the beach without friction, given by Carrier and Greenspan (1958), may be used. A solution derived by Thacker (1980) for two dimensional oscillation in a parabolic basin is very useful in predicting the extent of inundation.

Numerical Scheme Construction and Testing

To construct a numerical scheme, a space-staggered grid is applied which requires either sea level or velocity as a boundary condition. The first order scheme is applied in time and in space. An integration is performed along the x and y directions separately. For this purpose the set (1)-(3) is split in time into two subsets. Denoting m as an index of numerical integration in time, the method can be explained through the following difference-differential equations.

First, these equations are solved along the x direction,

$$\frac{u^{m+1} - u^m}{T} + (u\frac{\partial u}{\partial x})^m + (v\frac{\partial u}{\partial y})^m = -g(\frac{\partial \zeta}{\partial x})^m - (\frac{ru\sqrt{u^2 + v^2}}{D})^m \quad (8a)$$

$$\frac{1}{2}\frac{\zeta^* - \zeta^m}{0.5T} = -\frac{\partial(D^m u^{m+1})}{\partial x} \quad (8b)$$

and next along the y direction,

179

$$\frac{v^{m+1} - v^m}{T} + (v\frac{\partial v}{\partial y})^m + (u\frac{\partial v}{\partial x})^m = -g(\frac{\partial \zeta}{\partial y})^m - (\frac{rv\sqrt{u^2 + v^2}}{D})^m \tag{9a}$$

$$\frac{1}{2}\frac{\zeta^{m+1} - \zeta^*}{0.5T} == -\frac{\partial(D^m v^{m+1})}{\partial y} \tag{9b}$$

In this algorithm the calculation of the sea level starts from time step m, and along the x direction a preliminary value ζ^* is obtained. Afterwards, this value is carried over to the y direction to derive sea level at the $m+1$ time step.

To apply boundary conditions at the water-land boundary, first the boundary must be located at each time step. This was done by a simple algorithm proposed by Flather and Heaps (1975) for the storm surge computations and explained in Fig. 1 for the x direction only.

$$j-2 \qquad j-1 \qquad\qquad j \qquad\qquad j+1$$

water/land boundary

u(velocity)   water   land   ζ(sea level)
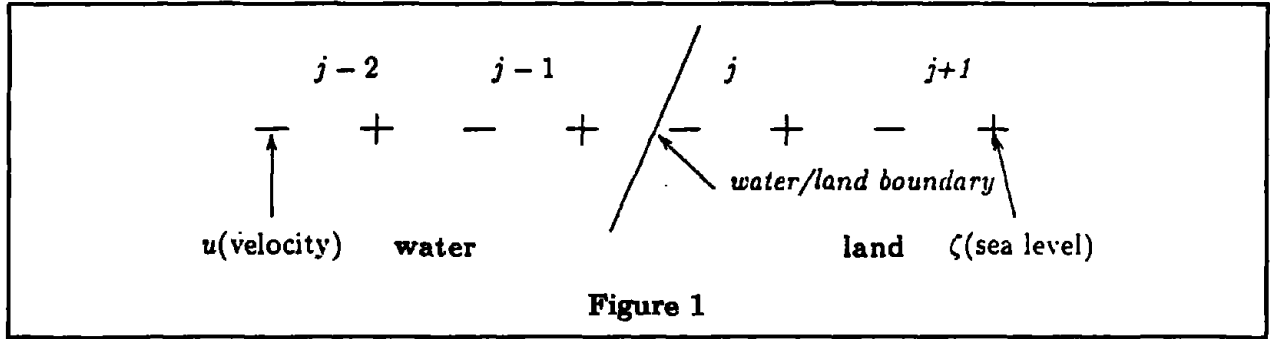
Figure 1

To answer whether u_j is a dry or wet point (see Fig. 1), the sea level is tested at this point

$$\begin{cases} u_j \ is \ wet \ point, & if \ 0.5(D_{j-1} + D_j) \geq 0; \\ u_j \ is \ dry \ point, & if \ 0.5(D_{j-1} + D_j) < 0 \end{cases} \tag{10}$$

It is obvious that total depth is positive at the wet points and equals zero at the boundary because here $\zeta = -H$. The small negative value of the total depth set at the dry points allows identification of the location of all dry regions in the computational process. Next, Sielecki and Wurtele's (1970) extrapolation (4-4b) of the sea level to the first dry point was used. The velocity in the first dry point was extrapolated linearly from the two last points. Linear extrapolation is easy to program but caution should be used in the case of a rough beach.

To test the above numerical method, we simulated a case which was solved analytically by Carrier and Greenspan (1958). A wave running up the beach without friction was considered and the problem was solved in the dimensionless coordinates. The distribution of the sea level along the sloping beach at the various times given both by analytical (dot line) and numerical (continuous line) solutions is plotted in Fig. 2.

One can see that the numerical method has reproduced the analytical solution quite well, but for time t=0.2 and 0.3 the short period oscillations occur in the numerical results. Small errors near the boundary, due to the different order of approximation of the general set of equations and boundary conditions are causing these oscillations. These oscillations were eliminated by a filter (6).
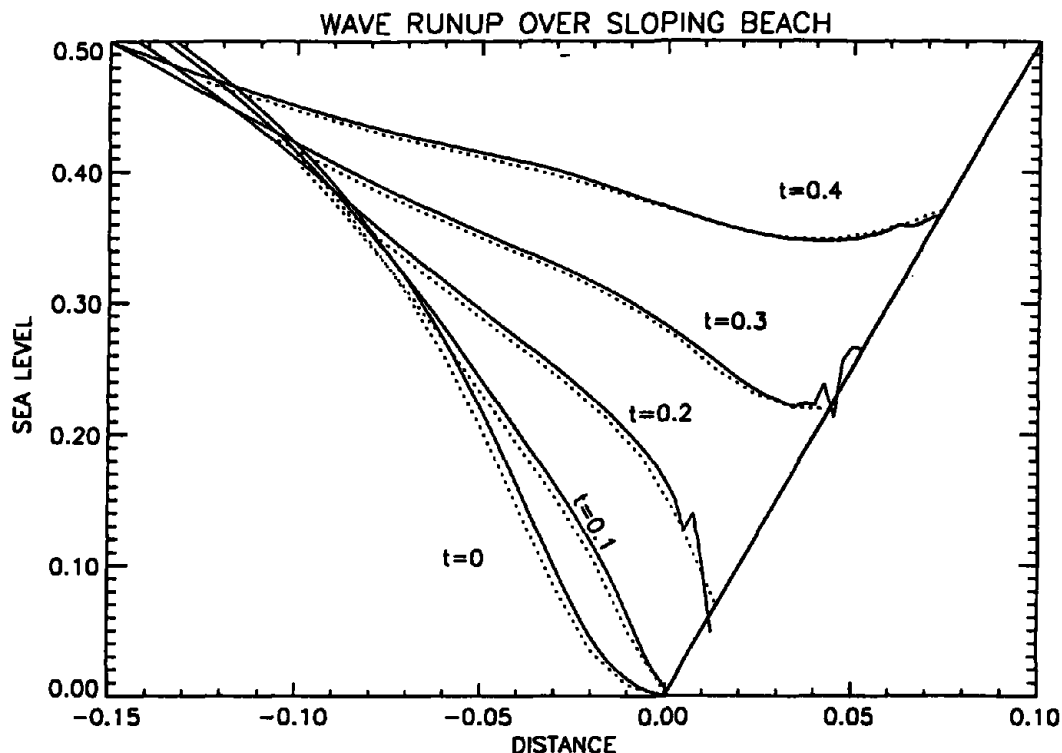
Figure 2

Besides, an analytical solution for the sloping beach the solution derived by Thacker (1981) for the parabolic basin may serve well to test the frictionless motion. The initial planar free surface motion will continue to be planar with a seiche period depending on the depth and horizontal distance. The motion in cross-section along the x axis is reproduced in the upper portion of Fig. 3. (The initial position is given by dotted line). In the lower portion of Fig. 3 the sea level computed both analytically and numerically is given at a few locations.

A constructed numerical algorithm has been applied to study a response of the coastal domain to the incoming sinusoidal wave. A sloping beach with the bottom slope equal to 0.01 is considered. At the open ocean boundary, located 1 km from the shoreline, a sinusoidal wave is given as a boundary condition. Two experiments were carried out. In the first experiment, at the open boundary a 1 m wave amplitude is prescribed and the wave period is varied from 1 min to 20 min. In the second experiment, the 2 m amplitude is considered. Fig. 4 depicts the maximum distance of wave penetration over dry land as a function of the wave period. This is run-up calculated from the first incoming wave. Since the wave at the open boundary pumps water in a continuous fashion is it interesting to see if this pumping mode influences run-up distance. Two experiments were performed with bottom friction coefficient $r = 0$ and $r - 0.03$. The results for the

181

WAVE RUNUP IN PARABOLIC BASIN

LEVEL AT 4000M, 4500M, 5000M

dotted lines - theoretical solution

Figure 3

182

Figure 4

Figure 5

183
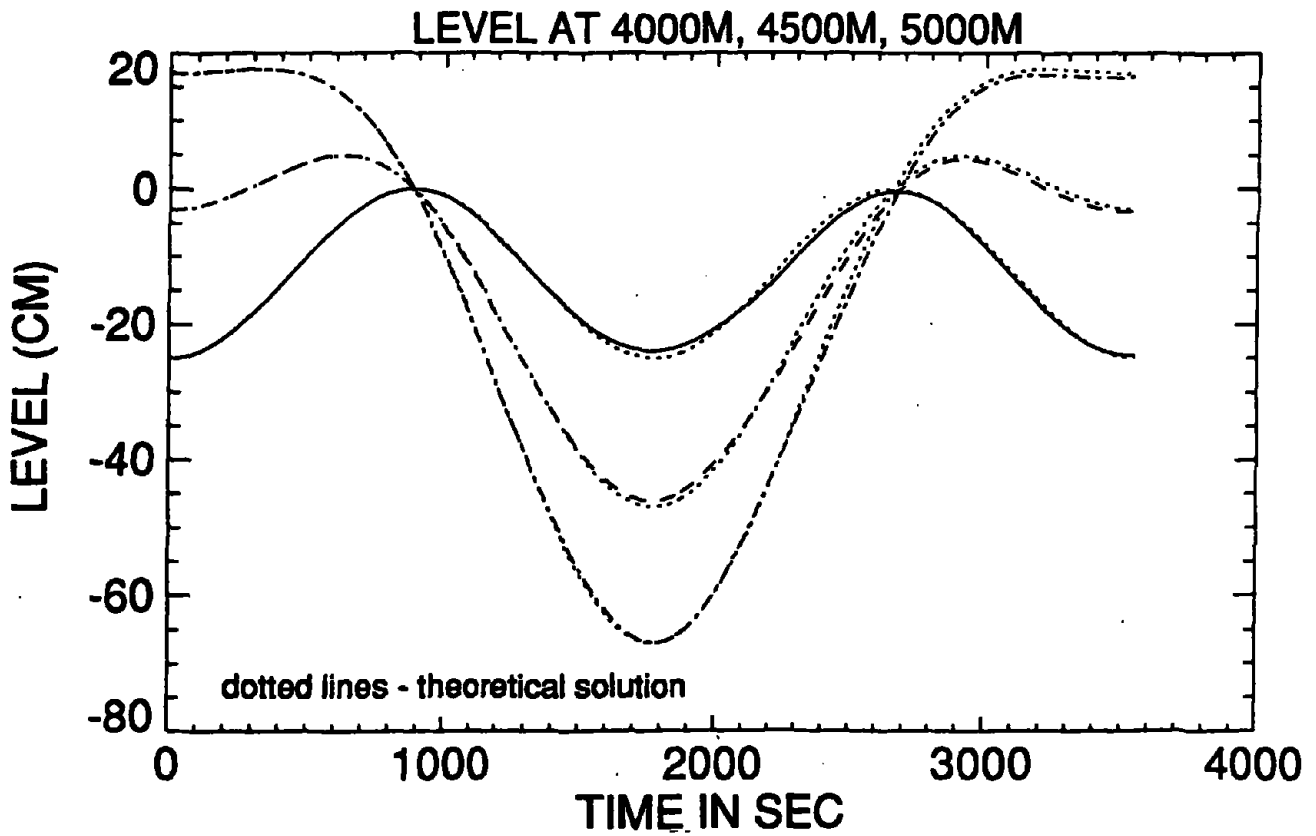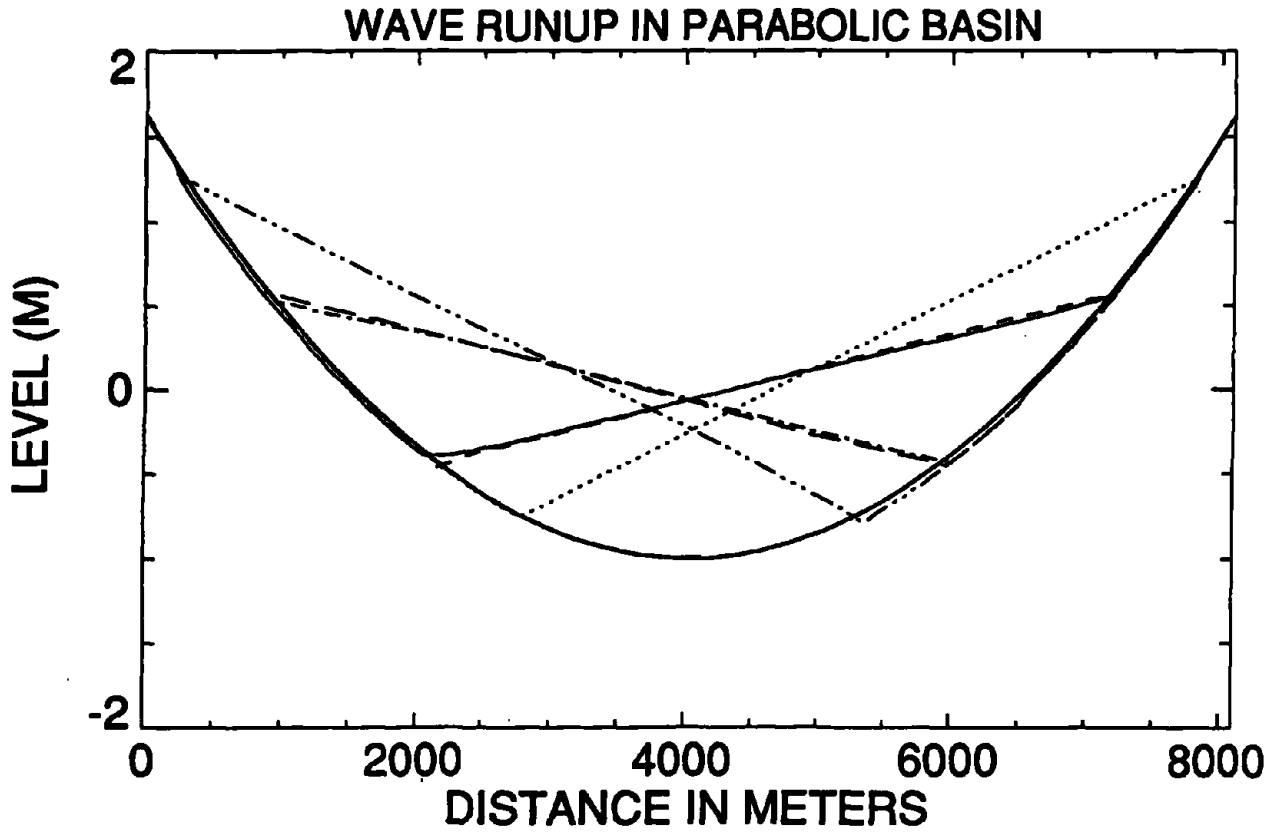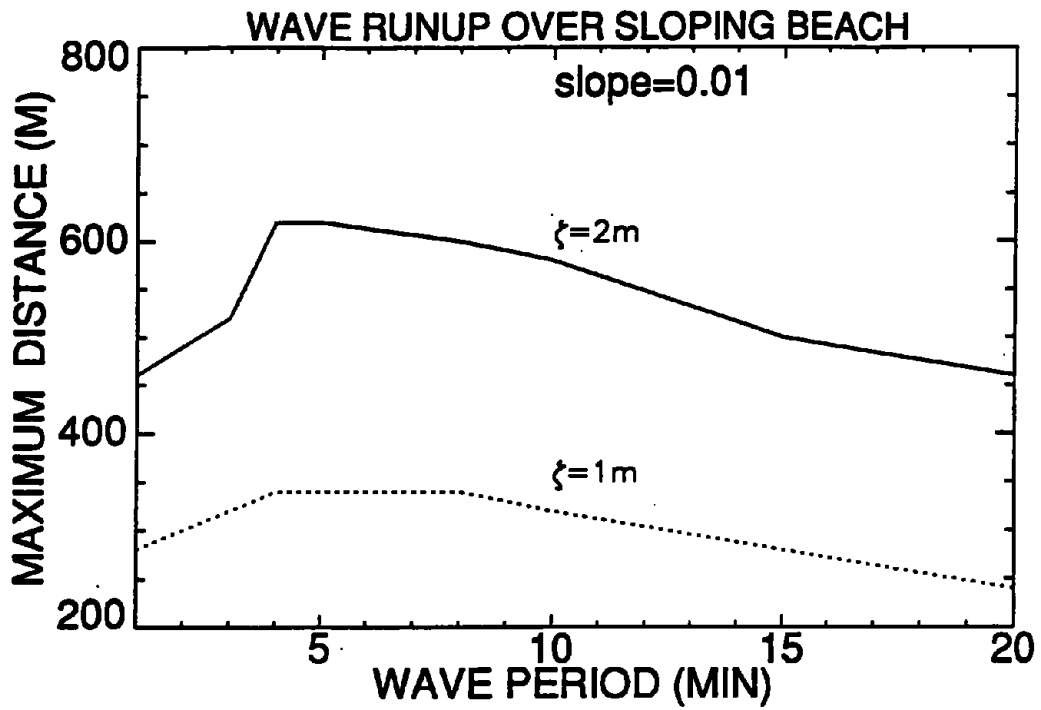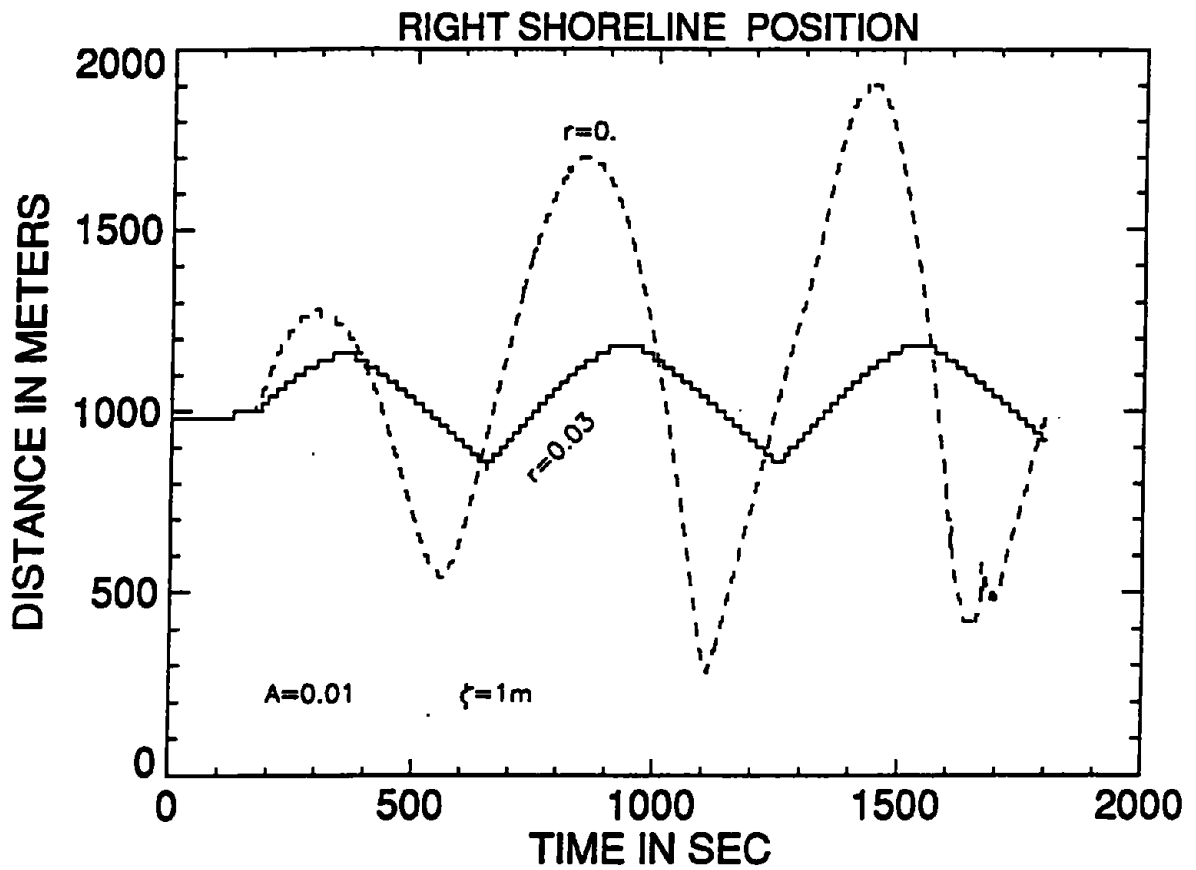
1 m amplitude are depicted in Fig. 5. For the high friction case the run-up does not change in time, but frictionless motion displays run-up increase for the second and third wave. This run-up practically stays constant after the third wave.

Realistic motion in two-dimensional space often takes place over discontinuous bathymetry where a simple extrapolation scheme for the moving boundary fails to produce the right answer. To account for the various cases of overtopped, submerged or exposed barriers, special boundary conditions have been introduced. For example, for the overtopped barrier the velocity is calculated by

$$u = \pm\sqrt{gD} \qquad (11)$$

Here D is depth of the water over the barrier. The water is transported from the top of the barrier to the foot by the above velocity. When water flows across a submerged barrier the velocity is calculated by the formula for a submerged weir (Reid and Bodine, 1968).

To illustrate a two-dimensional motion with discontinuous topography, two cases of waves running up the beach are considered. The channel which comprises a sloping beach along the x direction is 200 m wide along the y direction. As in the previous experiments, the open boundary is located 1 km from the shoreline and a 1 m amplitude sinusoidal wave is set at the open boundary. In the first experiment a depression in the beach profile is considered (Fig.6). The water running up the beach will flow into the depression from the various directions and eventually fill it up completely. The second experiment demonstrates wave interaction with an obstacle located on the beach (Fig.7). The obstacle reflects the wave, divides the flow into two branches, and finally the divided flow joins behind the obstacle and runs up the beach.

Figure 6

185
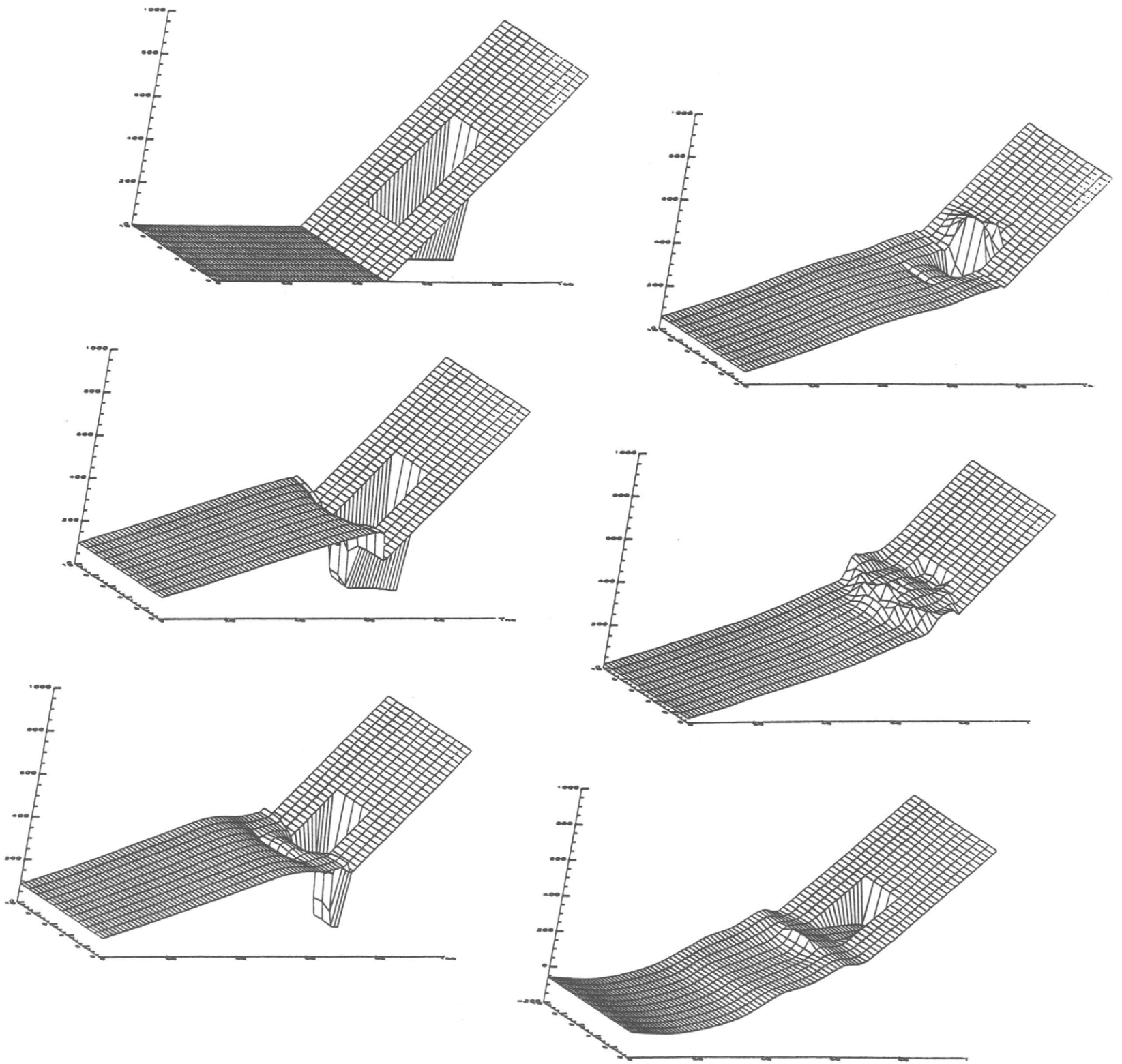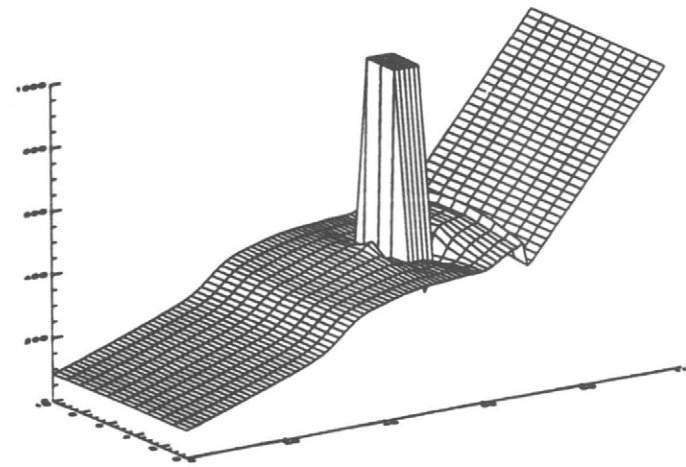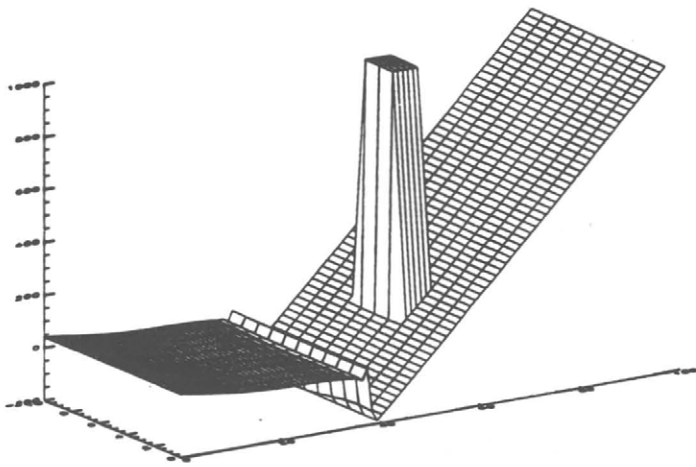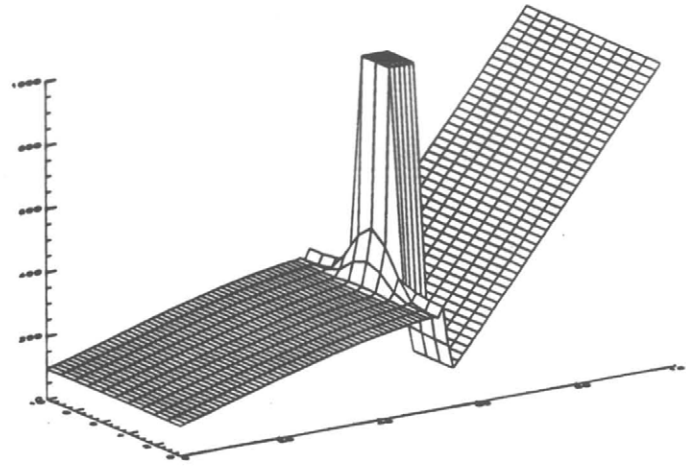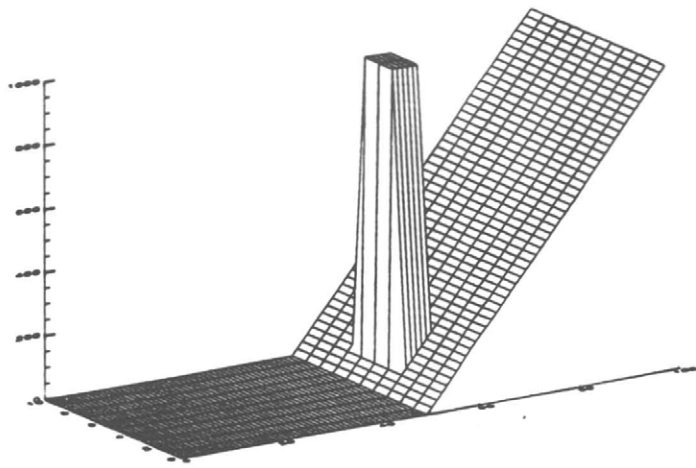
Figure 7

References

Carrier, G.F. and H.P. Greenspan, 1958. Water waves of finite amplitudes on a sloping beach. *J. Fluid Mech.*, **4**, 97-109.

Flather, R.A. and N.S. Heaps, 1975. Tidal computations for Morecambe Bay. *Geophys. J.R. Astr. Soc.*, **42**, 489-517.

Hebenstreit, G.T., F.I. Gonzalez and A.F. Morris, 1985. Hear-source tsunami simulation of Valparaiso Harbor, Chile. *Proc. Int. Tsunami Symp.*, Murty, T.S. and W.J. Rapatz, eds., Inst. Ocean Sciences, Sidney, B.C.

Hibberd, S. and D.H. Peregrine, 1979. Surf and run-up on a beach: a uniform bore. *J. Fluid Mech.*, **95**, 323-345.

Johns, B., 1982. Numerical integration of the shallow water equations over a sloping beach. *International J. for Numerical Methods in Fluids*, **2**, 253-261.

Kim, S.K. and Y. Shimazu, 1982. Simulation of tsunami run up and estimate of tsunami disaster by the expected great earthquake in the Tokai District, Central Japan. *J. Earth Sci.* Nagoya Univ., **30**, 1-30.

Kowalik, Z. and I. Bang, 1987. Numerical computation of tsunami run-up by the upstream derivative method. *Science of Tsunami Hazards, The International Jour. Tsunami Society*, **5(2)**, 77-84.

L'athkher, V.M., A.N. Militev and S.Ya. Shkol'nikov, 1978. Calculation of the tsunami run-up. In: *Tsunami Research in the Open Ocean*. Moscow, Nauka, 48-55.

Lewis, C.H., III and W.M. Adams, 1983. Development of a tsunami-flooding model having versatile formulation of moving boundary conditions. *The Tsunami Society, Monograph Series*, **no.1**, 128p.

Mader, L.C., 1988. *Numerical Modeling of Water Waves*. Univ. of California Press, Berkeley.

Marchuk, A.G., L.B. Chubarov and Iu.I. Shokin, 1983. *Numerical Modeling of Tsunami Waves*. Izd. Nauka, Novosibirsk. English translation, Los Alamos, 1985, 282p.

Matsutomi, H., 1983. Numerical analysis of the run-up of tsunamis on dry bed. In: *Tsunamis - Their Science and Engineering*, Iida, K. and T. Iwasaki, eds. Terra Sc. Publ. Company, Tokyo, 479-493.

Reid, R.O. and B.R. Bodine, 1968. Numerical model for storm surges in Galveston Bay. *J. Waterway Harbour Div.*, **94(WWI)**, 33-57.

Shapiro, R., 1970. Smoothing, filtering and boundary effects. *Review of Geophysics and Space Physics*, **8**, 359-387.

Sielecki, A. and M.G. Wurtele, 1970. The numerical integration of the nonlinear shallow-water equations with sloping boundaries. *J. Computational Physics*, **6**, 219-236.

Takeda, H., 1984. Numerical simulation of run-up by the variable transformation. *J. of the Oceanographical Society of Japan*, **40**, 271-278.

Thacker, W.C., 1980. Some exact solutions to the nonlinear shallow-water wave equations. *J. Fluid Mech.*, **107**, 499-508.

Yeh, H., 1987. Tsunami action on a beach - summary. In: *Proc. International Tsunami Symp., Vancouver, B.C.*, Bernard, E.N., ed. NOAA/PMEL, Seattle, 206-211.

Discussion

Comment: About 20 years ago Dr. Goto and Dr. Shuto used a LaGrangian approach and recently Jeff Zeld implemented their idea into a numerical scheme. A LaGrangian scheme is such that the runup tip is exactly determined, a known quantity, and regardless of which is better or which is worse, there are other alternatives already available these days.

Comment: This numerical method is more or less a finite difference approach. There are many different approaches that can be implemented. Dr. Shuto mentioned the need for a quick solution. The Mader solutions may be good for that but it is not a very exact solution. There are two possible approaches; one is an analytical solution for accuracy and another is a practical solution for a very fast solution.

ROUND TABLE DISCUSSION OF TOPIC B

Question: Basically of what specific value are the models? For example, the whole question of dispersion, has come up in a number of papers, including some of those in the last session, and its importance or non-importance in particular situations. Big tsunamis, which are really the primary type of tsunami of interest for the community since they do the most damage, are characterized by long periods and, perhaps especially in the near field, dispersion is not important. But there are really two different types of tsunamis, to over simplify. There are those kinds of tsunamis, which can cause damage around the Pacific and dispersion may or may not be important, especially in the near-field; those happen very infrequently, maybe once every 20 years. Then, there are the small tsunamis, which have been measured quite successfully in the ocean and those happen frequently. Pat Lockridge and Jim Lander have done some work that indicates that there are at least five small tsunamis in the Pacific that are observable and reportable every year. In that case, dispersion is clearly at least a feature of the observations and, it looks like the linear dispersion relationship fits it quite well. So at one end of the scale there are the big tsunamis where non-linear long-wave theory might be appropriate, with no dispersion. On the other end there might be small tsunamis where the linear dispersive theory might be needed. Given those circumstances, what good are the data from small tsunamis in terms of understanding the big tsunamis?

Comment: It is quite clear that there are many events in which dispersion is exceedingly important, and there may be, and there undoubtedly are, major events in which in the head-wave propagation, at least, the energetic part of the thing, dispersion is a minor thing.

Comment: There are a couple of terms that need to be defined a little better and dispersion happens to be one of them. That you can have a shallow wave theory with no dispersion and still have it be so that a pulse generates a wave in which the zero crossings get closer together as you go out, that is not dispersion in itself. That does not mean that there is dispersion in frequency and speed of transmission. The second terms that need to be further defined are near-field and far-field. In physics, near-field implies there are some additional force terms, like $1/r^4$, which decrease sharply with distance. But in hydrodynamics, whether you are close to the source or distant from the source, if the same equations apply, why would the terms near-field or far-field be used?

Response: The discussion is quite interesting, especially in relation to dispersion. When dispersion is said not to be important, non-linear terms are not important, or for that case, numerical dispersion is not important. It may have some different meanings. If the tsunami is in Chile and the wavelength is about 200 km, the dispersal effect on the near shore may be very small; but if you take a ten-wavelength dispersion, maybe numerical dispersion could be very big. This may not be physical, but this is why near-field, versus far-field is spoken of. Again, if the numerical modeling is compared with sources very close to your gage, maybe these effects are not really important, but would be in the far distance. These special effects can occur as was seen from Chile.

Comment: Two very important issues have been raised. One of them is the definition of dispersion and the need for clarification, and the second is the near-field/far-field question. The amplitude of frequency modulation has been used as sort a generic term that included things like the familiar linear wave dispersion, or amplitude dispersion, or non-linear dispersion. There does need to be some clarification in terms of what is meant by these different mechanisms in terms of the near-field/far-field. In the near-field, an earthquake imparts an impulsive force to the water column and there are significant vertical accelerations and movements. In the far-field, as the wave moves away from the near-field, after one or two wavelengths or maybe more, those vertical accelerations

are not going to be important. In fact, different equations might be appropriate in the near-field from the far-field because the qualitative nature of the ways a tsunami appears are different. The other point here is that in terms of human death and destruction, obviously, the near-field problem is the important one, and Jim Lander and Pat Lockridge have analyzed that hundred-year historical data base and shown that 90 or 95 percent of the death and destruction occurs within one or two wavelengths of the source.

Comment: Even in cases where fundamental forces are not in competition with each other, there are lots of phenomena, including tsunamis, in which the near-field is very largely a function of the details of the source distribution and timing of it. Whereas, later in the far-field, all of the short-wave length phenomena, which helps make up that picture, have been left behind. At a distance and what that distance is depends on what particular problem is being addressed, of course, but the distance can be characterized in terms of scale. Nonetheless, the far-field is very different from the near-field and it is a legitimate distinction. Even in linear problems where it is only the geometry of what happened in the source region that is different, it is important in understanding the phenomena.

Comment: The use of the Kajiura measurement, P value, is recommended. It is used to judge whether the dispersion effect is necessary for a far-field tsunami. It does not include the effect of the Coriolis force, but it includes the effect of the curvature. His P value is composed of four factors. One is the height of the tsunami at the time of generation, the second is water depth, and the third is the length of the minor axis of the fault - it is nearly equal to one wavelength of the tsunami generation. The final factor is the distance to the point where it is being considered whether or not the dispersion factor is needed. So his P value can be used to judge whether the dispersion effect should be included or not. This is a good measure to judge whether dispersion is necessary or not for a far-field tsunami. For the near-field tsunami, the situation is a little different. The frequency modulation will occur after it becomes larger due to the shoaling effect, then one can always see the very well developed cnoidal wave trains. If a tsunami enters a river, the current makes the propagation velocity decrease. It means that enough time is provided to develop fully the cnoidal wave. If the shore is very shallow, with a very gentle bottom, similar retardation of the propagation will occur. Therefore it is sometimes necessary to include the effect of dispersion; otherwise, the exact wave profile could not be found. This was seen in the case of the 1983 Nihon-Kai Chubu tsunami. As long as the maximum wavelength tsunami runup is concerned, perhaps the small oscillations in front of one huge tsunami wave have some small contribution to the maximum runup height because the volume of the water of the major part of the tsunami is huge compared to this type.

Comment: Whenever discussing physical dispersion, the numerical dispersion should also be considered. Most of the numerical studies do not provide a complete analysis of errors. Whenever an analysis of the errors is made using a fourier expansion, one can clearly see some dispersion terms – numerically generated dispersion terms. Three or four years ago, Dr. Imamura used these numerical dispersions to match physical dispersions to create better predictions. It is a very clever way to do it.

Comment: Considering the first order problem, there still is not a solution where someone will take a record, from the deep ocean, and project it all the way to the coast line to find the maximum run-up. As Dr. Shuto commented, the maximum run-up is unlikely to be much effected by the dispersion, particularly for extremely long waves. I think there are two different types of studies. For the first order one, it is important to find out what the maximum is so that we can define

inundation zones. For the second order, it is very important to have neat models where the exact details can be studied, such as the reflection of waves, and direction of waves, to be able to understand the process. But in the first order, which is to determine the maximum run-up, dispersion would not be all that important, and it is poorly understood.

Question: If observations from deep water gages of small tsunamis are used, these are clearly dispersive. What is the relevance of computations projecting these to the shore and on shore run-up to the problem of a big earthquake? Whose record off-shore does not show any dispersion?

Response: It is difficult to identify precisely if a record shows dispersion or not, because the record is almost like a snap shot of one particular event.

Comment: The data seems to agree well with the linear dispersion relationship $- \Omega^2 = gk \tanh kh$.

Comment: An approach would be to use a technique similar to the one of Dr. Shuto, which is to use the linear dispersive theory to slowly close to the shoreline and from then on, use whatever technique is best suited. Shallow wave equations are doing a good job; or if there is time and computational speed, the Boussinesq equations can be used. The linear shallow wave equations work close to the shoreline, even beyond the edge of the continental shelf. Consider a record with three different peaks, each one of different height. It appears to be dispersive because the amplitudes are different. But actually, how dispersive is not certain and it must be examined over time. In any case, the linear theory works extremely well. It can be used to bring the wave closer to the coastline.

Comment: I'd like to go back to the first question, "What good are the data?" It seems that there are two closely related reasons you want deep ocean records. They provide the testing ground for the understanding of the phenomena and are useful where information is needed for an operational decision. The latter, of course, depends in large measure on the understanding of the phenomena, but in some cases it is necessary to bypass a full understanding because it isn't adequate yet. There is a question as to whether part of the record in question is caused by the filtering that goes on by the geometry of the domain in which the instrument is situated or lies on the path to it, which can produce a wiggly artifact of a signal that was quite different then the dispersion. Dispersion, obviously, can also produce a wiggly contribution. To distinguish one of those from the other, without rather precise and high resolution data, could be a task beyond the scope of our data. The inverse problem is very hard, because there are so many mechanisms competing for attention and on an a priori basis, they are not identifiable. Again, the available data are used as a test to quantify hypotheses, whether there are numerical models or analytical models or even in semi-quantitative statements. The hypotheses are tested against the data, some hypotheses fail, and others are encouraging, leading to gradual improvement of skills. This is still a long way from having the kind of detailed data and knowledge about individual events that allows for a thorough test of models, except in the simpler cases where the geometry is not wholly an issue.

Comment: If one uses ordinary linear long-wave theory and polar coordinates, and a wave is generated by a cylinder displacement in the center, taking a profile of that at some later time will show the change of amplitudes and the zero-crossings changes. This may be confused with dispersion in amplitude or frequency. In fact, the problem was just a straight forward linear long-wave problem and polar coordinates.

191

Comment: There is a profound geometry change. It does, in the absence of dispersion, remain somewhat invariant except for its amplitude. Whereas, dispersion is the consequence of the fact that different wave-number waves travel at different speeds. Dispersion implies a rather different distortion of the geometry, and both of them are present in any real waves going out. One way to separate these effects is to deal with them individually, in one's analytical attempts at understanding, as well as together. One can begin to attribute what part is due to the geometry, what is due to dispersion, and what is due to non-linearity and all the other mechanisms not mentioned in this discussion.

Comment: Maybe one thing that could come out of this workshop is an agreement on terms – regarding these effects that modulate the amplitude and frequency of a tsunami signal.

Response: That is always difficult.

Comment: The most that could be done would be to get agreement among the participants. This could not be imposed upon people who are not here. People continually violate the language. The meaning of a phase which was very, very precise 30 years ago can encompass many, many things today and this will continue to happen.

Question: There are photographs and video images taken from helicopters of the Japanese tsunami of 1983 and also in other cases showing bores going upstream in the rivers. The wave-lines were straight, although the river is deeper in the center. In that case, the front of the bore is straight. Can this be explained?

Response: This is a very simple case of a wave propagating along the shoreline as an edge wave. Perhaps there is also some kind of wave focussing happening, along the shoreline.

Question: Dr. Uda's experiments look as if the tank may not be wide enough. Does this represent the results one would get in the open sea conditions?

Response: The edge wave example is a good one. It is a good example of a well-known phenomenon in which there is a crest perpendicular to the shoreline even though the wave propagation speed of any little local element differs with depth as you go up. And of course, what is happening is that if you are getting a readjustment from the fact that the amplitude of the wave is not uniform across the barge, and there are gradients in the lateral direction which must be taken into account in getting the composite. There is another mechanism too - which may be important in the problem which has been raised. If it is in a river, then there is a flow, and your wave is going against the river; the flow is faster in the deeper water on the average, and that is probably a compensating feature.

Comment: When the tsunami enters the river, there is a breaking bore effect. As it moves upstream, and encounters an island, then this bore split in two; on one side there is some kind of different shape and on the other this breaking bore is still propagating. For some reason, perhaps due to the gentle bottom, this first part becomes slower and there is a cnoidal bore following the refraction. There is a breaking bore and a cnoidal bore. And each wave on the cnoidal bore propagates following the ordinary refraction law. So it may be necessary to determine what conditions should be taken into account to determine which phenomena will occur. Goto's experiment shows the two cases. Under one condition we have the breaking bore propagating independently of this bottom trough. When the breaking bore is big, then some part will follow the

192

ordinary refraction law. No theory treats all of these phenomena.

Question: Recently some people prepared a paper which showed some analytical results from a sloping tunnel, very similar to Dr Uda's tunnel - one side of the tunnel was sloping. The essence of their results was that some of the crests of the waves were curved. Was this phenomenon actually observed?

Response: The axis of the slope is inclined to the central axis of the channel. There is the sloping wall and a vertical wall. The end of the sloping and wall, and the slope is 1 in 100, so that is not a flat bottom. No special shape of the crest waves was observed. Perhaps the width is not enough, but it is 50 meters which seems to be enough; but energy is squeezed to the narrow region.

About those observations, one is a cnoidal bore and the other one is a complete bore and also and as Professor Carrier commented, refraction can be caused by the current. Recently at Stanford they tried to produce laminar circulation and to make a uniform current for some waves. What they found is a complete wave on one side of the wall and a very, very weak one on the other side of the wall. What really happened was caused by wave refraction caused by backlash current. This is maybe a very close explanation for this phenomenon.

Comment: However, Dr. Shuto just showed that there is not a single phenomenon, but at least two in that particular configuration which he showed; one on one side of the obstacle and another one on the other. The geometry was different, and probably also the currents. There is not a single explanation. It is a set of mechanisms which, among them, in one proportion or another, may account for the effects observed.

Comment: The tsunami community must deal with the fact there are many mechanisms and many characterizations of individual configurations. It will be the different mechanisms and the different character of the configurations in differing proportions that help one to understand an outcome that occurs at one time and differing outcomes for other cases; it will not have any universal explanation.

TOPIC C: PROTECTIVE MEASURES IN JAPAN AND THE U.S. WITH REGARD TO THE USE OF NUMERICAL MODELS AND THE DESIGN TSUNAMI CONCEPT

C. Mader and G. Curtis, moderators

INUNDATION AND TSUNAMI WAVES

George D. Curtis
Joint Institute for Marine & Atmospheric Research
University of Hawaii
Honolulu, HI, USA

Abstract

If we are able to estimate the height of a wave as it approaches the shoreline, by a simulation or historical reconstruction, we may then be able to determine the resulting inundation onshore, in order to evacuate the people and save lives--the real goal of tsunami research. Methodologies for so doing have been developed with certain constraints and limitations, and lack adequate validation by actual observation. Thus, overly conservative results are often used, causing excess evacuation, construction limitations, or loss of public confidence.

We are applying the best methods available, in Hawaii, with generally good results. But in many locations we need to apply more complex (and expensive) three-dimensional methods and in most areas we need more observations of actual waves to verify or extend our predictions. Examples of the method currently used are given.

Purpose

The goal of tsunami research must always be, first, to save lives and when possible, to reduce property losses. Rapid evacuation of susceptible coastal areas upon a warning is the usual procedure to accomplish this. Obviously these zones must be clearly set ahead of time, must be safe, and yet must be as small as possible to facilitate movement of the populace in the short time available. Valid estimates of the maximum expectable inundation are required for each populated shoreline in tsunami-prone regions.

Definition of such areas has progressed from "low-lying areas" through "up to 50 feet above sea level" to inundation/evacuation zones developed and depicted on published maps. Hawaii is among the few areas in the Pacific which has mapped evacuation zones, but these were incomplete and obsolescent, dating from 1961. Clearly, there was a need to apply the years of tsunami research in this area, for the benefit of this, and other, areas. More formalized methods to determine runup and inundation are available (Table 1).

197

Table 1.

CALCULATION OF RUNUP (R) AND INUNDATION (I..L)

—ONE DIMENSIONAL SCHEMES
—SINGLE WAVE, INDEFINITE PERIOD(S)
—MAX. WAVE HEIGHT AT SHORELINE KNOWN OR ASSUMED (h)
—ON-SHORE TOPOGRAPHY KNOWN

HOUSTON & GARCIA (1974): R = h

CAMFIELD & STREET (1967) - EXPERIMENTAL-
   SIMILAR FOR SLOPES OF ~8°

KONONKOVA & REIHRUDEL (1976): < 8°, R = h; > 8°, R > h

FREEMAN & LE MEHAUTE (1964) - THEORETICAL:

$$\frac{R}{h_s} = \frac{6}{1 + \frac{32g}{C_s^2 s}}$$ WHERE: C_s = CHEZY COEF. (VARIES W/ DEPTH)
   h_s = SURGE HEIGHT

SPIELVOGEL (1975) - THEORETICAL -
   DIVIDED CALCULATIONS BY WAVE / SURGE RATIOS AND
   SHOWED DIFFERENCES W/ BORE:
   R may be much greater than h.

BRETSCHNEIDER & WYBRO (1976)
   DEVELOPED A FLUID FLOW FORMULA FOR A CHANNEL,
   TO BE USED FOR TSUNAMI RUNUP:

$$h_2 = h_1 - [\tan \theta + \frac{n^2 g f^2 h^{-\frac{1}{3}}}{(1.486)^2}] [\frac{f^2}{2} + 1]^{-1} \Delta x$$

(ADOPTED BY CORPS OF ENGINEERS)

Method

The basic two-dimensional method (2-D and 3-D are used here to include the water/land height as well as spatial dimensions) of Bretschneider and Wybro (1976), with minor modifications, was selected for the Hawaii coast. The U.S. Army Corps of Engineers (1977) had already used available historical data from our records in a numerical model to synthesize a wave height contour around the islands. This had been further revised after local review.

With additional historical input and conservative statistics, these provided a reasonably authentic worst-case wave height for any location around the islands, using a 200 year "return time" factor to ensure safety. The contour is checked to ensure it includes the envelope of all credible data we have from the 1946, 1957, and 1960 events; this should be so since it is based largely on our dataset, but a number of exceptions were found.

Transects were drawn on topographic maps at close intervals and the inundation calculated with regard to friction, bore, complexity, etc. Figure 1 is an example of the procedure; a 0.25 mile spacing was used here and is typical.

Where ample, reliable historical data on inundation limits are available to draw a worse-case envelope this may form the basis for the evacuation zone, but Hilo is the only location in the islands where this could be done. However, isolated inundation information elsewhere was compared with calculated limits where available; this showed our results were conservative except in one location (Kaiaka Bay, Oahu). Both there and Hilo Bay are examples too complex for good analysis by two-dimensional methods, which do not allow interaction between sections. Thus, we have a strong interest in using and validating three-dimensional models for special areas.

Figure 1.

Three Dimensional Models

One completed study comparing the 2-D method described above with a 3-D analysis using the non-linear SWAN shallow water code (Mader, 1990) showed good agreement on a specific case with fairly steep slopes. That example was also verified by others with a hydraulic model, but the actual configuration has yet to be constructed.

A more extensive comparison, with historical data, is currently being conducted for Hilo Bay, Hawaii. For this location, we have only fairly good wave height data, but excellent inundation records (Figure 2).

Figure 2.

The time and expense to produce and input a good numerical model of the bathymetry and topography of an area such as this, and run the model, is considerable and can only be justified in complex areas where it is necessary. '

Observational Data

One problem frequently noted in analysis of observational data was confusion of wave height (at the shoreline) and runup height. These factors are best described graphically (Figure 3).

DEFINITION SKETCH
TSUNAMI TERMS
NOTE · R MAY BE GREATER OR LESS THAN h ; DO NOT CONFUSE.
PRESENT WATER LEVEL/LINE MAY BE USED IN LIEU OF MSL, IF STATED.
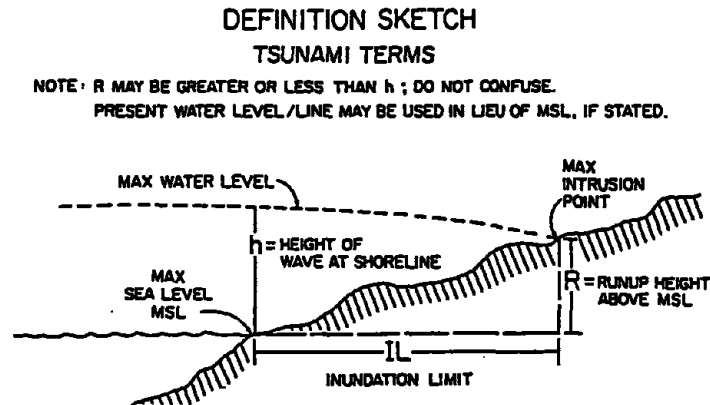
Figure 3.

Careful evaluation of such figures is required. It is usually safe to assume the runup height was the wave height, but this will accordingly produce greater assumed wave heights and an over-conservative analysis in any model. We also note that in most methods only the first, single wave is considered (although in the 3-D SWAN codes successive waves are involved because period is a factor), although statistically the third wave is the highest and also sweeps over an area already wet and damaged.

These problems show the need for more good observational data to provide both input and validation for analyses and models. Lack of such has forced many workers to turn to other types of waves to provide experimental results for tsunamis. The great gap in our actual knowledge is illustrated by Figure 4.

Figure 4.

200
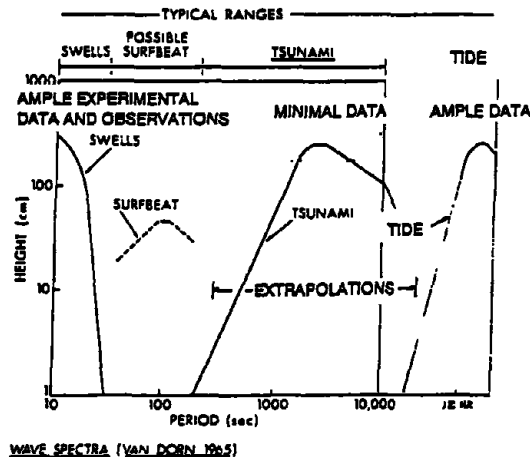
Clearly, these are order-of-magnitude extrapolations, and it is important to gather more real-world data from even small tsunamis, to improve our predictive capabilities.

Figure 5 shows the final result of the work discussed above - a map used to evacuate the endangered areas upon a tsunami warning.
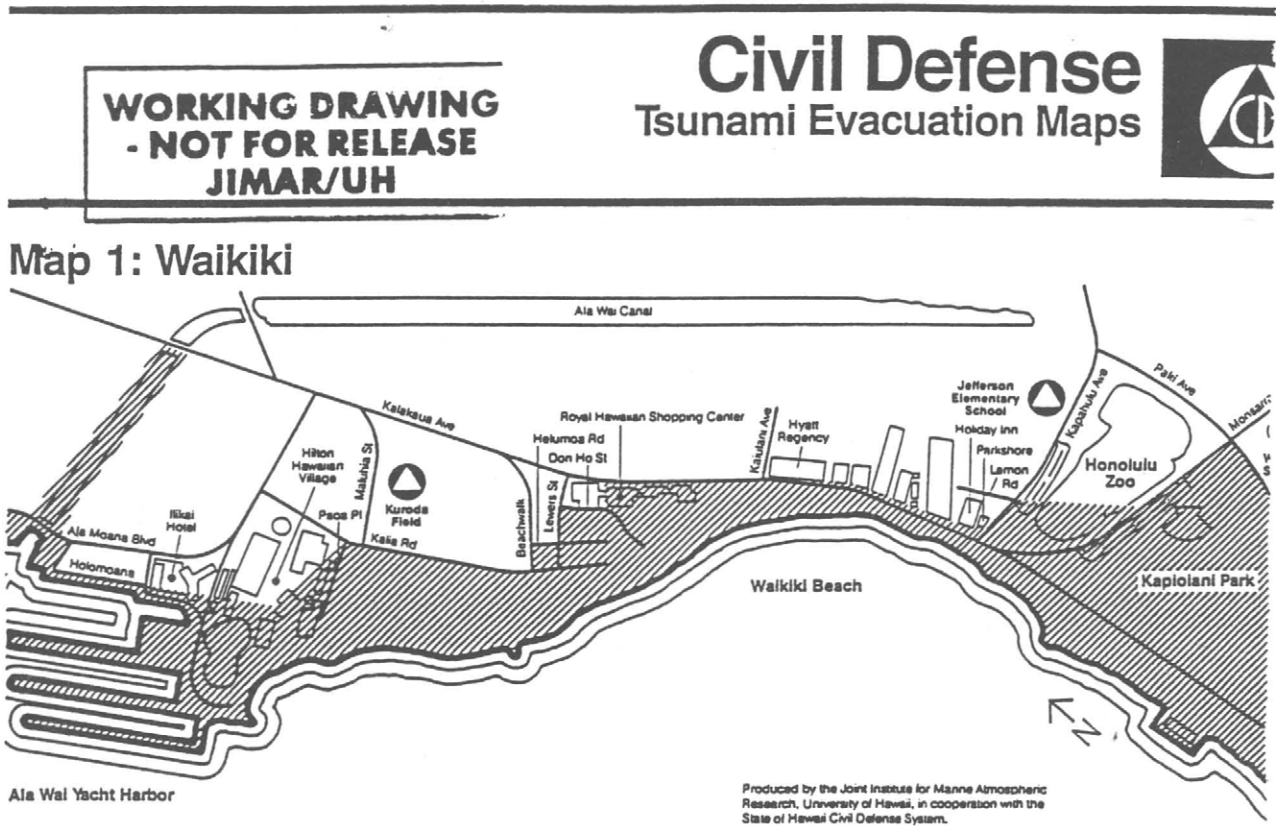
Figure 5.

Conclusions

- Runup (R) is still often confused with coastal wave height (h) in reports--additional analyses are needed to verify values in use

- 2-D models are adequate for most areas, and far easier and faster

- 3-D (SWAN code) models are important for complex areas, but need much more and better source data

- Bretschneider and SWAN results compare well at higher friction (roughness) levels and steeper slopes

- More validation with real-world results is needed to avoid over-conservative, but safe, answers.

References

Bretschneider, C. L. and P.G. Wybro, 1976. Tsunami inundation prediction. In: *Proceedings of the 15th Coastal Engineering Conference*, ASE.

Houston, J.R., R.D. Carver and D.G. Markle, 1977. Tsunami-wave elevation frequency of occurrence for the Hawaiian Islands. *Technical Report H-77-1*, U.S. Army Engineer Waterways Experiment Station, Vicksburg, Mississippi.

Mader, C.L., 1990. Modeling tsunami flooding. *Proceedings of the 4th Pacific Congress on Marine Science and Technology*, Tokyo.

URBAN PLANNING FOR TSUNAMI HAZARDS
GRAYS HARBOR, WASHINGTON AND LIMA, PERU

Jane Preuss
Urban Regional Research
Seattle, WA, USA

Abstract

Grays Harbor, Washington, and Lima, Peru, are used as case examples for application of an urban planning methodology which treats the tsunami/flood event as the initiator of a complex set of interrelated hazards. The integrated methodology considers the tsunami as a <u>system</u> rather than a single physical process. The methodology consists of four components:

- Define characteristics and dimensions of direct tsunami threat
- Define vulnerability patterns based on distribution of population and land use
- Identify potential secondary effects including loss of ground support, battering, and fire
- Microzonation based on two categories of risk reduction strategies
  - damage reduction
  - warning and evacuation

Assumptions

The projects described in this paper developed and applied an urban planning methodology which treats the tsunami/flood event as the initiator of a complex set of interrelated hazards. This methodology is based on the assumption that the physical threat including inundation, strong currents, and a potential for ground subsidence, must be correlated with land use characteristics. An integrated (physical/social/economic) basis is thereby created for projecting potential damage caused by floating debris, fire, and contamination from hazardous substances. In essence, this integrated methodology treats the tsunami threat as a <u>system</u> rather than a single physical process. It also serves to highlight the reality that hazards are cumulative since the water hazard, while itself dangerous, can precipitate still other hazards with even farther reaching consequences.

In order to demonstrate its viability, the methodology has been applied to two very different communities. One is Grays Harbor in the State of Washington with a population of approximately 30,000. The other is Lima, Peru. Greater Lima, with a population of approximately 7,000,000, has experienced both the direct earthquake effects and the impacts of distantly generated tsunamis.

The methodology used by both projects has four underlying components:

- **Define characteristics and dimensions of direct tsunami threat**
  Direction of energy, wave height, run-up and arrival time were estimated.

- **Define vulnerability patterns**
  Land use and population distribution patterns constitute the basis for defining susceptibility.

- **Identify secondary hazards**
  - Secondary hazards include subsidence/ground failure, battering, fire and potential for toxic release.

- **Microzonation for risk reduction**
  - Urban planning strategies include land use, building construction standards, and circulation layouts.
  - Preparedness programs include evacuation routes and warning procedures.

Direct Tsunami Impacts

Characteristics of direct tsunami risks essentially define the geographic area of vulnerability. Delineation of tsunami run-up characteristics therefore constituted the first step of each project. The primary methodological difference in the two case studies was the technique used to project the tsunami threat. Both are described in this section.

In Puget Sound/Grays Harbor the threat was simulated numerically (Hebenstreit, 1988; Hebenstreit and Murty, 1990; Preuss and Hebenstreit, 1990). The simulations indicate that the primary exposure to extreme wave heights are on the outer coasts within the hypothesized source region of a subduction earthquake in the Puget Sound region. This finding generally corresponds to the location of sand lenses discovered on the outer Washington coast at Willapa Bay and Grays Harbor (Atwater, 1987; Bourgeois and Reinhart, 1988). This paleogeologic evidence has been interpreted as the area which experienced tsunami impacts from recurring great subduction events between 1500 and 500 years ago. Figure 1 generally indicates the location of grid points with the greatest exposure.

The interior of Grays Harbor appears to be relatively well protected from a serious tsunami threat. The minimal threat is in part because of its diamond shape which is a 2.2 km narrow configuration at the mouth of the harbor and widens to approximately 21 km, then narrows again at the mouth of the Chehalis River. Another factor contributing to the relatively moderate level of tsunami threat is that extensive shallow mud flats will quickly dissipate a large portion of the wave energy, resulting in reduced wave height inside the harbor. The amplitude continues to decline as the wave travels inland up the harbor to the Chehalis River.

Although simulations were not run under flood conditions, historic flood levels are well documented. For example, Aberdeen has experience serious floods 6 times between 1975 and 1990. The highest river and harbor water states in the Aberdeen area result from a combination of high astronomic tides, low barometric pressure, strong onshore winds, and heavy rains. Tidal influence from Grays Harbor extends up the Chehalis and Wishkah rivers. High river flows often coincide with high tide to increase flooding during winter and spring. These conditions can be aggravated during rainstorms by backup of the city's storm drainage system when intense local runoff is prevented from entering the rivers because of high water.

204

Flooded Blocks, Run 6
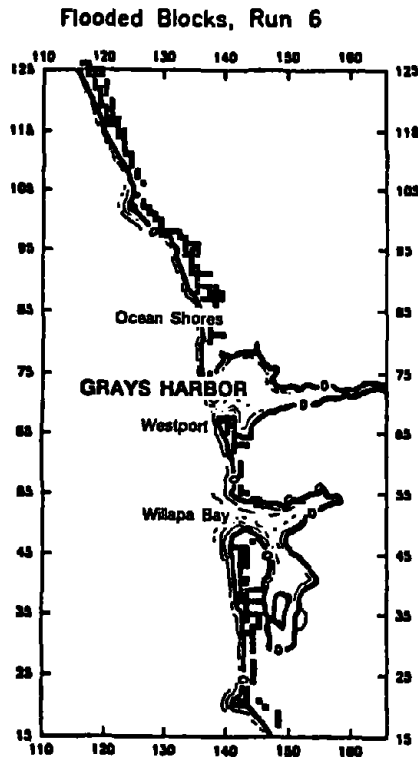
Figure 1. Locations of coastal grid points which
were under water at some time during the simulation.

A tsunami occurring at high tide and/or during near flood levels would arrive when the harbor is significantly deeper than normal. Under these conditions, it would carry more wave energy into the Hoquiam/Aberdeen area. Thus, if the tsunami occurs during high winter tide conditions, the additional 0.5 m could easily overtop and/or weaken the dikes protecting Aberdeen. The drawdown from the first tsunami wave can be expected to cause severe scouring on inland sides of the dikes; the second tsunami wave would probably destroy them. As Figure 2 indicates an initial wave amplitude of 2 to 3 m above the tidal level at the mouth of the harbor would diminish to 0.5 m by the time the incident wave reaches Aberdeen.

Hydrograph Station Locations

**Post Uplift Water Elevations
Along Inner Harbor Shore**
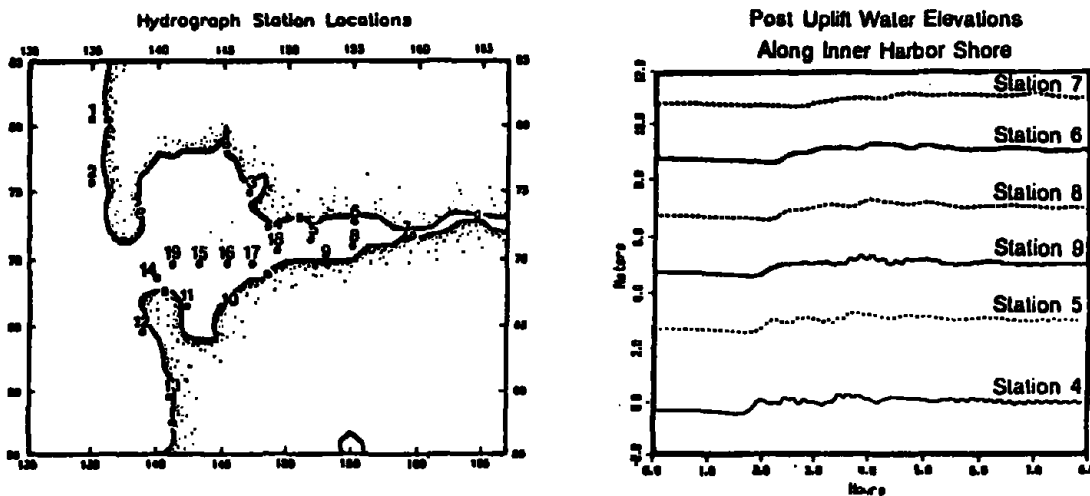
Figure 2. Time series taken at several channel locations during simulation.
(To minimize overplotting, each series is offset by 2 meters from the previous one.)

205

In Lima the tsunami threat could be reconstructed from documented historical records. On October 28, 1746, an 8.4 earthquake occurred 100 km off the coast. The 7 m tsunami inundated and destroyed the low lying portions of Lima called Callao (Figure 3) killing all but 200 of the 4,900 inhabitants.

Severe damage to greater Lima occurred on several other occasions. The most notable events include the 4 meter tsunami of October 20, 1687, generated by an 8.2 earthquake 95 km off the coast, and the magnitude 8.2 earthquake of May 24, 1940, which was centered approximately 200 km north and 40 km inland of Lima. The tsunami was approximately 3.2 meters. Since 1940, thirteen tsunamis have resulted in varying amounts of damage to this low-lying area (Kuroiwa, 1983). Since the 1746 event was considered the maximum possible event, the wave amplitude, inundation limits and estimated arrival time constitute the assumed characteristic for the study.
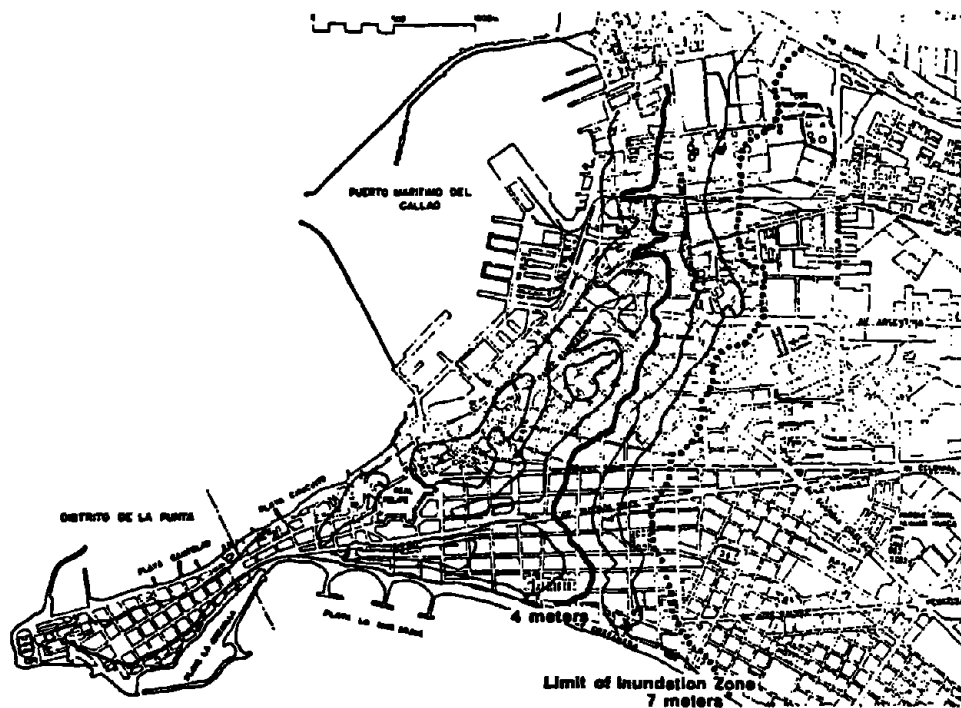
Figure 3. Topography and Inundation Zone: Callao

Vulnerability

The vulnerability analysis consisted of two primary components. One focuses on definition of the population at risk within the inundation area. In Grays Harbor the hazard zone is generally defined as below the 6 m contour; in Lima, below the 7 m contour. In both case study communities, the slope is between zero and two percent. The other component defines land use patterns and identifies specific characteristics of those uses which could result in secondary hazards; for example, presence of stored/or frequently transported hazardous materials.

206

Population

The largest year round population center in Grays Harbor County is the Aberdeen/Hoquiam/Cosmopolis/Montesano area with an estimated population of 30,785 (Washington State, 1990). All three communities are in the inner harbor area. The majority of the residential areas are outside the flood zone.

The 6.5 square kilometer portion of Callao inundated by the 1746 tsunami is inhabited by approximately 150,000 residents. About 90,916 would need to be evacuated. It is estimated that 38,244 persons live in buildings that may be destroyed by earthquake and tsunamis or damaged beyond the possibility of repair. Table 1 shows the estimated losses caused by earthquakes and tsunamis within the boundary of the Callao inundation area. In addition, 67 schools, the Peru Navy Academy, the Maritime Academy, and the nation's principal port and industrial zone are in the inundation experience area.

TABLE 1
VULNERABILITY TO EARTHQUAKE AND TSUNAMI DAMAGE

ZONE	TOTAL RESIDENCES	POPULATION THREATENED	SUSCEPTIBLE TO TOTAL LOSS*	% SUSCEPTIBLE TO MAJOR DAMAGE
1	6,264	6,264	18% (1129)	28
2	3,462	3,462	24% (831)	31
3	5,564	5,564	20% (1132)	30
4	16,368	16,368	35% (5729)	35
5	23,222	11,161	33% (7663)	34
6	13,480	6,740	28% (3774)	29
7	9,189	9,189	54% (4967)	31
8	11,468	9,174	25% (2867)	26
9	19,074	11,444	28% (5340)	32
10	19,250	11,550	25% (4813)	29
TOTAL	127,341	90,916	38,244	30.5

*Number of people who live in buildings subject to collapse or irreparable damage.

Land Use Disruption

In Grays Harbor the primary urban/industrial concentrations of Hoquiam and Aberdeen are on the coastal lowlands. Approximately 25 percent of the workforce in Grays Harbor County are employed in manufacturing activities most of which are located along the shoreline. ITT-Rayonier

and Grays Harbor Paper have a combined pulp and fine paper production facility on the waterfront in Hoquiam. A large wood pulp facility (owned by Weyerhaeuser) is located in South Aberdeen. The port is the busiest port in the Northwest with respect to distribution of northwest produced lumber.

The area of potential inundation encompasses all of the industrial areas, numerous bridges, and the state highway linking Grays Harbor with points to the north and the south. The headquarters fire station in Hoquiam and both fire stations in Aberdeen are within the coastal hazard zone. Correlation of topography with land use shown in Figure 4 permits rapid assessment of geographically based vulnerability.
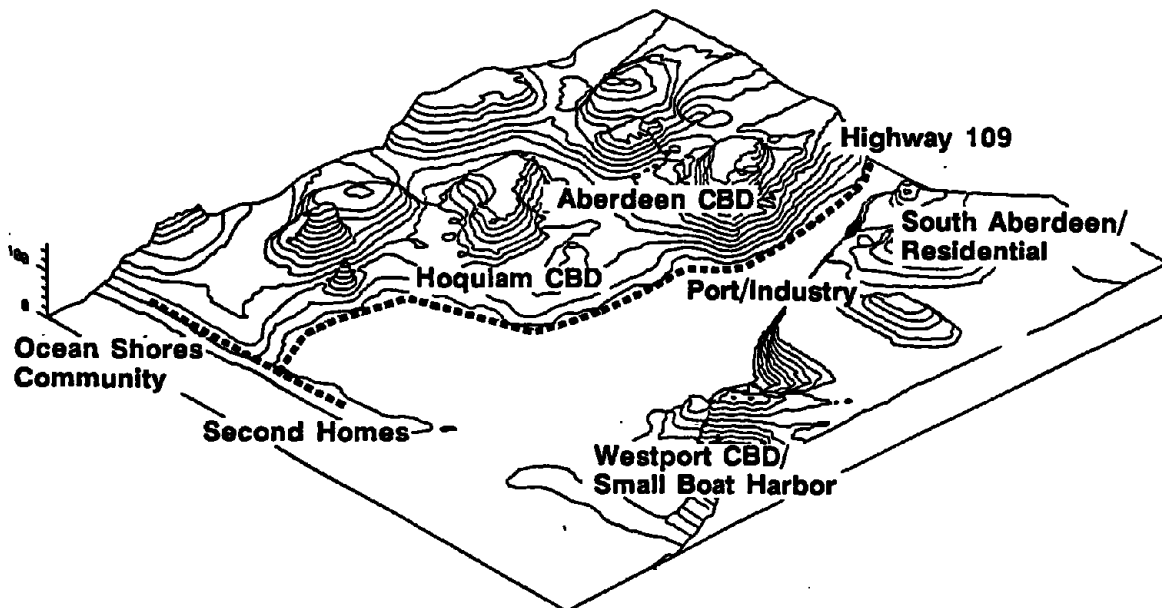
Figure 4. Existing Land Use: Grays Harbor

More than 60% of Peru's export/import volume passes through the port of Callao. The port consists of four subareas:

- the commercial port occupying approximately 60% of the water frontage;
- the navy base occupying approximately 30%;
- the moorage for the fishing fleet occupying the remaining 10%;
- industrial back-up and fuel storage.

The greater port area is extremely congested. Storage facilities for combustible and toxic substances are concentrated in the port and back-up industrial areas. They are virtually surrounded by dense squatter settlements. The fishing fleet lies between the navy base and commercial port. The juxtaposition of uses results in high risk of boats, vehicles or buildings becoming projectiles causing further damage.

In close proximity to the port is the historical zone which consists of the Fort Real Felipe built by the Spaniards and numerous wood frame structures. (It should be noted that the fort withstood the 1746 tsunami.) Once fine manor houses have fallen into advanced stages of deterioration and are occupied by low income tenants. Throughout the remaining area is extensive middle income residential use. The predominant construction types are adobe and brick. A high percentage of buildings have deteriorated through lack of maintenance and damage from past seismic events.

Other assumptions of the scenario are that transportation facilities will suffer damage. This expectation is critical because the main evacuation routes are built on poor soil with organic materials which will also lead to extreme difficulties for search and rescue activities as well as immediate relief. The port of Callao may be out of service because of fire and/or because the docks and piers will be destroyed. Figure 5 indicates land use relationships in Callao.
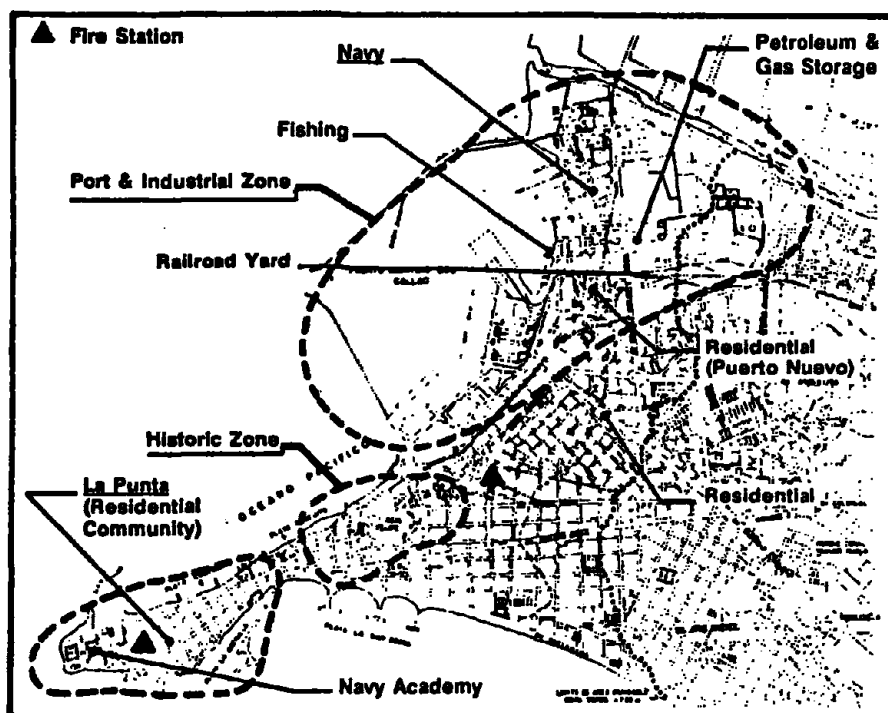
Figure 5. Existing Land Use: Callao

Secondary Hazards

Subsidence

A critical variable in projecting inundation and risk is determination of areas prone to subsidence caused by compaction under strong ground motion and/or tectonic displacement. Coastal subsidence commonly accompanies great subduction earthquakes where coseismic subsidence occurs in a primarily onshore belt flanked by a mostly offshore zone of coseismic uplift (Atwater, 1987). This subsidence is most pronounced in areas of saturated soils. In Grays Harbor the projected inundation areas are predominantly non-engineered fill and/or highly saturated alluviums; both soil types are prone to compaction. For the most part, the Callao peninsula is 1.5 to 2 meters above sea level and the water table is 1 to 2 meters. Soil consists of 6 to 8 meters of medium to small size

gravel overlying 40 to 50 meters of fine particle. Because of the saturated soils, the intensities of past earthquakes have been about 2 MM higher in Callao than in Lima proper.

In both case study areas it can reasonably be assumed that a combination of tectonic displacement, subsidence, and consolidation will occur. It is anticipated that the amount of subsidence will be approximately equivalent to the 1964 Chile, 1969 Alaska, and the Holocene period Puget Sound events. In each of these subsidence events between 1.5 and 2 m of displacement occurred.

⁻ In Grays Harbor the implications of the lowered ground elevation on inundation patterning were assessed. The peak astronomical tide for Grays Harbor coincides with the greatest threat of winter storm surge and rainfall. This combination of factors potentially result in flooding every year between November and February. Ordinary high tides can be approximately 1.6 m at MHHW; an additional 0.5 m of tsunami inundation brings the level to 2.1 m. In the past, flooding problems have developed at 2 to 2.3 m. The extra 0.5 m during winter flood conditions added to 2.3 to 2.6 m ordinary flood would cause severe flooding. Table 2 indicates critical flood levels.

TABLE 2
CRITICAL FLOOD ELEVATIONS

	METERS	FEET
Mean High Tide	1.60	5.10
Tsunami (approx.)	.57	1.60
Subsidence (approx.)	1.50 - 2.15	5.00 - 7.00
Total Susceptible Elevations	2.07 - 2.72	6.60 - 8.50
Critical Flood Levels	2.00 - 2.30	6.50 - 7.50

Low lying areas will be subject to flooding during low tide; during high tide the entire urbanized area will be subject to extensive flooding which, because of the deeper water level, could be relatively high velocity.

Battering

Coastal debris (such as logs, boats, freight cars, vehicles, and storage tanks) can become floating projectiles. In a fishing enclave, the greatest water-related hazard is the fishing boats. Any dockside complex, such as the marinas in Westport, contains boats which, if torn from their moorings by currents set up by rapid rising and falling of sea level, could easily become floating projectiles, capable of damaging not only each other but also coastal structures such as buildings and processing plants.

A wood pulp facility such as the Weyerhaeuser facility in South Aberdeen contains a number of characteristics which could result in a hazard from battering. Most notable are the log piles near the water's edge awaiting processing. Smaller piles could be floated under severe conditions and, like the fishing boats, become projectiles. Vessels moored at the plant's dock could suffer the same fate or be battered by other vessels and/or the logs.

In Lima the risks from floating debris are even more numerous and more damaging. The small boat harbor is surrounded by the industrial port. The fishing boats pose a danger to the flammable facilities and exposed electrical vaults in the port area. Conversely the unanchored or poorly anchored tanks pose a very real threat to the squatter settlements and wood frame historic district adjacent to the port.

Fire and Air Contamination

The primary concern in both study areas is the potential for fire and hazardous material release erupting in the industrial port areas. Such fire would quickly spread out of control beyond its source to neighboring residential and commercial areas posing a significant risk to populations. Although the precise cause and dimensions of fire or contamination have not been predicted, it is clear that toxic chemicals could pose a devastating hazard if, for whatever reason, ground motion, wave action, or flotation, their storage containers were breached.

Grays Harbor is a principal port for the northwest forest products industries, including the manufacture of a wide range of products, for example, wood shakes and paper. An extensive range of chemicals is used. When toxic materials are released through tank rupture or spill, contamination could occur in two ways. One would be contamination of surface and/or groundwater. Surface water contamination would essentially be coterminous with the projected inundation area. The other would be airborne release. Downwind chemical concentrations from a chemical accident in Grays Harbor were simulated using CAMEO's air dispersion model developed by NOAA. Figures 6 and 7 show the extent of potential airborne contamination from a release of 45 kg (100 lb) of chlorine gas at a paper production plant. When reviewing these spill scenarios, it is important to realize that CAMEO tends to understate heavy gases such as chlorine by a factor of approximately two.

In Lima there is a severe conflagration risk within the industrial zone. The risk is a function of the port installations including gas and petroleum storage, military installations, in close proximity to uses that would constitute fuel in the event of ignition (fishing boats, squatter settlements, historic structures).

A case study analysis of blast and bleve (boilover, leakage, explosion) experiences occurring in Mexico, Brazil, and the United States was conducted in order to delineate the boundaries of the blast/fire risk hazard zone. Results of the study indicated three concentric zones of risk: the primary direct blast zone with projected temperatures over 1200, the area vulnerable to exploding and flaming debris, and finally, a zone within which secondary fires could be ignited. Figure 8 illustrates the fire hazard zones.

The Lima industrial and transport intensive area is also vulnerable to hazardous material spills such as from chlorine and ammonia, e.g. railroad derailment or truck overturn. Air contamination plumes for selected chemicals were also projected for nine chemical products using the CAMEO air contamination model developed by NOAA.
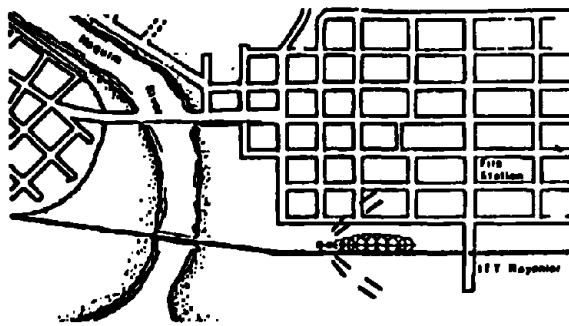
211

IDLH
Immediately Dangerous to Life and Health
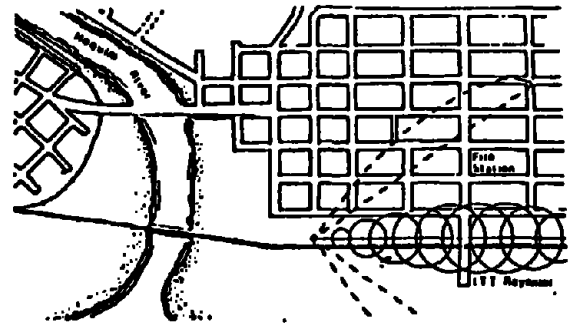
TLV-TWA
Threshold Limit Value - Time Weighted Average

Figure 6. Potential spread of chlorine gas from vicinity of paper
plant under Summer temperature and wind patterns: Grays Harbor
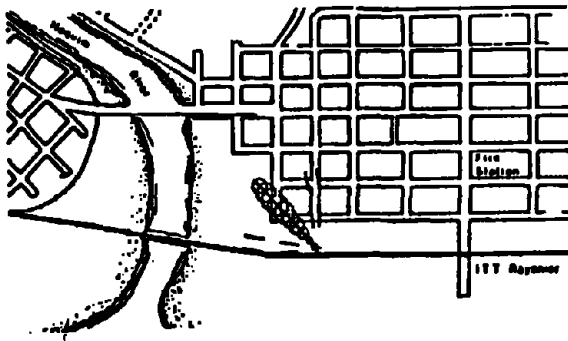
IDLH
Immediately Dangerous to Life and Health
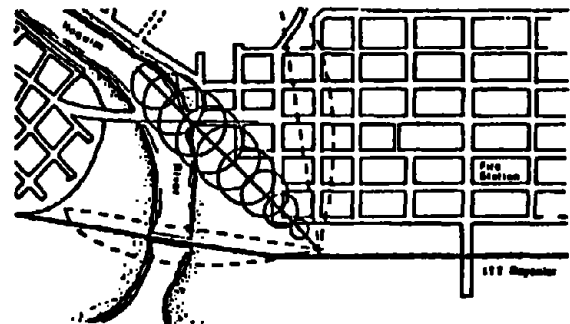
TLV-TWA
Threshold Limit Value - Time Weighted Average

Figure 7. Potential spread of chlorine gas from vicinity of paper
plant under Winter temperature and wind patterns: Grays Harbor

■ SOURCE STRENGTH: 100 pounds

■ TLV-TWA= 1.00 PPM

■ IDLH= 30.00 PPM

■ CHLORINE
Extreme Irritant to mucous membranes; can react to cause fires or explosions upon contact with
some substances; emits highly toxic fumes when heated; reacts with water to produce toxic and
caustic fumes.

212
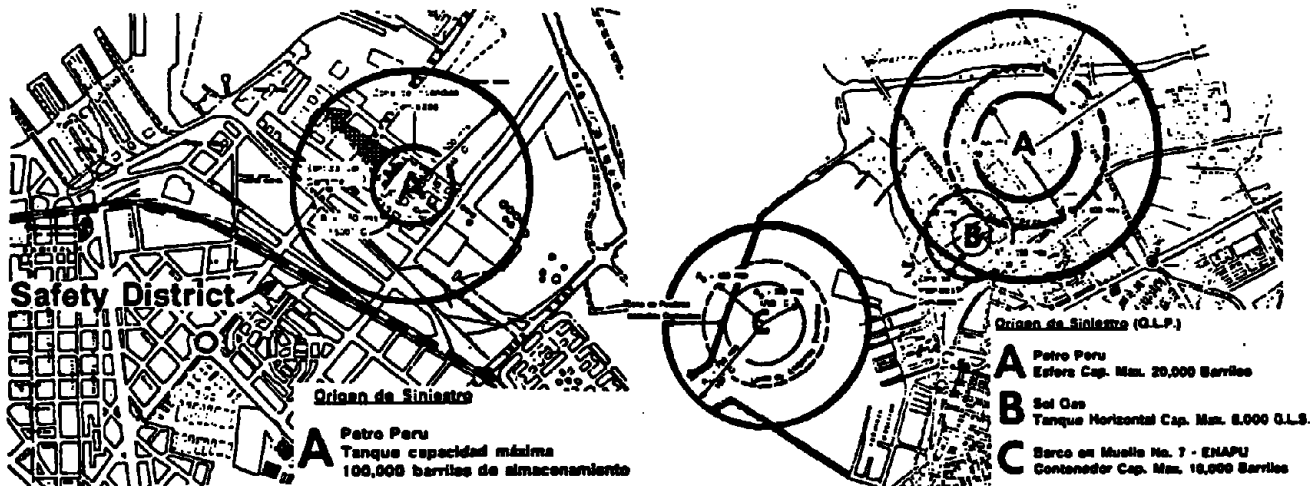
Figure 8. Boundaries of safety zone were determined by the direct fire hazards.

Risk Reduction Program

The hazard and vulnerability analysis has been used for a two part risk reduction program. Part one is a system of zonation which can be used to plan for damage mitigation. Part two is a preparedness plan for warning and evacuation.

Land Use Zonation

Based on differences in vulnerability, land use, socio-economic profile of residents, and governmental jurisdiction, a series of microzones was created for Grays Harbor as shown in Figure 9. The plan consists of short range action measures which could be implemented immediately and long range evolutionary-type recommendations pertaining to changes in land use patterning. This long range planning adopted by the city council would also serve as a guide for construction in the event of a major event.

In Lima, 10 microzones were defined. The most important land use recommendations pertain to creation of a security/safety district when the outer parameter would be defined by the blast zone as shown in Figure 8. Fire potential will be lessened when crowding at the port is reduced and incompatible land uses are eliminated. The plans therefore propose to relocate the navy base, the fishing fleet, and the squatter housing to facilitate this objective.

The main roadways would be widened in order to improve truck access to the port and to create a defined edge to the industrial district which could constitute a fire break. A buffer zone is also needed to separate combustible uses from the remainder of the urban area. The area recommended as the buffer zone is presently, for the most part, the railroad yards. Safety based isolation recommendations are proposed which are based on standards in the U.S. Uniform Fire Code. For example, storage tanks which are less than 30.5 meters from major access routes should be relocated. Figure 10 illustrates the fire district.
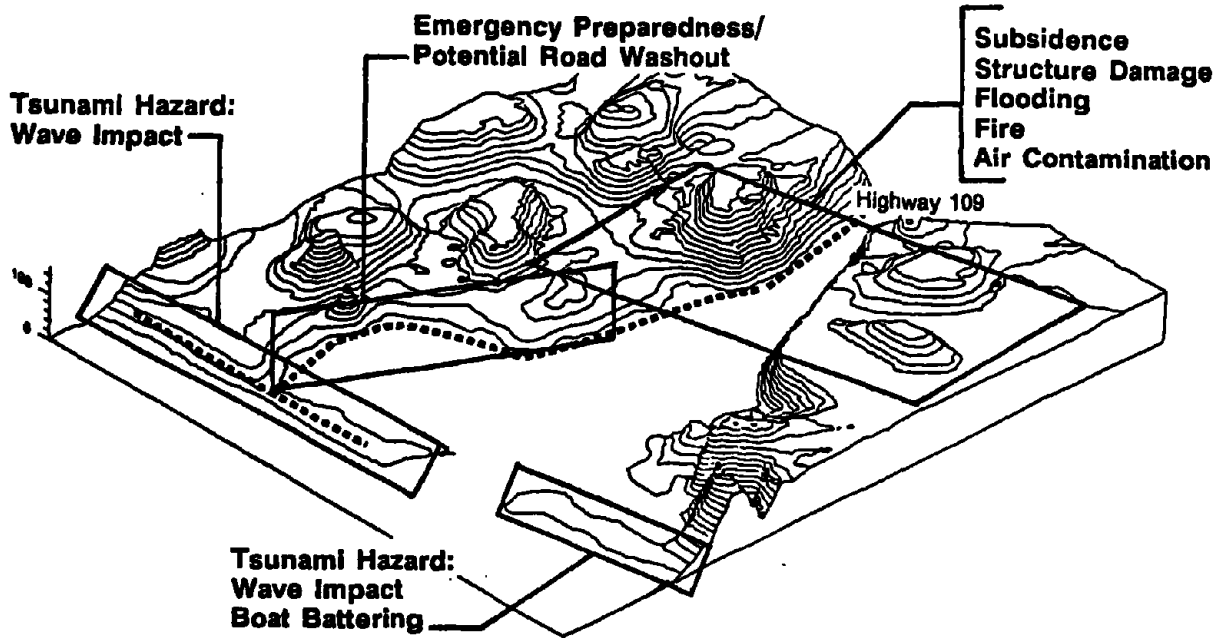
Figure 9. Microzonation of Grays Harbor for Tsunami Hazards.
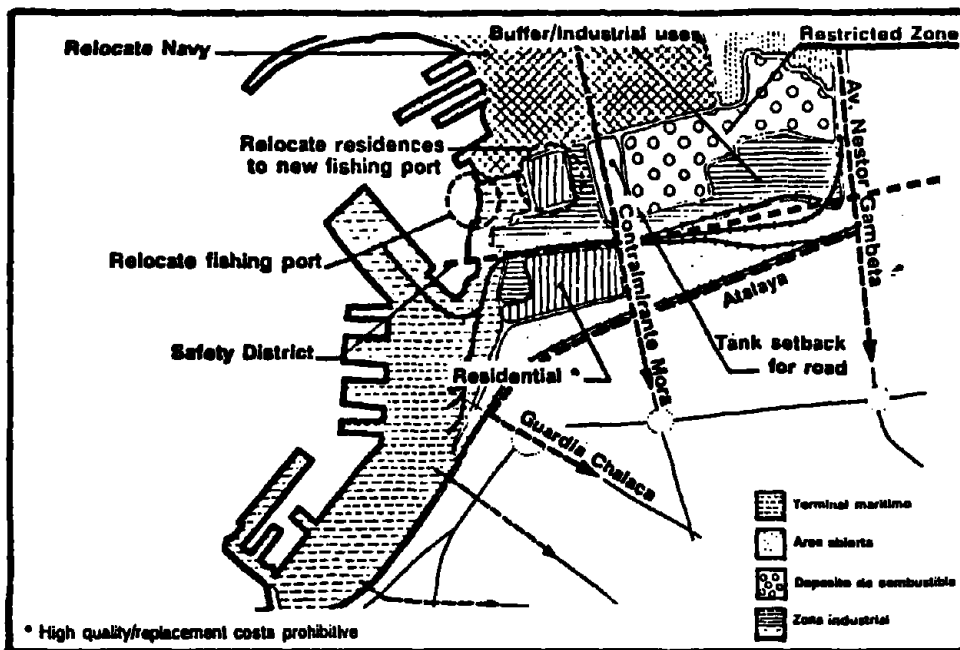
Figure 10. Callao Fire Safety Zone with Inundation Area.

214

Preparedness and Evacuation District

In the event of a tsunami warning, the most effective way to protect lives is to evacuate the inundation zone. This assumes the existence of a warning system, procedures and a network for disseminating the warning information and an evacuation plan. In Grays Harbor County, the population to be evacuated would be approximately 15,000. The preparedness plan develops procedures and routes to evacuate the population to above the 20' contour, which is a distance of approximately 1/2 mile. Communication will be through radio. In Lima, with between 90,000 and 150,000 to be evacuated, and some deficiencies the communication and warning systems, the problems are more complex.

The first step in developing the evacuation plan for Callao was to calculate the number of people who could be evacuated within the estimated 25 minute time. This number was determined by organizing the inundation district into ½ kilometer zones (the approximate distance which can be walked in six minutes) and projecting the travel time of residents in each zone as illustrated in Figure 11.

A drill was then held to verify projected timing and to test the organizational process which had been developed for receiving evacuees. On October 28, 1988 (the anniversary of the 1746 earthquake and tsunami), a practice evacuation drill was performed. The exercise evacuated selected classrooms from each of the 67 schools located in the inundation zone to a designated temporary refuge center. On November 2, 1988, nearly 20,000 students in the 67 schools were evacuated. The Callao Red Cross and the Callao Fire Department collaborated in planning, supervising, and (after the event) evaluating the evacuation exercise.
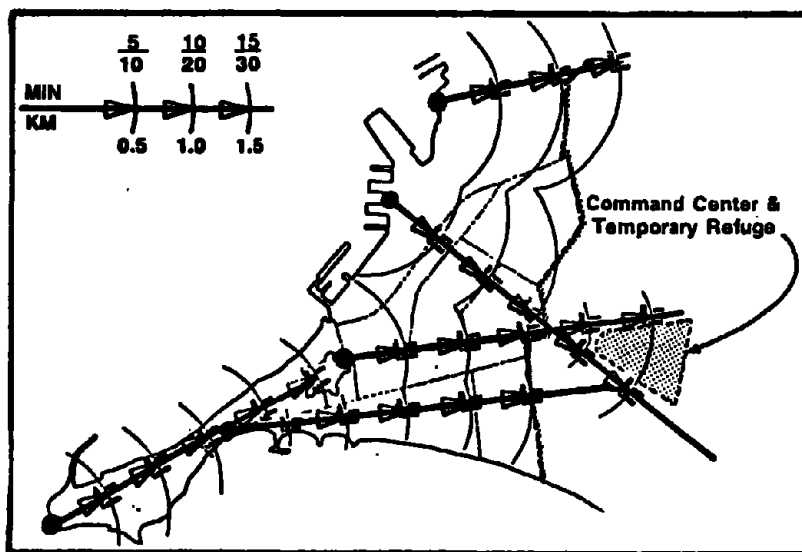
Figure 11. Evacuation/Travel Time Analysis for Callao

The exercise demonstrated that within an estimated twenty to thirty minutes the majority of the population in the inundation zone can be evacuated. Exceptions are the very old and young as well as the handicapped. A supplementary vertical evacuation plan using existing structures over four

215

stories in height was, therefore, prepared for the "special needs" population. Prior to designating the buildings as sites for vertical evacuation, a computerized seismic analysis was conducted of "candidate structures" to verify the presence of sufficient strength to withstand either tsunami impact or a major seismic event. Recommendations were then made for retrofitting selected strategic structures over four stories. Buildings requiring individual evacuation plans and procedures were also identified, e.g., the fire stations within the inundation area, the radio station, and the hospitals.

Evacuation Routes

- Routes designated for pedestrian and vehicular evacuation are primarily the wide avenues which can accommodate movement of large numbers of people. See Figure 12. They are also directly oriented toward the command center/temporary refuge. The primary problem with respect to the street network is that the capacity of evacuation routes must be improved since traffic congestion is severe. The saturated fine soil and organic material have caused settlement throughout the area which has made street maintenance a continuing problem. The project has recommended that street improvement priorities be established in relation to the facility's designated role during evacuation. Another major source of congestion is the high volume of street vendors. It has been recommended that the street vendors be relocated to a market presently being constructed outside of the inundation zone.
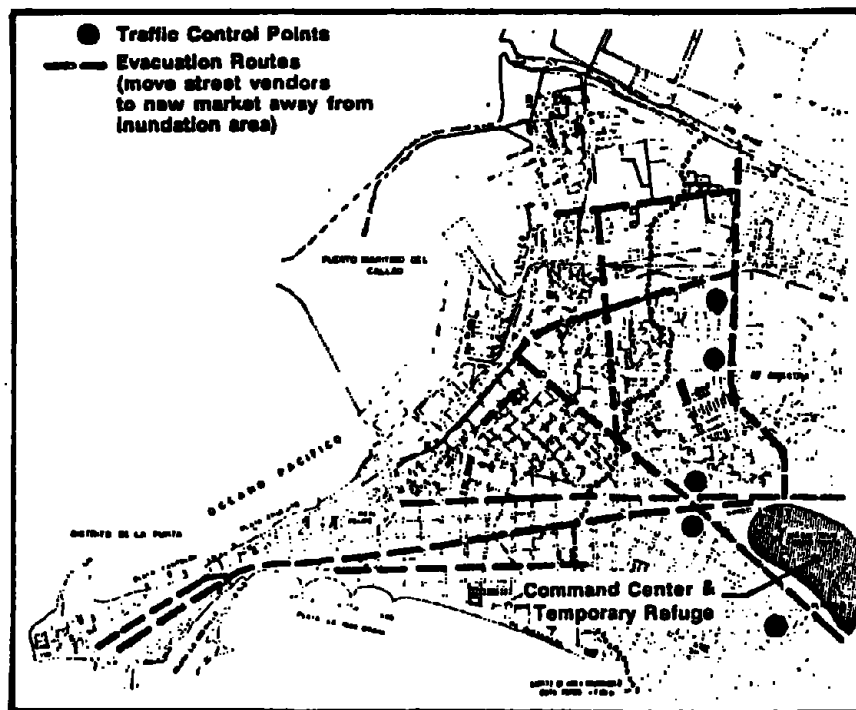
Figure 12. Designated Evacuation Routes for Callao

Conclusions

Since tsunamis are infrequent but potentially very severe events, it is critical that both the capability and commitment to reduction of property damage and loss of life be enhanced. In this

way communities can be encouraged to include tsunamis as an integrated aspect of their emergency planning efforts. Both objectives can be furthered through improved predictive capabilities to project run-up, especially when these estimates take into consideration the range of factors which will influence damage patterns, e.g., influence of riverine flooding or susceptibility to subsidence. There is also a need to address the interaction between the tsunami and the coastal uses, e.g., the potential to spread toxic contamination and/or fire. Finally, enhanced ability to predict arrival time is a critical aspect of an improved warning system. Warning and evacuation planning can then be coordinated with transportation planning and with procedures for preparedness.

Acknowledgements

Selected References

Atwater, B.F., 1987. Evidence for great Holocene earthquakes along the outer coast of Washington State. *Science*, no.236, p.942-236.

Bourgeois, J. and M.A. Reinhart, 1988. Potentially damaging waves associated with earthquakes, coastal Washington. In: *Workshop on Evaluation of Earthquake Hazards and Risk in Puget Sound and Portland Areas. Proceedings. U.S. Geological Survey Open File Report*, 88-541, p.96-99.

Heaton, T.H. and H. Kanamori, 1984. Seismic potential associated with subduction in the northwestern United States. *Bulletin of the Seismological Society of America*, 74(3), p.933-941.

Hebenstreit, G.T., 1988. Local tsunami hazard assessment for the Juan de Fuca Plate area. McLean, Virginia, Marine Analysis Division, Science Applications International Corporation. *U.S. Geological Survey, Technical Report*.

Hebenstreit, G.T. and T.S. Murty, 1990. Tsunami amplitudes from local earthquakes in the Pacific Northwest Region of North America. Part I: The outer coast. Submitted to Marine Geodesy.

Kuroiwa, J.H., 1983. *Tsunamis Effectos Sobre Los Costas de Lima Metropolitana*. Auspiciado por la Officina de Naciones Unidas para la Atencion de Desasters UNDRO.

Plafker, G., 1969. Tectonics of the March 27, 1964 Alaska earthquake. *U.S. Geological Survey Professional Paper*, 543-I.

Preuss, J., 1987. Coastal high hazard mitigation: comprehensive planning for areas vulnerable to tsunamis. In: *American Society of Flood Plain Managers. Proceedings*, p.317-322.

Preuss, J. and G.T. Hebenstreit, 1989. The tsunami threat in the Pacific Northwest under today's land use conditions. In: *Third Annual Puget Sound/Portland Area Workshop on Earthquake Hazards. Proceedings.*

Preuss, J. and G.T. Hebenstreit, 1991. Integrated hazard assessment for a coastal community: Grays Harbor. In: *U.S. Geological Survey Professional Paper on Subduction Zone Earthquake Hazard in Puget Region.* (In Press)

Preuss, J. and J. Kuroiwa, 1990. Urban planning for mitigation and preparedness: the case of Callao, Peru. *U.S. National Conference on Earthquake Engineering, 4th, Radisson, Palm Springs, California, 20-24 May 1990.*

Reinhart, T.J. and J. Bourgeois, 1987. Distribution of anomalous sand at Wallapa Bay, Washington, evidence for large scale land/word directed process (Abstract). *EOS*, 68(44), p.1469.

Urban Regional Research, 1986. *Hazard Mitigation and Preparedness Plan: City of Aberdeen.* State of Washington, Department of Emergency Management, Federal Emergency Management Agency.

Washington State Office of Financial Management, 1990. *Population Estimates.*

Discussion

Question: Are vehicles to be used for the evacuation of Callao, Peru?

Response: Evacuation will be by foot. There was a plan initially that permitted some vehicles, but that meant that there would be one-way streets and unusual traffic patterns. It was decided that a stressful time is not a good time to change traffic patterns. Emergency vehicles have to get in there and there is need to evacuate the invalids and elderly. The other reason is that in case of a fire, emergency vehicles need access.

Question: How much traffic was invisioned and are there any plans for a drill?

Response: There have not been any drills. In Peru, the Ministries have participated in different aspects. In Washington, the county and local city council have adopted an evacuation plan, but no one has had any drills.

Question: Is it possibile to use the entire floor of a substantial building as a shelter in Peru?

Response: In Peru, buildings were identified that were substantial and a survival analysis of those buildings was done to see which could be designated as refuge sites. The problem is that with the current terrorism and unrest, it is difficult for a non-resident to gain access to a building.

OCEAN BOTTOM PRESSURE GAUGE FOR TSUNAMI WARNING SYSTEM IN JAPAN

Masami Okada
Meteorological Research Institute
Tsukuba, Japan

Introduction

The Japan Meteorological Agency (JMA) has been routinely operating two Permanent Ocean Bottom Seismograph Systems (OBS). One was developed and installed off Cape Omaezaki in 1978 by the Meteorological Research Institute (MRI, 1980). The other was deployed by the Headquarters of JMA in 1986 off the Boso Peninsula, Kanto District. The OBS off Cape Omaezaki has four seismographs and one pressure gauge for detecting tsunamis, and another system has four seismographs and three pressure gauges. In the USA, Deep Ocean Bottom Pressure Recorders (BPR) have been developed and are operating in PacTOP Project (Gonzalez et al., 1987). These BPRs are a pop-up system and the records should be retrieved one year after the deployment. The OBS system of JMA has a long cable for transmitting signals to the station on land. It is mainly used for operational works such as tsunami warning and earthquake prediction. The tsunami data obtained with OBSs are, of course, very useful for tsunami research.

System

Figure 1 shows the concept of the OBS laid off Cape Omaezaki. Four apparatuses on the sea bottom are linked in series to the shore monitoring stations by submarine coaxial cable, in which the signals are transmitted in real time. Electric power is supplied through the same line by a DC constant current and its circuit is completed through a ground electrode buried in the beach at Omaezaki. The pressure gauge to observe tsunamis is kept in the terminal apparatus. The OBS off the Boso Peninsula is very similar to the one at Omaezaki except that sensors for pressure and temperature are put in the cases at three points different from the seismographs.

Signals from both OBSs are monitored at the shore stations, at Omaezaki and Katsuura, then telemetered to the tsunami warning center in the JMA headquarters over telephone lines. All data on water pressure are processed and preserved on magneto-optical disk by the Earthquake Phenomena Observation System (EPOS) at JMA. Locations of the pressure gauges are listed in Table 1 and also shown in Figure 2. Cables were put on rather gentle bathymetry and they are about 150 km and 120 km long for the Omaezaki and Boso systems, respectively.
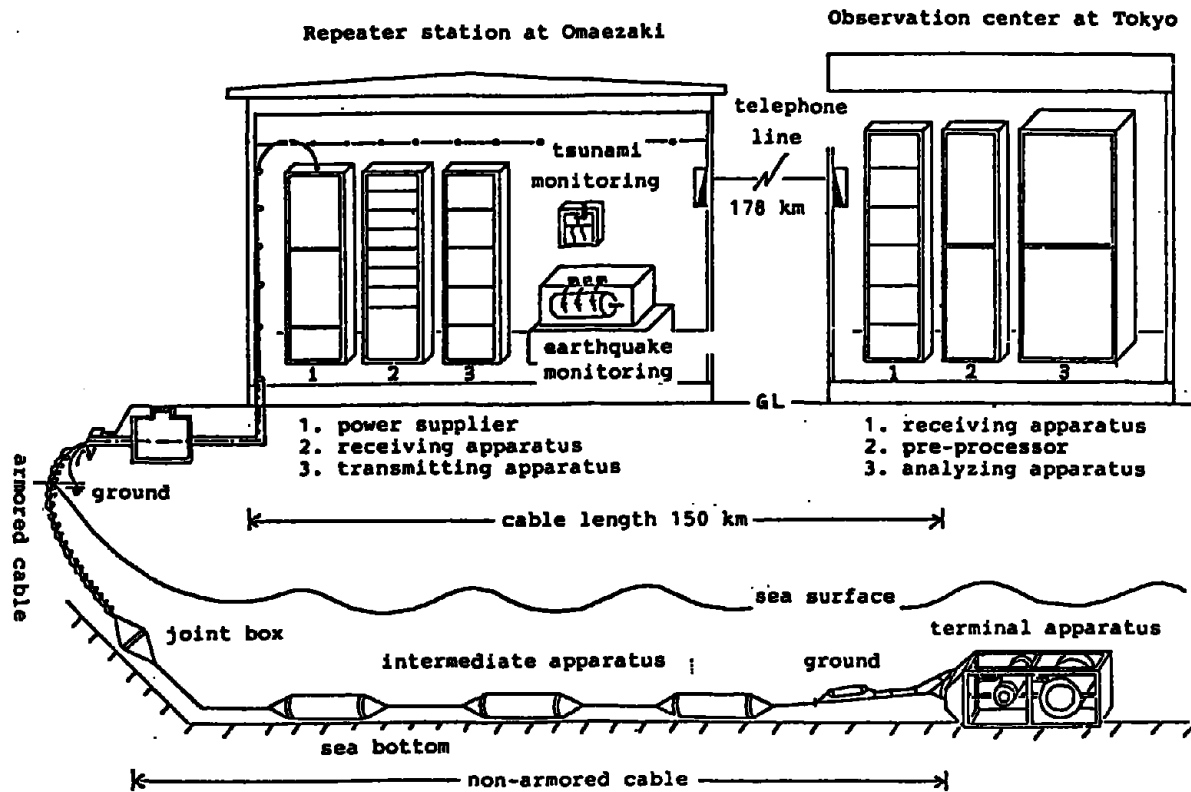
Figure 1. Ocean bottom seismograph system off Cape Omaezaki. Seismographs are kept in the intermediate apparatus and the terminal one, and the pressure gauge (tsunami-meter) is stored in the terminal one.

Table 1. Locations of ocean bottom pressure gauges.

station	latitude	longitude	depth
TKI	33 45.90'N	137 35.38'E	2,202m
BSI	34 39.21'N	140 58.68'E	4,011m
BS2	34 44.95'N	140 45.49'E	2,098m
BS3	34 47.97'N	140 30.70'E	1,912m

We use the quartz sensor made by Hewlett Packard Co., Ltd., in USA. Output frequency from the sensor, f, in Hertz is given as

$$f = 8,000 + 20.0 \ (Tr - 0.99 \ Ts) + 2.0D \tag{1}$$

where Ts and Tr are the temperatures of the quartz pressure transducer and quartz temperature compensator stored in a closed case, respectively. D is water depth in meters. Non-linearity due to temperature must be negligible, since it is used in deep water where the temperature is fairly stable. Output frequency depends not only on pressure but also on temperature. Frequency is determined by measuring the mean time interval of pulses in the period of 1 sec for low gain and 20 sec for high gain, respectively. The resolution is 1 cm in sea level change (1 mb) for low gain and 0.5 mm (0.05 mb) for high gain.

The pressure response on the bottom to sea surface waves depends on the wave length and water depth. The ratio of pressure at the bottom in meters of water to surface wave height is

$$R = sech \ (2\pi h/L) \tag{2}$$

where h and L are water depth and wave length, respectively. Figure 3 shows frequency response for OBS pressure gauges. We cannot expect to observe waves shorter than a few minutes in period.

Thermally induced fluctuation of output frequency is mostly derived from the difference between Tr and Ts in equation (1), generated by environmental water temperature change. If water temperature changes suddenly, the output data fluctuate for about one hour.

Tsunami Records

The OBS systems have observed two cases of tsunamis that have traveled long distances. From a large earthquake, Ms 7.5, which occurred near the Aleutian Islands on May 7, 1986, a small tsunami of about 20 cm in total amplitude was observed at many tide stations along the Japanese Islands. We can find the fluctuation of the tsunami on the record of the BS3 tsunami-meter shown in Figure 4. The amplitudes of the tsunami are much smaller at the deep sea than at the coast. As we did not have a digital data recorder for the tsunami-meter on that day, we cannot look at the details of the tsunami.

On April 5, 1990, another small tsunami was generated by an earthquake of Ms 7.5 near the Mariana Islands, and it was observed at many stations in Japan. Some traces are shown in Figure 5, which are represented from the data base on the optical disk; the refraction diagrams are drawn in Figure 6. In Figure 5 four traces on the upper side are pressure records on the sea bottom, and the others are sea level fluctuations measured at some tide stations. We can find in the records of the OBS tsunami-meter not only sea level changes, such as tide and tsunami, but also thermally induced fluctuations and pressure variations caused by ground motion. Traces at TK1 and BS1 show the ocean tide fairly well, however the ones at BS2 and BS3 are surely deformed by thermally induced effects. Another type of thermal noise appears around eight o'clock and continued for about two hours on the records of TK1. Ground motion noise begins at the same time as the earthquake at 6:13 on April 6, JST (9 hours ahead to Greenwich Mean Time) and continues for about two hours. This noise is larger, as the water is deeper. Tsunami waves can be seen for several hours from about ten o'clock, however the amplitudes in the deep sea are much smaller than sea level fluctuations at the tide stations.

221
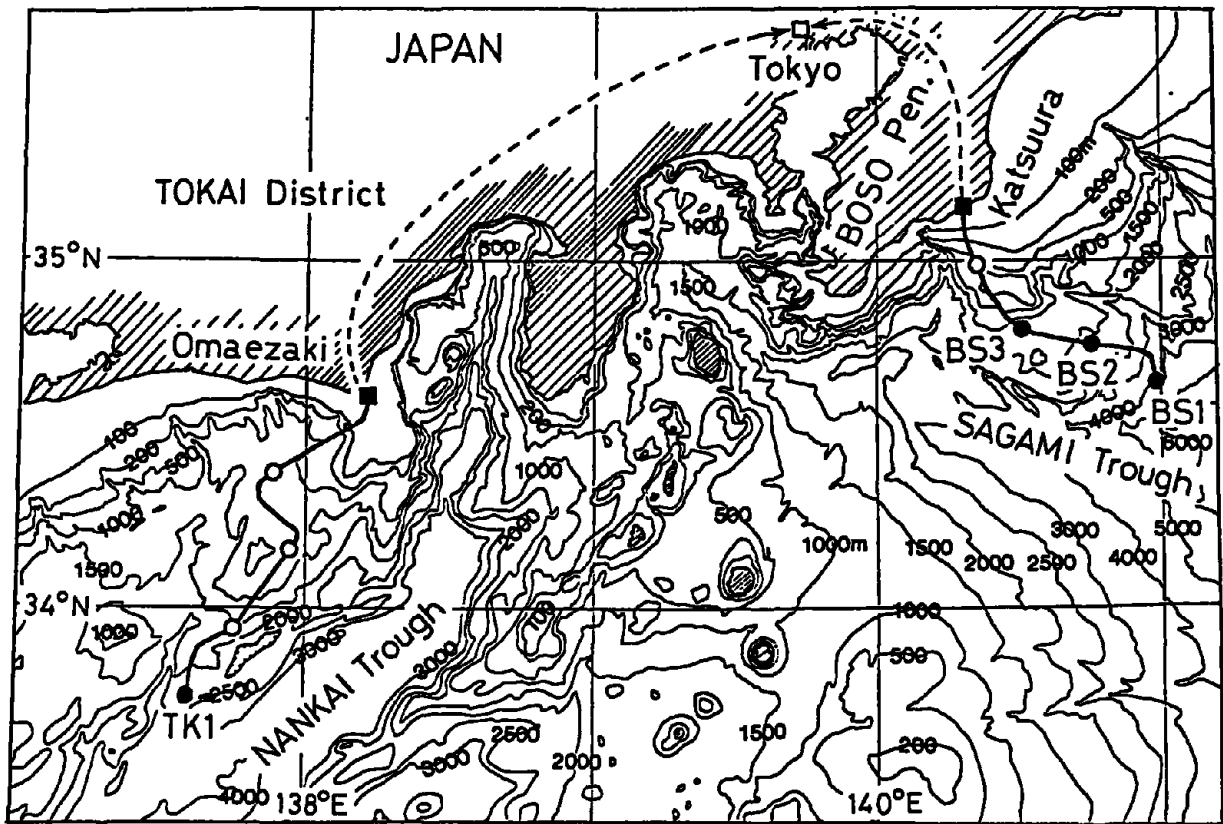
Figure 2. Bathymetry and cable routes of ocean bottom seismograph system. Seismographs are laid at the open and closed circles and tsunami-meters are installed at the closed ones.
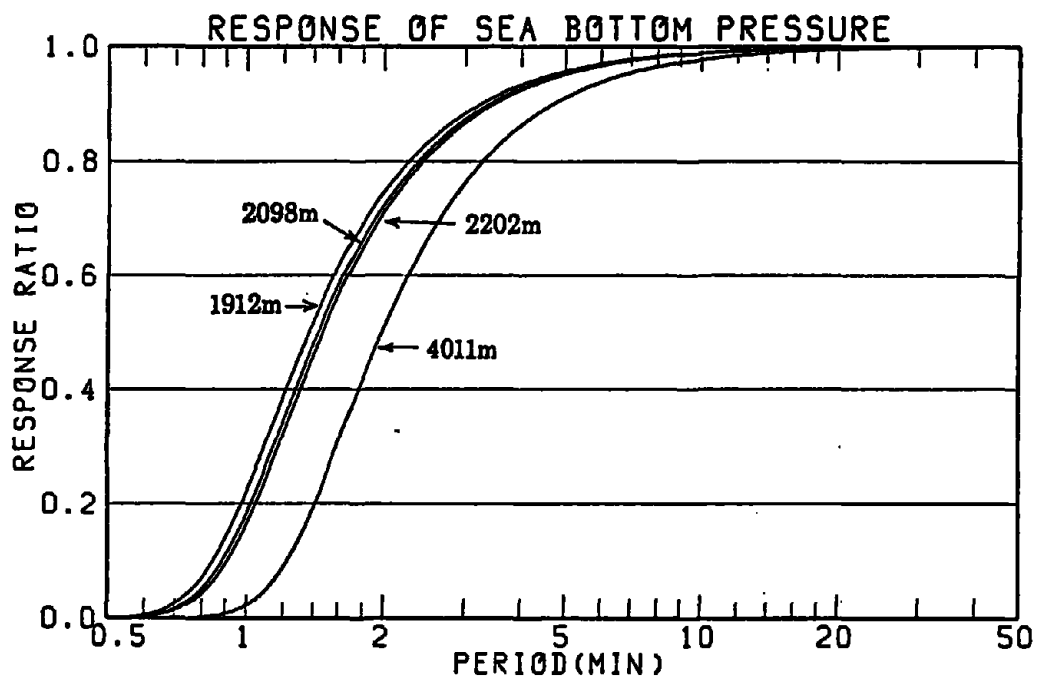
Figure 3. Frequency response of bottom pressure to sea wave at depths of tsunami-meter.

222
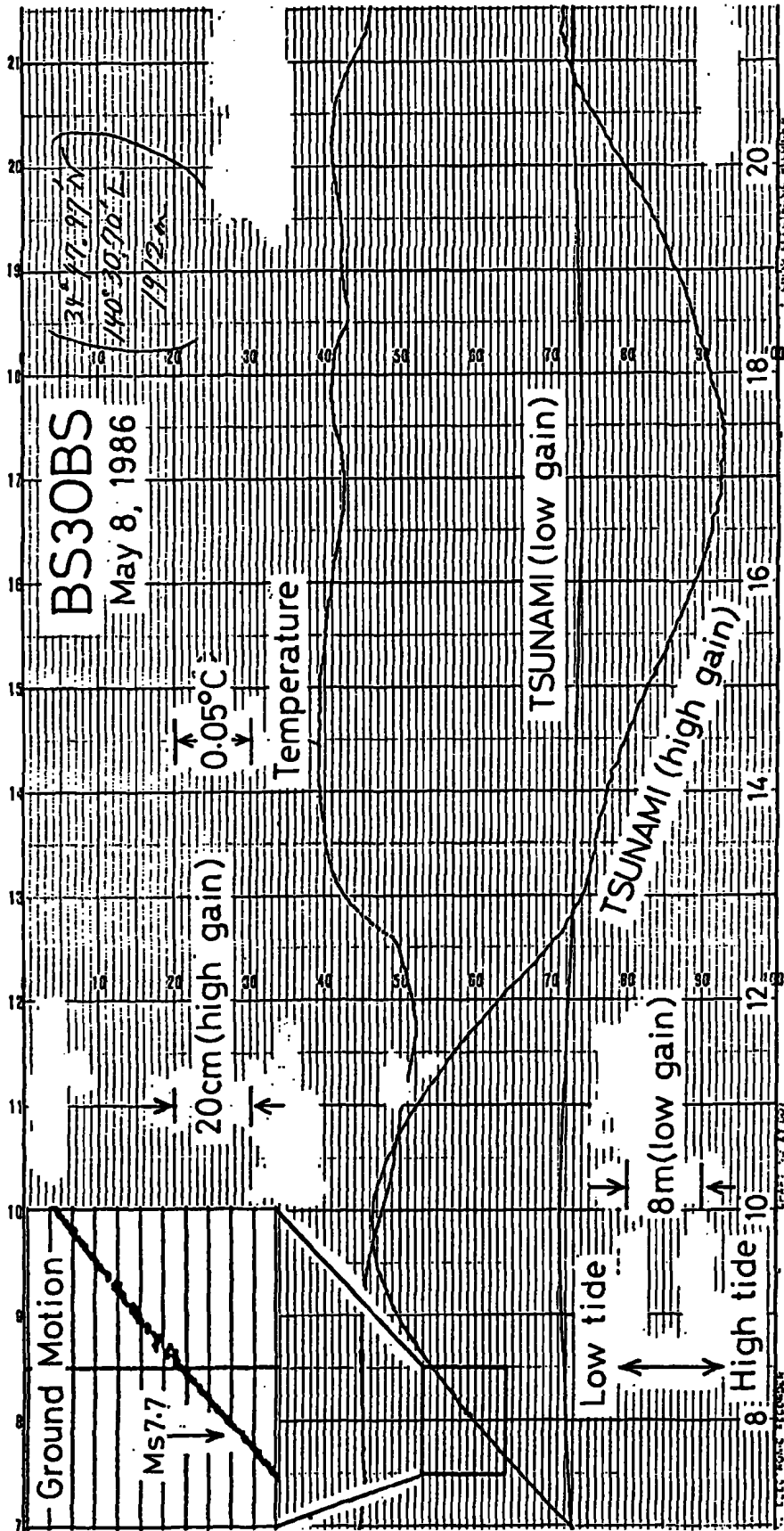
Figure 4. Small tsunami accompanying the earthquake of M7.5 which occurred near the Aleutian Islands. Noise, shown in inlet figure, is induced by ground motion.
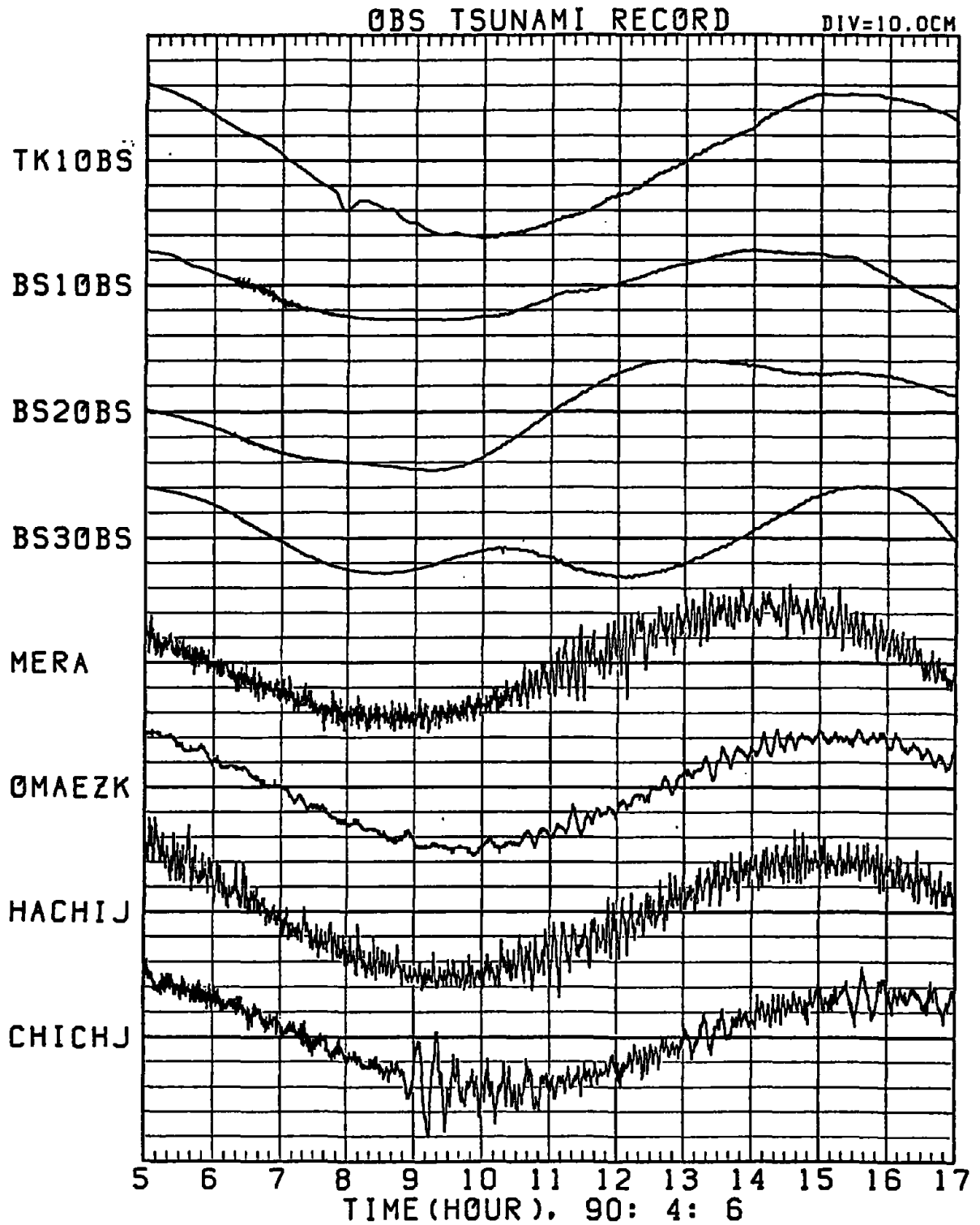
Figure 5. Tsunami-meter and tide gauge records for Mariana tsunami. Upper four traces are pressure on the sea bottom, others are sea level at tide station. Horizontal axis is the Japan Standard Time.

224
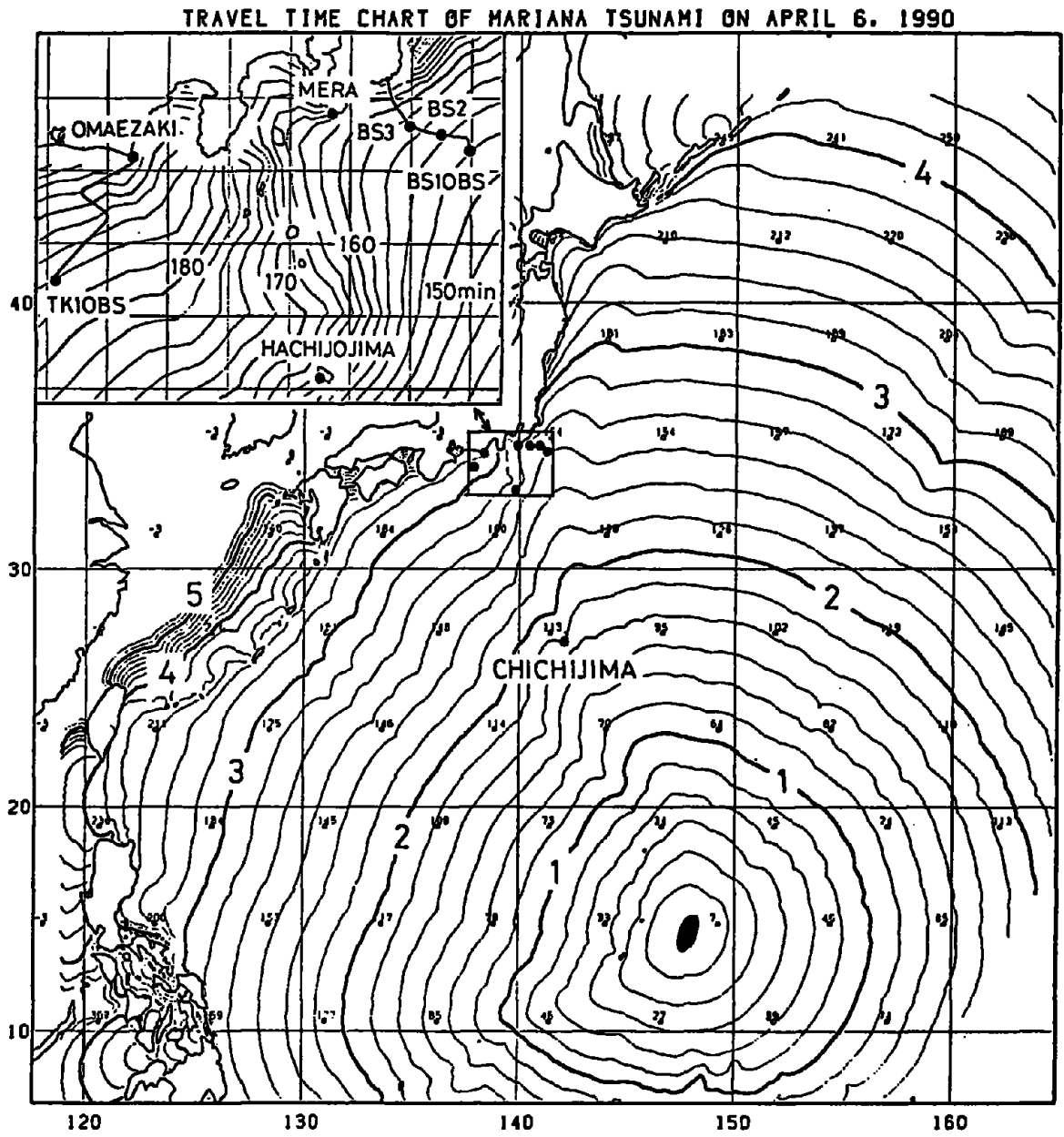
Figure 6. Refraction diagram of Mariana Tsunami on April 5, 1990.
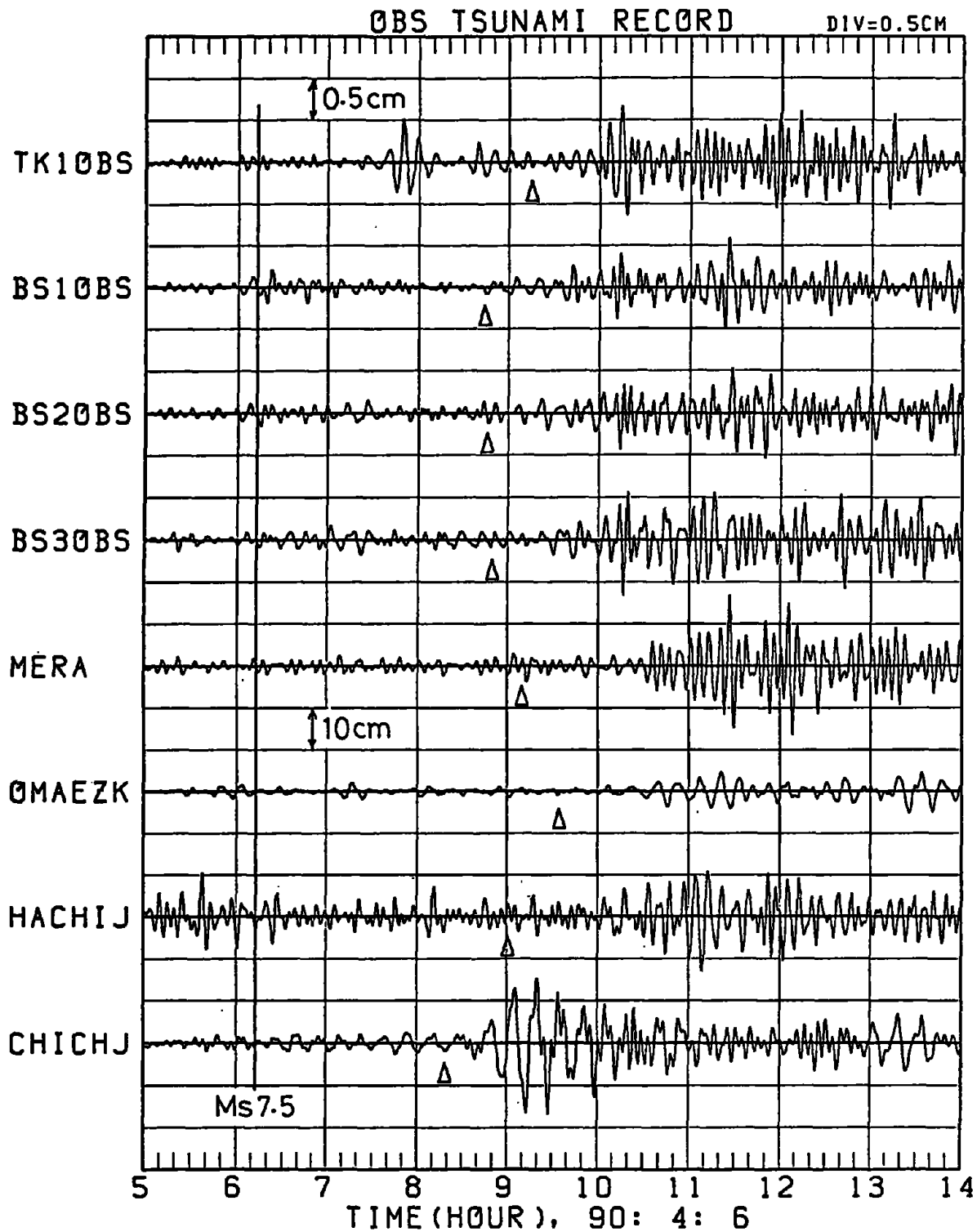
Figure 7. Mariana Tsunami records processed by a band pass filter of 4 to 17 min (4 to 11 min for TK1OBS). One division corresponds to 0.05 mb for OBS tsunami-meters and 10 cm for sea level at tide stations.

Tsunami waves are processed by a band pass filter (Butterworth BPF) of 4 to 17 minute except for the one at TK1, for which a narrow band from 4 to 11 minutes is applied for suppressing thermally induced noise. Filtered waves are shown in Figure 7 in which records of the tsunami meter are substantially multiplied by 20 in amplitude in comparison with ones at the tide station. Triangles indicate the tsunami arrival time estimated with the travel time charts. A forerunner observed at stations around the Japanese Islands propagated in a deep ocean trench, so it was very small in amplitude. Large waves slowly traveled in shallow water along the Izu-Mariana Ridge and arrived late. This fact has been revealed with numerical simulation by Satake et al. (1990). Envelopes and the predominant period of tsunamis recorded by a tsunami-meter off the Boso Peninsula are fairly similar to the one at Mera. However, the tsunami at Omaezaki is much smaller than at Mera and has quite a different waveform from the one near OBS station, TK1. The station at Mera is in a small port facing the open ocean, and the one at Omaezaki is located at the head of a rather larger port which has long breakwaters and relatively smaller mouth backing to the Pacific Ocean.

Tsunamigenic earthquakes occurred east off the Sanriku Coast, northeast of Honshu, on November 2, 1989, and south off the Tokai District, south of Honshu, on September 24, 1990. Those tsunamis were observed at some tide stations near the source, but it is difficult to find traces of their effects on the tsunami-meters.

References

Gonzalez, F.I., E.N. Bernard, H.B. Milbum, D. Castel, J. Thomas, and J.H. Hemsley, 1987. The Pacific tsunami observation Program (PacTop). *Proc. Inter. Tsunami Sympo. 1987, Vancouver, Aug. 18-19*, pp. 3-19.

Meteorological Research Institute, 1980. Permanent ocean-bottom seismograph observation system. *Tech. Rep. MRI*, vol. 4, 233 pp. (In Japanese with English abstract.)

Satake, K., Y. Yoshida, and K. Abe, 1990. Mechanism of Mariana earthquake (2) – Analysis of tsunami waveforms – . *Proc. Seismo. Sci. Japan*, No. 2, A70, 70 p.

AUTOMATIC ESTIMATIONS OF TSUNAMI RISK FOLLOWING A DISTANT EARTHQUAKE USING THE MANTLE MAGNITUDE M_m

Emile A. Okal
Department of Geological Sciences
Northwestern University
Evanston, IL, USA

Jacques Talandier and Dominique Reymond
Laboratoire de Géophysique and Centre Polynésien de Prévention des Tsunamis
Papeete, Tahiti, French Polynesia

Abstract

We have developed a new magnitude scale, M_m, based on the measurement of mantle Rayleigh wave energy in the 50 to 300 s period range, and directly related to the seismic moment through $M_m = \log_{10}M_0 - 20$. Measurements are taken on the first passage of Rayleigh waves, recorded on-scale on broadband instruments with adequate dynamical range. This allows estimation of the moment of an event within minutes of the arrival of the Rayleigh wave, and with a standard deviation of ±0.2 magnitude units. In turn, the knowledge of the seismic moment allows computation of an estimate of the high-seas amplitude of a range of expectable tsunami heights. This method, combined with automatic detection and location of distant epicenters, has been integrated into an automated procedure of tsunami warning by the Centre Polynésien de Prévention des Tsunamis [CPPT], in Papeete, Tahiti.

Introduction

In this paper, we report on an automatic method to determine in real time the seismic moment of a distant earthquake, and an estimate of its tsunami risk, based on a one-station analysis of mantle Rayleigh waves recorded on broadband instruments. Combined with automatic event detection and location, it has been implemented since November, 1987 at the "Centre Polynésien de Prévention des Tsunamis" [CPPT], operated by the Geophysical Laboratory in Papeete, Tahiti. A more detailed description of the algorithm can be found in *Talandier and Okal* [1989] and *Reymond et al.* [1991].

This paper is not concerned with effects such as the so-called "run-up" which amplifies the wave in shallow water, and resonance due to the particular shape of bays and harbors; the latter can be successfully modeled through computational techniques, such as finite element codes, given an adequate model of coastal bathymetry. Rather, we focus on what amounts to the seismological input (as a space-time boundary condition) to such calculations, namely the relationship between the parent earthquake and the amplitude of the tsunami on the high-seas, prior to the initiation of run-up.

The Importance of the Seismic Moment M_0.

About twenty years ago, *Aki* [1967] introduced the seismic moment M_0 as a physical measurement of the "size" of an earthquake, and later, *Kanamori* [1972] and *Abe* [1973] identified M_0 of the parent earthquake as the major factor controlling tsunami generation. Figure 1 gives an example of the linear correlation between seismic moment and tsunami amplitude (in this case at Papeete, Tahiti, where run-up and resonance effects are minimal). That the static seismic moment (ideally measured at zero-frequency) should control the excitation of tsunamis, expresses their very low-frequency character, with most of their energy typically concentrated around 1 mHz.

17 TSUNAMIS AT PAPEETE
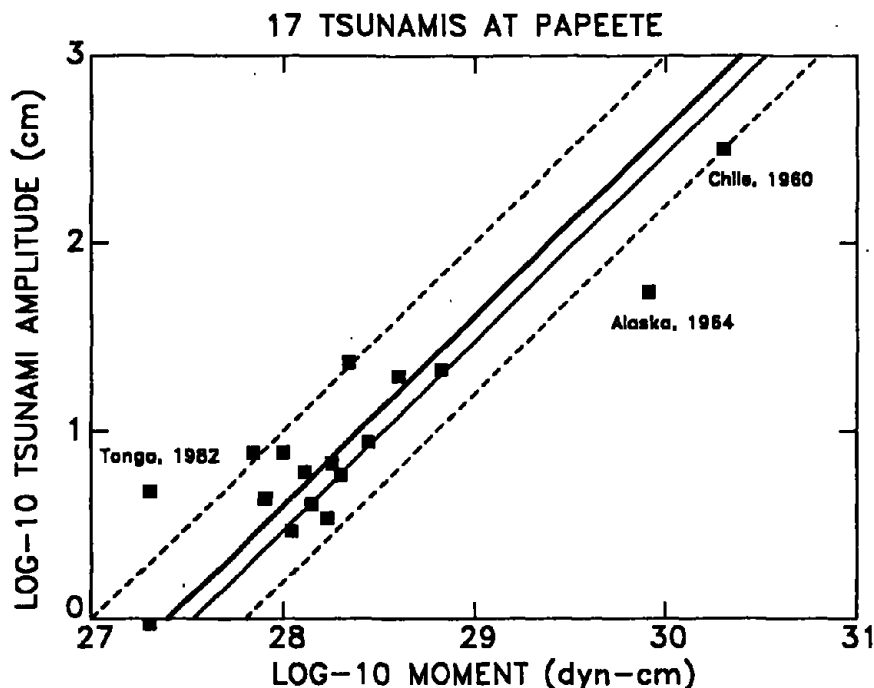
Figure 1. Peak-to-peak equalized tsunami amplitude (TS^*) vs. seismic moment of the parent earthquake, for 17 tsunamis recorded at PPT (1958—1986). The thin solid line is the theoretical relation (6); the thick line the linear relation (8), best-fitting the dataset under the constraint of a slope of 1; the dashed lines are the upper and lower bounds, ((9) ± 0.4 units). The individual events discussed in the text, notably those two not fitting within these bounds are identified.

We refer to *Ward* [1980] for an application of the general formalism of normal mode theory to the case of tsunami excitation, and to *Okal* [1988] for a discussion of the "pseudo-Rayleigh" wave continuing the tsunami eigenfunction into the solid Earth, under various conditions of coupling between ocean and hard rock, including in the presence of sediments. An important, if somewhat surprising, result of our previous study [*Okal*, 1988] was that the effect on tsunami excitation of such factors as focal geometry and precise hypocentral depth is to a large extent secondary. A practical consequence is that the accurate resolution of the focal geometry of an earthquake and of its hypocentral depth is not of prime necessity in the assessment of its far-field tsunamigenic character, and may even be a waste of time and resources under operational real-time conditions. Rather, we seek a one-station estimate of the earthquake's moment, irrespective of depth and geometry: such a measurement follows the philosophy of the *magnitude* concept.

Figure 1 illustrates that very large seismic sources (typically $M_0 \geq 10^{28}$ dyn-cm) are required to generate significant, and *a fortiori* damaging, tsunamis. However, in this range of earthquake size, it has long been known that any magnitude scale measured at a constant period T, such as the standard body- and surface-wave magnitudes m_b and M_s, saturates when the duration of rupture along the fault becomes comparable to T (1 s for m_b, 20 s for M_s) [*Kanamori and Anderson*, 1975; *Geller*, 1976]. Classical magnitude scales then become useless for accurate tsunami warning, and their use can lead to failures and false alarms, both of which are highly undesirable from a social standpoint.

On the other hand, M_0 measured at least in principle at zero-frequency, keeps growing with earthquake size, rather than saturating. For this reason, the real-time measurement of the seismic moment M_0 remains a primary goal of observational seismology. The recent development of broadband seismometers offering both a good response even at very low frequencies, and an appropriate dynamic range, opens the door to a real-time, single-station, measurement of the seismic moment, using the first passage of Rayleigh waves. The development of such a technique, leading to a "mantle" magnitude M_m measured at very-long periods, is the subject of our research.

230

The mantle magnitude M_m

In this section, we discuss the principal features of the new magnitude scale, M_m, which we have developed in order to obtain reliable real-time estimates of seismic moments. Its key ingredient is the use of a *variable* period guarding against the effects of saturation, as the size of the event keeps growing. A full description and justification of M_m, is given in *Okal and Talandier* [1989]. In the present paper, we only review rapidly the various terms used in its calculation. We then give experimental results from the broadband station at Papeete, Tahiti, and describe the resulting estimation of the tsunami risk as a function of M_m, and the automation of the method.

Specifically, we seek a magnitude M_m such that

$$M_m = \log_{10} M_0 - 20 \tag{1}$$

where M_0 is in dyn-cm. The *ad hoc* constant 20 provides a simple link between M_m and M_0, and keeps M_m values in the general range of conventional magnitudes. In this fashion, we impose a slope of 1 between M_m and $\log_{10}M_0$, which is a reflection of our use of variable, but sufficiently large periods, allowing us to stay below the corner frequency of the source, in a range where no saturation effects are present [*Geller*, 1976]. Finally, in this study, we restrict ourselves to shallow sources ($h \leq 75$ km), characteristic of large subduction zone events, and bearing substantial tsunami risk.

Theory

As discussed in detail in *Okal and Talandier* [1989], we base the development and measurement of M_m on the theory of excitation of normal modes and surface waves by seismic sources, leading to an expression of the form

$$\log_{10}M_0 = \log_{10}X(\omega) + C_D + C_S + C_0 , \tag{2}$$

to recover the seismic moment from the amplitude spectrum of a Rayleigh wave. Here, $X(\omega)$ is the spectral amplitude at an angular frequency ω, C_D is a distance correction, C_S a source correction, and C_0 a constant. Equation (2) lays the ground for the definition of a magnitude scale at variable frequency.

The distance correction is simply $C_D = 0.5 \log_{10} \sin\Delta + (\log_{10}e) \omega l_{deg}\Delta/2UQ$, where Δ is the epicentral distance in degrees and l_{deg} is the length of 1 degree (111.2 km). Both terms are independent of focal geometry and depth. The first one reflects geometrical spreading on the spherical Earth, the second one corrects for anelastic attenuation. In order to compute the latter, we generally use a model of the Earth regionalized into seven tectonic provinces along a $10° \times 10°$ coordinate grid. However, we have shown in *Okal and Talandier* [1989] that the performance of our method is not affected significantly by the use of an average model of dispersion and attenuation.

The source correction C_S is computed by averaging over the orientation of the focal mechanism. We have shown in *Okal and Talandier* [1989] that the following expression

$$C_S = 1.6163 \, \theta^3 - 0.83322 \, \theta^2 + 0.42861 \, \theta + 3.7411 \tag{3}$$

where $\theta = \log_{10}T - 1.8209$ (T in s), gives an adequate source correction, to within ± 0.2 units of magnitude, in all cases when the focal mechanism is not "pure" (either pure horizontal or pure vertical slip on a pure vertical fault plane, with the station at a node of radiation), and for depths between 10 and 75 km. Equations (1) and (2) then yield:

$$M_m = \log_{10}X(\omega) + C_D + C_S - 0.90 \tag{4}$$

where $X(\omega)$ is in μm-s.

Measurements at Papeete and performance of M_m

Instrumentation and method

M_m measurements at Papeete, Tahiti (PPT) are taken on broadband records, available at the station since 1973. The instrumental response of the broadband system is flat in displacement from 1 s to 150 s and decreases by a factor $\sqrt{2}$ at 300 s. Along the lines discussed in detail in *Okal and Talandier* [1989], we now have

154 EVENTS at PAPEETE
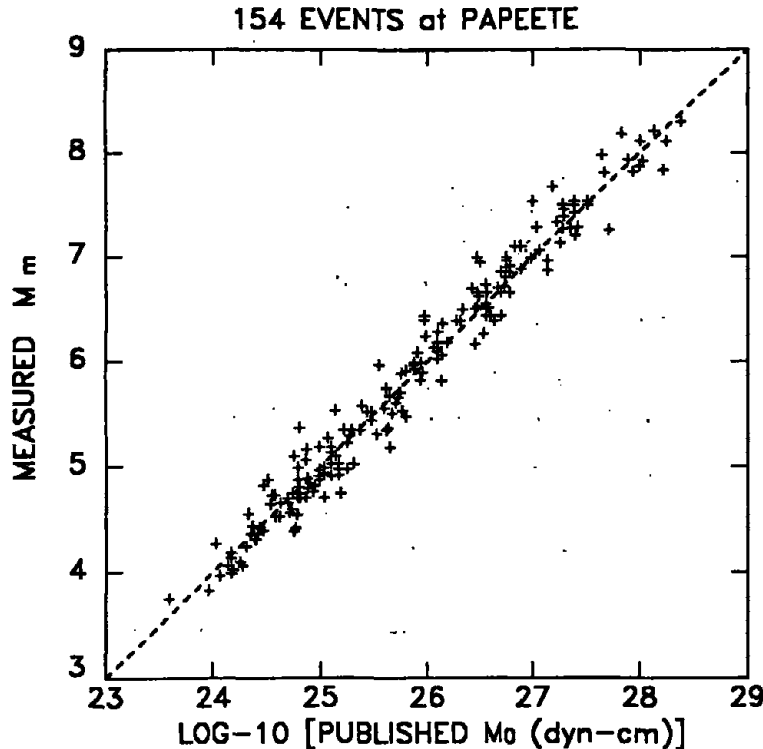
Figure 2. Plot of spectral measurements of M_m, obtained through (4), against published values of M_0. The dashed line is the theoretical relation (1).

compiled M_m values for 154 earthquakes, ranging in moments from 8×10^{23} to 1.8×10^{28} dyn-cm, and having occurred at distances ranging from 23 to 85°.

For each record, a 4096-point digital time series (with a sampling rate of 0.2 s) is Fourier-transformed, and at each period $T = 2\pi/\omega \geq 50$ s, the spectral amplitude $X(\omega)$ is retained. We then apply the distance and source corrections C_D and C_S. We keep the largest among the values of M_m computed at various frequencies. As explained in detail in *Okal and Talandier* [1989], this procedure attempts to guard against the possibility of the station sitting in a node of Rayleigh wave radiation at a particular period.

The average residual $\bar{r}$ between the computed and published values of M_0 is less than 0.02 unit of magnitude, and their standard deviations 0.19 unit. The latter corresponds to an uncertainty of a multiplicative or divisive factor f of 1.55 on the seismic moment (which we will write as $f = */1.55$). These results are shown on Figure 2. We regard them as generally excellent. First, it should be remembered that individual estimates of seismic moments published by different investigators regularly show deviations on the order of $*/1.3$. Also, in the case of conventional magnitude scales (*e.g.*, M_s at 20 s), few single seismic stations can boast of having a systematic magnitude bias of less than 0.2 units, and a standard deviation also less than 0.2 units.

In *Okal and Talandier* [1989], we extended the concept of M_m to other stations by considering an additional 211 records at various ultra-long-period and broadband stations. This extensive dataset was used in a series of tests, in an unsuccessful search for any possible bias of the measurements with either period, distance, or individual station. Our most important results were (i) that "station corrections" are not warranted; (ii) that the method works well even at distances as short as 8°; and (iii) that the influence of the procedure of ignoring focal geometry and depth in computing the source correction (3) degrades the goodness-of-fit by only 30%. As a result, we believe that Equation (4) provides a satisfactory means of computing M_0.

Time-Domain Measurements

Most magnitude measurements have traditionally been taken in the time domain. On the basis of the strong inverse dispersion of Rayleigh waves in the 50—250 s period range, *Okal and Talandier* [1987] discussed

a relationship of the form $X(\omega) = \frac{1}{2} a \cdot T$ where a is the zero-to-peak amplitude of a time-domain oscillation of period T, within a strongly dispersed wavetrain; its theoretical justification, based on phase-stationary asymptotics, is given in *Okal* [1989]. This in turn suggests the direct measurement of M_m in the time domain using

$$M_m^{TD} = \log_{10}(a \cdot T) + C_D + C_S - 1.20 \tag{5}$$

where a is in microns, and T in seconds (if a peak-to-peak measurement is taken, the constant in (5) should be -1.50). For the purpose of tsunami warning at Papeete, we have to consider only distances less than 120°, for which (5) is accurate to within ±0.2 units of magnitude, as long as $T \le 200$ s.

The possibility of directly obtaining M_m in the time domain was tested by measuring the amplitudes and periods of the arches making up dispersed Rayleigh waves, and retaining the largest value of M_m^{TD} computed through (5). As described below, this procedure lends itself well to automation. We have measured M_m^{TD} for 45 earthquakes, resulting in $\bar{r} = -0.07$; $f = \ast/1.60$. This excellent agreement between computed and measured values upholds the concept of a mantle magnitude, measured directly in the time domain.

Estimation of tsunami risk and warning procedures

Once an estimate of the seismic moment M_0 is computed, the tsunami risk can be evaluated using the flow chart on Figure 3. The most important ingredient to this procedure is the proportionality of observed tsunami heights to the seismic moment.
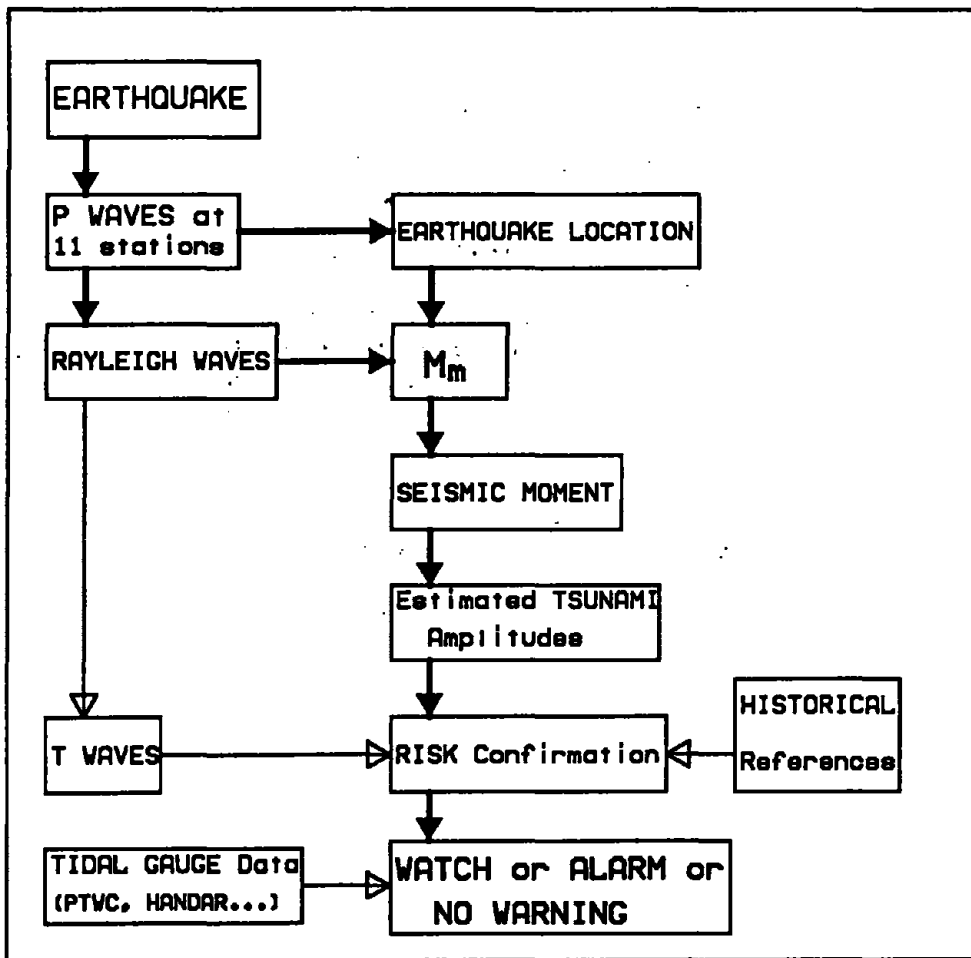
Figure 3. Flow chart of tsunami warning organization at PPT. The thinner traces involving T waves and historical references indicate the complementary nature of these ingredients.

From moment to tsunami height: Theoretical marigrams.

In order to study accurately the dependence of tsunami amplitude with distance, we have computed a series of synthetic marigrams at distances ranging from 5° to 175°. As described in detail in *Okal* [1988], we use a variation of normal mode theory, introduced by *Ward* [1980]. We chose a hypocentral depth of 20 km and a pure thrust-faulting mechanism on a 45°-dipping fault (the so-called "T45" geometry in the notation of *Okal* [1988]). We located the station at the maximum of radiation, *i.e.*, 90° from the strike of the fault plane. The solid line on Figure 4a shows the variation of the amplitude of the resulting tsunami as a function of distance. The peak-to-peak tsunami amplitude can be modeled as

$$TS = 0.3 \, M_0 \, \frac{1}{\sqrt{\sin\Delta}} \, \sqrt{\frac{90}{\Delta}} \tag{6}$$

where TS is in cm, Δ in degrees, and M_0 in units of 10^{27} dyn-cm. This curve is shown as the dashed line on Figure 4a. Both terms in this expression are readily explained: the first one represents the geometrical spreading of the tsunami wave on the sphere; the second one is due to the slight dispersion of the tsunami wave with frequency, and can be derived mathematically from phase-stationary asymptotics [*Erdélyi*, 1956; *Okal*, 1989]. This approximation is expected to break down at short distance, for which dispersion is unsufficient; it is clear on Figure 4 that the two curves separate at short distances, but Figure 4b shows that the modeling of the tsunami amplitude by (6) does not entice errors greater than 10% in amplitude at distances greater than 15°.
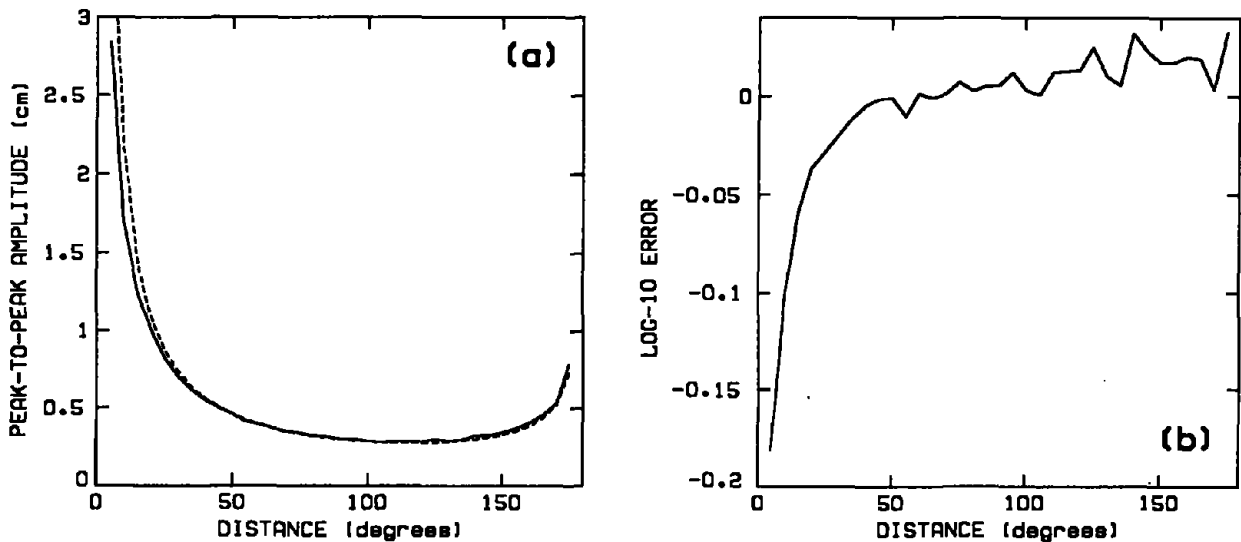
Figure 4. Theoretical peak-to-peak tsunami amplitude as a function of distance. *(a):* The full trace results from normal mode summation carried out at distance increments of 5°. The dashed line is the result of modeling according to (6), and for a moment of 10^{27} dyn-cm. *(b):*Plotted is the decimal logarithm of the error involved when modeling the tsunami height by (6), taken as the ratio of the two curves in *(a)*. Note that except at very short distances, it is usually less than 0.1 magnitude units, and therefore negligible.

Comparison with data at Papeete

On Figure 1, the peak-to-peak amplitudes of the 17 tsunamis recorded at Papeete since 1958 have been equalized to a common distance of 90° through multiplication by a factor $\sqrt{(\Delta \sin\Delta)}/90$. The light solid trace is the theoretical tsunami amplitude expected from (6) and the value of the seismic moment, as published in the literature. In general, we find excellent agreement between the theoretical and expected values. This illustrates the fact that focal geometry plays little role in tsunami excitation [*Okal*, 1988], and further that run-up and resonance at Papeete are minimal. The best-fitting straight line through the dataset is

$$\log_{10}M_0 = (1.22 \pm 0.12) \, \log_{10}(TS^e) + 27.17 \tag{7}$$

(the superscript *e* denoting an amplitude equalized to 90°). Since the slope is not significantly different from 1, it can be constrained to this theoretical value, yielding

$$\log_{10}(TS^e) = \log_{10}M_0 - 27.39 \qquad (8)$$

Figure 1 shows that for 15 out of the 17 data points, this relationship correctly predicts the tsunami height if the constant in (8) is allowed to range between 27.0 and 27.8 . The other two cases are the Alaska earthquake of March 28, 1964, and the Tonga earthquake of December 19, 1982. The former shows a significant deficiency in its tsunami height, resulting from a strong directivity effect at the source, due to the exceptional geometry of the plate boundary in this part of the Pacific rim [*Okal*, 1988]. The latter case is an example of a so-called "tsunami earthquake" [*Kanamori*, 1972; *Fukao*, 1979] for which the tsunami is much more intense than expected from the seismic moment (in this case by a factor of 8). Source complexity has been suggested for this event [*Christensen and Lay*, 1988], but a recent study has shown that the earthquake can be modeled as a simple pulse if the dipping of the ocean floor is taken into account, and that the rupture possibly reached the ocean floor, thus involving seismic release in a sedimentary layer, and enhanced tsunami excitation [*Okal*, 1988; *Lundgren et al.*, 1989]. In the case of the 1960 Chilean earthquake, the slight deficiency in tsunami amplitude could be due to a defocusing effect caused by the heterogeneity in ocean depths, and hence in tsunami velocities [*Woods and Okal*, 1987].

Finally, the difference of 0.13 magnitude units between the experimental constant 27.39 in (8), and the constant expected (27.52) from the theoretical relation (6) can be ascribed to the combined effects of departure from the average focal mechanism assumed in (6), and run-up and resonance at Papeete harbor. Its extremely small value is an illustration of the power of the method.

On the basis of the above dataset, we define an average peak-to-peak amplitude for the expected tsunami amplitudes,

$$\log_{10}(TS)_{aver.} = \log_{10}M_0 - 0.5 \log_{10} (\Delta \sin\Delta) - 26.4 \qquad (9)$$

with a possible window of ± 0.4 units in $\log_{10}(TS)$. These must be taken as amplitudes in Papeete harbor; for other receiving sites, local bathymetry entices additional corrections, which, for example, can reach a factor of 3 for resonant bays in the Marquesas chain. The upper bound of the window is related to a couple of events in the 10^{28} dyn-cm range, and may not be realistically extrapolated to extremely large moments. We interpret it as an absolute maximum for events with $M_m \leq 9$.

Risk levels as a function of M_0.

In establishing seismic thresholds for tsunami warning, we assume that tsunami risk is substantial when the upper bound on the window of peak-to-peak amplitudes predicted at PPT (Equation 9 + 0.4) reaches 1 m. Data from Figure 1, as well as the compilation of historical references [*e.g.*, *Pararas-Carayannis*, 1977; *Solov'iev and Go*, 1984] suggests the following criteria for substantial tsunami risk: $M_0 \geq 5 \times 10^{28}$ dyn-cm for Samoa—Tonga—Kermadec epicenters; $M_0 \geq 10^{29}$ dyn-cm for all other epicenters. The former figure, obtained here experimentally, is in agreement with *Ward*'s [1980] theoretical threshold for destructive tsunamis. We treat separately the case of epicenters from the region Samoa—Tonga—Kermadec, which can be as close as 22° from PPT; for such events, geometrical spreading is significantly reduced, resulting in substantial distance corrections in (9).

In this framework, the following risk levels have been identified as a function of the magnitude M_m:

1. $M_m < 7$ $(M_0 < 10^{27}$ dyn-cm): No tsunami risk.

2. $7 \leq M_m < 8$ $(10^{27} \leq M_0 < 10^{28}$ dyn-cm): The generation of a very large tsunami remains improbable, but a "tsunami earthquake" cannot be totally ruled out. Although it may be improper to describe it in terms of M_m of M_0, the Aleutian earthquake-landslide of April 1, 1946 apparently belonged to this range of seismic measurements [*Kanamori*, 1972], and yet it created one of the two largest tsunamis in the past 150 years. Further interpretation, for example of T wave durations [*Okal and Talandier*, 1986], may be warranted.

3. $8 \leq M_m < 8.7$ $(10^{28} \leq M_0 < 5 \times 10^{28}$ dyn-cm): A tsunami will probably be generated, but except for the possible case of a tsunami earthquake, should not be catastrophic at teleseismic distances from the epicenter. Interpret T waves.

4. $8.7 \leq M_m < 9.3$ $(5 \times 10^{28} \leq M_0 < 2 \times 10^{29}$ dyn-cm): Probable generation of a potentially destructive tsunami. Immediate tsunami watch issued if epicenter is in Samoa—Tonga—Kermadec, or otherwise closer than 4000 km.

235

5. $M_m \geq 9.3$ ($M_0 \geq 2 \times 10^{29}$ dyn-cm): Generation of a very large, probably very destructive tsunami. Immediate alarm issued for Samoa—Tonga—Kermadec epicenters; immediate tsunami watch issued for other regions.

The following are definitions of "Tsunami Watch" and "Tsunami Alarm" as they are used by CPPT:

A Tsunami Watch is a first-level warning, designed to acquaint Civil Defense authorities of the possibility of a substantial tsunami, in order to allow them to achieve readiness in case of the later issuance of a tsunami alarm. A tsunami watch issued by CPPT includes predicted arrival times of the wave in Polynesia.

A Tsunami Alarm warrants immediate action on the part of Civil Defense authorities, in compliance with relevant governmental procedures. In most cases, it will follow a tsunami watch, but could be issued early in the case of close-by epicenters. The tsunami alarm confirms arrival times at Polynesian islands.

Obviously, our estimate of tsunami risk is later updated, taking into account tidal gauge data, as they become available following propagation of the tsunami wave, through retransmission to CPPT by the Pacific Tsunami Warning Center in Honolulu, and from the HANDAR GEOS platforms at Rarotonga (Cook Islands), Nuku-Hiva (Marquesas Islands), Easter Island, and in the near future, Niue Island.

Automation of the measurements

In this section, we discuss briefly an algorithm allowing for automation of the measurement of M_m, which is now used routinely by CPPT. Full details can be found in *Reymond et al.* [1991]. Our algorithm is based on the following steps: First, a strong event detector is triggered, based on the use of 11 short-period stations in the 350-km aperture Polynesian array continuously telemetered to PPT, and a classic multiple criterion of amplitude threshold, frequency content, duration and simultaneity. Next, an automated locator uses P times across the array to estimate an epicentral region and an arrival window for R_1. We also obtain an independent estimate of the location from 3-component long-period records at a single station (PPT), by retrieving the back-azimuth from the polarity of the three components of the P wave, and distance from the $S - P$ time interval. After the location is obtained, the process triggers acquisition into the computer of 819.2 s at a 0.2 s sampling rate. The computation of M_m then proceeds in two independent ways, providing redundancy of the final results:

Frequency-domain measurement.

The time series is simply run through a standard FFT algorithm and the correction C_S applied at each FFT frequency between 50 s and 300 s. C_D is computed by splitting the path into "pure" segments, and applying the adequate attenuation factors. M_m is then computed from Equation (3) at the various periods, and the largest value retained.

Time-domain measurement.

, The signal is run through an analog band pass filter eliminating periods outside the 50—300 s range. The resulting time series (see Figure 5) is searched for subsequent maxima and minima reaching at least 10% of the absolute maximum amplitude of the signal; the resulting amplitudes and periods of the corresponding arches are retained. For each of them, M_m is computed through Equation (5), and the maximum value retained.

Once these estimates of M_m are obtained, and for both of them, the computer prints out automatically estimates of tsunami heights (Equation 9), and of arrival times at various Polynesian sites. On the basis of these results, and if necessary of an interpretation of T waves, a Geophysicist (on call 24 hours a day) has the ultimate responsibility of issuing a tsunami watch or alarm.

Conclusions

1. The mantle magnitude M_m developed by *Okal and Talandier* [1987, 1989] and *Talandier et al.* [1987] allows recovery of the seismic moment of teleseismic Pacific earthquakes with a standard deviation on the order of ± 0.2 units of magnitude.

2. Estimates of expected tsunami heights for Papeete can be reliably derived from the measurement of M_m, and hence M_0. When completed by such effects as known resonant factors for harbors and bays, and high-seas focusing due to lateral heterogeneity in bathymetry, this approach can easily be generalized to other Pacific sites.

Aleutian Islands, 07 MAY 1986
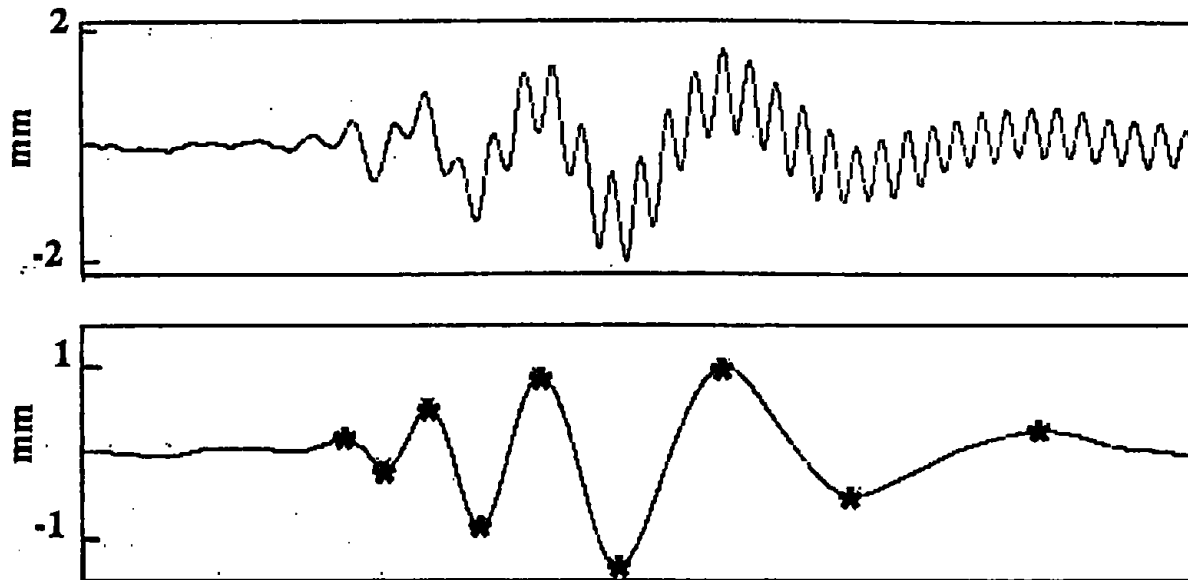
Figure 5. Principle of automatic determination of time-domain magnitude. *Top:* Original record of May 7, 1986 Aleutian event at PPT. *Bottom:* Same record after filtering out periods greater than 50 s. The stars indicate the automatic picks of peaks and troughs, from which the amplitudes and periods are estimated for use in (5).

3. The more easily taken time-domain measurements show no significant difference with frequency domain estimations; they can be extended down to $M_0 = 5 \times 10^{24}$ dyn-cm, while keeping the same constants in the Equation (5) defining M_m^{TD}. The possibility of using time-domain records means that the method can be used even in the absence of computing facilities, once a chart of the corrections C_D has been prepared for a given observatory, as a function of frequency and for all potentially active epicentral areas.

Finally, we wish to emphasize that while this method was being developed, we were able to obtain a correct estimate of $M_0 = 1.0 \times 10^{28}$ dyn-cm for the Aleutian event of May 7, 1986 (see Figure 5), within a little more than two hours of the origin time. As a result, no tsunami warning was issued for French Polynesia, and a false alarm avoided [*Talandier et al.*, 1986], while an estimate of tsunami danger for the same event based primarily on M_s resulted in the unnecessary evacuation of thousands of residents of Hawaii, Oregon and Washington. We wish to stress that while the final decision on such matters as evacuation of low-lying areas, and implementation of emergency procedures is clearly the responsibility of governmental agencies, the scientific community has the duty of providing the latter with the best *quantitative* information possible. We believe that the use of M_m, and of formulae such as (9), which are fully justifiable from a theoretical point of view, and have been verified against experimental datasets, represents significant progress in this direction.

References

Abe, K. (1973) Tsunami and mechanism of great earthquakes, *Phys. Earth Planet. Inter.,* **7**, 143-153.

Aki, K. (1967) Scaling law of seismic spectrum, *J. Geophys. Res.,* **72**, 1217-1231.

Christensen. D.H.; Lay, T. (1988) Large earthquakes in the Tonga region associated with subduction of the Louisville Ridge. *J. Geophys. Res.,* **93B**, 13.367-13.389.

Erdélyi, A. (1956) *Asymptotic Expansions,* 108 pp., Dover, New York.

Fukao, Y. (1979) Tsunami earthquakes and subduction processes near deep-sea trenches, *J. Geophys. Res.,* **84**, 2303-2314.

Geller, R.J. (1976) Scaling relations for earthquake source parameters and magnitudes, *Bull. Seismol. Soc. Amer.,* **66**, 1501-1523.

Kanamori, H. (1972) Mechanism of tsunami earthquakes, *Phys. Earth Planet. Inter.,* **6**, 346-359.

Kanamori, H.; Anderson, D.L. (1975) Theoretical basis of some empirical relations in seismology, *Bull. Seismol. Soc. Amer.,* **65**, 1073-1095.

Lundgren, P.R.; Okal, E.A.; Wiens, D.A. (1989) Source characteristics of the 1982 Tonga and 1986 Kermadec earthquakes, *J. Geophys. Res.,* **94**, 15521-15539.

Okal, E.A. (1988) Seismic parameters controlling far-field tsunami amplitudes: A review, *Natural Hazards Journal,* **1**, 69-96

Okal, E.A. (1989) A theoretical discussion of time-domain magnitudes: the Prague formula for M_s and the mantle magnitude M_m, *J. Geophys. Res.,* **94**, 4194-4204.

Okal, E.A.; Talandier, J. (1986) T-wave duration, magnitudes and seismic moment of an earthquake; application to tsunami warning, *J. Phys. Earth,* **34**, 19-42.

Okal, E.A.; Talandier, J. (1987) M_m: Theory of a variable-period mantle magnitude, *Geophys. Res. Letts.,* **14**, 836-839.

Okal, E.A.; Talandier, J. (1989) M_m: A variable period mantle magnitude, *J. Geophys. Res.,* **94**, 4169-4193.

Pararas-Carayannis, G. (1977) Catalogue of tsunamis in Hawaii, World Data Center, NOAA, Boulder, pp. 24-43.

Reymond, D.; Hyvernaud, O.; Talandier, J. (1991) Automatic detection, location and quantification of earthquakes: application to tsunami warning, *Pure Appl. Geophys.,* **135**, in press.

Solov'iev, S.L.; Go, Ch. N. (1984) Catalogue of Tsunamis of the Pacific Ocean, Nauka Publishing House, Moscow, 1974; Can. Transl. Fish. Aquat. Sc., **5077-5078**, 2 vol., Sidney, 722 pp.

Talandier, J.; Okal, E.A.; Reymond, D. (1986) Mantle magnitude M_m: a new approach for the rapid estimation of seismic moments; application to the 1986 Aleutian earthquake [abstract], *Eos, Trans. Amer. Geophys. Un.,* **67**, 1081.

Talandier, J.; Reymond, D.; Okal, E.A. (1987) M_m: Use of a variable-period mantle magnitude for the rapid one-station estimation of teleseismic moments, *Geophys. Res. Letts.,* **14**, 840-843.

Talandier, J.; Okal E.A. (1989) An algorithm for automated tsunami warning in French Polynesia, based on mantle magnitudes, *Bull. Seismol. Soc. Amer.,* **79**, 1177-1193.

Ward, S.N. (1980) Relationships of tsunami generation and an earthquake source, *J. Phys. Earth,* **28**, 441-474.

Woods, M.T.; Okal, E.A. (1987) Effect of variable bathymetry on the amplitude of teleseismic tsunamis: a ray-tracing experiment, *Geophys. Res. Letts.,* **14**, 765-768.

Discussion

Comment: There are pre-computed results for a number of modes and then we integrate in between the modes; so we do the computations in the frequency domain.

Question: How many modes are used?

Response: There are about 80 modes, which are computed once and for all. And then in any kind of frequency domain, one can interpolate between these modes to find the excitation coefficients and fit in the frequency spectrum and do a Fourier transform.

Comment: The particular orders would vary from about 10 to 15, at periods of 4,000-5,000 seconds to, maybe, 500-600 if we go down to 200-300 seconds. Now, we need not compute all these modes -- just compute a few of them at representative frequencies and then interpolate in between. This is the same thing done in seismology when one computes surface waves. The surface waves are computed by setting up modes, but it is not necessary to compute the entire 200 modes. What is usually done is to use 10-15 frequencies and interpolate in between them.

Comment: The normal mode is different. What the seismologist call the normal mode is for the whole spherical earth. It is assumed here that the ocean is flat and just one layer. It is not a normal mode of two-dimensional body and it is not a normal mode of a bay or harbor or seiche.

Comment: A constant depth of the ocean is assumed, but it is not necessary to assume that the ocean has only one layer. As many layers as you want can be added.

REAL-TIME DETERMINATION OF EARTHQUAKE SOURCE PARAMETERS AND ITS APPLICATION TO TSUNAMI WARNINGS

Kenji Satake
Department of Geological Sciences
University of Michigan
Ann Arbor, MI, USA

Abstract

Recent developments in earthquake seismology, both theoretical and observational, make it possible to forecast tsunamis before their arrival. Seismic waveform data recorded on very broad band seismographs are available in real-time, and the analysis to estimate source parameters and the computation of realistic tsunamis can be made within a few hours of the earthquake. Thus more reliable and detailed tsunami warnings are technically possible now. The Mariana earthquake of April 1990 $(M_s 7.5)$ is described as an example.

Introduction

Most destructive tsunamis are caused by large shallow earthquakes. The study of earthquake sources is important to understand tsunami generation. From the viewpoint of hazard reduction, the reliable forecast of coming tsunamis based on seismological observation is expected. Recent developments in earthquake seismology make it possible to estimate earthquake source parameters in real-time. The tsunami source model can be obtained within a few hours of the earthquake and realistic computation of tsunamis can be made before the actual tsunami travels a long distance. It is technically possible to make more realistic and detailed tsunami warnings than is currently in operation at least for far-field tsunamis.

There are two factors, theoretical and instrumental, that contributed to this seismological development. In the next two sections, theoretical developments about the seismic source and the recent observation system will be discussed. In the last section possible use of these seismological developments for tsunami warnings will be discussed.

The example given here is the Mariana earthquake $(M_s 7.5)$ of April 5, 1990. Since this earthquake occurred near Guam, very far from both Japan and Hawaii (Figure 1), neither the Japan Meteorological Agency or Pacific Tsunami Warning Center at Hawaii could get appropriate earthquake source parameters. Although the tsunami height was not very high

239

anywhere and no damage was reported, this event was a kind of "unexpected" type by seismologists and the occurrence of this event suggests the possibility of even larger earthquakes in this region. The method described here will be expected to help future tsunami warnings in this and other regions.
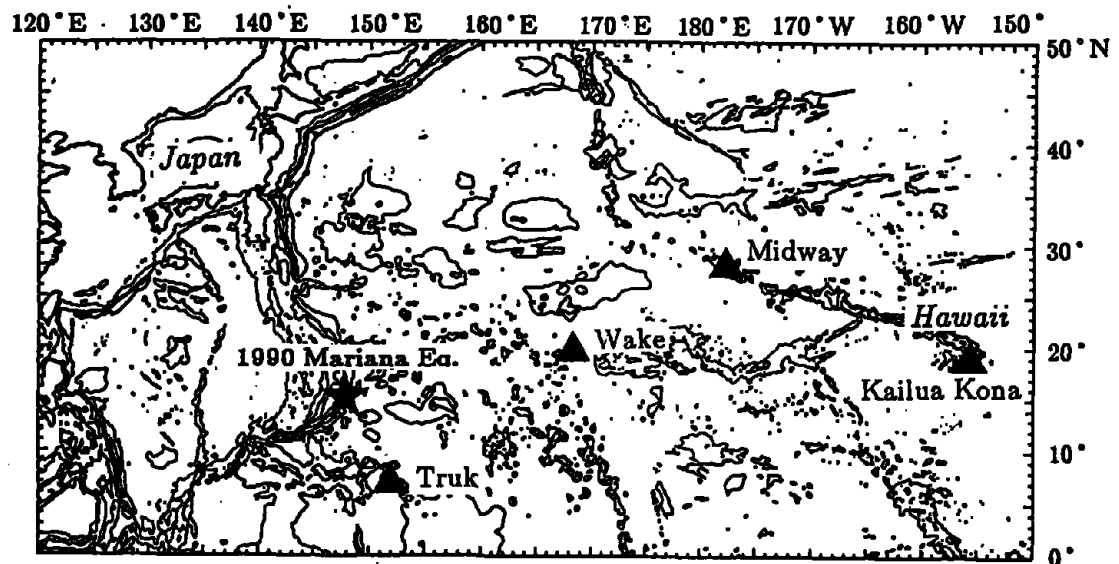
Figure 1. Map showing the location of the Mariana earthquake (star symbol). The solid triangles show the tide gauge locations in the Pacific Ocean.

Earthquake Source Parameters

Many earthquakes on land have shown that an earthquake is a rapid fault motion. The equivalent body force system to the fault motion is a double couple, and its moment, called seismic moment, indicates a physical size of an earthquake. In terms of fault motion, seismic moment is a product of fault area, slip amount and rigidity at the source region. The source of tsunami, on the other hand, is a water disturbance above the earthquake source, usually caused by shallow faulting. Once the fault parameters are obtained, the crustal deformation due to faulting, or initial field of tsunamis, can be readily computed (e.g. Okada, 1985). To obtain the fault parameters, focal mechanism (geometry of fault motion) and seismic moment must be estimated from seismic observations. These are usually estimated from the polarity of first motion and waveform data, respectively.

Seismic source can also be presented in a form of a stress tensor at the source area (Gilbert, 1970). This is called seismic moment tensor and is a more general expression of the

240

seismic source than the double couple. Another merit of introducing moment tensor is that the seismic displacement, or theoretical seismic waveform, can be expressed as a linear combination of moment tensor elements. This means that it is straightforward to make an inversion to estimate the moment tensor elements from observed seismograms. This is called moment tensor inversion and has become popular in the last decade. Further, Dziewonski et al. (1981) has developed a technique to estimate not only the moment tensor elements but also centroid location and time of the moment tensor. This is called Centroid Moment Tensor (CMT) inversion and is now made routinely by Harvard University.

The CMT inversion has been made for the Mariana event twice. The first one was made right after the event using the data from dial-up stations. At the time of the event, only four stations (Pasadena, Harvard, Corvallis and Kipapa) had dial-up capability and the seismic data at those stations were used for the first inversion. After a few months of the event, the data from more stations with a better azimuthal coverage became available. The second inversion was made using the data from 18 stations. The focal mechanism obtained from the CMT inversions is shown in Figure 2. As seen in the figure, the results are very similar, indicating that the only four stations are enough to analyze this particular event. Figure 3 shows the fault model of the Mariana event and the crustal deformation pattern computed from the fault model. The faulting primarily caused a subsidence up to 3 meters just above the fault area, because of the normal fault mechanism.

1.78e+27 (Mw 7.4) -0.14

37/65/-75 184/29/-119

1.62e+27 (Mw 7.4) -0.08

24/65/-80 181/26/-111
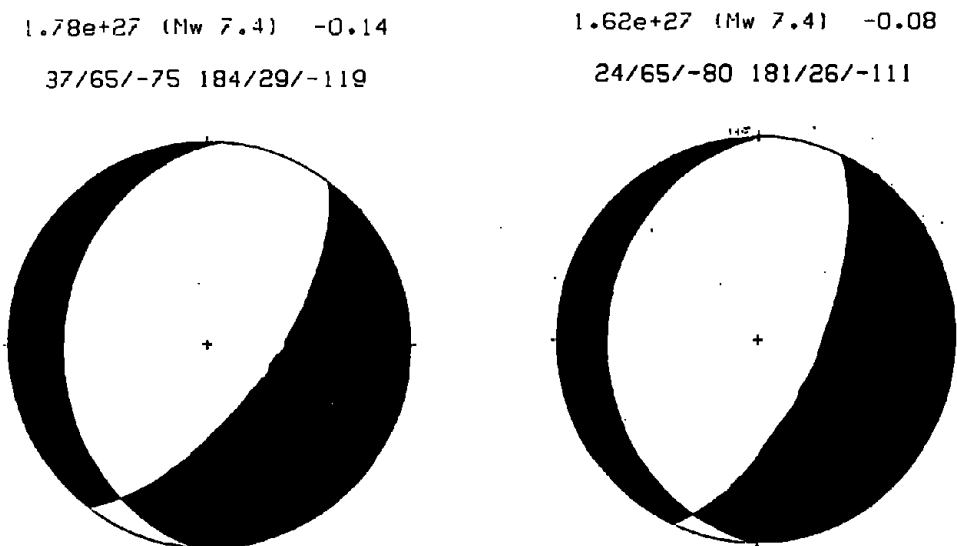
Figure 2. The results of the CMT inversion for the Mariana earthquake. The left is preliminary solution using only four stations while the right is final solution using 18 stations.

241

April 5, 1990 Mariana Earthquake

fault model   crustal deformation
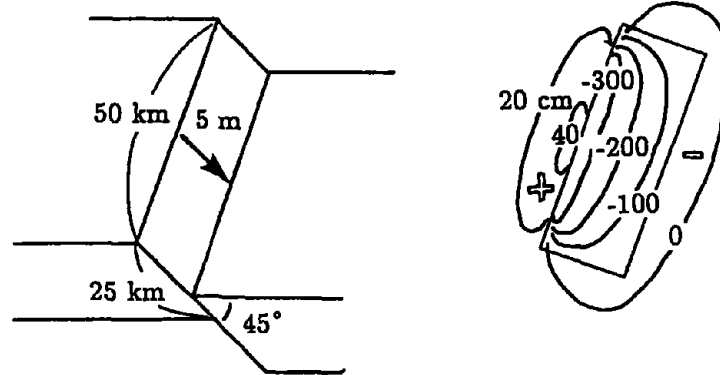
Figure 3. The fault model and the computed crustal deformation pattern for the Mariana event.

Observation System

Since the late 1970s a few kinds of global digital seismographic networks such as IDA (operated by Scripps Inst. Oceanography), GDSN (USGS), GEOSCOPE (France), have been in operation. The routine determination of CMT solution has become possible using these digital data. Although they provide a large amounts of valuable seismological data, the dynamic range has not been wide enough. For example, the direct seismic waves from large (M = 8) events are often too large to be recorded on scale and cannot be used for analysis. In such a case, we had to wait several hours until later phases arrive with moderate amplitudes.

More recently, very broad band seismometers with a wide dynamic range have been developed and are in operation. These instruments can record seismic waveforms from almost any size of earthquake. Further, some stations have dial-up capability; the seismic station has a modem and users can make a phone call to retrieve data right after an earthquake. IRIS (Incorporated Research Institutions in Seismology) is now developing a global network of the broad band instruments. The Data Management Center of IRIS is making phone calls to each station to get the waveform data. Once the DMC computer gets the data, they are stored on the disk system and we can access them using a computer network.

Figure 4 shows this real-time data flow.
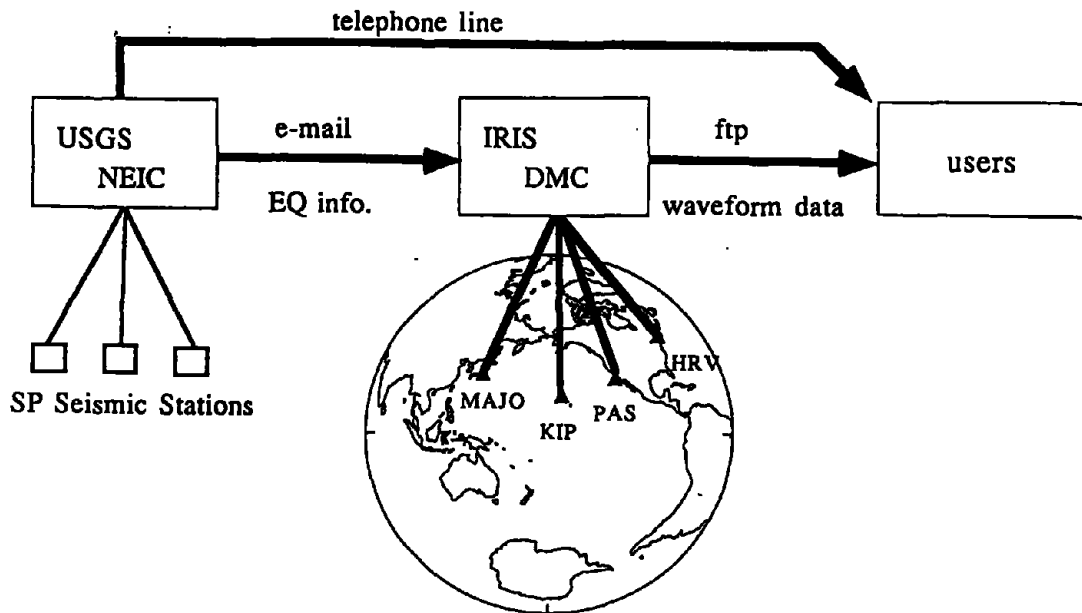
Figure 4. The schematic diagram showing the real-time data flow.

Among the several future scientific plans, two of them being planned in Japan have a great potential for tsunami warnings. The first one is the Poseidon project which started recently. The goal is to install about 50 seismic stations including ocean bottom seismometers in the western Pacific region in much denser station distribution than the other global network. Another project is a scientific re-use of ocean bottom telephone cable. TPC-1 cable, between Japan and Guam, is now under consideration. Along the cable, there will be two seismic stations and a geophysical observation station and all the data will be transmitted through the telephone cable in real-time.

Implications to Tsunami Warnings

Tsunami propagation can be computed numerically on actual bathymetry. The total wavefield can be computed using a finite-difference method from an initial condition computed from fault model. Because of recent developments in computer technology, it is possible to make a large computation in a short time. For example, Goto et al. (1988) showed

243

that the seven hours of tsunami propagation in the northern Pacific can be computed in only three minutes using a supercomputer. The computation of total wavefield will actually simulate the tsunami; not only the arrival times but also the waveforms including the maximum amplitude can be obtained. The computation will also give a realistic boundary condition for coastal behavior of tsunamis such as resonance or run-up.

The tsunami from the Mariana event was observed at many places in Japan but the amplitude distribution was not as simple as expected from a simple theory. The tsunami propagation from this event towards Japan was computed. Figure 5 shows the snapshots for every hour after the earthquake. The interesting feature of the tsunami propagation is that the tsunami propagates very fast with a small amplitude along the deep Japan trench whereas the velocity is slow but the amplitude is large on the ridge system, forming a kind of edge wave. The observed distribution of tsunami amplitude was very similar to that expected from this computation.

Mariana earthquake of April 5, 1990   land : 10cm

1 hr   2 hrs   3 hrs
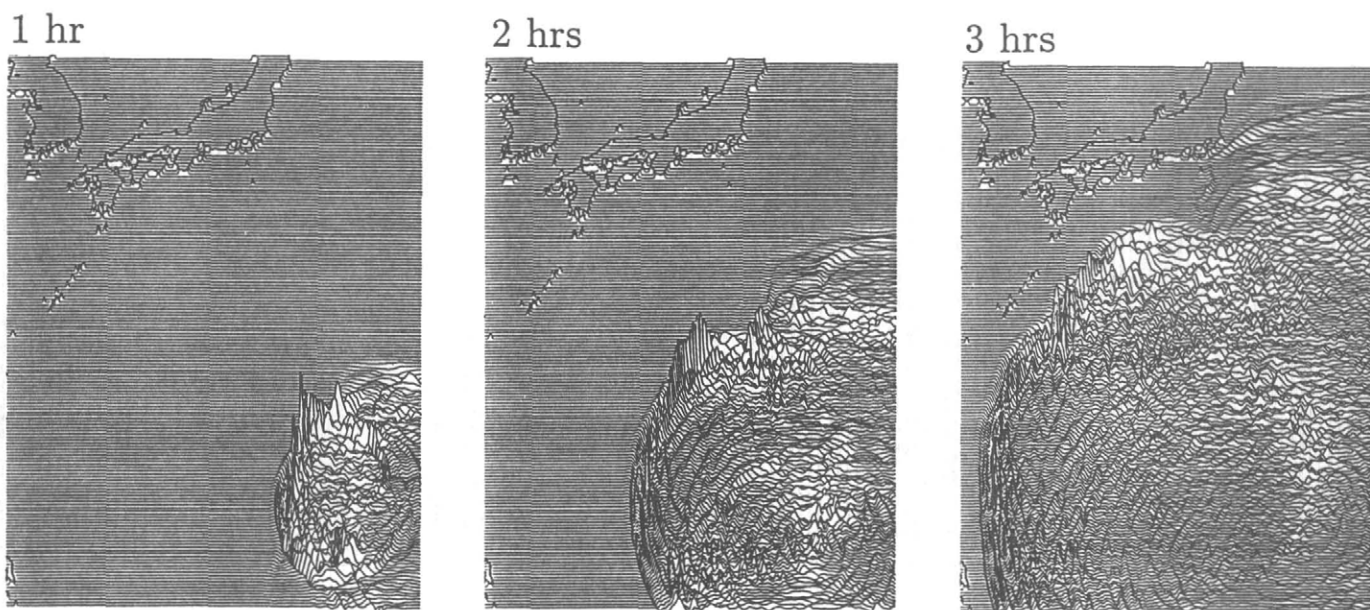
Figure 5. Snapshots of tsunami propagation for each hour after the Mariana event. The land height corresponds to 10 cm of water surface elevation.

References

Dziewonski, A.M., T.-A. Chou and J.H. Woodhouse (1981), Determination of earthquake source parameters from waveform data for studies of global and regional seismicity. J. Geophys. Res., 86, 2825-2852.

Gilbert, F. (1970). Excitation of the normal modes of the Earth by earthquake sources. Geophys. J. R. astr. Soc., 22, 223-226.

Goto, C., F. Imamura and N. Shuto (1988). Study of numerical simulation of the transoceanic propagation of tsunami: part 1, governing equation and mesh length. Zisin (J. of Seism. Soc. Japan), 41, 515-526.

Okada, Y. (1985). Surface deformation due to shear and tensile faults in a half-space, Bull. Seism. Soc. Am., 75, 1135-1154.

Discussion

Question: To generate the tsunami using the fault-plane model, is it correct that all the parameters for that fault-plane model are obtained from the inversion of the seismic wave forms? The USGS has published this Harvard Moment Tensor solution, but from the published information, it is not possible to determine the length of the fault, the width of the fault, and the total slip along the fault.

Response: That is a very good point. Some sort of empirical relationship must be used. Seismic moment is a product of the area (fault length and width), the displacement and the shear modulus. There are empirical correlations between these elements. Unfortunately, the product is known for these, but not each element. There is one thing from the Harvard solution that can give you an indication of the length - and that is the central location as opposed to the hypocenter.

Comment: On this particular computation a 1° grid was used.

ASSESSMENT OF PROJECT THRUST: PAST, PRESENT, FUTURE

Eddie N. Bernard
Pacific Marine Environmental Laboratory
National Oceanic and Atmospheric Administration
Seattle, WA, USA

Abstract

Project THRUST (Tsunami Hazards Reduction Utilizing Systems Technology) was a demonstration of satellite technology, used with existing tsunami warning methods, to create a low cost, reliable, local tsunami warning system. The major objectives were successfully realized at the end of the demonstration phase in September 1987. In June 1988, the Chilean government held a workshop to assess the value of THRUST to national interests. Two recommendations came forth from the workshop: (1) the technology was sufficiently reliable and cost-effective to begin the development of an operational prototype and (2) the prototype would be used as the Chilean Tsunami Warning System. As of August 1989, the equipment was in operational use. In September 1989, major improvements were made in the satellite operations that reduced the response time from 88 to 17 seconds and enlarged the broadcast area by 50 percent. The implications of the recent improvements in satellite technology are discussed for application to reductions in disaster impacts.

Past--Development of a Local Warning System

Throughout history, natural disasters have killed and disrupted people of every nation on the globe. Rapid-onset natural hazards such as earthquakes, landslides, tsunamis, hurricanes, tornadoes, floods, volcanic eruptions, and wildfires have claimed more than 2.8 million lives worldwide in the past 20 years, adversely affecting 820 million people. The world's vulnerability and the social and economic cost of these hazards will only increase in the future due to population growth and urban concentration, increased capital investment coupled with new technologies, the existence of vulnerable critical facilities and fragile lifelines, and increasing interdependence of local, national, and international communities (Housner, 1987).

Tsunamis are one such rapid-onset hazard. Over 51,000 coastal residents have been killed by 94 destructive tsunamis in the past century. Lander and Lockridge (1986) have found that *99 percent of all tsunami-related fatalities occur within 400 km of the earthquake epicenter*. Since tsunamis are generated over the area of uplift (which could be up to 600 km), most of the fatalities probably occurred on the coasts directly opposite the source with travel times less than 10 minutes.

Existing tsunami warning systems are effective on a *Pacific-wide* time scale of 1 hour and a *regional* time scale of 10 minutes (Sokolowski, 1990). They are not effective, however, on a *local* time scale--i.e., within 2 minutes of a local, potentially tsunamigenic earthquake (Bernard et al., 1988). Project THRUST has successfully designed and developed a warning system to meet this need by establishing a pilot system in Valparaiso, Chile. The three major components that make up the THRUST system's approach to tsunami hazard mitigation on the local level are:

- pretsunami preparedness, consisting of historical data base studies, numerical model simulations, and development of a detailed emergency operations plan;

- real-time local hazard assessment, achieved by utilizing seismic triggers with predetermined threshold levels;

- rapid dissemination of information to local officials, achieved by exploiting satellite communications technology.

The satellite-based communication system is shown schematically in Figure 1. A threshold detector sensor (A) provides a signal in response to a change that exceeds a preset level. (Sensors can monitor seismic activity, water heights, nuclear radiation, chemical concentrations, or any other activity for which a threshold detector is available.) The sensor signal activates a satellite uplink transmitter (B) into a preprogrammed transmission sequence. The transmitted signal is a unique address that identifies the sensor and transmitter. The GOES (Geostationary Operational Environmental Satellite) satellite (C), which resides in geosynchronous orbit, relays the coded message to the ground station (D). The ground station computer (E) processes incoming signals and decodes the message. The computer is programmed to react to the unique signal by commanding the ground station to transmit a short coded message (related to the sensor) to the satellite. This coded message is broadcast through the satellite and is received at the alert station (F). The alert station is a low-cost receiver and antenna tuned to the downlink frequency of the satellite and a decoder and processor that continuously monitor incoming data. The processor continuously scans all incoming messages from the downlink receiver. The processor is programmed to respond upon receipt of specific messages. The response is typically a printed alert message indicating the time and location of the sensor trigger and action that should be taken by the owner of the receiver. The processor can also activate lights, acoustic alarms, telephone dialers, and other emergency responses.
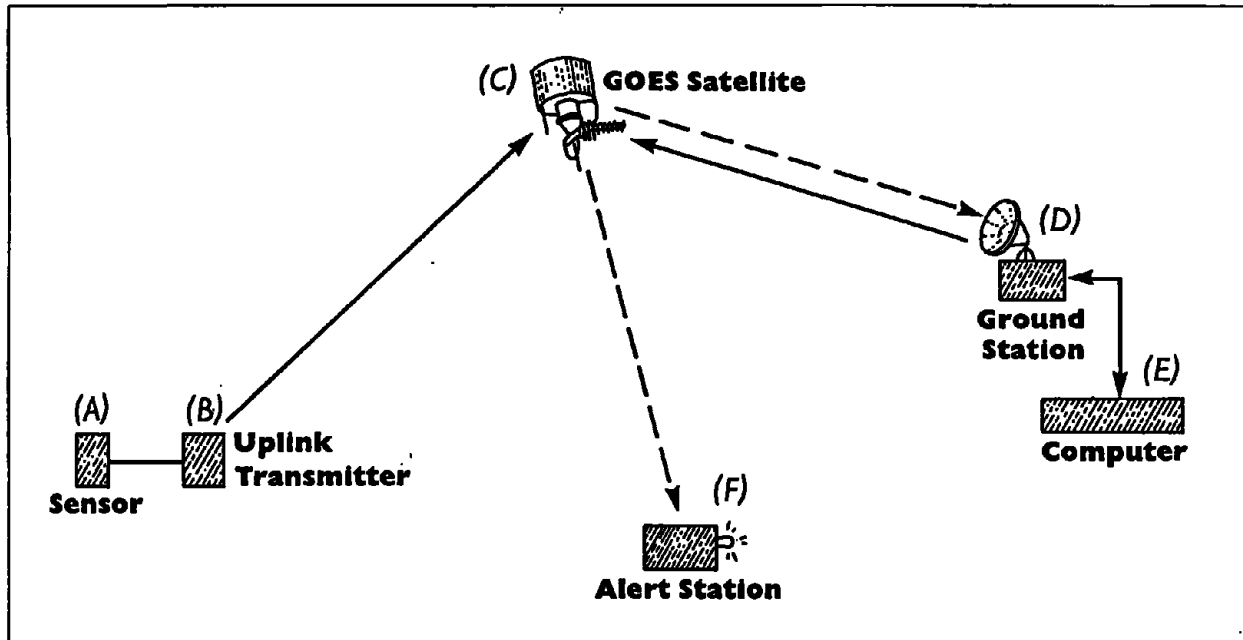
Figure 1. Satellite communication system used for THRUST project.

After the pilot system was installed in September 1986, Project THRUST researchers began a lengthy evaluation program. Over a period of 9 months, the average response time of the communication technology was found to be 2 minutes. Transmission performance tests conducted during this period also demonstrated that the GOES communication system could be used in a warning mode. The THRUST team found that after 1 year of operation, hardware reliability was acceptable for first-generation pilot instrumentation.

The major objective of project THRUST had thus been achieved—the development of a *low-cost* system to deliver tsunami warnings useful on a *local* level. Hardware for the most basic THRUST system configuration, consisting of a seismic station and a tsunami warning station, cost about $15,000. Furthermore, the fundamental system delivered the primary THRUST product—life-saving tsunami hazard information—in an average elapsed time of 2 minutes simultaneously to anyone under the communication umbrella (Figure 2) with the appropriate receiver.

Present—Acceptance of THRUST Technology into Warning Operations

In June 1988, the Instituto Hidrografico de la Armada de Chile (IHA) hosted a THRUST workshop to evaluate the use of this early warning technology. The 3-day workshop was attended by 50 scientists, emergency experts, and emergency administrators from 7 American countries. Two days were dedicated to the technical details of the hazard assessment (historical data analysis, inundation modeling, and emergency operating plan development), the equipment (engineering development, satellite operations, and performance evaluation), and the scientific methodology (seismic threshold setting, flooding maps) used in the project. The third day was used for demonstrations of the system and a session to formulate recommendations and conclusions (Espinosa, 1989).
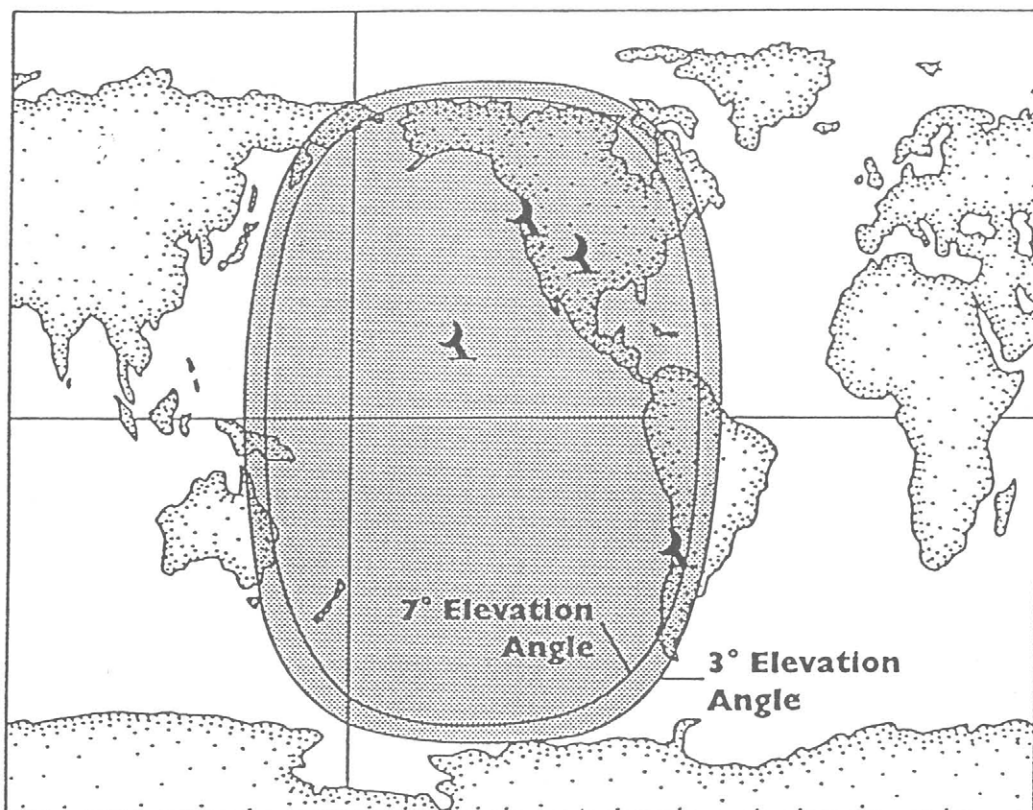
Figure 2. Communication coverage of the GOES west satellite and locations of THRUST receivers.

The participants adopted the following recommendations at the end of the THRUST workshop:

-- The THRUST pilot project demonstrated that the technology exists to develop an operational system. It is recommended that a two-step approach be adopted for the operational development:

Step 1: Use existing equipment to instrument more sites of potential large earthquakes.

Step 2: Write specifications for second-generation equipment based upon deficiencies found in the pilot project.

-- Local emergency authorities should be encouraged to reexamine numerical simulations for a wider range of most probable earthquakes.

-- Local emergency authorities should be encouraged to maintain close ties with the tsunami and seismological research communities to assimilate new technologies into warning, planning, and relief efforts.

-- The capability for planning and carrying out numerical simulations
should be transferred to local hazard planning and management
authorities as efficiently and expeditiously as possible. The use of
local resources (such as personal computers) should be encouraged.

With these recommendations, the experts at IHA continued the integration
of the THRUST technology into the Chile Tsunami Warning System. Details of
the process are explained in E. Lorca's paper, "Integration of the THRUST
Project into Chile Tsunami Warning System," (to be published in 1991 in a
special tsunami issue of *Natural Hazards*). Lorca concludes that THRUST
technology has improved the Chile Tsunami Warning System.

It should be noted, however, that the system has yet to experience an
earthquake of sufficient magnitude to trigger the system. This is a common
problem with the testing of local/regional tsunami warning systems. The
Hawaii regional system, for example, was installed for over 4 years before it
was jolted by a magnitude 6 earthquake. A good way to overcome the absence of
earthquakes is to devise robust testing procedures.

Present--Improvements in Satellite Operations

In September 1989, the National Oceanic and Atmospheric Administration
upgraded the GOES satellite ground station that included the capability to
retransmit messages such as those used in the THRUST project. The new
satellite ground station, with its more advanced computer, significantly
decreased the time of message processing. A special feature of these
"trigger" messages is a broadcast over both the NOAA GOES east and west
satellites, which increases the area of broadcast by approximately 50 percent
(Figure 3). This improved response time and broader coverage (about
62 percent of the surface of the Earth), along with low-cost, low-maintenance
communication equipment makes the case for satellite-based, local early
warning systems very appealing.

To quantify the improvements of the satellite ground station upgrades,
two communication experiments were conducted--one before the upgrade and one
after the new ground station was operational. Each experiment was conducted
as a series of communication tests. The first experiment was conducted from
1 March 1989 to 30 May 1989. The communication tests were designed to
exercise the satellite system as if a real earthquake had occurred. The
system was tested twice each week. One test was conducted during peak load
(Monday 1300-1700 and Friday 1700-2200 GMT) while the other test was at random
during that week. For the first experiment, a total of 44 tests were
conducted with an average response time of 88 seconds and a median response
time of 47 seconds. Eighty-four percent of the tests were executed properly.
Of the seven failures, three occurred at peak load while five of the failures
occurred at 1300 GMT (0800 local time). This experiment indicated that the
GOES satellite communication system response and reliability were about the
same in 1989 as in 1986.
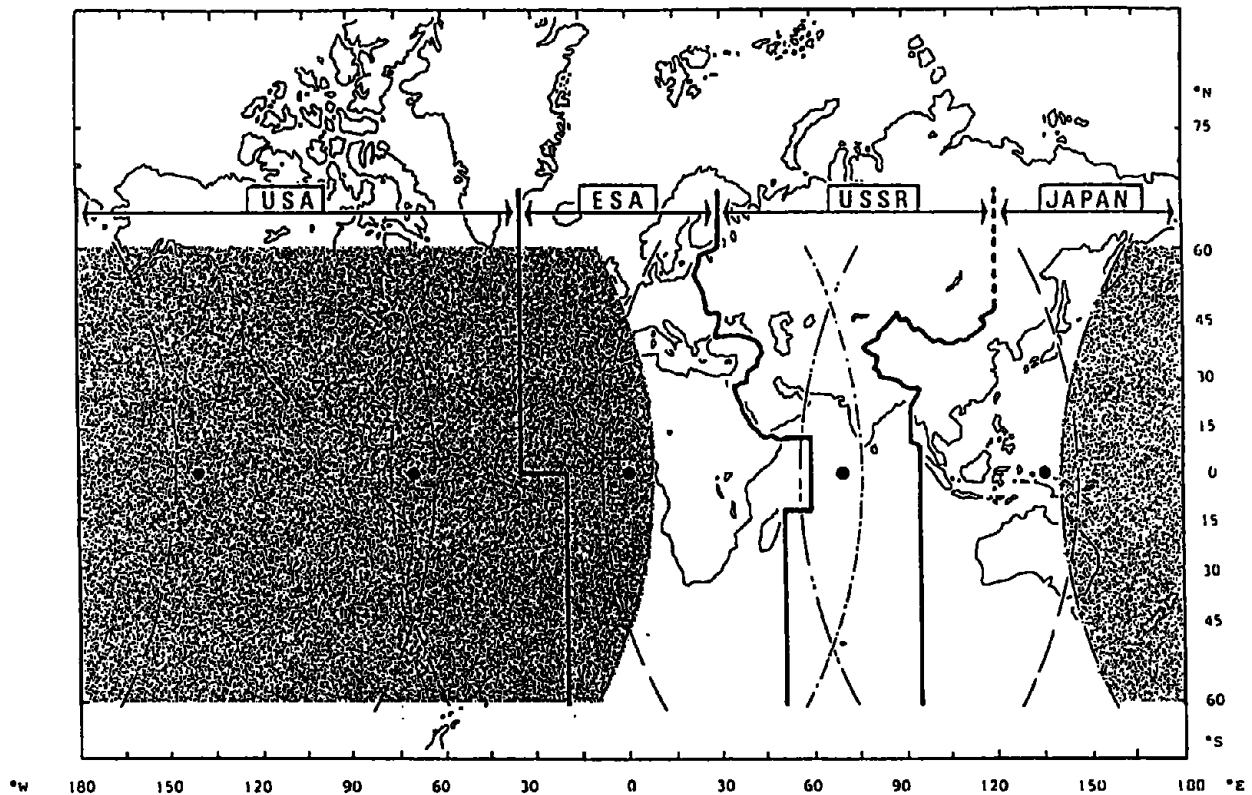
Figure 3. Global coverage of GOES communication footprints. Darkened
areas have THRUST emergency response capability.

The second experiment was conducted after the new satellite ground
station was operational during April, May, and June 1990. The procedures in
the first experiment were repeated as carefully as possible. During the
second experiment, 23 tests were conducted with an average response time of
17 seconds. All of the tests were executed properly. This experiment
indicated that the changes in the GOES system have improved the response time
by a factor of 5 (Figure 4).

The improved satellite system has an additional feature that tracks the
time of receipt of a "trigger" message and the time of transmission. For all
the tests conducted during the second experiment, the satellite processing
time was 1 second. That is, the time the GOES satellite received the THRUST
transmission to the time the GOES satellite system processed the message and
retransmitted the response was 1 second. The delays greater than 1 second
were due to processing within the THRUST equipment. With some engineering
design work, it seems feasible that the response time could be reduced even
more. At this stage of development, response times of 5-10 seconds appear to
be within technical reach. This signal tracking feature is also helpful in
diagnosing problems in the system. A malfunctioning receiver was identified
by tracing the signal through the system in November 1989. Upon replacement
of the receiver, the system functioned properly.

252

Average Response Time
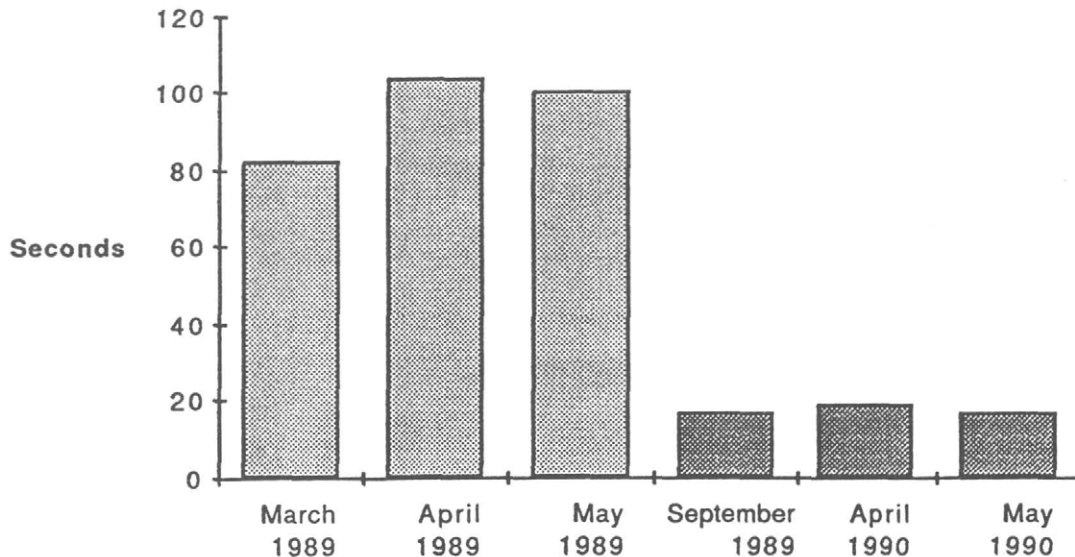
Figure 4. Comparison of response time of communication tests conducted before and after the ground station upgrade.

Future--Additional Applications of THRUST Technology

After 4 years of testing and improvements, the THRUST-type system's approach to hazard mitigation appears to work quickly (17 seconds) and reliably (greater than 90 percent). Application to other hazards would be straightforward and should include preevent preparedness, real-time local hazard assessment through environmental monitoring, and rapid alert through satellite communications. Of these three, the satellite communications offer the broadest application. THRUST experience has demonstrated that satellite communications is the preferred way to alert populations of hazards. Satellite communications are fast, reliable, and inexpensive, require low power (battery backup power is practical), and the satellite is removed from the local disaster (making it durable). These qualities are desirable for disaster mitigation.

Unlike conventional systems, this satellite-based alerting system does not rely on telephone lines and microwave links to connect sensors to people who must respond to the sensor activity. Instead, low-powered and inexpensive sensor transmitters utilize a satellite and its operational support system to relay coded information in a near-real-time mode. Communications with the satellite can be maintained during periods of power outages, ground motion, and local disturbances that cause conventional communication systems to fail at critical times. The large broadcast area of the satellite coupled with the low cost of transmit and alert stations makes it possible to locate sensors in multiple hazard locations and place numerous alert stations in potentially

affected areas for fast, effective response. The sensor and alert placement can be within a few feet of each other or as much as 12,000 miles (or any distance in between). Conventional alert systems require extensive human intervention and costly installations to provide similar, broad geographical coverage. In addition, the nature of conventional communication systems is to transmit through a network of retransmission units that deliver information in a serial fashion. The satellite-based system broadcasts the same information from space such that all receivers are alerted at the same time.

Summary

The chronology of Project THRUST can be summarized as follows:

Year	Event
1982	-- initial ideas
1984	-- project begins
1986	-- equipment installed and testing begins
1987	-- project "officially" ends (see Bernard et al., 1988)
1988	-- evaluation workshop (see Espinosa, 1989)
1989	-- equipment in use as operational system (see Lorca, 1990)
1990	-- improvements in satellite operations (average response time decreases from 88 to 17 seconds)

The string of successes for the project in this chronology indicates the robustness of satellite communications. The fast response time makes this system attractive for alerting people for rapid-onset disasters (such as earthquakes, landslides, flash floods, volcanoes, and even man-made events like nuclear power plant accidents and toxic material releases) that can be monitored by detection instruments. The broad geographical coverage makes the system desirable for alerting interested parties at near or far distances from the activity for taking evasive emergency action.

Acknowledgments

References

Bernard, E.N.; Behn, R.R.; Hebenstreit, G.T.; González, F.I.; Krumpe, P.; Lander, J.F.; Lorca, E.; McManamon, P.M.; Milburn, H.B. (1988) On mitigating rapid onset natural disasters. Project THRUST, EOS Transactions, American Geophysical Union, 69(24), p.649-661.

Espinosa, F. (1989) Proceedings of THRUST Workshop. Instituto Hidrografico Armada de Chile.

Housner, G.W. (1987) Confronting Natural Disasters: An International Decade for Natural Hazard Reduction. National Academy Press, Washington, DC.

Lander, J.F.; Lockridge, P.A. (1986) Uses of a tsunami data base for research and operations (abstract). EOS Transactions, American Geophysical Union, 67, p.1003.

Lorca, E. (1991) Integration of the THRUST Project into Chile's Tsunami Warning System. To be published in Natural Hazards.

Sokolowski, T.J. (1990) The Alaska Tsunami Warning Center. NOAA TM NWS AR-38, National Weather Service, Anchorage, AK.

Discussion

Question: Has the THRUST system triggered?

Response: No. Similarly, the Hawaii local warning system, installed in 1978, did not trigger until 1984. This has only been installed for four years. The infrequency of tsuanami occurrence is a problem for researchers. But, it is tested twice a day, and has been for four years; it is above 99 percent in its reliability. Those tests averaged about a 17 second response time. There are now over 200 actual simulations, and out of the 200, in the last 6 months, it has been 100 percent reliable. A 98 percent reliability from the Hawaii system would have been considered excellent. The first year operated, it was 73 percent reliable; the second year it was 86; and the third year, it was 94. Now it is operating at 99 percent. Any system, including JMA's which relies on microwave transmitters, can have big problems. In fact, the recent earthquake in San Francisco is a good example. The USGS has been adopting a satellite method of transmitting emergency data; they have one GOES transmitter. When the earthquake happened in 1989, their microwave tower fell down. The data stopped transmitting into Menlo Park. In fact, the PTWC was cut off, because that is their link to get data. The GOES satellite worked; it was the only data they got. That is how they knew that the earthquake occurred where it occurred. So that is an independent check on the robustness of the system - and in fact, the USGS has adopted a policy that has gone more and more to these kind of receivers instead of microwave towers.

Question: The information is still limited from the THRUST system, that is, simply an on/off communications that an earthquake occurred. Is there any possibility of expanding the bit word so that more data such as the arrival time or amplitude can be transmitted?

Response: Yes, the satellite people believe that with bit compaction techniques and the new software they have, that is certainly possible. In fact, before this idea was expanded globally, this capability would be a part of it. There are some keys that identify the kind of a disaster, and the place. Also GOES broadcasts a time code every 30 seconds; the time code leaves a few blank bits that can be stuffed with data, and sent out.

255

ROUND TABLE DISCUSSION OF TOPIC C

Comment: A discussion of the importance of the run-up over dry land part of the problem is in order here. There is a paper by Keller a number of years ago, where he demonstrated that in a solution of the linear long-wave problem with a wall right at the shoreline, the amplitude to which the water moves is exactly the same amplitude as the flooding amplitude on a sloping beach without friction. Furthermore, the high point on the wall and the high point on the sloping beach are exactly synchronized with each other; they go up and down together. If this is so, it seems that there is already a very good measure of how high the water would go without actually treating flooding over the dry land, if there was no friction, and that is about 98 percent of what needs to be known.

Question: It seems that this is something that is affected greatly by the slope.

Response: No, it is not affected at all by the slope. Some years ago, George Carrier talked about the Keller solution of the non-linear problem with flooding and the equivalence of that, at least as far as high water is concerned, to the linear problem with the wall right at the shoreline. And so, where there is complicated topography, it will not be possible to handle the details of flooding. On the average, the level of the flooding is going to be the same, excepting for the effect of friction, as the level of the water would rise right to a reflecting shoreline; and it is not dependent on the slope.

Question: Does that not depend very delicately on the fact that you have a plane slope? And particularly on no upslope changes that enhance the probability of breaking, because once breaking occurs the run-off probably will not be the same. I don't think you get that same run-off.

Response: Yes, that is right. It is a plane sloping beach.

Comment: It seems that much of what has been presented, and presumably observations indicate that the actual topography does induce breaking in many, many instances, and therefore the run-up is considerably smaller than the reflective wall analogy would give.

Comment: This can be 60 or 70 percent smaller than the predictions. For that topic, the maximum amplitude predicted by a non-linear theory on the plane beaches is exactly the same as the linear predictions, including wave conditions. The interesting part is that the time histories are completely different. Probably it has something to do with the energy conservation. The evolution is different. The maximum height for the plane beach is the same, but Professor Shuto has mentioned that the maximum amplitude for the real situation is not the same as on a plane beach. The real situation is a three-dimensional world with all kinds of lateral movement, including flow expansion, flow contraction, etc.

Question: The comment about the slope factor was assuming that in the real world there is some friction and so if the friction comes into play, then would it be independent of slope?

Response: The friction is only going to decrease the amount of flooding, so that the linear theory with no friction in a wall is going to give you a conservative or high limit.

Comment: The perfect reflection boundary condition we used for the present work because the information is needed rapidly. The values are not as good, compared with the ordinary case. For that case, the run-up boundary conditions are always obtained by using the natural topography. If the topography is one-dimensional, or only one plane beach composed of one or two slopes, then the linear theory and also the shallow water theory can give the same run-up height, but with different wave forms. But the practical application is different from this kind of one-dimensional case because there are steep slopes here and gentle slopes over there. This makes a lateral gradient which works to make the water particles move laterally, and as result of the sum of these kinds of things, we can determine the final inundated area. Therefore, for a rough idea of the run-up height, the perfect refraction at the boundary conditions and linear theory can be used. But this is not for detailed practical work.

Question: On a a different note, there have been three or four suggestions for various large-scale or observational systems, or ocean bottom sensors or shore-line sensors or satellite communications. Are there some ideas of how we are going to fund such programs?

Response: Is there any possibility this could be considered under the International Decade for Natural Disaster Reduction (IDNDR)? Bernard expanded the idea of the THRUST Project from tsunamis to volcanoes, landslides, etc., which is, of course IDNDR territory. That might be a possible source of funding.

Comment: I've been discussing this with the United States Decade program, and as of right now, there is a pilot proposal in the system to study five hazards simultaneously using this type of system. This will have the acronym, WARN, which stands for Warning and Alert Response Network. What has been discussed at the national committee is five disasters including earthquakes, volcanoes, landslides, floods, and storm surges.

Question for Dr. Okada: When are the estimates that the cable mounted deep water sensors near Guam are going to become operational and able to contribute to a warning system?

Response: The ocean bottom cable from Japan to Guam, the PPC cable, hopefully will be operational within two years. Next fiscal year, near the end of March 1992, funds for the main improvements for measuring, including tsunamis and seismicities will be received. Actually, just in the beginning of November 1990, the cable was accepted by the Earthquake Research Institute from the telephone company, and within two years, all the sensors will be on the PPC cable.

Question: There was a meeting just a few months ago and the U.S. was going to try to put sensors in from its end, as well as on the Japanese end. Have you heard anything from it since the meeting?

Response: Well, reaction of the oceanographic community to this cable was that it was a rather expensive way to get low data rates into the system. From a seismological standpoint, it is

needed because they have such high data streams. But it has not been well received by the oceanographers. No one knows what the price tag is for collecting the data.

Question: What about putting a couple of pressure gages on it too?

Response: Well, it is one of those things that is pay as you go and the price tag may be something like $300,000. Lots of deep-sea instruments could be deployed for that price, perhaps even those able to transmit to the surface acoustically.

Response: Discussion for this project is now falling under the purview of IRIS program and they are promoting it. The seismologists need the high data rate.

Comment: The topic was changed to of the use of the numerical model in relation to the potential measures. Seven years ago, just before we had the UJNR workshop in Tsukuba, the Japanese Ministry of Construction and the Ministry of Agriculture cooperatively proposed to make plans to protect the coastal areas, which often are hit by tsunamis. The proposal was made in March 1983, and had three major parts. The first part is for disaster prevention structures, the second is for local regional planning for disaster prevention, the third is a disaster prevention system. Disaster prevention structures, including sea walls or sea dikes, tsunami breakwaters, and tsunami river dikes, are called for. Numerical models are necessary to assess the effectiveness of these structures. The second part of the plans calls for local and regional planning for disaster prevention, including the relocation of houses to higher ground. It is necessary to determine the possible flooded area, and the limitations of the land use. Maps have been prepared which show the tsunami inundation limits without a sea wall. To evaluate this kind of reduction in the area, a very accurate inundation numerical model is necessary to evaluate the effects of buffer zone on the tsunami by use of a control forest and sea walls. Another aspect calls for analyzing the location and site of the public buildings, such as hospitals, schools and administrative offices. To determine the risk to public buildings, a more accurate numerical model than we have now is needed. The model now available is good enough to evaluate the maximum height of the runup and to determine the flooded model, but it is not sufficient to evaluate the actual force on the strucutre. Further study is needed to evaluate how to control or how to protect traffic facilities from tsunamis. Roads and railways useful as rescue roads or evacuation roads must be identified. Again, a numerical model may be needed for this. To summarize these items, we need to strengthen existing buildings, and design resistent buildings, and learn how to protect against the dangerous impact of an oil slick or dangerous gases, etc. The behavior of oil slicks needs to be estimated, just as Dr. Goto and Dr. Matsutomi did. Also, fisheries and harbors are important to Japan because of the large numbers of aquaculture industries. These are additional reasons for the development of a reliable numerical simulation. For effective forecasting and warning, numerical simulations are necessary. Also, a reduction of the time required to determine the location of the epicenter is needed. Another aspect of tsunami awareness is public education. A computer graphic tsunami simulation can help the public school understand the hazard. There are many ways to use numerical simulations of tsunamis for disaster prevention.

Comment: Regarding those timbers and other dangerous objects affected by a tsunami – those are water borne missiles! They have been studied quite a bit in the United States. About 15-20 years ago, when nuclear power plants were planned, the Nuclear Regulatory Commission

259

required that the effects of water borne and also airborne missiles be considered. There is a lot of data available which somebody still should look at.

Lander: In closing, I would like thank you for your participation. I think we had a very good meeting. I was gratified that this general discussion idea seemed to work. I was impressed with the good quality of papers. But there is one question that I would like to comment on. We are all very busy and there seem to be too many meetings to go to, but there is some advantage to having UJNR workshops on a regular basis.

These workshops do take time, but I feel that it helps us all in a lot of ways. First of all, it requires us to focus our attention back onto a problem and get it into some sort of shape so we can present it. You heard how many people were still thinking about their problems the morning before they were going to give their talk. I think that is a plus. I do know, or I believe, if these meetings are held on a regular schedule, it would cut down on the inertia in trying to organize one. When we had an open-ended time for a future meeting, it was easy to put it off to a less busy time, that never seemed to come. When the urgency is gone from it, the problem of trying to get it scheduled can very easily put off. There is an advantage of having them on a regular basis, but I am also conscious of the fact that we are very busy and that you don't want to have so many meetings that there is no time left to do any work. Perhaps such meetings should be scheduled every two or three years.

Thank you all for your good efforts to share the results of your work and your thoughtful comments.